THE UNIVERSITY *of* EDINBURGH

Harnessing Resonance with Adjustable Stiffness for Persistent Peak Efficiency: Design, Fabrication, and Characterization of a Heart-Inspired Pulsatile Pump.

Paul Baisamy

Doctor of Philosophy

THE UNIVERSITY OF EDINBURGH

2025

To my family,

"What a blessing to be tired in the pursuit of a challenge of your own choosing."
Anonymous.

Abstract

Pulsatile flow is a fundamental mode of fluid transport in biological and environmental systems. This unsteady flow regime is exemplified in cardiovascular circulation, in the locomotion of cephalopods and jellyfish, in the roots of certain plants and many other natural phenomena. The temporal and spatial variations inherent in pulsatile flow not only regulates mass transport but can also support efficient energy usage, underscoring its importance in physiological functions. In the field of mechatronics, the capability to produce highly unsteady flow regimes constitutes a critical asset for the actuation of pressure-driven soft robotic systems, the regulation of fluidic circuitry, and the propulsion of autonomous aquatic platforms. Notably, in biomedical engineering, the generation of controlled pulsatile flow patterns is of particular significance for the development of cardiac assist devices that more faithfully emulate the physiological dynamics of the native heart. By enabling flow characteristics more closely aligned with natural cardiovascular function, this technological approach offers a promising pathway for improving therapeutic outcomes and addressing the increasing prevalence of cardiovascular diseases in an aging global population.

Despite its significance, generating controlled and efficient pulsatile flow across a broad range of frequencies remains a challenge that current pumping technologies fail to meet. This thesis addresses this gap by investigating the physics underpinning optimal pulsatile pumping and by developing a novel pumping system capable of optimal operation over a wide frequency bandwidth.

Inspiration is drawn from biological shape-changing mechanisms such as the beating heart or the mantle-driven propulsion of cephalopods as they present four highly sought-after features: pulsatility, compactness, efficiency and preservation of fluid integrity. Specifically, pulsatile self-propelling systems have been shown to successfully exploit resonance to enhance propulsive efficiency, similarly to what certain sea-dwelling organisms do, hinting at the opportunity to exploit the same benefit in pumping systems. Although resonance has been widely exploited in mechanical systems, its potential in fluid pumping mechanisms, and particularly in pulsatile flows, has never been systematically investigated. This work introduces, for the first time, a resonance-based approach to pulsatile fluid pumping, demonstrating its efficacy in improving flow performance and system efficiency. In order to leverage resonance across a broad range of pulsation frequencies, this work introduces variable stiffness as a means to actively tune the system's natural frequency. Although

stiffness modulation has been implemented in other engineering systems, its use for controlling transition to resonance is sparse and almost unheard of in the context of fluid displacement technology making this approach the first of its kind.

This thesis presents the design, development, and experimental validation of a variable-stiffness, heart-inspired, pulsatile pump.

We begin by designing a custom variable stiffness mechanism, specifically developed for seamless implementation within robotic artefacts that require adaptable mechanical properties. Building upon this, we engineer a pulsatile pump inspired by the heart's dynamic pumping strategy, integrating the variable stiffness mechanism to actively modulate system compliance. The resulting device is experimentally tested, revealing how its flow patterns evolve as the pump approaches resonance. Characteristic features emerge in the pressure–flow rate relationship, including amplitude magnification and phase shifts, which collectively identify regions of maximum operational efficiency. Crucially, we demonstrate that the introduction of variable stiffness can enable the pump to transition smoothly across a range of pulsation frequencies while persistently maintaining peak performance. To our knowledge, this represents the first demonstration of a heart-inspired pumping system with the potential to sustain optimal efficiency across variable operating conditions through active stiffness modulation.

In summary, this thesis proposes and validates a novel approach to harnessing mechanical resonance in pulsatile pumping through stiffness modulation. This new technology lays the groundwork for advanced soft robotics actuation systems and, crucially, for the development of next-generation cardiac implants. By enabling a mode of operation more closely aligned with the physiological dynamics of the human heart, while offering enhanced performance and persistent autonomy, this approach addresses some of the most critical challenges in the treatment of cardiac diseases. Moreover, by combining higher operational efficiency with a nature-inspired pulsatile pumping strategy, it promises to enhance biocompatibility and extend device longevity, overcoming longstanding limitations of both commercial and state-of-the-art cardiac assist systems and advancing the design of durable, adaptive, and physiologically harmonious cardiovascular therapies.

Lay Summary

Heart failure is one of the world's leading causes of death and disability. Many patients rely on mechanical pumps to help circulate blood, but most of these devices provide a continuous flow, unlike the natural pulsing of the human heart. This lack of pulsation can cause long-term complications and limits how well these devices integrate with the body.

This thesis explores how principles found in nature—particularly those governing the rhythmic, efficient movements of the heart and other living organisms—can be used to design better artificial pumps. The research focuses on the concept of resonance, a physical phenomenon that allows systems to move more efficiently when they vibrate at their natural frequency. By designing a pump that operates in resonance, energy use can be reduced while maintaining strong, rhythmic flow.

To make the system adaptable, the pump includes a variable stiffness mechanism—a way to change how flexible or rigid parts of the pump are in real time. This allows the pump to adjust its natural frequency automatically, much like the human heart changes its rhythm and force under different conditions such as rest or exercise.

The result is a heart-inspired pulsatile pump that can sustain efficient, rhythmic flow across a range of speeds. Experiments confirmed that adjusting stiffness enables the pump to stay at peak efficiency even as conditions change. This marks the first demonstration of resonance tuning through stiffness control in a heart-scale pumping system.

In the future, this technology could improve artificial hearts and cardiac assist devices, making them more energy-efficient, adaptable, and physiologically natural. Beyond medicine, the findings may also benefit soft robotics and other engineering fields that require efficient, rhythmic motion.

Acknowledgements

Well, it has been quite a journey. People often say that doing a PhD is an adventure full of unexpected turns, but I could never have imagined how profoundly life-changing this experience would be. These past years have transformed me in ways I could not have foreseen, shaping not only my knowledge but also my values, my resilience, and my outlook on life. I am deeply grateful to have taken this path and to have met the people who made it so meaningful.

First and foremost, I wish to express my deepest gratitude to my supervisor, Dr. Francesco Giorgio-Serchi, for his unwavering support, patience, and kindness throughout these years. From our very first interview to the final stages of this journey, Francesco has been an extraordinary mentor: compassionate, understanding, and always ready to help when I needed it most. I had been told before starting my PhD that the supervisor can make or break the experience, I could not have hoped for a better one.

Francesco was always there for long conversations that never failed to lift my spirits and bring clarity to my thoughts. He guided me through personal, academic, and even financial challenges with generosity and calmness, and continually reminded me of the value of my work when my own perfectionism clouded my perspective. Even when I stubbornly ignored his advice or went down unpromising rabbit holes, he remained patient, smiling, and supportive. His openness allowed me to explore ideas well beyond the original scope of the project, which taught me more than I could have imagined and helped me grow both as a researcher and as a person. The trust, encouragement, and freedom he gave me have been among the greatest gifts of my PhD, and I will be forever grateful. I have created countless happy memories under his supervision, and I will carry them with me always. Thank you Francesco, truly.

I would also like to thank Dr. Yunjie Yung and Delin Hu at the University of Edinburgh, for their kindness and with whom I had the pleasure of collaborating on side projects. The experiences and insights gained from these collaborations have inspired ideas that may one day blossom into future research endeavours. I am equally grateful to Professor Adam A. Stokes for his co-supervision and for his valuable advice and perspective whenever called upon.

I would also like to thank Jonah Mack, Maks Gepner, Zurong Zhang, Bingchao Wang, and Dr. Leo Micklem for their camaraderie and the many enjoyable days we shared in the lab.

This work was made possible through financial support from the Engineering and Physical Sciences Research Council (EPSRC) via UK Research and Innovation (UKRI). I also wish to express my sincere thanks to the Innovation Fund of the Centre for Doctoral Training in Robotics and Autonomous Systems, whose belief in my project on resonant cardiac assist devices gave me the freedom to pursue this vision from the very beginning.

Finally, I would like to thank my friends, both in Edinburgh and back in France, for their constant presence, laughter, and encouragement. To my sisters, who have shaped me more than they realise, and to my parents, who have always invested everything they had in our happiness: thank you for your unwavering love and support. And yes, I may have quit my engineering job to do this, but I think we can all agree now: it was worth it.

Declaration

I declare that this thesis was composed by myself, that the work contained herein is my own except where explicitly stated otherwise in the text, that this work has not been submitted for any other degree or professional qualification except as specified, and that any included publications are my own work, except where indicated throughout the thesis.

Paul Baisamy

Contents

Figures and Tables

Figures

Tables

Abbreviations

Abbreviations

- FDM: Fused Deposition Modeling (3D printing technique)
- FFT: Fast Fourier Transform
- ID: Inside Diameter
- MSD: Mass-Spring-Damper
- OD: Outside Diameter
- PD: Positive Displacement
- PET: Polyethylene Terephthalate
- SLA: Stereolithography (3D printing technique)
- VSM: Variable Stiffness Mechanism
- LTI: Linear Time Invariant.

Chapter 1

Introduction

This chapter provides an initial introduction to the motivation behind the work, discussing the relevance and importance of the topic before detailing a set of specific research objectives. Next, the specific contributions are listed, before finally giving an overview of the thesis structure and chapter organisation.

1.1 Motivation

In many modern engineering applications, the ability to generate and control unsteady or oscillatory flows holds immense promise for improving performance and energy efficiency. In industrial systems such as fluid transport, mixing and heat-exchanger networks, imposing temporal variations in flow can reduce losses, suppress instabilities or enhance transfer rates compared to steady operation (21). In robotics and soft actuators, fluidic systems increasingly rely on compliant components and dynamic motion. Yet, many still default to quasi-steady pumping, which fails to exploit their inherent elastic and inertial characteristics (22). By operating these systems in an oscillatory regime, they can harness natural system dynamics to improve performances (23).

This need for non-continuous efficient flow generation is critical in biomedical engineering given the widespread occurrence in the human body of organs which operate under unsteady flow conditions, such as the oesophagus (24), the intestine (25), the pulmonary system (26) or the ureter (27). It is especially acute in the design of cardiac assist devices. Indeed, in the world, sixty million people suffer from heart failure and during the last 30 years both heart failure prevalence and years lost due to disability have increased respectively by 3.9 % and 4.5 % (28). In 2020, for the six millions Americans suffering from heart failure, the total expenditure on heart 2 failure is estimated at 43.6 $ billion. This amount is expected to keep growing as scientists predict a 24 % increase in the number of Americans suffering from this medical condition in 2030 (29). In Europe, in 2020, more than 15 million people lived

with heart failure (30) and hospital admissions for this condition have been projected to rise by 50% between 2010 and 2035 (31). While the native heart produces rhythmic pressure–flow pulses, most mechanical circulatory support systems today employ continuous-flow pumps (32) (33) for reasons of simplicity, size and durability. However, the absence of physiological pulsatility has been linked to adverse vascular remodeling, impaired end-organ perfusion and increased complications (34), (35), (36), (37), (38). Currently, in the two years following the implantation, around 80 % of patients develop a severe complication requiring rehospitalization which sometimes prove fatal. Reintroducing pulsatile flow into implantable devices therefore remains a major research challenge: achieving true pulsatility in a compact, low-power system adapted for long-term implantation. To date, few solutions have successfully balanced physiological flow dynamics, device miniaturisation and energy efficiency. Additionally, current solutions require patients to carry large battery packs in backpacks to power the device, highlighting the need of optimal efficiency for reduced footprint.

Nature provides compelling examples of how oscillatory or pulsatile flows can be generated and exploited efficiently via elastic and resonant mechanisms. In the cardiovascular system, the heart contracts rhythmically and interacts with compliant blood vessels, forming a coupled elastic–inertial system that stores and releases energy cyclically—a form of resonant behaviour enabling efficient circulation (39). In soft-bodied aquatic animals, like certain jellyfish or squid, locomotion arises from harnessing body elastic recoil and fluidic added mass to achieve propulsion with minimal muscular effort (40). These organisms illustrate how a finely tuned balance between elasticity, inertia, and active muscular contraction can provide a level of adaptability and performance that artificial systems have yet to replicate. Particularly, they show how resonance, the matching of excitation to a system's natural frequency, yields improved energetic return (41). By adopting these principles in engineering design, pulsatile pumps might similarly exploit system compliance and inertial interactions to achieve higher outputs for the same or lower input energy.

In summary, the generation of unsteady flows is a critical and timely challenge across both engineering and biomedical domains. The biomedical imperative to reintroduce physiologically relevant pulsatility in cardiac assist devices aligns with the broader engineering goal of efficient fluidic actuation in robotics and industry. By drawing inspiration from nature's elastic and resonant systems, there lies a promising pathway: leveraging resonance and adjustable stiffness mechanisms to amplify output and enhance efficiency in pulsatile pump design.

This thesis focuses on bridging the gap between physical understanding and

engineering implementation. Rather than optimizing a single technological aspect such as actuation or biocompatibility in isolation, it aims to identify and validate the fundamental physical mechanisms that underlie efficient pulsatile flow. By demonstrating the feasibility of resonance-based pumping and active stiffness modulation within a heart-scale prototype, this work contributes both to the understanding of energy transfer in oscillatory fluid systems and to the development of next-generation implantable cardiac assist devices.

1.2 Research objectives

The primary objective of this research is to investigate the potential of mechanical resonance as a means to enhance the efficiency of pulsatile pumping systems. Specifically, the thesis seeks to:

1. Demonstrate the feasibility of operating a compact pump at or near its resonant frequency to amplify output flow and pressure while minimizing energy input.

2. Develop and integrate a variable stiffness mechanism that enables active tuning of the system's natural frequency, allowing resonance to be maintained under changing operating conditions.

3. Establish an analytical framework linking actuation force, displacement, and power transfer in resonant systems, and use it to predict and interpret experimental results.

4. Experimentally characterize the resonant response of the developed pump and quantify the effects of damping, stiffness, and hydrostatic loading on energy efficiency.

5. Evaluate the scalability and adaptability of the resonance-based approach for biomedical applications, particularly in cardiac assist systems where compactness, controllability, and energy efficiency are critical.

Together, these objectives aim to translate a physical principle - resonance - into a practical design strategy for efficient, adaptable, and physiologically compatible pumping technologies.

1.3 Thesis Contribution

This thesis provides both theoretical and experimental contributions to the field of resonant pumping and variable-stiffness actuation. The main achievements can be summarized as follows:

1. Conceptual contribution: A comprehensive analysis of resonance as a design paradigm for pulsatile pumps, establishing the conditions under which energy transfer is maximized and losses minimized.

2. Analytical contribution: The development of a simplified rigorous mathematical framework describing the coupled electromechanical–hydraulic dynamics of a resonant pump, including harmonic power transfer and efficiency scaling laws.

3. Technological contribution: The design and realization of a novel Compact Modifier of Active Coils (C-MAC) mechanism, capable of continuously tuning stiffness through electromagnetic coupling while remaining compact, low-power, and easily manufacturable.

4. Experimental contribution: The construction and validation of a heart-scale prototype incorporating variable stiffness, enabling the first experimental demonstration of resonance-induced performance enhancement in a pulsatile pump.

5. Practical impact: The establishment of experimentally validated design guidelines that can inform the development of future cardiac assist devices and adaptive fluidic systems relying on similar resonant dynamics.

Collectively, these contributions demonstrate that resonance and stiffness modulation can be exploited as fundamental principles for improving the efficiency and adaptability of pulsatile flow systems.

1.4 Structure Outline

The thesis is organized as follows:

- Chapter 2 surveys the state of the art in industrial and biomedical pumping technologies, the role of pulsatility in cardiovascular function, and the potential of resonance and adaptive stiffness in energy-efficient systems.

- Chapter 3 defines the functional and design criteria for a resonance-driven pump and introduces the conceptual architecture, including the variable stiffness mechanism.
- Chapter 4 details the mechanical realization of the prototype, its integration with sensing and control systems, and the experimental setup used for characterization.
- Chapter 5 develops the mathematical framework for predicting the system's response under harmonic excitation and for identifying key parameters in resonance exploitation.
- Chapter 6 presents the experimental validation of resonance effects, analysing the relationships between frequency, amplitude, and efficiency and validating the mathematical predictions.
- Chapter 7 explores how changes in stiffness shift the resonance frequency and affect dynamic performance, establishing scaling laws for tunable resonance.
- Chapter 8 synthesizes the results, outlines the limitations of the current study, and provides recommendations for future work, including applications to cardiac assist devices and adaptive robotic systems.

Chapter 2

Literature review

2.1 Introduction

The purpose of this chapter is to situate the present work within the broader scientific and technological context of pumping systems, pulsatile flow generation, and adaptive actuation. While pumps are among the most mature and widely used energy-conversion technologies in engineering, their design principles remain largely grounded in steady-flow operation. In contrast, most biological systems—particularly the cardiovascular system—rely on inherently unsteady or pulsatile flows to achieve efficient, adaptable, and physiologically compatible transport. Understanding this contrast between engineered and biological paradigms is essential to motivate the development of resonance-based and stiffness-modulated pumping strategies explored in this thesis.

The chapter begins by reviewing industrial pumping paradigms, distinguishing between rotodynamic and positive-displacement designs and analysing their characteristic pressure–flow behaviour, control strategies, and limitations when applied to unsteady operation. This establishes a baseline for understanding the physical and energetic constraints that conventional pumps face when attempting to generate pulsatility.

The discussion then transitions to bioinspired pumping mechanisms, focusing on how nature exploits unsteady flows to optimise energy efficiency, mixing, and adaptability. Examples are drawn from biological systems ranging from peristaltic transport in soft-bodied organisms to the human cardiovascular system, where pulsatility and compliance are fundamental to sustaining efficient flow and regulating shear stresses. Particular attention is given to the heart, which operates as a positive-displacement pump whose coupled interaction with the vascular network results in resonant-like energy exchange between elastic and inertial components.

Building on this physiological foundation, the review examines the evolution of car-

diac assist devices, tracing the shift from early pulsatile designs to modern continuous-flow systems and discussing the consequences of this transition for patient outcomes, vascular health, and device efficiency. The analysis highlights the ongoing challenge of achieving physiological pulsatility within the severe constraints of implantable devices—where compactness, controllability, and energy autonomy are paramount.

The final sections of the chapter focus on resonance and adaptive stiffness as emerging design principles for efficient actuation. Resonant operation allows mechanical and fluidic components to exchange energy cyclically with minimal losses, while tunable stiffness offers a means to adapt the natural frequency of the system to changing operating conditions. Together, these mechanisms offer a promising route toward compact, energy-efficient, and adaptive pumps capable of reproducing the dynamic behaviour of the heart.

Overall, this literature review provides the conceptual and theoretical groundwork for the experimental and analytical investigations that follow. It identifies the limitations of current industrial and biomedical approaches and establishes the scientific motivation for exploring resonance and stiffness modulation as complementary strategies for the next generation of pulsatile pumping technologies.

2.2 Industrial Pumping Paradigms

Pumps are among the most widespread energy-conversion devices in engineering, serving to transfer mechanical energy from a driver—typically an electric motor—into the hydraulic energy of a working fluid. Their operation can be broadly divided into two physical principles: *rotodynamic* pumping, based on the continuous exchange of momentum between a rotating impeller and the fluid (42), and *positive displacement* (PD) pumping, based on the periodic confinement and expulsion of a finite fluid volume (43). Although both classes accomplish the same overall task, their internal mechanisms, flow–pressure characteristics, and control strategies differ fundamentally. Understanding these differences is essential before exploring how biological systems diverge from these industrial paradigms.

2.2.1 Working Principles and Types of Pumps

In rotodynamic pumps, energy is imparted dynamically through angular-momentum transfer. As the impeller rotates, it accelerates the fluid, increasing its kinetic energy; this velocity is subsequently converted into pressure energy in a diffuser or volute casing. Depending on impeller geometry and specific speed, rotodynamic pumps are further categorized as *centrifugal*, *mixed-flow*, or *axial-flow* types (44). Centrifugal pumps dominate industrial applications: fluid enters axially and exits radially, making them effective at producing moderate heads with steady flow. Axial-flow pumps, by contrast, use impeller blades acting as hydrofoils to impart energy primarily along the pump axis, producing very high flow rates but low heads. Mixed-flow pumps occupy an intermediate regime and are employed when both head and flow requirements are moderate (42) (45).

Positive-displacement (PD) pumps operate by mechanically displacing a confined volume of fluid into the discharge line. During each cycle, valves or clearances control suction and delivery, so that a specific volume V_d is transferred per stroke or revolution. The theoretical flow rate is therefore:

$$Q = V_d N, \tag{2.1}$$

where N is the rotational or reciprocating speed (46). The PD family includes reciprocating pumps, such as piston, plunger, and diaphragm designs, and rotary pumps, including gear, screw, vane, and progressing-cavity configurations. Reciprocating pumps deliver very high pressures and precise volumes with pulsatile flow, while rotary designs generate smoother output and are particularly effective for viscous or shear-sensitive fluids (43). In both cases, the pump's role is to deliver a defined volumetric displacement, while the pressure it develops depends on the resistance of the connected system (46).

This approach ensures predictable performance and is well suited to industrial environments demanding steady, controllable output.

2.2.2 Flow–Pressure Characteristics and Control Strategies

The differing energy-transfer mechanisms of rotodynamic and PD pumps give rise to distinct flow–pressure relationships. A rotodynamic pump behaves as a *pressure source*. For a given rotational speed, it produces a characteristic head–flow curve where the head decreases as flow increases (47). The operating point of the system is found at the intersection of this curve with the system's resistance curve, which depends on pipeline friction and static head. Adjusting speed shifts the pump curve and thereby regulates the flow rate.

A positive-displacement pump, on the other hand, behaves as a *flow source*. The flow rate is nearly independent of system resistance, and the discharge pressure simply rises to whatever level is needed to deliver the displaced volume (48). In practice, small leakage paths cause a modest pressure-dependent reduction in flow known as "slip," but this effect is minor compared with the steep flow–pressure coupling of rotodynamic pumps (49).

From a control perspective, industrial pumps are typically operated in one of two modes: (i) *speed control*, in which the motor speed is adjusted to meet target flow or head conditions (common for rotodynamic pumps) (50) (51) (52); and (ii) *displacement control*, in which the stroke or speed of a PD pump is prescribed to achieve a precise volumetric delivery. In both modes, the objective is to impose predictable, steady behaviour. Dynamic interactions between pump inertia, fluid compressibility, or structural elasticity are regarded as disturbances to be minimised (53). Any oscillatory effects such as pulsation in PD pumps or surge in rotodynamic pumps are mitigated using dampeners, accumulators, or feedback loops.

2.2.3 Limitations of conventional control

Although displacement and speed-based control strategies ensure stability and reliability, they inherently suppress the dynamic adaptability of the pump–fluid system (54). By prescribing motion or speed, the system's degrees of freedom are constrained: potential interactions between inertia, elasticity, and damping are effectively frozen out. As a result, conventional pumps operate efficiently only in steady regimes and cannot take advantage of resonant amplification or elastic energy storage that might reduce energetic cost in oscillatory operation.

In industrial design, such dynamic effects are typically seen as undesirable because they introduce noise, vibration, and wear (55). However, this suppression of natural dynamics also prevents energy recovery or self-tuning behaviour and high-

lights a fundamental drawback of conventional control strategies. As a result, these strategies often impose continuous energy input to compensate for disturbances, damping, and load variations, leading to reduced overall efficiency.

In contrast, the approach proposed in this thesis seeks to leverage the natural dynamics of the system through force-driven actuation and resonance (further detailed in Section 2.5.1). By allowing the motion to emerge from the interaction between actuation, compliance, and fluid loading, the need for strict trajectory control is reduced. This enables more efficient energy transfer, as the system can exploit cyclic energy exchange between inertial and elastic components rather than opposing it through active control.

This approach is found in biological systems, where compliant elements and force-based actuation enable adaptive, pulsatile, and often resonant operation. In biological systems, force generation and structural compliance produce inherently pulsatile flows that adapt to changing loads—a paradigm that offers valuable inspiration for more efficient and adaptive artificial pumps (56).

2.3 Bioinspiration and Physiological Flow

The limitations of conventional industrial pumps, which rely on speed or displacement control and are often optimized for continuous flow generation motivate the search for more adaptive and efficient pumping strategies. Nature offers a rich source of inspiration in this regard. Across biological systems, fluid transport is rarely steady: it is typically pulsatile, compliant, and dynamically coupled to the surrounding structure. This section explores how biological systems achieve efficient and adaptive pumping through force generation, elasticity, and self-regulation, with particular attention to the cardiovascular system.

2.3.1 Unsteady and Pulsatile Flow in Nature

In contrast to the steady output sought in engineered pumps, most biological fluid-transport systems exhibit intrinsically unsteady behaviour. Fluid ejection mechanisms are found in countless animals spanning various taxa, timescales, and physical scales (57).

In the human body, different processes are used for non-continuous flow generation. Peristaltic pumping is observed in tubular organs. Rhythmic, wave-like contractions of smooth muscle in the gastrointestinal tract (25) and ureter (27) propel

contents in pulses rather than steady flow. Ciliary fluid transport is also observed in the human body. It harnesses the coordinated beating of motile cilia (small hair-like protuberances) to generate directional, time-periodic fluid currents. To carry the mucus away from the respiratory tract, cilia beat in an organized manner displacing the mucus along a wave called the metachronal wave beating at around 15Hz (58). Cilia are also found in the brain to circulate cerebrospinal fluid which acts as a shock absorber providing protection to the brain inside the skull (59)(60). Finally, pulsatile waves induced by cilia are also present in the fallopian tubes where cilia propel the ovulated egg from the ovary towards the uterus and distribute tubal fluid throughout the tubes (61). Finally, the heart is certainly the most evident example of a source of unsteady flow, specifically *pulsatile* flow.

In a similar manner, some sea-dwelling animals use pulsed-jet propulsion to swim (62). Similarly to the heart, these natural pumps rely on periodic cycles of compression and relaxation that alternately accelerate and decelerate the working fluid, leading to time-varying flow and pressure patterns. The geometry of these biological pulsatile thrusters can lead to various performances. Whether optimized for efficiency, such as with the Aurelia Aurita (40) (63) (64), or for fast power generation in squids for instance(65) (66), the extend of the capacities provided by pulsatile swimming is outstanding. Even some insects such as the dragonfly larvae exploits pulsatile propulsion (67).

The prevalence of non-continuous or intermittent locomotion in nature is appears to be mostly justified by energy gains. In fish and birds, intermittent motion often reduces energetic cost by alternating active thrust phases with passive coasting, thereby minimizing drag (68) (69). Hydrodynamic models show that this strategy can outperform continuous propulsion when duty cycle and body stiffness are optimized (69). However, its efficiency advantage depends on drag ratios and kinematic parameters, and may not always surpass continuous swimming (70). From a broader evolutionary perspective, rhythmic patterns of rapid propulsion followed by drift—seen in frogs, jellyfish, and fliers—reflect a universal design tendency toward energy-efficient movement (71). Overall, the prevalence of intermittent motion suggests it is an evolved, adaptive strategy to balance power generation and energy conservation across taxa (72).

In regards to the human vascular system, pulsatility serves several physiological advantages. It enhances mixing and mass transport, prevents stagnation, and allows momentary pressure peaks that facilitate perfusion in distributed networks such as capillaries (73)(74). In addition, pulsatile flow helps the cells lining the blood vessels

sense and respond to mechanical forces. These oscillations in shear stress are important because they regulate how the vessels contract and relax and control the production of nitric oxide, a key signaling molecule that keeps blood vessels healthy and flexible (75) (76). From an energetic standpoint, periodic motion allows biological systems to store and release energy elastically, improving efficiency through temporary energy recycling rather than continuous work input.

The prevalence of pulsatility in nature arises not from deliberate flow modulation but from the way biological actuators generate motion, through active force production rather than prescribed displacement.

2.3.2 Force Control in Biological Pumps

Muscular systems in living organisms function as *force generators*. At the cellular level, contractile units (sarcomeres) develop active tension by actin–myosin cross-bridge cycling, and the resulting shortening depends on the external load (77)(78). This principle is described by the classical Hill muscle model, where the shortening velocity decreases as load increases, reaching zero under isometric conditions (79) (80). Hence, muscles do not impose a fixed displacement; they generate force, and the movement that follows is the outcome of the interaction between muscle force, tissue elasticity, and fluid pressure.

This force-controlled nature of biological pumps has profound implications. It allows natural systems to self-regulate and adapt instantaneously to changing mechanical conditions. If external resistance increases, muscles generate the same contractile force but shorten less, maintaining functional equilibrium without explicit feedback control. Conversely, under reduced load, the same contractile activation results in greater displacement and higher flow. Such self-adjustment is exemplified by the Frank–Starling mechanism of the heart, where ventricular filling (preload) stretches myocardial fibers, enhancing force generation and stroke volume (81) (2).

In addition to active contraction, biological pumps include compliant components—elastic tissues, membranes, and vessels—that store and release energy throughout the pumping cycle (82). This coupling between active force generation and passive compliance produces complex dynamic behaviours. While industrial designs often suppress such dynamics, nature exploits them to achieve efficiency, resilience, and adaptability.

Among all biological pumps, the human heart represents one of the most sophisticated example of force-driven positive-displacement pumping and thus provides a

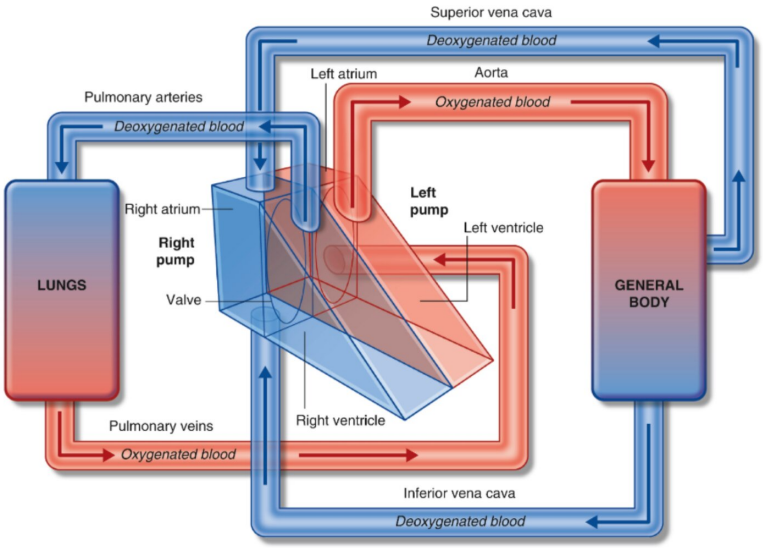

Figure 2.1: Simplified representation of the human heart (1). The heart has two pumps, one on the left side and one on the right side. The right pump sends blood the lungs in order to be oxygenated. The left pump distributes the oxygenated blood to the body.

valuable model for understanding the principles of bioinspired pumping.

2.3.3 The Human Heart as a Positive-Displacement Pump

The human heart functions effectively as a positive-displacement pump, rhythmically ejecting blood into the arterial system through a well-coordinated sequence of chamber contraction, valve opening/closing and vascular interaction. It is made of two individual pumps that are responsible for pumping deoxygenated blood to the lung and oxygenated blood to the body as presented in Fig. 2.1. Figure 2.2 presents a cut-view of the heart where each pump, made of an atrium and a ventricle and separated by one-way valves is shown. Anatomically, the left ventricle contracts against the aortic valve, generating systolic pressures on the order of about 120 mmHg and relaxing to diastolic pressures near 15 mmHg in healthy adults (83)(84). This cyclic pressure waveform, as seen in Fig. 2.3, underpins the corresponding volumetric flow rate through the left ventricular outflow tract and systemic arteries. On average, the flow rate generated oscillates between 0 to 10 liters per minute with peaks up to 20 liters per minute during exercise (83)(84). The human heart is approximately the size of a fist, around 8 cm in width and 12 cm in length (85).

During each cardiac cycle, the flow rate exhibits a characteristic pattern: rapid up-stroke of flow upon aortic valve opening (early ejection), a decelerating phase of

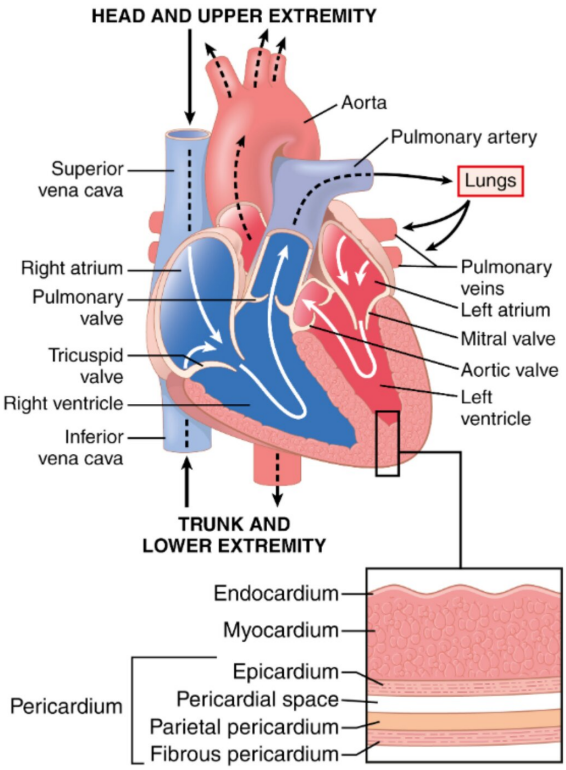

Figure 2.2: Cut-view of the human heart (2). The heart is made of four chambers, one atrium and one ventricle on both sides. Blood is drawn from the atria into the ventricles which propel it in the vascular system. Atria and ventricles are separated by one way valves.

ejection as ventricular volume reduces, followed by flow reversal or cessation when the valve closes and the ventricle enters diastole. For example, detailed studies of left ventricular and arterial waveforms show the complex coupling between pressure and flow-velocity profiles, including forward and reflected waves in the vascular system (86)(87). In these waveforms, peak instantaneous flow often occurs early in systole, followed by slower decline, and the interaction between pressure wave propagation, arterial compliance and flow inertia shapes both the amplitude and timing of the circulation. Importantly, the pressure and flow waveforms in the heart are not purely steady or sinusoidal but are inherently pulsatile, with steep rises and sharp peaks. In signal-processing terms, such waveforms contain multiple frequency components: in addition to the fundamental cardiac frequency, higher-order harmonics with different amplitudes and phases contribute to the overall waveform shape. This rich harmonic composition—referred to here as complex harmonic content—arises from valve action, ventricular and arterial compliance, and wave reflections within the vascular system. This behaviour underpins the physiological efficiency of the cardiovascular pump and suggests why engineered systems aiming to mimic the heart's output must confront the dynamic complexities of pulsatile pressure and flow generation, rather than assuming quasi-steady behaviour.

Unlike mechanical pumps operated under displacement control, the heart's motion is not prescribed but arises from *force balance*. The myocardial fibers generate tension, while blood pressure and tissue elasticity determine the extent of chamber deformation (88)(89)(90). This interplay is captured by the pressure–volume P–V loop, which characterises the mechanical work performed by the ventricle during each cycle (91). For a given contractile state, the heart automatically adjusts its stroke volume in response to changes in preload and afterload (the Frank-Starling and Anrep effects) thereby maintaining equilibrium without external regulation (92)(93).

The cardiovascular system further illustrates how compliance contributes to efficiency. This efficiency arises from the Windkessel effect, by which arterial compliance stores part of the energy generated during systole and releases it in diastole, reducing the mechanical load on the heart (94) (95) (39). This compliant energy exchange resembles the use of elastic elements in engineered resonant systems, hinting at the possibility of leveraging similar mechanisms in artificial pumps.

The heart's success as a self-regulating, force-driven pump has inspired decades of research in mechanical circulatory support. However, existing cardiac assist devices often revert to the displacement- or speed-controlled paradigms typical of industrial pumps. The following section examines this technological gap and the

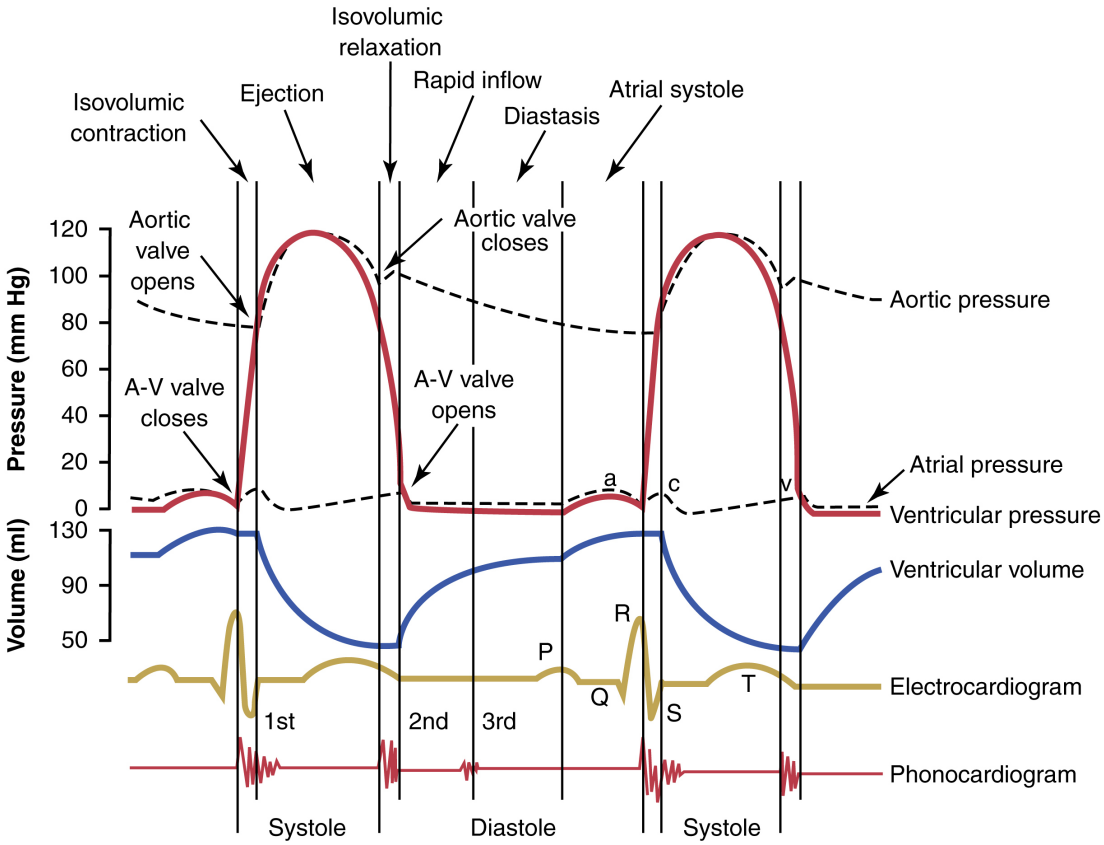

Figure 2.3: Typical pressure waveforms measured in the left ventricle and atrium as well as the aorta. The left ventricular volume is also plotted with the systole and diastole phase respectively corresponding to the compression and expansion of the ventricle (3).

efforts to reproduce physiological pulsatility in artificial systems.

2.4 Cardiac Assist Devices and the Challenge of Biomimicry

Implantable cardiac assist devices (CADs) are mechanical circulatory support systems designed to aid or replace a failing heart in patients suffering from advanced heart failure. They have saved thousands of lives by restoring adequate cardiac output when pharmacological or surgical interventions are no longer sufficient. Despite decades of development, reproducing the full physiological and adaptive function of the native heart remains an unsolved challenge. Modern devices have achieved remarkable durability and miniaturisation, yet they still struggle to replicate the heart's pulsatile dynamics and its ability to self-regulate in response to changing physiological demands in a compact and efficient format.

2.4.1 From Pulsatile to Continuous-Flow Devices

Two main categories of implantable assist devices exist: *ventricular assist devices* (VADs) and *total artificial hearts* (TAHs) (96). VADs are typically implanted in parallel with the native heart to support one or both ventricles, most commonly assisting the left ventricle (LVADs). They draw blood from the ventricle and pump it into the systemic circulation, thereby reducing cardiac workload and maintaining perfusion. TAHs, by contrast, replace both ventricles entirely and assume the full pumping function of the heart (97).

Early generations of VADs were conceived as miniature versions of the natural heart. They used pneumatic or hydraulic actuation to drive flexible diaphragms or bladders, producing fully pulsatile flow. These systems—such as the original Jarvik-7 (98) and early Berlin Heart EXCOR devices—closely mimicked the human heartbeat and achieved physiologically realistic pressure and flow profiles. However, their complexity, large size, and mechanical wear limited long-term reliability and patient mobility (98). The drive toward miniaturisation and full implantation motivated the development of rotary blood pumps, which use impellers to generate nearly continuous flow. This shift marked the transition from pulsatile positive-displacement pumping to rotodynamic, continuous-flow technology.

Modern continuous-flow (CF) devices such as the HeartMate 3 (Abbott), shown in Fig. 2.4a, and the now-discontinued HeartWare HVAD (Medtronic) represent the

current clinical standard (99). The HeartMate 3 employs a magnetically levitated (maglev) impeller that eliminates mechanical contact within the blood path, drastically reducing shear stress, friction losses, and component wear (100) as shown in Fig. 2.4b. This innovation enables long-term durability and compact form factors that allow full implantation within the chest cavity. Although primarily continuous, the HeartMate 3 introduced an artificial pulse feature that momentarily varies impeller speed to create small pressure oscillations intended to reduce thrombosis and endothelial dysfunction. Despite this improvement, the flow waveform remains far from physiological.

Continuous operation, combined with the absence of natural pulsatile pressure, has been linked to vascular stiffening, loss of baroreceptor sensitivity, gastrointestinal bleeding, and aortic valve fusion (34), (35), (36), (37), (38). Moreover, CF-VADs still depend on a percutaneous driveline to supply power from external batteries and controllers, introducing a persistent risk of infection and limiting patient autonomy, as shown in Fig. 2.4c. Each battery typically lasts only a few hours, requiring regular recharging or replacement.

Figure 2.4: a. HeartMate 3 pump. **b.** HeartMate 3 magnetic levitation technology to limit blood damage. **c.** The HeartMate 3 and the batteries located outside the patient's body are connected though a driveline going through the patient's abdomen. Images from (4).

Following the recall of the HVAD in 2021 due to safety concerns, Abbott's HeartMate 3 became the dominant LVAD worldwide. Meanwhile, new competitors have

emerged, such as CH Biomedical's CH-VAD (China) (101), which features fully magnetically levitated centrifugal impellers similar in concept to the HeartMate 3 (102). Other companies are exploring novel architectures: for instance, CorWave (France) is developing a biomimetic LVAD (Fig. 2.5a) using an undulating polymer membrane (Fig. 2.5b) inspired by aquatic locomotion (103) (104). Instead of spinning blades, the membrane oscillates in a traveling wave to propel blood forward, producing naturally pulsatile flow at lower shear stress. Early prototypes have demonstrated promising hemocompatibility and pulsatility but remain in preclinical testing (105).

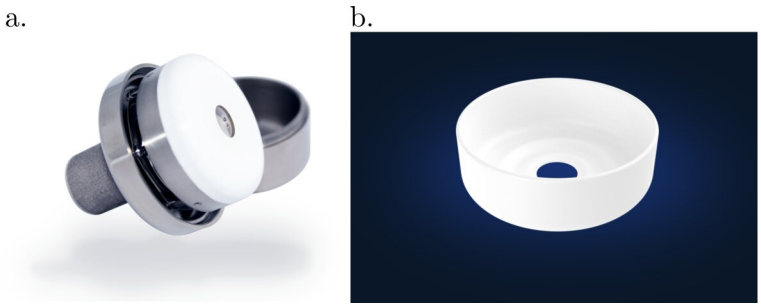

Figure 2.5: Corwave LVAD (5). **a.** Corwave LVAD opened to visualize the blood propeling membrane. **b.** The bio-inspired membrane oscillates to generate flow and pressure.

2.4.2 Total Artificial Hearts and Industry Landscape

In the TAH segment, devices are inherently more complex since they replace the entire heart rather than assist it. The only TAH with established long-term clinical use is the SynCardia TAH, a modern successor of the Jarvik-7 (98). SynCardia consists of two polyurethane pumping chambers actuated pneumatically through external air lines connected to a large console or portable driver unit. It provides fully pulsatile flow and has kept patients alive for months or years as a bridge to transplant (over 2,000 implants worldwide)(106)(107). However, the pneumatic drive requires a bulky external unit, limiting mobility and quality of life. The system's beat rate is fixed and cannot automatically adapt to activity level, unlike the physiological heart. As a result, it is mainly reserved for critically ill patients awaiting transplant (108).

To address these drawbacks, newer TAHs have focused on miniaturisation, autonomy, and biomimetic control. Carmat's Aeson TAH, shown in Fig. 2.6a and b, is one of the most advanced designs to date. It uses hydraulic actuation to drive two pumping chambers lined with bovine pericardium tissue, improving biocompatibility and reducing clot formation (109). Figure 2.6c shows a cut view of the Carmat heart

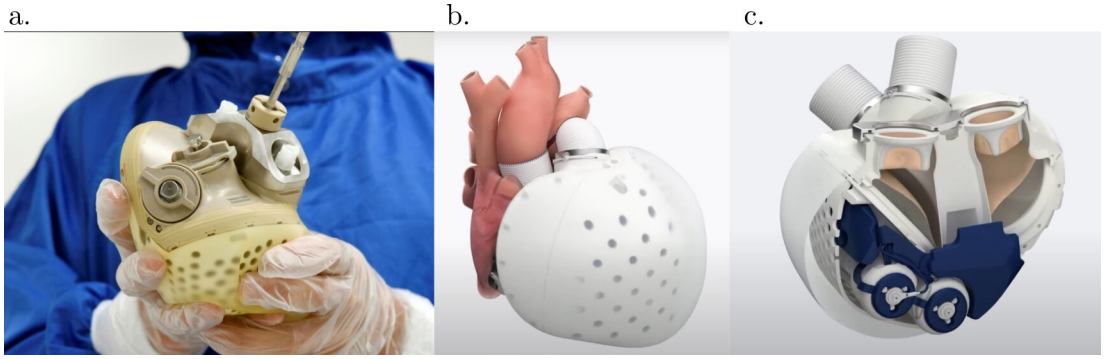

Figure 2.6: a. The Carmat heart is designed to be approximately the same size as a human heart. **b.** 3D view of the Carmat heart connected to the vascular system. **c.** Cut view of the Carmat heart. It uses fluidc pumps to actuate mebrane that ingest and expel blood through human-like valves. Images from (6) (7).

with the hydraulic pump at the bottom and the blood chambers and valves at the top. Embedded pressure sensors enable automatic adjustment of beat rate and stroke volume according to patient demand, providing partially self-regulating output (110). Aeson received CE Mark approval in Europe in 2020 for bridge-to-transplant indications and has shown encouraging results in clinical trials. Nevertheless, the device faces practical challenges: battery autonomy of roughly four hours per charge limits mobility, and manufacturing difficulties have periodically interrupted production. This year, Carmat experienced severe financial difficulties and, despite decades of research and nearly half a billion dollars invested (111), is now facing liquidation. This case highlights the significant economic and technical challenges associated with developing fully implantable total artificial hearts (TAHs).

Another notable development is the BiVACOR TAH (Fig. 2.7) (96) (112)(113), which employs a single magnetically levitated rotor with dual outlets to pump blood simultaneously into the systemic and pulmonary circulations. By using one rotating disk to drive both flows, BiVACOR achieves mechanical simplicity with only one moving part for extended lifespan. Pulsatility can be introduced through rapid speed modulation, although the resulting waveform is less physiologically shaped than that of diaphragm-based pumps (107). The device has received FDA Breakthrough Device designation and is progressing toward first-in-human trials. BiVACOR's emphasis on efficiency and mechanical robustness may eventually yield a durable alternative to conventional pulsatile pumps, though its flow remains quasi-continuous rather than naturally pulsatile.

a. b.

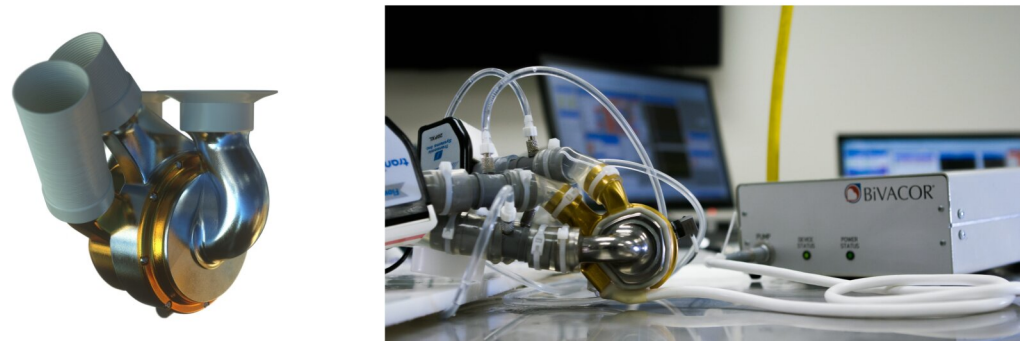

Figure 2.7: a. BiVACOR Total Artifical Heart. **b.** BiVACOR Total Artifical Heart connected to an experimental bench.

2.4.3 Research Directions: Actuation, Biocompatibility, and Energy Autonomy

Despite major progress, no existing device fully reproduces the adaptive, efficient, and self-regulating behaviour of the natural heart (97) (96). Both VADs and TAHs face three persistent challenges: (i) developing compact actuation systems capable of generating physiologic pulsatility; (ii) improving blood compatibility and device safety; and (iii) achieving reliable, fully implantable energy delivery. Although the present work focuses primarily on energy efficiency in pulsatile operation, the challenges related to actuation and biocompatibility remain central to the development of cardiac assist devices. They are therefore briefly reviewed here to provide a comprehensive overview of the design constraints and research directions in the field. The specific design requirements of the proposed pump in this thesis are introduced later in Chapter 3.

Actuation. The actuation mechanism is a central component of any cardiac assist device, as it determines how mechanical energy is transferred to support or replace the heart's pumping function. Traditionally, rotary blood pumps—particularly continuous-flow designs based on impellers—have dominated the field due to their compact size and energy efficiency. However, these systems often lack physiological pulsatility and impose shear stresses that challenge long-term biocompatibility.

In response to these limitations, several research efforts have explored new actuation strategies aimed at reintroducing pulsatile flow while improving integration with biological tissues. One significant direction involves soft robotic actuation, which seeks to replicate the heart's natural deformation using compliant materials and bio-

mimetic mechanics.

A landmark study by Roche et al. (12) introduced a soft robotic sleeve that wraps around the heart and supports systolic function via pneumatic actuators embedded in silicone elastomers (Fig. 2.8e). This extracardiac solution synchronized with native myocardial motion and demonstrated restoration of cardiac output in porcine models without direct blood contact. A follow-up study by Payne et al. (10) proposed a prototype whereby soft actuators wrapped around the ventricles are programmed to contract and relax in synchrony with the beating heart as shown in Fig. 2.8c,

Other groups have explored artificial muscle-based systems, such as fluidic actuators (114) and soft linear pumps that mimic myocardial helical contraction (13) (Fig. 2.8f). These devices provide distributed actuation forces across the ventricle wall, reducing mechanical mismatch and energy concentration. Saeed et al. (11) further demonstrated with a septum (wall separating left and right ventricle) bracing soft VAD shown in Fig. 2.8d, that actuating the interventricular septum improved systemic arterial pressure and arterial flow with a pulsatile wave comparable to natural pulsation.

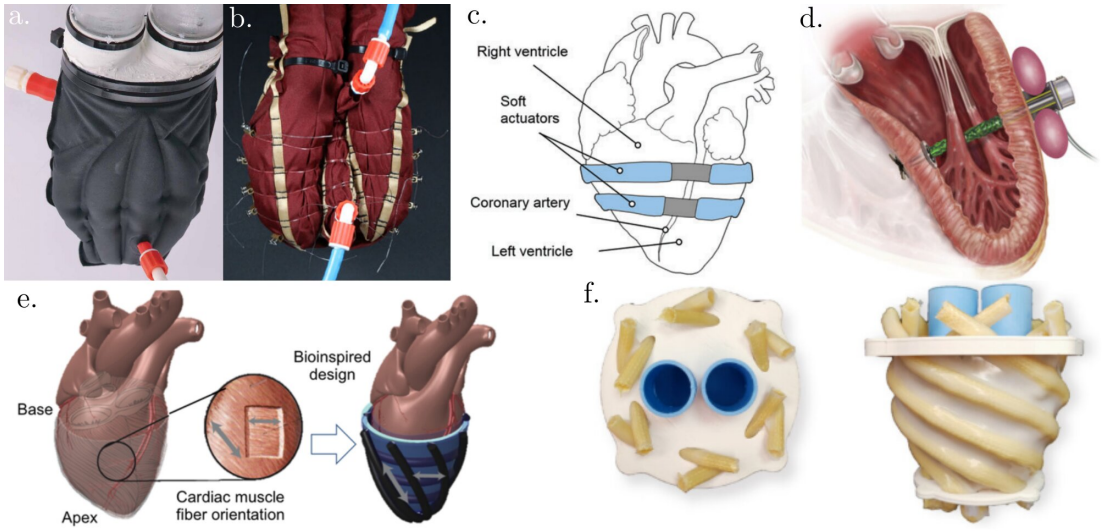

Figure 2.8: a. Soft robotic chamber actuated with pressurized air (8). **b.** Extension of the work presented in **a.** to multiple chambers to closely mimic the heart anatomy (9). **c.** Soft pneumatic actuators wrapped around the heart the help it contract (10). **d.** Soft pneumatic actuator connected to the left ventricle with septal bracing (attachment to the wall separating left and right ventricle) (11) **e.** Soft robotic sleeve with pneumatic actuators embedded in silicone elastomers (12). **f.** Fluidic actuators mimicking myocardial helical contraction (13).

While promising, these soft and compliant actuation systems face notable chal-

lenges. Their response speed, force output, and implantation complexity still lag behind conventional electromechanical systems. Moreover, achieving precise synchronization with the native cardiac cycle—essential for functional support—remains a critical barrier. Rogatinsky et al. (115) addressed this by developing a multifunctional soft robot capable of sensing, adapting, and responding to local cardiac cues in real time, although this remains at a preclinical stage.

The pursuit of fully soft total artificial hearts (TAHs) is also gaining momentum. Arfaee et al. (8) (116) presented two versions of a soft robotic hybrid heart with active contraction chambers pneumatically actuated (Fig. 2.8a and b). Although not yet miniaturized for implantation, this work represents a conceptual shift toward distributed, tissue-compatible actuation.

Finally, Weymann et al. (117) provided a comprehensive review of actuation techniques for soft cardiac devices, emphasizing the trade-offs between compactness, control, and mechanical output. They argue that while soft devices offer unmatched compliance, most prototypes still require bulky external controllers or tethered power sources—limiting their autonomy and long-term viability.

These developments underscore a growing interest in biomimetic actuation as an alternative to rotary systems. However, the transition from benchtop demonstrations to implantable, clinically viable devices remains hindered by issues of force transmission, power density, and long-term durability. Despite this, the convergence of materials science, robotics, and cardiac physiology holds substantial promise for the next generation of assist devices.

Biocompatibility. Biocompatibility remains a core challenge in the development of cardiac assist devices, as all such systems involve prolonged contact between artificial materials and circulating blood. Thrombosis, hemolysis, immune responses, and infection are significant risks that can compromise device performance and patient outcomes (118). These risks are amplified in rotary pumps, where high shear stresses and complex flow paths are unavoidable. Modern devices mitigate these issues through careful design and advanced material selection.

Magnetically levitated impellers, as used in the HeartMate 3, are a notable advancement that eliminate mechanical bearings, reducing friction and stagnant flow zones that contribute to clot formation (119).

Surface engineering is another critical strategy. Coatings such as heparin-bonded polymers, phosphorylcholine layers, and diamond-like carbon films aim to reduce platelet adhesion and protein adsorption on blood-contacting surfaces (120). Bey-

ond coatings, some devices such as Carmat's Aeson TAH use biological materials like bovine pericardium to create interfaces that better mimic the mechanical and immunological properties of native tissue.

Additionally, researchers are exploring surface microstructuring and endothelialization to promote a living, anti-thrombogenic lining on device surfaces. As Jana (120) emphasizes, engineered surfaces that support endothelial cell attachment and growth under flow conditions could eventually reduce or eliminate the need for systemic anticoagulation.

From a hemodynamic standpoint, computational fluid dynamics (CFD) and in vitro flow visualization techniques are widely used to map shear gradients and recirculation zones within devices (121) (122). These tools enable optimization of flow paths to reduce regions of stagnation and high shear, both of which are known contributors to thrombus formation.

Finally, novel mixed-flow VADs that combine axial and centrifugal stages have been proposed to further smooth the flow and improve hemocompatibility (123).

Despite these advances, long-term biocompatibility remains a limiting factor. Most implantable devices still require lifelong anticoagulation, and clinical data beyond 5-10 years remain limited. Moving forward, progress in bioinspired materials, smart surface coatings, and tissue-integrative design will be essential for the safe and durable function of next-generation cardiac assist technologies.

Energy delivery. The generation of pulsatile flow remains a major engineering and physiological objective, but it comes with a persistent energy-efficiency challenge. Within cardiac assist devices, efforts to quantify this trade-off began with the formulation of Energy-Equivalent Pressure (EEP) and Surplus Hemodynamic Energy (SHE), which mathematically describe the extra energy content of pulsatile flow compared with steady flow at equal mean pressure (124) (125). Experimental work has shown that generating pulsatility through speed modulation of rotary blood pumps increases electrical demand: for example, Shiose et al. (126) demonstrated that imposing physiologic pulse pressure on a continuous-flow total artificial heart required roughly 16 % more power, while Soucy et al. (127) and Pirbodaghi et al. (128) reported similar increases in left-ventricular assist devices under pulsatile conditions. Computational and lumped-parameter studies have attempted to find energetic "sweet spots" where physiologic benefit is maximized per unit energy input, showing that waveform shape, duty cycle, and phase synchronization critically influence efficiency (129) (130). Recent approaches combine these models with CFD-based waveform optimization to

minimize viscous and inertial losses while maintaining desired pulsatility.

Beyond the cardiovascular domain, general fluid-mechanics studies have explored how unsteady flow generation affects energy use. Jerónimo and Rival (131) showed experimentally that pulsatile flows enhance fluid replacement in recirculating zones, suggesting more efficient transport in systems dominated by mixing or flushing. Martin (132) compared steady and pulsatile flow through the aortic arch using CFD and found that although unsteadiness raises instantaneous shear and pressure gradients, it can improve overall convective efficiency. Likewise, Morsi (133)reported that pulsatile flow through a valve model produced lower mean pressure losses at equivalent volumetric flow rates, implying a possible energy benefit under certain conditions. More recently, Chun et al. (134) examined viscoelastic pulsatile flow in deformable channels and demonstrated experimentally that oscillatory driving can modify the pressure–flow relation and, in some regimes, reduce energy dissipation. These findings from outside biomedical engineering highlight that time-structured flow can, under specific conditions, redistribute mechanical work more effectively, a principle increasingly investigated for blood-pump control as well.

Complementary advances in energy autonomy seek to offset the unavoidable overhead of pulsatile actuation. High-efficiency transcutaneous-energy-transfer (TET) systems have achieved reliable wireless power delivery in the 10–20 W range, sufficient for modern rotary or pulsatile pumps, and are expected to close the autonomy gap between tethered and fully implantable systems (135)(136)(137). Together, these research directions—quantitative metrics (EEP/SHE), optimized waveforms, cross-disciplinary insights from unsteady-flow physics, and efficient power transfer—outline a path toward pulsatile devices that combine physiological fidelity with true energetic sustainability.

However, despite these advances, the deliberate exploitation of mechanical resonance to improve energy efficiency has been only marginally explored in the context of cardiac assist devices. While resonance is widely used in other engineering systems to enhance energy transfer, as explained in Section 2.5.3, its application to macro-scale pulsatile pumping remains limited, suggesting a promising yet underdeveloped direction for improving device performance which is explored in this thesis.

2.4.4 The Challenge of Biomimicry

The history of cardiac assist devices reveals a clear trade-off between *physiological fidelity* and *engineering simplicity*. Pulsatile, displacement-driven pumps mimic the natural heart but remain bulky and mechanically demanding, whereas continuous-flow rotary pumps achieve compactness and reliability at the cost of physiological realism. The next generation of devices aims to bridge this gap by integrating pulsatility, compliance, and adaptive control without sacrificing durability.

Achieving this balance requires rethinking actuation and control philosophy. Rather than prescribing displacement or speed, a *force-controlled* approach could enable the device to interact dynamically with its environment, allowing chamber motion to emerge from the balance between actuation force, elastic compliance, and hydraulic load—just as in the native heart. When combined with compliant or variable-stiffness elements, such systems could operate near resonance, amplifying motion and improving energy efficiency to reduce the batteries size and improve patients mobility. These principles motivate the development of the resonant, force-driven positive-displacement pump investigated in this thesis.

2.5 Resonance for Power and Efficiency Optimization

2.5.1 Principles of Resonance

Resonance is a fundamental phenomenon in dynamical systems, occurring when the frequency of an external excitation coincides with a system's natural frequency, leading to a large amplitude response and efficient energy exchange. The simplest model to illustrate resonance is the mass-spring-damper system (MSD), shown in Fig. 2.9. When the mass is driven by a periodic input force $F(t)$, Eq. 2.2 describes the system's dynamic (20). The mass, damping, and stiffness are denoted with m, c, and k respectively.

$$m\ddot{x} + c\dot{x} + kx = F_0 \sin(\omega t), \tag{2.2}$$

When the driving frequency ω approaches the natural frequency ω_n, Eq. 2.3, the displacement amplitude increases significantly, reaching a maximum limited only by damping. This amplification enables large output motion or flow with comparatively small input energy.

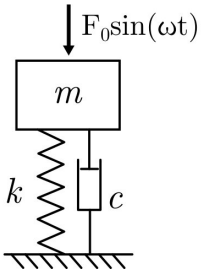

Figure 2.9: Mass-spring-damper (MSD) system.

$$\omega_n = \sqrt{\frac{k}{m}} \tag{2.3}$$

The way a resonant system behaves is highly dependent on how it is actuated. In a *displacement-driven* setup, such as when a motor enforces a fixed stroke, the mass cannot freely oscillate and resonance is suppressed in its motion. Nevertheless, resonance is still present from the actuator's perspective, which must deliver progressively more energy to sustain the imposed displacement. The actuator acts against the inertial, elastic and dissipative forces, leading to high energy dissipation and a high overall energetic cost. In other words, in displacement-driven systems, resonance manifests as increased energy demand rather than amplified motion. In this sense, a displacement-driven strategy effectively acts against the natural dynamics of the system: the actuator must continuously supply energy to counteract the tendency of the system to resonate. In contrast, under *force-driven* excitation, no such constraint is imposed, the system is free to respond dynamically, allowing it to naturally evolve toward its resonant response without being opposed by the actuator. Specifically, at resonance, energy circulates efficiently between elastic and inertial components so that the actuator primarily compensates for dissipative losses (20). As a result, a large motion can be sustained with relatively low net energy input. Consequently, a force-driven strategy is particularly well suited to applications where energy efficiency is a primary objective, as in this thesis. Finally, as later presented in Chapter 5, the pump can be modeled as a MSD system which further motivates the force-control approach.

2.5.2 Resonance in Biological and Bioinspired Pumps

Biological systems often exploit resonance to amplify motion and minimise energy cost. Jellyfish and cephalopods use the natural elasticity of their bodies to store and release energy during swimming cycles, achieving propulsion efficiencies exceeding 80–90% (40)(41)(138)(63).

The vascular system of the human body also exhibits resonant behaviours. However, a distinction must be made between the intrinsic mechanical resonance of the heart tissue and the functional resonance of the coupled heart-arterial system. Several studies have modelled the myocardium as a viscoelastic structure exhibiting natural vibration modes in the tens of hertz range (139) (140). For instance, Bahramali *et al.* (141) treated the mechanical response of the contracting myocardium as that of an under-damped harmonic oscillator and identified a characteristic natural frequency between approximately 13 and 20 Hz in healthy hearts. Similarly, Papadacci *et al.* (142) used four-dimensional ultrafast ultrasound imaging to visualise shear-wave propagation within the myocardium, demonstrating wave-like vibratory behaviour consistent with higher-frequency structural resonances of the cardiac wall. These findings confirm that the myocardium possesses intrinsic elastic and inertial properties capable of supporting resonant oscillations. However, these structural modes occur at frequencies far above the heart rate and are therefore unlikely to play a direct role in the energetic efficiency of blood pumping.

In contrast, the classical *Windkessel* theory (39) and arterial-impedance analyses describe a lower-frequency resonance that emerges from the interaction between the ventricle, arterial compliance, and blood inertia. This system-level resonance produces an impedance minimum around 2-5 Hz in humans, corresponding closely to physiological heart rates and enabling efficient energy transfer between the heart and the arterial tree (82). The compliant arteries store part of the stroke energy during systole and release it in diastole, effectively reducing the mechanical workload of the ventricle. Thus, while the myocardium itself exhibits higher-frequency structural resonances, the *functional* resonance that governs circulatory efficiency arises primarily from the coupled dynamics of the heart and vascular system. In other words, myocardial resonances reflect local elastic behaviour of the tissue, whereas the Windkessel-type resonance represents the global haemodynamic coupling that underlies efficient pulsatile flow.

2.5.3 Resonant Efficient Mechatronic Devices

Force-driven resonance is widely exploited across engineering disciplines to amplify motion or reduce energy expenditure. Specifically, in robotics and biomechanics, resonance has inspired numerous designs that leverage natural dynamics for efficient locomotion and actuation. *Passive dynamic walkers*, for instance, exploit the pendular resonance of their limbs to achieve human-like walking without continuous actuation (143) (144). Similarly, jumping (145)(146) and running robots (147) such as the MIT Cheetah (148) coordinate actuation with the natural oscillatory response of compliant legs to recover energy from elastic deformation. In these systems, resonance acts as an energetic amplifier: by synchronising actuator timing with the system's natural frequency, motion is sustained with minimal control effort. Despite its pervasive use in locomotion, vibration energy harvesting, and compliant robotics, resonance has been rarely applied to *pumping systems*, where unsteady oscillations are traditionally viewed as undesirable. This omission represents an untapped opportunity: a pump that intentionally operates near resonance could, in principle, exploit the same efficiency gains observed in biological and robotic oscillators.

In fluidic systems, resonance arises through the coupling of fluid inertia, chamber compliance, and damping due to viscous losses. As an example, such behaviour is observed in compliant hydraulic lines (149)(150). Operating near resonance can yield large volumetric oscillations and high flow amplitudes with limited actuation effort. Although most industrial pumps suppress such dynamics to prevent vibration and noise, deliberately exploiting resonance may provide a new route to energy-efficient pumping. Some researchers have explored at the micro scale resonant pumping. Piezoelectric, electrostatic, and electromagnetic micro-pumps frequently operate at their structural resonances to maximise volumetric flow per input power(151) (152) (153). At resonance, the actuator's driving forces produce large diaphragm displacements, greatly enhancing flow. However, translating such resonance-based strategies to macro-scale pumps has proven difficult. It is only recently that the benefit provided by passive elasticity in ameliorating the efficiency of a macro-scale pulsatile pumping system is for the first time observed. In a study analysing the performances of a self-propelled squid-inspired vehicle, researchers successfully demonstrated that an harmonically excited hydraulic actuator was able to minimize energy expenditure during locomotion when operating at its natural frequency (154). This work brings evidence that operation at resonance allow to match the performances of living organisms, yielding a propulsive efficiency and cost of transport of 0.56 and 0.08,

respectively. While these results are indicative of the striking benefit of exploiting the passive dynamics of fluidic actuators for performance optimization, they also highlight that operating outside of the resonant regime drastically reduces the power output of the mechanism. Reliance on resonance inherently dictates that only a narrow bandwidth of actuation frequencies can benefit from efficiency optimization, limiting its operational mode to excessively constrained actuation routine.

2.6 Adaptive Stiffness Systems

In order to exploit resonance on a broad range of operational regimes, stiffness can be tuned to shift the natural frequency ω_n. For instance, for a MSD, the natural frequency scales with the root square of the stiffness k as presented in Eq. 2.3.

2.6.1 Variable Stiffness Approaches

In natural systems, the ability to adjust stiffness dynamically is crucial for maintaining resonance across different operating conditions. Animals and humans continuously modulate the stiffness of muscles, tendons, and connective tissues to synchronise with their preferred movement frequency. Numerous biomechanical studies have shown that animals actively modulate the stiffness of their musculoskeletal system with speed. Specifially, legged animals adjust joint stiffness when changing gait or speed, preserving resonance between limb inertia and muscular elasticity (155) (156) (157) (158) (159) (160). This adjustment ensures efficient energy exchange and stable dynamics despite varying load or terrain. The cardiovascular system exhibits similar adaptability: arterial smooth muscle controls vascular stiffness to regulate pulse-wave velocity (161)(162)(163)(82), a mechanism thought to be a physiological response to optimize coupling between the heart and the arterial system .

Inspired by biology, researchers in robotics and actuation have developed *variable-stiffness actuators* (VSAs) capable of tuning their compliance in real time (164). Different methods and techniques can be employed to tune stiffness. However, before presenting them, a rigorous definition of stiffness is necessary.

In the context of compliant systems and actuators, stiffness is often casually described as the force required to produce motion, but this overlooks critical distinctions that are essential for rigorous modeling and design. In its strict mechanical sense, stiffness k is defined as the incremental ratio of force to displacement ($k = dF/dx$). However, in many robotics and biomechanical applications what is labelled “increased

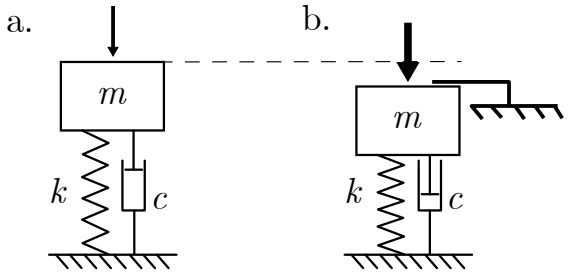

Figure 2.10: a. Classic mass-spring-damper. **b.** An increase in preload induced by an external mechanism only alters the equilibrium force. The force to produce from the equilibrium position for a given displacement is higher in than for a mass-spring-damper without preload but the stiffness k remains the same.

stiffness" actually arises from higher preload or baseline force rather than a change in the slope of the force–displacement curve. This is explained visually in Fig. 2.10.

Studies of variable-stiffness actuators (VSAs) highlight this nuance: while VSAs modulate physical stiffness via changes in elastic element geometry or pre-tension, many implementations exploit preload change as well, which alters equilibrium force but not necessarily the incremental stiffness (17) (165). Awareness of these subtleties is crucial when designing systems for resonance or adaptive compliance, as true stiffness modulation affects natural frequency and energy transfer, whereas preload alone does not. The vast majority of the VSA can be classified in three major groups (17).

First, the transmission ratio between the output and the restoring element can be adjusted. Several techniques have been proposed to modify this transmission ratio. A common approach relies on adjusting the lever arm (166), for instance by changing the pivot position or the geometry of the linkage, which directly alters the mechanical advantage between the actuator and the elastic element. This method enables continuous tuning of stiffness through purely geometric means. It's principle is depicted in Fig. 2.11b. Figure 2.12a illustrates the operation of such a variable stiffness actuator (14). When the intermediate link rotates, one of the springs is compressed, exerting force on the green armature and causing the output link to move. The stiffness is modulated based on the concept of a variable lever arm: the springs can slide along the intermediate link, thereby changing their effective lever arm. For a constant input torque at the intermediate link, a longer lever arm results in a lower stiffness. Alternatively, the transmission ratio can be modified using mechanical transmission systems such as continuously variable transmissions (CVTs), which adapt the ratio between input and output motion without discrete steps

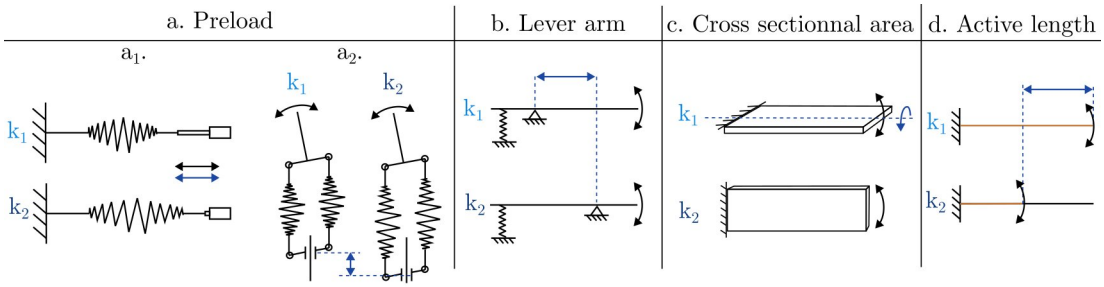

Figure 2.11: Examples of mechanisms used to achieve variable stiffness. Each mechanism is represented in two different stiffness settings k_1 and k_2. The black arrows represent the output motion and the blue arrows represent the motion creating the change of stiffness. **a.** Two examples of mechanisms using preloading with nonlinear springs. In a_1, the linear actuator is used to both create the output motion and the variable stiffness. In a_2, a linear motion is used to preload nonlinear antagonistic springs. The output is a rotational motion. **b.** Changing the pivot point affects the lever arm length thus modifying the force necessary to generate a given output motion and hence the stiffness. **c.** Rotating a beam around its main axis changes its second moment of area directly affecting its stiffness.**d.** Changing the effective length (in brown) of a beam can be used to change its stiffness.

(167)(168).

Second, the physical properties of the elastic element can be altered. This can be achieved by modifying key parameters that govern the stiffness of the elastic element. In particular, the effective stiffness can be adjusted by altering the geometry of the element, including its second moment of area as shown in Fig. 2.11c or varying the active length of the elastic element, as longer elements generally exhibit lower stiffness for a given material and geometry as illustrated in Fig. 2.11d. The latter is further exemplified in Figure 2.13 with the Jack spring (16), a variable stiffness mechanism that adjust the number of active coils of a compression spring. This mechanism has the same working principle of a leadscrew, with the exception of the threaded shaft being replaced by a spring. In other words, a leadscrew can be regarded as a type of Jack spring with an infinitely large stiffness. In Fig. 2.13, the yellow-coloured component acts as a static nut around which the spring is allowed to rotate and translate axially. When the spring rotates, its length or, equivalently, the number of coils varies, affecting the stiffness of each spring on each sides of the nut. Indeed, a spring's stiffness is inversely proportional to the number of active coils (169) as shown in Eq. 2.4 where k is the spring stiffness, d is the wire diameter, G is the shear modulus, D is the mean coil diameter and N is the number of active coils. Alternatively, changing the material properties, such as the elasticity modulus (170)

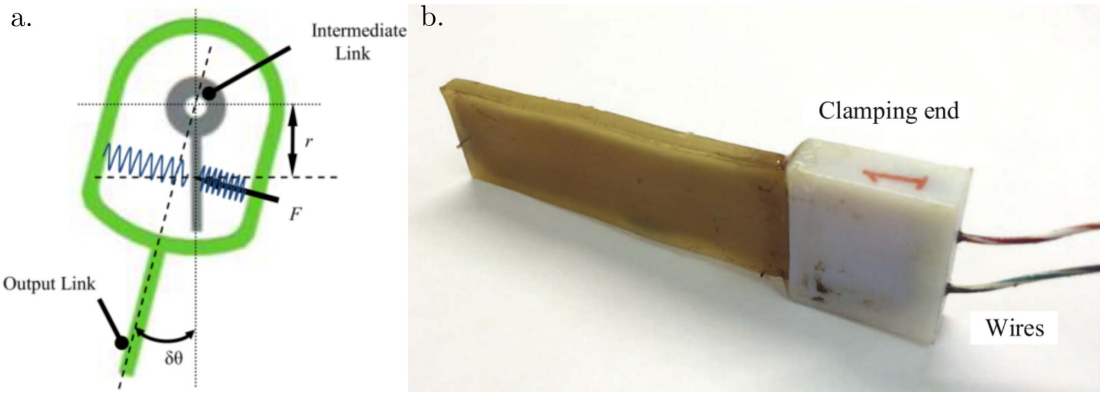

Figure 2.12: a. Variable stiffness mechanism using transmission ratio tuning (14). **b.** Fin embedding electrorheological fluid inducing stiffness variation when submitted to an electric field (15).

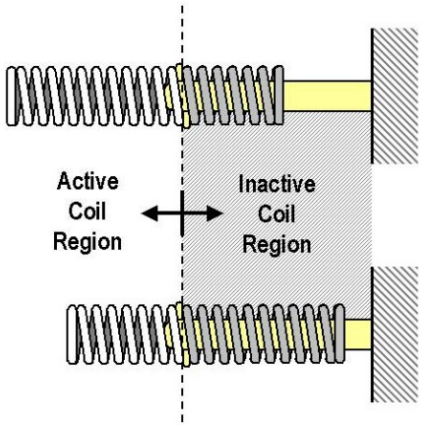

Figure 2.13: Jack spring concept used to change the number of active coils of a spring to change its stiffness (16).

(171) (172) or the viscosity provides another means of tuning stiffness. Figure 2.12b presents an electrorheological (ER) fluid-based variable stiffness fin for a robotic fish (15). The viscosity of an ER fluid changes reversibly in response of an electric field. This property was exploited by encapsulating ER fluid in a fin made out of copper and rubber. When exposed to an electric field, the fluid viscosity and, consequently, the fin stiffness vary.

$$k = \frac{d^4 G}{8D^3 N} \tag{2.4}$$

Third, preloading can be used to adjust stiffness, but only when the elastic element exhibits a nonlinear force-displacement relationship (173). In the linear case (Fig. 2.10), preloading shifts the equilibrium force without affecting stiffness k. How-

ever, for nonlinear elastic elements, preload alters both equilibrium and effective stiffness. This effect is illustrated in Fig. 2.14. Figures 2.14a and 2.14b correspond to linear and nonlinear restoring elements, respectively. In both cases, the brown curves represent preloaded conditions and the blue curves the unloaded ones. Preloading increases the y-intercept, corresponding to the equilibrium force. In the linear case, the slope over the displacement interval x remains unchanged, indicating constant stiffness. In contrast, in the nonlinear case, the slope (and thus the stiffness) increases with preload, reflecting the overall nonlinear behaviour of the elastic element. It should be noted that this behaviour also applies to systems exhibiting piecewise-linear stiffness, such as bilinear springs. In these systems, the force–displacement relationship is composed of multiple linear regions with different slopes. Although each region is locally linear, the overall response of the system is nonlinear because the stiffness depends on the displacement range considered. In such cases, preloading can shift the equilibrium position of the system from one stiffness region to another. When this occurs, the effective stiffness around the operating point changes, similarly to the behaviour observed in continuously nonlinear elastic elements.

Such nonlinear stiffness modulation using preloading is commonly achieved through antagonistic actuation, where two elastic elements or actuators are arranged in opposition so that they generate forces in opposite directions (174)(175). By increasing the preload in these opposing elements, the effective stiffness of the system can be tuned through the resulting nonlinear force–displacement relationship (Fig. 2.11a2). In its simplest form, this can be implemented using a single actuator to preload a non-linear spring (Fig. 2.11a1). More advanced configurations employ independent antagonistic actuators, allowing the equilibrium position and stiffness to be controlled separately. While these approaches provide increased flexibility in shaping the system dynamics, they also introduce additional mechanical and control complexity.

Figure 2.15 compares the different techniques according to two criteria relevant to the efficiency objectives of this thesis, building on the classification of variable impedance mechanisms proposed by Vanderborght et al (17). These criteria are further used and discussed in Chapter 3 to guide the selection of an appropriate mechanism for the pump. The first criterion assesses whether the energy stored in the compliant element remains fully available regardless of the stiffness setting. In other words, it evaluates whether the entirety of the compliant element or part of it is used to store energy. The second criterion concerns the energetic cost of maintaining stiffness at the equilibrium position. It determines whether a continuous energy input is required to sustain a given stiffness level, which is a critical factor for

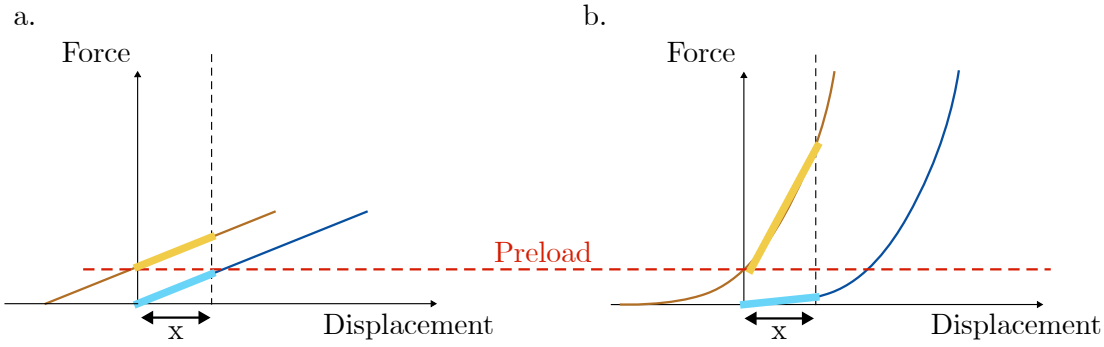

Figure 2.14: Stiffness variations under preload for a linear spring **a.** and a non-linear spring **b.**. The blue and brown colored curves show the force versus displacement profile without and with preload respectively. For the displacement x considered, the stiffness (slope) remains constant for a linear spring but does not for a non-linear spring.

overall efficiency and energy consumption.

2.6.2 Adaptive Stiffness and Tunable Resonance

A large body of research in legged and articulated robotics has demonstrated that variable stiffness can significantly improve energetic efficiency, robustness, and dynamic performance. Early work by Hurst *et al.* (176) and Raibert (177) showed that mechanically adjustable compliance allows legged robots to store and release elastic energy during cyclic locomotion, effectively recovering part of the work performed at each stride. Subsequent studies on variable-stiffness legs and actuators (178) (165) confirmed that tuning stiffness to match the dominant stride frequency enhances stability and reduces motor power consumption. Figure 2.16a presents the hexapod robot used by Galloway et al. (18) to test controlled-stiffness legs for efficiency gains. Secord and Asada (179) extended these findings by designing actuators capable of varying both stiffness and resonant frequency, thereby maintaining operation near resonance for maximum efficiency. A comprehensive review by Wolf *et al.* (180) emphasised that variable stiffness actuators (VSAs) provide an intrinsic means of energy optimisation by synchronising the system's natural frequency with its driving rhythm.

Despite these advances, the use of variable stiffness mechanisms in systems that interact directly with fluids remains rare. Most research has focused on solid–mechanical or robotic locomotion rather than fluidic propulsion or pumping. Unlike legged robots, where stiffness tuning can easily modulate resonance between body and actuator dynamics, fluid–structure systems introduce additional complexity through fluid inertia

	Preload	Transmission ratio		Change in physical properties		
		Lever arm	Continuous variable transmission	Elasticity modulus	Cross sectionnal area	Active length
Full energy capacity of the compliant element available at output	No	No	Yes	Yes	Yes	No
Energy required to maintain stiffness at equilibrium point	Yes	No	No	No	No	No

Figure 2.15: The three main techniques used to tune stiffness: preloading a nonlinear spring, adjusting the transmission ratio between the compliant element and the output link and changing the physical properties of the compliant element. Two categories are used to differentiate them: whether changing the stiffness affects the ability to exploit the entire energy storing potential of the compliant element and whether energy is necessary to sustain a given stiffness level (17).

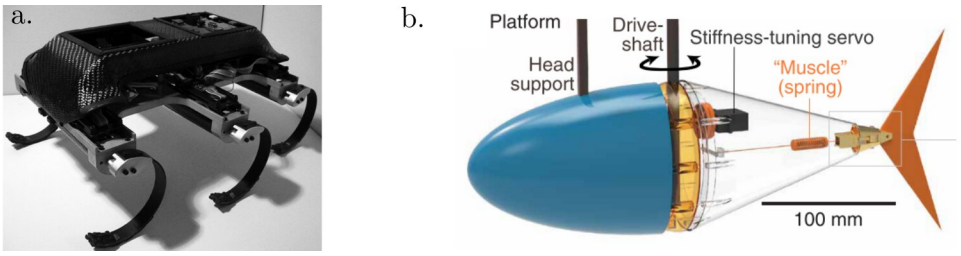

Figure 2.16: a. Edubot used by Galloway et al.(18) to test their controlled-stiffness legs for efficiency improvements. **b.** Robotic fish with variable stiffness fin for efficient swimming (19).

and damping. As a result, the potential of variable stiffness to enable persistent resonant operation and efficient energy exchange in pumps or fluidic devices has received very limited attention. While multiple studies have demonstrated the benefits of resonance for thrust enhancement in fish-like robots (181) (180) (182), it is only recently that researchers have begun to explore this concept for energy-efficient swimming. Zhong *et al.* (19) demonstrated that tunable stiffness enables fast and energy-efficient swimming by maintaining near-resonant oscillations of their robot's body and tail. Their prototype is presented in Fig. 2.16b. This pioneering work highlights the broader promise of stiffness adaptation in systems coupled with fluids, yet no comparable studies have been conducted in the context of pumping.

The present thesis therefore addresses this gap by investigating how force-driven actuation combined with adaptive stiffness can be exploited to achieve persistent resonance and energy-efficient fluid transport.

2.7 Conclusion

The literature reviewed in this chapter highlights that, despite decades of research in both industrial and biomedical fluid systems, the efficient generation of pulsatile flow remains an unsolved engineering challenge. In industrial and robotic applications, unsteady flows are often avoided due to their complexity, yet biological systems consistently exploit pulsatility to achieve higher transport efficiency, adaptive energy storage, and reduced mechanical stress. This discrepancy underscores the potential value of adopting biomechanically inspired design principles in engineered systems.

In the biomedical domain, particularly for cardiac assist devices, the need for efficient, physiologically relevant pulsatility is even more pressing. Continuous-flow pumps have demonstrated clinical viability but still fail to replicate the adaptive and compliant behaviour of the native heart. Numerous studies have shown that pulsatile flow contributes to vascular health and end-organ perfusion, yet no device has successfully combined small size, reliability, biocompatibility, and true physiological pulsatility. This persistent gap between function and feasibility has motivated research into new physical mechanisms that could enhance energy efficiency without compromising simplicity or compactness.

Among the strategies investigated, mechanical resonance has emerged as a particularly promising approach. Operating a pump near its natural frequency allows stored elastic energy to oscillate between mechanical and hydraulic domains, amplifying output with minimal energy input. Moreover, introducing variable stiffness provides a means to tune this resonance dynamically, enabling adaptive operation under changing loads or physiological conditions. While the theoretical potential of resonance and stiffness modulation has been recognized in other fields, such as soft robotics and bio-inspired actuation, their application to pulsatile pumping remains underexplored.

In cardiac assist devices, the integration of resonance and adaptive stiffness offers a transformative route toward biomimetic performance. Operating near the natural frequency of the fluid–structure system could amplify stroke volume without increasing actuator force, thereby reducing energy consumption. Resonant operation would also yield more physiological pressure and flow waveforms, enhancing vascular compatibility compared with steady continuous-flow devices.

This review therefore establishes the scientific and technological motivation for the work presented in the following chapters. The remainder of the thesis focuses on developing and experimentally validating a compact, heart-scale resonant pump with

tunable stiffness, aiming to bridge the long-standing gap between biological efficiency and engineering implementation in pulsatile flow generation.

Chapter 3

Conceptual Framework and Design Requirements

3.1 Introduction

The previous chapter reviewed the state of the art in pulsatile pumping technologies, emphasizing the physiological importance of pulsatility and the current limitations of mechanical systems attempting to reproduce it. Despite the numerous designs explored for cardiac assist devices, few studies have rigorously addressed the efficiency of pulsatile flow, and none of the commercially available systems are capable of replicating the natural dynamics of the human heart. As highlighted in the literature, resonance - particularly when combined with natural frequency tuning - offers a promising route to enhance performance while minimizing energy losses.

Building on these findings, this chapter establishes the conceptual foundations and functional requirements for a resonant pulsatile pump designed to operate near its natural frequency. The goal is to bridge the gap between theoretical resonance-based efficiency gains and practical device implementation. The chapter begins by defining the performance and mechanical requirements that guide the design of a compact, heart-scale prototype. It then presents the conceptual layout of the pump and the rationale behind the integration of a variable stiffness mechanism. Finally, a proof-of-concept prototype of the variable stiffness mechanism is introduced and tested, laying the groundwork for the complete system developed and characterized in the following chapters.

3.2 Pump Concept and Requirements

Building upon the theoretical foundations established in the Chapter 2, this part introduces the conceptual design of the resonant pulsatile pump and defines the criteria guiding its development. The objective is to translate the general functional goals - compactness, energy efficiency, and tunable resonance - into concrete design specifications and mechanical principles. Section 3.2.1 formulates the functional and structural requirements derived from both physiological analogies and practical constraints. Section 3.2.2 then presents the conceptual layout of the pump, outlining the rationale for the chosen actuation and transmission mechanisms. Finally, Section 3.2.3 describes the integration of the variable stiffness mechanism, which enables dynamic tuning of the system's natural frequency and underpins the adaptive behavior central to this study.

3.2.1 Requirements

To constrain the design space of the pump and guide development, a set of functional and mechanical requirements is established.

Functionally, the pump must replicate the operating principle of biological systems such as the human heart or the squid mantle, whereby cyclic expansion and compression of a cavity results in alternating fluid intake and expulsion. Furthermore, the overall size of the device - including the actuation module, control electronics, and pump housing - should remain within the same order of magnitude as a human heart. This constraint addresses a common limitation observed in the literature: many high-performance prototypes are coupled with bulky actuation or control systems that are impractical to miniaturize (117), thereby limiting their translational potential.

Considerations related to biocompatibility and surgical implantation are deliberately excluded from the current scope. Specifically, from a design perspective, no particular attention is dedicated to limiting sharp edges and protrusions in the fluid path which can cause blood damage, recirculations and thrombosis. While these factors are essential for eventual clinical deployment (183), this study focuses on characterizing the pump's dynamic behavior and performance metrics. Moreover, biocompatibility typically depends on advanced materials (184) and fabrication methods (e.g., titanium and medical-grade coatings), which are cost-prohibitive at this stage and better addressed in later phases once the core technology is mature.

Although performance indicators such as efficiency, flow rate, and pressure are

critical to validate the proof of concept, the primary objective here is to investigate the underlying physical mechanisms responsible for performance enhancement, particularly those related to resonance and variable stiffness. Consequently, at that stage, no quantitative requirements is defined for the pump performance. The objective is simply set as getting as close as possible from the human heart performances as presented in the literature review in Chapter 2.

From a mechanical perspective, additional design requirements are defined. The prototype should be modular and designed for ease of assembly and disassembly to support rapid iteration and maintenance. It must also demonstrate mechanical robustness over extended testing sessions at various actuation frequencies, with minimal drift in its mechanical properties to ensure experimental repeatability. The actuation system should be based on well-established technologies to minimize the risk of unanticipated dynamic behaviors, allowing for the isolated study of the variable stiffness mechanism. Finally, variable stiffness mechanisms with well-characterized or analytically tractable relationships between input perturbation and output stiffness are preferred to simplify modeling and interpretation. Additionally, the solution chosen should not operate on a constant energy supply to maintain a new level of stiffness to maximize overall efficiency.

3.2.2 Pump Concept

The objectives of using well-established actuation technique combined with using the compression-expansion of a cavity were the core requirements that shaped the concept. First, any actuation mechanism requiring customized fluid pressurizing system are not considered as deemed too cumbersome, complex to develop and for which well-established equations to quantify used powers would have not been readily available due to its customized nature. Second, electric motors are also excluded. Indeed, while miniaturized motors able to generate high-powers are available off the shelves, they usually present high rotational speeds and low torques. For a system needing to propel fluid at frequencies in a range of a few Hertz, this would imply using a reduction mechanism usually in the form of a gear train. As one of the central goal of this thesis is to focus on efficiency, losses introduced by friction in gears are deemed too high to use an electric motor. Consequently, the choice of using a linear actuator appears to be the most sound approach for the prototype's need for their ability to generate high forces at low frequencies without any transmission system combined to a well established understanding of their dynamic and energy consumption.

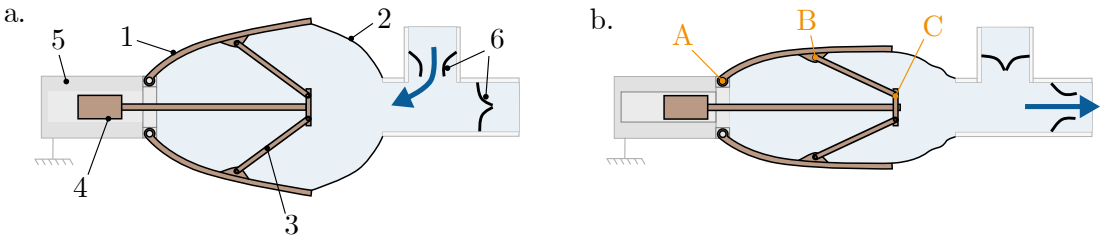

Figure 3.1: Concept of the pump. **a.** Pump expansion and fluid ingestion phase. **b.** Pump compression and fluid ejection phase.

To reduce any design challenges associated to electric leakages and to facilitate replacement of the actuator if needed, the actuator is placed outside the cavity, not in direct contact of the fluid. To convert the linear motion into a compression/expansion of the cavity, an umbrella-like mechanism is chosen. This well-known mechanism offers an easy to manufacture solution with straightforward calculations of the transmission ratio.

Consequently, the pump concept presented in Fig. 3.1 is established. Figures 3.1a and b provide a top cross-sectional view of the pump during the expanding and compressing phases of the cavity, resulting in the ingestion and expulsion of fluid. In these diagrams, the brown-colored components represent moving parts, while all others remain static. The pump cavity is constructed from rigid ribs (labeled 1) that are evenly distributed and attached to a flexible membrane (2). Each rib is mechanically linked to a lever arm (3), which is in turn connected to a rigid assembly referred to as the mover (4). Actuation is achieved using a linear actuator (5). During the expulsion phase, the actuator pushes the plunger forward causing the lever arms (3) to rotate around fixed pivot points B and C. The resulting motion pulls down the ribs (1), which themselves rotate about pivot point A, thereby compressing the cavity and expelling fluid. Inlet and outlet one-way valves (6) ensure unidirectional flow during each phase of the actuation cycle.

3.2.3 Variable Stiffness Mechanism Concept

Stiffness tuning can be achieved through a wide range of approaches, as outlined in Chapter 2. However, only a limited number of designs satisfy the specific requirements of this study, namely: simplicity of stiffness estimation, zero energy consumption to maintain a given stiffness level, and compatibility with the pump architecture defined in Fig.3.1.

First, mechanisms relying on preload adjustment were excluded, as they do not

satisfy the second requirement (see Fig. 2.15), requiring continuous energy input to maintain a given stiffness.

Second, mechanisms based on varying the transmission ratio were deemed unsuitable due to their bulkiness, which prevents straightforward integration within or around the pump. In addition, transmission elements inherently introduce mechanical losses, which is incompatible with the efficiency-driven objectives of this work.

A third category involves modifying the physical properties of the compliant element. Approaches based on varying the elastic modulus or viscosity were not retained. Changes in elastic modulus—typically achieved through temperature variation—result in limited stiffness modulation (170) (171) (172), while other methods may require high voltages that are incompatible with implantable medical devices (15). Similarly, viscosity-based approaches inherently alter damping, thereby directly impacting system efficiency (17).

The remaining viable strategies consist in modifying geometric parameters of the compliant element, such as its second moment of area or its effective length. These approaches differ in terms of energy availability: varying the cross-section preserves full access to the stored elastic energy across stiffness settings, whereas varying the effective length does not. However, although this distinction is often emphasized in the literature on variable stiffness mechanisms, it is not central to the present study. Indeed, full energy availability does not imply that the stored energy remains constant with stiffness; in both cases, stiffness variations inherently affect the energy storage capacity of the compliant element.

Consequently, the selection was primarily guided by geometrical and integration considerations. Given the translational motion imposed by the linear actuator, a linear compression spring was identified as a particularly suitable solution. Among the candidate mechanisms, the Jack Spring mechanism (16) presented earlier in Chapter 2 is especially well adapted to this application. It also fulfills the requirement of simplicity in stiffness estimation, as the inverse linear relationship between stiffness and the number of active coils—expressed in Eq. 2.4 and recalled below for clarity—provides a straightforward means of stiffness control.

$$k = \frac{d^4 G}{8 D^3 N} \qquad \text{(2.4 revisited)}$$

Nevertheless, the Jack spring mechanism presents one major flaw for its implementation in the pump. Indeed, the longitudinal space required for covering the entirety of the spring stiffness is equal to two times its length L_s as shown in Fig. 3.2a.

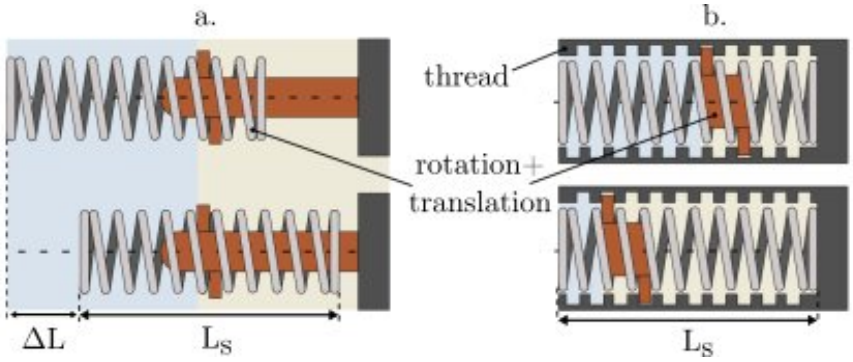

Figure 3.2: (a) Original Jack Spring design concept. Rotation of the spring around the nut (brown colored part) drives the spring translation along the nut axis, resulting in a change of the spring length on either side of the nut. When the number of coils is changed, the stiffness in the blue and yellow sections is modified according to eq. 2.4. The total length necessary to fit this system is $\Delta L + L_s$. (b) Proposed concept. The nut rotates and translates while the spring is static. The thread is used to make sure the nut does not translate when a load is applied on the spring. The total length necessary to fit this system is now only L_s.

To reduce its footprint, a novel design is proposed drastically improving on the existing Jack spring approach by making it extremely compact to be able to fit it in the pump. To do so, the change in spring length is dictated by the combined translation and rotation of the nut (brown colored part), Fig. 3.2(b), as opposed to the translation and rotation of the spring itself, Fig. 3.2(a), as seen in the Jack spring mechanism. This modification allows for significant improvements in compactness of the overall assembly.

3.3 Variable Stiffness Mechanism Proof of Concept

Having established the conceptual design of the pump and the rationale for integrating a variable stiffness element, this section focuses on validating the feasibility of the proposed stiffness modulation principle. A proof-of-concept mechanism - termed the Compact Modifier of Active Coils (C-MAC) - is developed to demonstrate controllable and repeatable stiffness variation within a compact form factor suitable for integration into the pump architecture. The section details the design strategy, fabrication process, and testing methodology used to assess the mechanism's scalability, linearity, and efficiency. These preliminary results serve to confirm the viability of the C-MAC concept before its full implementation in the resonant pump prototype described in Chapter 4.

3.3.1 Design and Manufacturing

Compact Modifier of Active Coils (C-MAC)

In this section, the variable stiffness mechanism concept introduced in Section 3.2.3 is implemented in the form of a physical prototype termed the C-MAC for Compact Modifier of Active Coils. The C-MAC VSM is detailed in Fig. 3.3. It is made of three constitutive parts: the *main body*, the *shaft* and the *slider*. The *main body* consists of the supporting structure, threaded on its lower section with a pitch p, of the spring having the same pitch p and of the *load connector*. The *main body* is assumed to be completely static while the *load connector* acts directly on the spring and can translate axially to compress or extend the spring. The *shaft*, connected externally to an actuator which drives a rotation around its central axis, is constrained from translation by the *main body* at points A and B, Fig. 3.3(b). When the *shaft* rotates, the *slider* rigidly rotates along with it, thanks to the rotation of the *stopper*. Guided by the thread in the *main body*, the *slider* undergoes a rotation around and a translation along the *shaft* relative to the *main body* and, consequently, relative to the spring. This translation of the *slider* affects a change in the number of coils located in between the *load connector* and the *slider*, ultimately modifying the mechanism's stiffness. The spring section located in between the *slider* and point B is not affected by the load exerted by the *load connector*, because the *slider* and the thread prevent the force transmission to this part of the spring.

This C-MAC VSM offers a number of remarkable benefits over its predecessor. Firstly, the mechanism which modifies the spring's active coils is entirely contained within the spring itself, thus making the C-MAC much more compact than the Jack Spring. Indeed, as shown in Fig. 3.2, no additional length than the length of the spring itself L_s is required to fit this mechanism in a larger assembly, making the new design particularly compact. Consequently, for a given available length, the range of stiffness attainable is twice as high as the original design as no space has to be dedicated to spring translation. Secondly, this VSM lends itself to monolithic 3D printing by stereolithography, making it extremely simple, inexpensive and fast to manufacture.

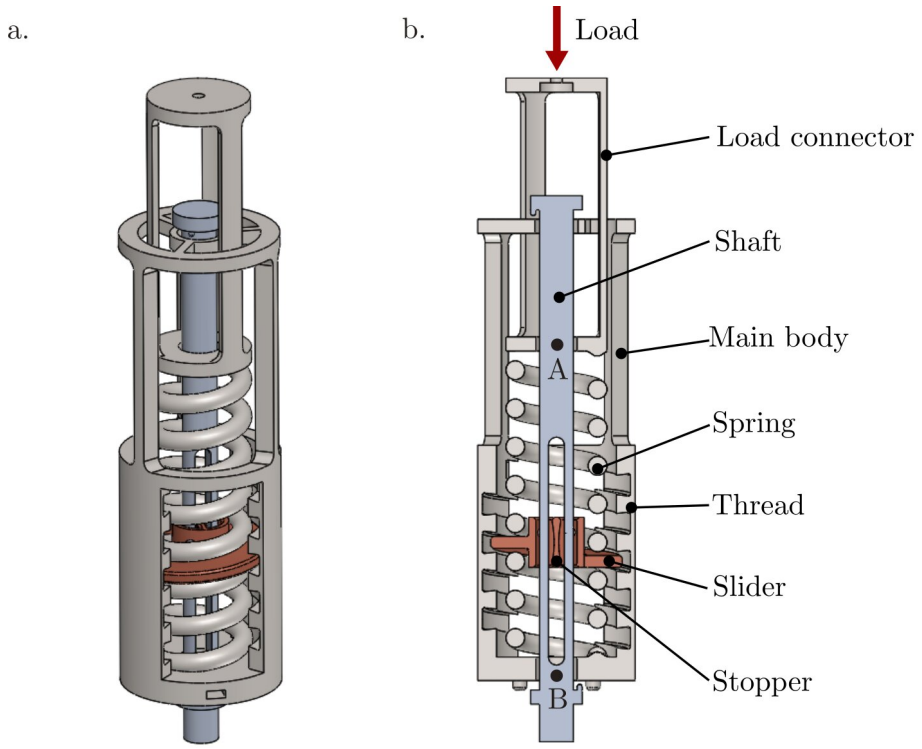

Figure 3.3: (a) 3D view of the C-MAC Variable stiffness mechanism design. (b) Cut view with the key components annotated and the constraint points A and B of the *shaft*.

Design for Monolithic 3D Printing

While the C-MAC can be manufactured with metals in traditional ways, it also lends itself to being entirely 3D printable with stereolithic 3D printers. In addition to reduced lead time and cost of production, this feature allows individuals and institutions without dedicated manufacturing capabilities (CNCs, lathes, milling machines) to easily produce custom VSMs, thus facilitating quick design iterations. Moreover, it emphasizes the possibility of designing entire high performance 3D printed robotics systems that can be mass manufactured for a fraction of their machined counterparts. The VSM design presented in this section showcases a number of specifications intended for the purpose of monolithic 3D printing. These are reviewed here and depicted in Fig. 3.4. In particular, purposely designed openings were added to either ensure the outflow of resin from the mechanism during printing or to prevent the creation of printing supports in places otherwise hard to reach. These features are essential to ensure a smooth functioning of the mechanism and an easy removal of the supports after printing. These are highlighted in Fig. 3.4(a) and (b) respectively, for the *slider* and the *main body*. These features directly affect the printing orientation and con-

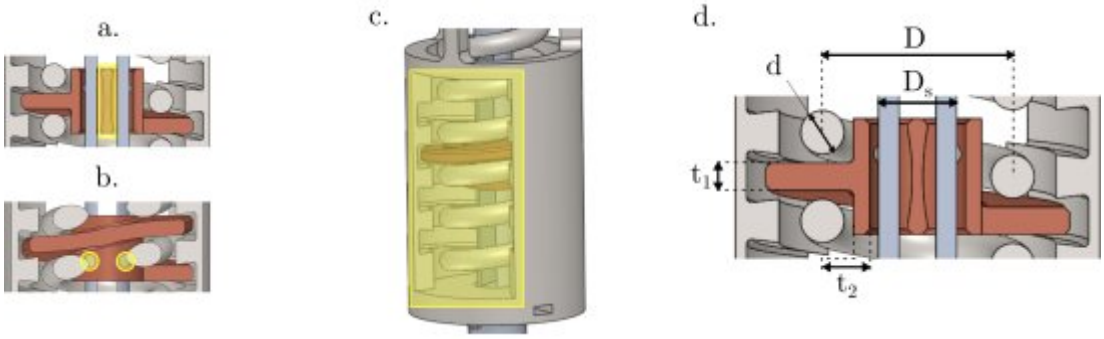

Figure 3.4: Design features added to ensure proper 3D printing. Figure **(a)** and **(b)** illustrates features added to limit entrapment of the resin against the *shaft*. Specifically, the stopper is made concave and holes are added on the *slider* to facilitate the resin flow. The openings on Fig. **(c)** are added in order to be able to access and remove the printing supports inside the *main body*. **d.** Key dimensions for robust VSMs. D_s, d, t_1, and t_2 should be higher than 6.5 mm, 2 mm, 1.5 mm and 1.5 mm, respectively. These are conservative values that can be adjusted on a case by case basis.

sequently the position of the printing supports. In particular, the openings and holes presented in Fig. 3.4(b) and (c) face the print bed. Similarly, the oblong cavity in the *shaft*, Fig. 3.4(a), is also facing the print bed. A 5° angle between the build plate and the axis running along the VSM shaft is added to reduce cupping effects between the part being printed and the resin tank in order to ensure that the part does not detach from the print bed. Finally, the slider was deemed best positioned around the centre of the openings in the main body threading to reduce the likelihood of bonding with the main body. Following an iterative design optimization process, we identified a number of minimal key dimensions which guarantee a robust product. Firstly, all the clearances e in the system should not be smaller than 0.8 mm. Secondly, as shown in Fig. 3.4d, the spring wire diameter d should measure at least 2 mm. Thirdly, the thicknesses t_1 and t_2 should both be no lower than 1.5 mm and the stopper thickness no smaller than 1mm. Fourthly, the shaft diameter D_s should measure at least 6.5 mm. These are conservative values that should always ensure a good functioning but can be adjusted on a case by case basis. These key dimensions directly predetermine the values of the mean spring diameter D and the pitch p as follows:

$$D \geq D_s + 4e + 2t_2 + d \tag{3.1}$$

$$p \geq t_1 + d + 2e \tag{3.2}$$

The parametric 3D files used in this study can be found at (185).

VSM Manufacturing

The VSMs were printed with a Formlabs 3+ (firmware rc-2.1.0-2005) with the Clear v4 resin (RS-F2-GPCL-04). The software used to generate the printing files was Preform 3.30.0. The VSM was positioned on the printing bed according to the recommendations given in Section 3.3.1. A layer thickness of 0.1 mm and a full raft with supports having a touchpoint size of 0.35 mm were used. The supports were generated by using the auto-generate function of the software with no internal supports. This ensures that, after removing the supports, few asperities remain on the thread, the *shaft* or the *slider* to guarantee a smooth functioning. However, when using the auto-generate function, a small amount of unsupported minima usually remain. Consequently, a few internal supports are added manually where needed.

After printing, the supports are removed and the parts are immersed in a bath of isopropyl alcohol (IPA) 99.9%. With a soft brush, excess resin is removed from the VSMs before putting them in a second bath of IPA 99.9% for ten minutes. The VSMs are given their final mechanical properties by curing them with 405 nm UV lights during eight hours. Finally, the supports are removed and silicone lubricant is applied to ensure a smooth functioning.

Experimental Setup

In order to evaluate the performance of the proposed VSM, the mechanism is tested under compression and tension. Scalability of the mechanism is also addressed here by manufacturing six VSMs with different wire diameters d and mean spring diameters D. These six configurations are presented in Table 3.1. The overall length of each VSM is $140\ mm$ with a maximal stroke length of $22\ mm$.

Testing of the VSMs involved subjecting them to a prescribed force F which generates a displacement x. This displacement is measured to determine the stiffness k as shown in Eq. 3.3.

$$k = \frac{F}{x} \tag{3.3}$$

Configurations	1	2	3	4	5	6
d (mm)	2	3	4	5	5	5
D (mm)	17.5	17.5	17.5	22.5	27.5	32.5

Table 3.1: VSM configurations for which the stiffness was measured.

For each configuration, the stiffness was measured for 6, 5, 4 and 3 active coils.

The test rig presented in Fig. 3.5 was used to perform the stiffness measurements. It can be both used for characterization of the compression, Fig. 3.5(a), and tension, Fig. 3.5(b), of the VSM. The test rig consists of the *main structure* 1, the *guiding platform* 2, the *weights holder* 3, the *measurement slider* 4 and the *caliper* 5, indicated in Fig. 3.5(a).

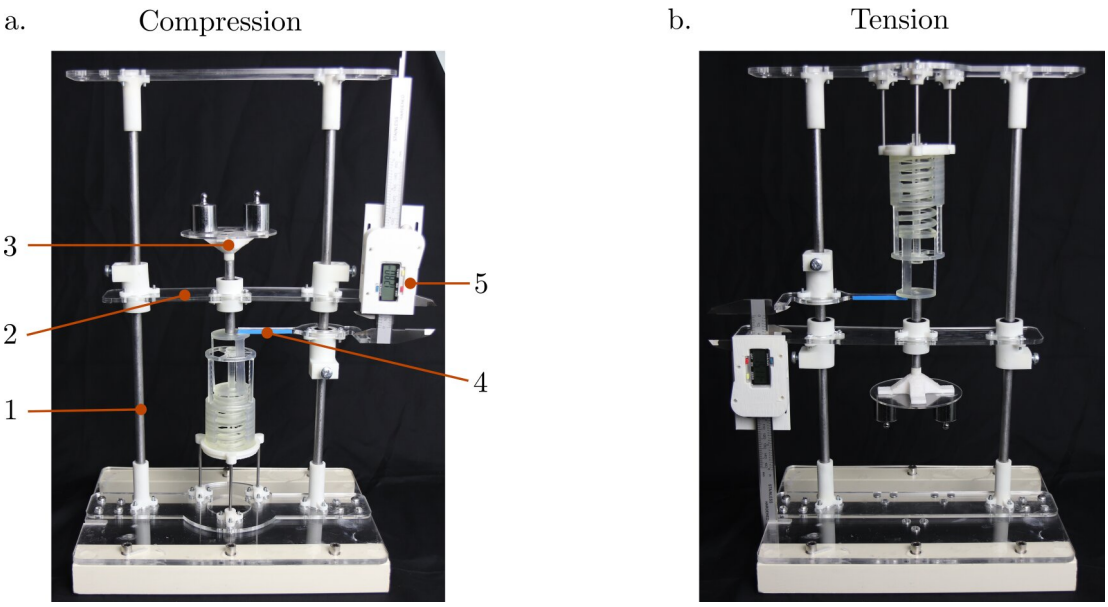

Figure 3.5: Test rig used to perform stiffness measurements. It can be used both in compression (a) and traction (b).

The procedure to perform a stiffness characterization in tension or in compression is as follows:

- Step 1: The VSM is installed on the VSM holder which is part of the *main structure* 1.
- Step 2: The *measurement slider* 4 is aligned with the top of the load connector and the *caliper* 5 is used to set the displacement at $x = 0\,mm$.
- Step 3: The weights are installed on the *weights holder* 3 which is connected to the load connector of the VSM. The weights holder translates in a straight line thanks to the *guiding platform* 2. A linear bearing is used to minimize friction.
- Step 4: After 30 seconds which ensure stabilization of the spring, the *measurement slider* 4 is realigned with the top of the load connector and the *caliper* 5 is used to measure the displacement x.

- Step 5: Steps 3 and 4 are repeated with new weights.

In each case, the VSM was first loaded and unloaded in compression and then loaded and unloaded in tension. For a given configuration and stiffness, 28 measurements were taken.

3.3.2 Performances of the 3D Printed C-MAC

Figure 3.6: From left to right: VSMs in configurations 1 to 6 (Table 3.1) after supports removal, IPA cleaning and additional curing in UV chamber.

The prints of the six configurations as per Table 3.1 are shown in Fig. 3.6. Following the protocol of Section 3.3.1, the data collected from the experimental test for each of these configurations is reported in Fig. 3.7, where the blue, orange, yellow and purple curves respectively correspond to 3, 4, 5 and 6 active coils. Fig. 3.7 brings evidence of a quasi-linear relationship between load and displacement of the springs associated with a slight hysteresis. The occurrence of non-linearities in the spring behaviour is mostly observed for smaller loads and especially for reduced number of active coils, Fig. 3.8(b). This type of non-linearity is not attributed to the spring material properties, but rather to the clearances implemented in the design to facilitate manufacturing. Indeed, as depicted in Fig. 3.8(a), systematic clearance of extent $c = p - t_1 - d$ arises when the VSM is at rest, due to the spring not engaging with the slider. In other words, when at rest, the VSM stiffness is not impacted by the slider's position and is always equal to the entire spring stiffness. However, upon loading the VSM, the clearance c disappears and the relationship between stiffness and spring length is reinstated. This transition between two different stiffness profiles is responsible for the non-linearities observed. In particular, this phenomenon is prominent for low number of active coils because the stiffness increases when the number of coils is reduced.

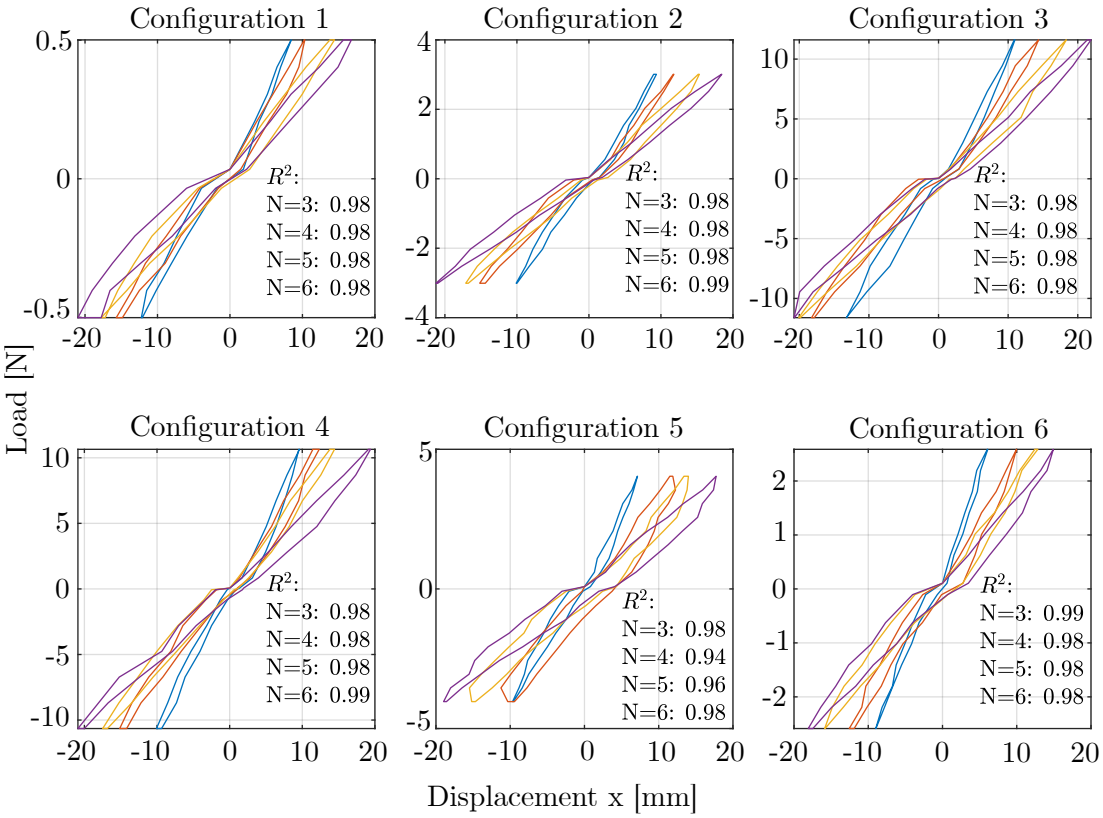

Figure 3.7: Force versus deformation x for each configuration of VSM. Blue, orange, yellow and purple respectively represents 3, 4, 5 and 6 active coils N indicating linear stiffness scaling. The coefficient of determination R^2 in each subset indicates divergence from linearity for each case tested. Each curve is obtained from a single measurement session; no repeated trials or averaging were performed.

Figure 3.7 also highlights clear hysteresis loops for each case tested, underscoring the presence of internal viscoelastic losses. An estimate of the VSM's energy efficiency η is obtained by integrating along the load curves , Eq. 3.4, yielding the result in Fig. 3.9(d). The efficiency ranges between 0.64 and 0.88 across the whole range of coil activation and with an average of 0.78, confirming contained dissipation.

$$\eta = \frac{\int_{loading} F\ dx}{\int_{unloading} F\ dx} \tag{3.4}$$

For what concerns derivation of the stiffness of the VSM, we rely on Eq. 2.4. In order to determine the stiffness of the VSMs, a least squares linear regression is performed for each hysteresis loop of Fig. 3.7 and a shear modulus of $G = 401MPa$ provides the best fit for each of the configurations tested. Using the shear modulus equation for isotropic material $G = E/(2(1+\nu))$ (186), and assuming that the

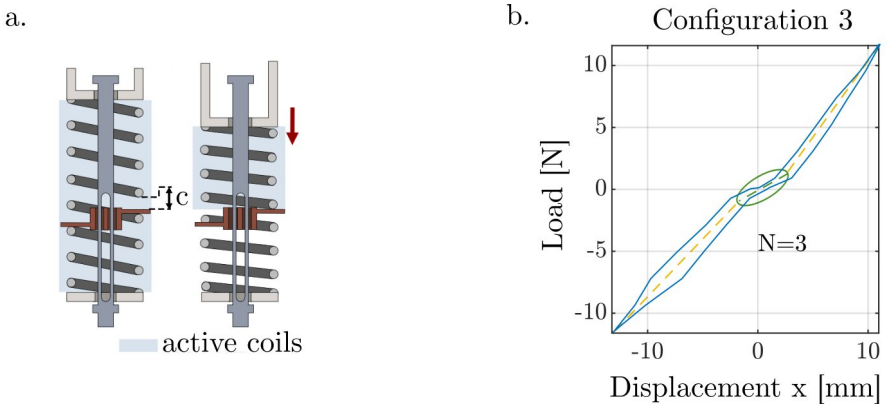

Figure 3.8: Onset of non-linearity explained: a. Until the clearance c is present the VSM stiffness is dependent on the number of coils. However, once the load applied is sufficient to obtain $c = 0$, the stiffness is now dependent on the coils between the slider and the load connector. b. This phenomenon can mostly be observed for low number of active coils, as for instance, for configuration 3 with 3 active coils.

Poisson's ratio ν is in between 0.3 and 0.45 (187) while the Young's modulus E is in between 1.6 Gpa and 2.8 Gpa (188), the theoretical shear modulus is expected to range between 551 Mpa and 1077Mpa. While the value found with our experiments is lower than the theoretical minimal bound, the characteristics of the resin provided by the supplier data-sheet (188) emphasizes that its mechanical properties can be drastically impacted by temperature, part geometry and curing conditions, suggesting that values outside the nominal range are to be encountered. The coefficients of determination R^2 for each regression are presented alongside the curves in Fig. 3.7. With $R^2 \geq 0.94$ the assumption of a linear stiffness profile is further confirmed. Values of R^2 are reported for all the reminder of stiffness measurements for readers' convenience.

Figures 3.9(c) and (b), respectively present the stiffness as a function of spring mean diameter D and wire diameter d for different number of active coils. These are compared against the theoretical trends based on Eq. 2.4, recalled below for the reader's convenience.

$$k = \frac{d^4 G}{8 D^3 N} \qquad \text{(2.4 revisited)}$$

Finally, we assess the stiffness tuning performance of all the configurations manufactured: Fig. 3.9(a) depicts the stiffness variation as a function of number of active coils. The highest stiffness observed was 1.02 N/mm, obtained for configuration *four* with three active coils; the lowest stiffness of 0.15 N/mm was obtained for configuration *one* with six active coils. The range of $0.63 \leq R^2 \leq 0.96$ with a mean value $\overline{R^2} \approx 0.78$ gives confidence in the VSMs' performance closely matching theory and

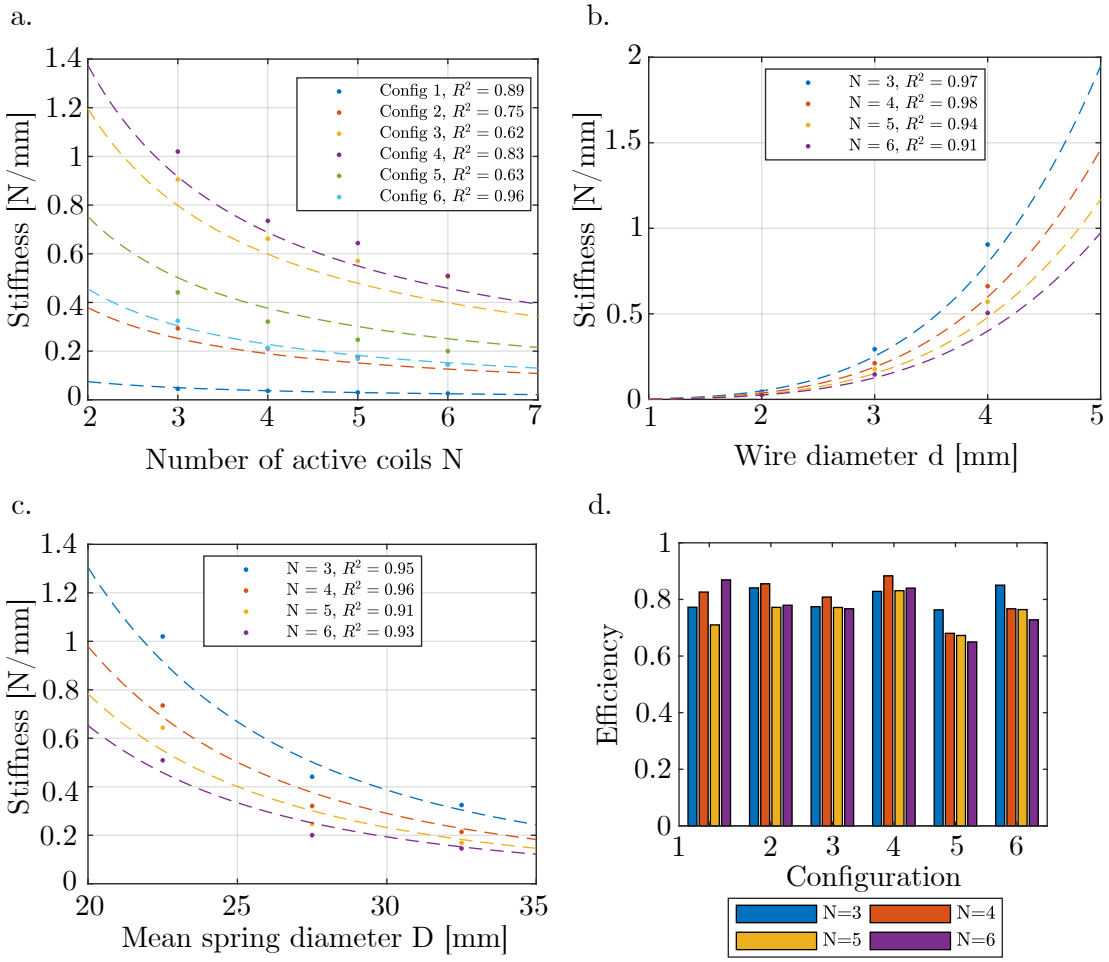

Figure 3.9: The dots represent the stiffness derived from the experimental data. The dotted lines represent the theoretical trends obtained with equation 2.4 with shear modulus G of $415.5MPa$. **a.** Stiffness versus the number of active coils N for each configuration. **b.** Stiffness versus the mean spring diameter d. **c.** Stiffness versus the mean spring diameter D. **d.** Efficiency for each configuration of VSM and each number of active coils.

thus confirms that stiffness tuning scales with $k \propto N^{-1}$.

It should be noted that, for each stiffness and configuration, the system response was characterised over a range of operating points (28 measurements per condition), allowing the overall trends in the hysteresis behaviour to be captured. However, the experiments were not repeated multiple times under identical conditions. As a result, no cycle-to-cycle averaging or statistical analysis of variability was performed. Repeating the measurements for a given stiffness and configuration and averaging the resulting hysteresis loops would improve the robustness of the results by reducing the influence of measurement noise and experimental variability. This represents

a potential avenue for improving the experimental protocol in future work. Despite this, the observed trends were consistent across configurations and stiffness and sufficiently pronounced to support the conclusions drawn.

3.4 Conclusion

This chapter defined the conceptual and functional basis for the resonance-driven pulsatile pump developed in this work. By translating theoretical insights on resonance and frequency tuning into practical design criteria, it established the need for a compact, energy-efficient system capable of varying its stiffness in real time. The resulting concept combines a linear actuator with a novel variable stiffness mechanism, the Compact Modifier of Active Coils (C-MAC), enabling controlled modulation of the pump's natural frequency.

The proof-of-concept experiments demonstrated that stiffness can be accurately tuned and that the C-MAC behaves predictably, validating the feasibility of embedding variable stiffness into a compact architecture. These results set the stage for the mechanical realization of the full pump, described in Chapter 4, which details the design, fabrication, and initial testing of the complete system and its integration into a controlled experimental environment.

Chapter 4

Prototype Design and Experimental Platform

4.1 Introduction

Following the establishment of the pump's conceptual design and functional requirements, this chapter presents the mechanical development of the full prototype and its associated experimental setup. The objective is to translate the conceptual framework into a physical system that can be tested under controlled conditions to assess its dynamic and resonant behaviour.

The chapter begins by detailing the overall pump architecture, including the integration of the C-MAC variable stiffness mechanism within the housing and the actuation subsystem based on a voice-coil actuator. The design emphasizes modularity, precision, and repeatability to facilitate both mechanical testing and future iterations. The manufacturing process, relying on stereolithography (SLA) 3D printing and metallic parts machining, ensures high dimensional accuracy in order to reduce the footprint of the overall prototype and fullfill the size requirement defined in Section 3.2.1.

The second part of the chapter describes the characterization of the pump's mechanical response and the design of the experimental setup used to measure displacement, force, flow rate, and pressure. Different configurations are introduced to study the effects of hydrostatic pressure. These foundations allow for the subsequent analysis of resonance phenomena and performance metrics explored in Chapter 6 and 7.

4.2 Pump Mechanical Design

This section details the mechanical architecture of the developed resonant pulsatile pump, describing how the conceptual principles established in Chapter 3 are translated into a functional prototype. The design integrates the variable stiffness mechanism, the actuation system, and the compliant pumping chamber into a compact, modular structure that replicates the alternating compression–expansion behaviour of a biological pump. Emphasis is placed on manufacturability, assembly, and durability to ensure reliable operation under dynamic conditions, while maintaining a form factor comparable to that of the human heart.

4.2.1 Overview of the Pump

Figures 4.1a and b present the final pump concept with the C-MAC embedded in its center respectively during expansion and contraction. The mover (4) is elastically coupled to the pump's housing via the spring (7) of the C-MAC which will drive the pump's resonant behavior. The fluid ingestion phase results in the stretching of the spring, while the expulsion phase results in the compression of the spring. In order to control the stiffness, a motor (8) is added to drive the rotation of the VSM shaft (9) which induces the rotation and translation of the slider (10). A 3D rendering of the pump is provided in Fig. 4.1c, which shows a four-rib configuration implemented in the experimental prototype.

Furthermore, an exploded view of the manufactured pump assembly is shown in Fig. 4.2, detailing the main structural and functional components. The ribs, the membrane, the actuator, the VSM and the valves are identified with the notations (1), (2), (3), (4) and (5) respectively. The mover and VSM are enclosed in a tube (6) to protect them from rust and corrosion. A protective membrane (7) through which the lever arms protrude prevents liquid ingress and accommodates movement via moulded bellows. In addition to providing protection, the tube represents the backbone of the pump as it connects the actuator and the inlet/outlet manifold (8) to form a rigid subassembly.

The next section presents in more details the key components of the pump, their manufacturing process and the rationale of the overall design.

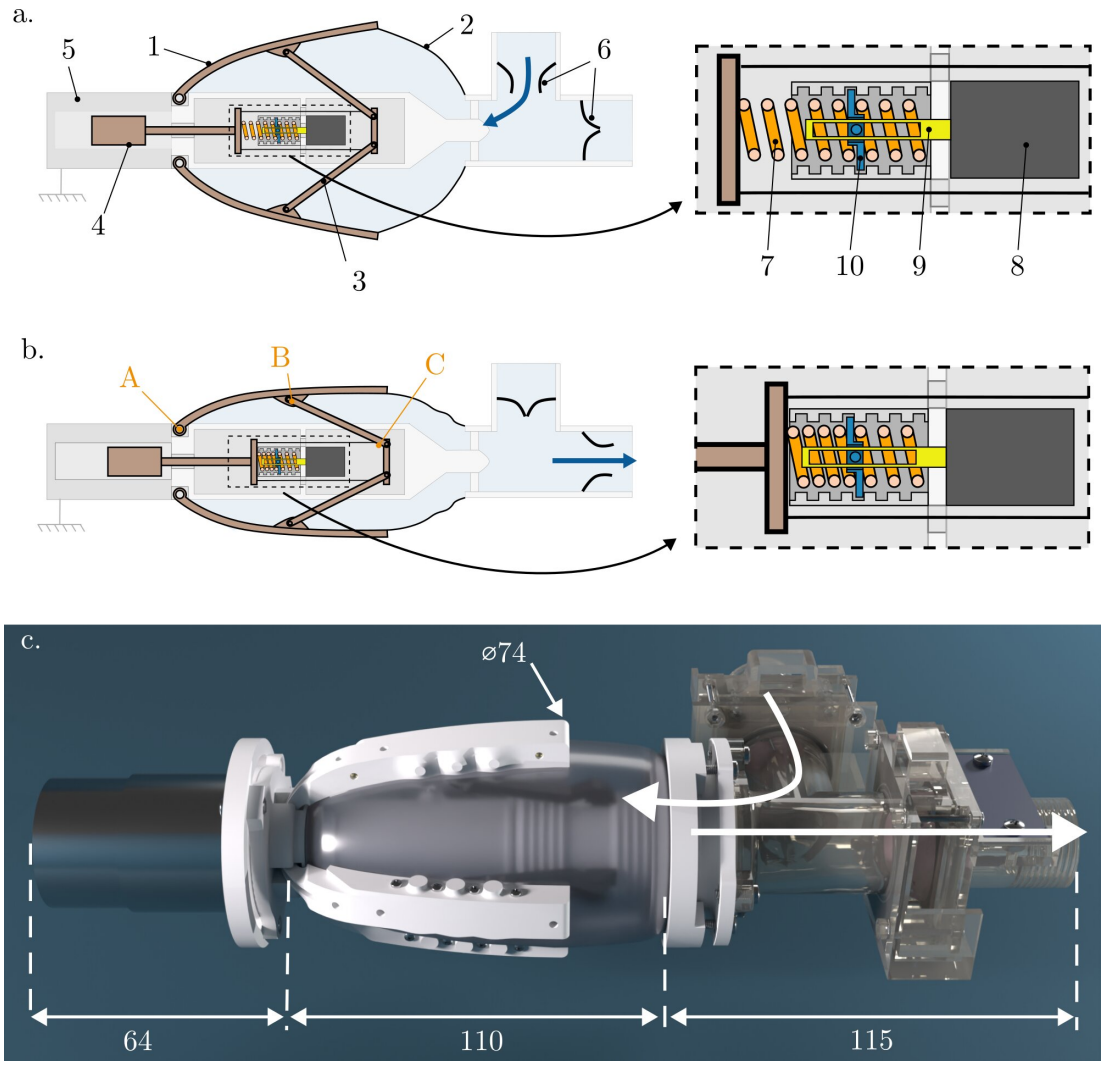

Figure 4.1: a. and **b.** Top cut view of the pump respectively during the ingestion and expulsion phase. Brown-colored components represent moving parts of the mechanism, while gray ones are static; light blue identifies the volume occupied by the fluid. **c.** Three dimensional render of the pump used in this study (units: mm).

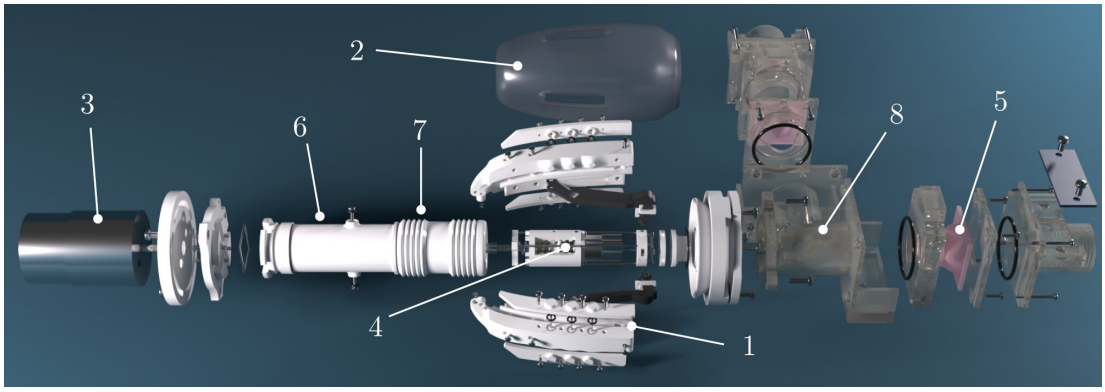

Figure 4.2: Exploded view of the pump developed.

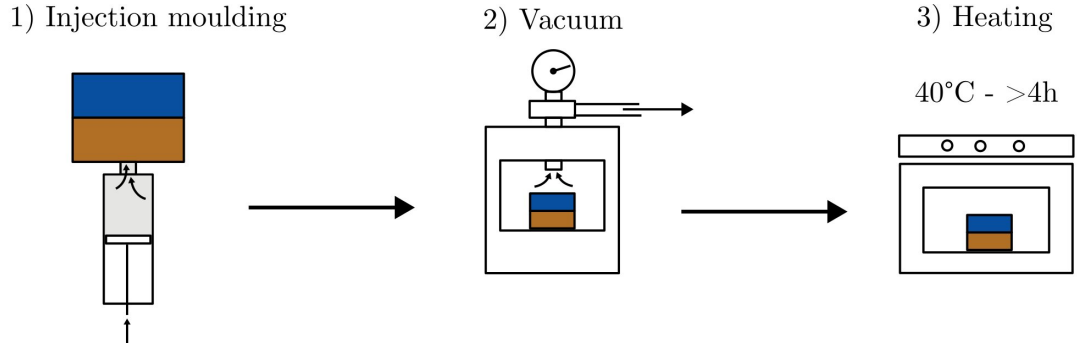

Figure 4.3: General process used to manufacture the flexible membranes and valves. Silicone rubber is injected in the moulds with a syringe. The moulds are then placed in a vacuum chamber to remove air bubbles. Finally, they are heated at 40 °C during four hours to cure the silicone rubber.

4.2.2 Pump Manufacturing and Design Choices

Unless stated otherwise, all the rigid components are fabricated using stereolithography (SLA) 3D printing with a Formlabs 3+ printer, utilizing either Clear v4 or White v4 resin. SLA technology offers high precision, with layer resolutions down to 50 microns, and produces parts with more uniform mechanical properties compared to Fused Deposition Modeling (FDM), reducing anisotropy and orientation-dependent behavior. In addition, materials used in SLA 3D printing are a less porous than FDM ones making them less prone to mechanical performances variations and ensuring a better protection of sensitive components.

All the moulded parts are made with silicone rubber using injection moulding. This material is chosen for its wide off the shelf availability and its low shore (10A) limiting the introduction of additional stiffness and damping. Each moulding follows a similar process as presented in Fig. 4.3. Mould release is sprayed on all the surfaces that will get in contact with the silicone rubber. The silicone rubber is then manually injected in the moulds using a syringe. Once the moulds are full, they are placed in a vacuum chamber to remove air bubbles (three cycles of three minutes minimum). They are then placed in an oven at 40 °C for at least 4 hours before opening them. The moulds are made with SLA 3D printing which limits layer lines and facilitate demoulding. Moulding was chosen over 3D printing as current printers do not allow the use of material with shores lower than 50A which was deemed too high.

The references of the different components, glues, materials used to manufacture the pump are all listed in Appendix 11.

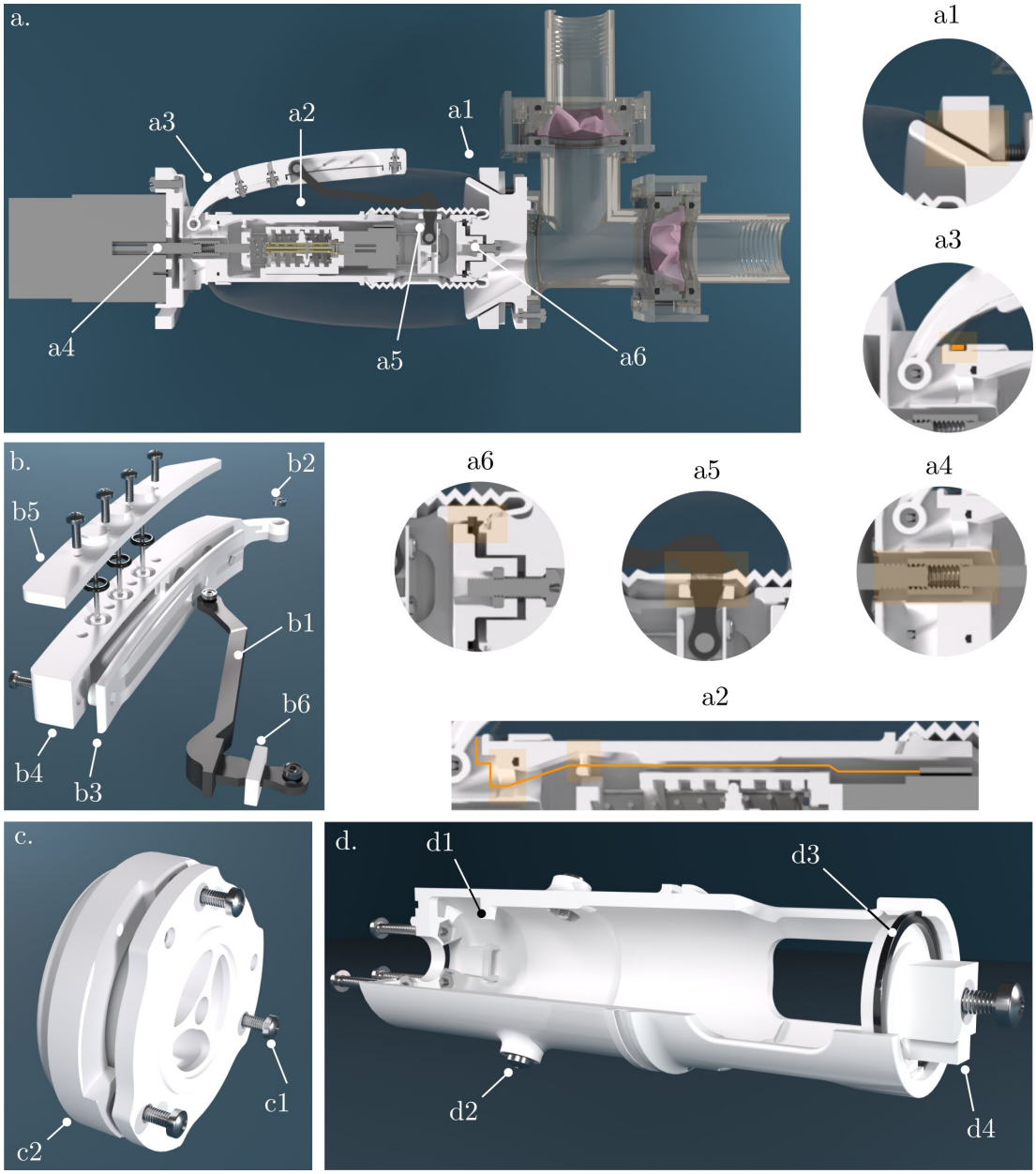

Figure 4.4: a. Cut view of the pump showing selected design features.**b.** Exploded view of the rib-lever arm assembly. **c.** Cone locking mechanism used to secure the main membrane. **d.** Partial section view of the protective tube.

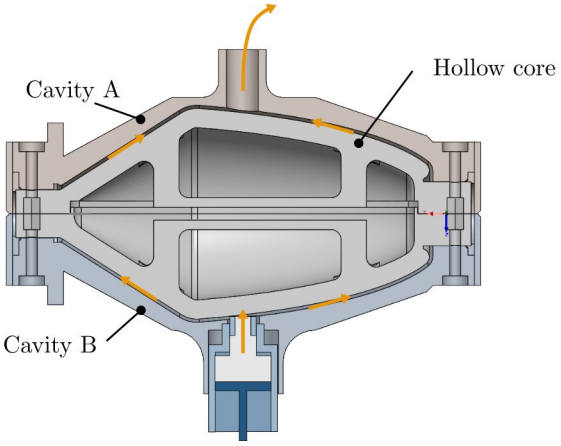

Figure 4.5: Cut view of the moulding assembly used to fabricate the main membrane. The orange arrows indicate the paths of the silicone rubber.

Main Membrane. The mould used to fabricate the main membrane is shown in Fig. 4.5. It consists of three parts: a central core and two outer cavities. Silicone rubber is injected from the bottom of the mould until it fills the cavity and exits through the vent at the top. The membrane's geometry was selected based on the dimensions of the human heart (≈ 80mm in diameter and ≈ 120mm in length (85)) and the average volume capacity of the left ventricle. The resulting membrane can contain approximately 120 mL, which closely matches the typical expanded volume of the left ventricle (3).

Figure 4.4a presents some of the key design features of the pump. Particularly, on the actuator's side, the membrane is held in place with superglue spread along the surface highlighted in orange in Fig. 4.4a - *a3*. On the inlet/outlet side, the main membrane is held in place by a conical locking mechanism as seen in Fig. 4.4c. The lock *c2*, pushed by the screws *c1* translates on top of the cone to hold the membrane in place as seen in Fig. 4.4 - *a1*. When clamped, the membrane acts as a seal. This design is chosen to facilitate quick assembly/disassembly and to maintain the stretching capacity of the membrane which facilitates the insertion of the lever arms, the tube and the different components inside it.

Actuation Mechanism. For the linear actuation, a voice coil actuator is chosen. As opposed to solenoids, voice coil actuators present the characteristic of developing an almost constant force for a given current throughout their entire stroke (189). This specificity is essential to facilitate the dynamic analysis of the pump by limiting interdependence between variables and to simplify power and energy consumption estimations, as presented later in Chapter 5.

The lever arm and rib subassembly is detailed in Fig. 4.4b. The lever arms *b1* are FDM-printed with Polyethylene Terephthalate (PET) reinforced with carbon fiber for strength and low moisture absorption. They are coated in epoxy to further enhance their water-tightness and prevent drifts in mechanical performances.

Micro bearings are press-fitted to both ends of the lever arms to ensure smooth rotations. Similarly to the lever arms, a micro bearing *b2* is press fitted at the pivot point between the rib and the static parts. Micro ball-bearings are used for durability purposes, as opposed to flexible linkages which are prone to breakage and to variations in mechanical performances through time. While they slightly complexify the overall assembly process, the durability benefits are deemed to be higher than the disadvantages.

To connect both membranes to the rib assembly, a combination of clamping mechanism and gluing is used. The main membrane is clamped between the membrane holder *b3* and the rib *b4* providing a watertight connection. The rib lid *b5* secures the metallic shafts around which the lever arm rotates and applies pressure on the O-rings to prevent leakages. The protective membrane is clamped between the shoulder on the lever arm and the membrane holder *b6*. The membrane holder is press-fitted and glued on the lever arm permanently connecting it to the protective membrane. Figure 4.4a - *a5* provides a cut zoomed in view of this connection.

Miniaturized Variable Stiffness Mechanism and Mover. The Variable Stiffness Mechanism (VSM) is composed of both metallic and 3D-printed components to balance miniaturization with mechanical durability. Figure 4.6a shows the manufactured VSM held in a support while Fig. 4.6b. presents an exploded view and a cut view of the mechanism to visualize each of the internal components.

In Fig. 4.6b, the main body *b3* is fabricated following the printing approach presented in Chapter 3. The slider *b2* is also 3D printed but the stopper *b4* inside it is made of a 1 mm steal rod glued in place. The shaft *b5* is constructed from a copper tube (ID 3mm - OD 4mm), machined with precision slots to accommodate the slider's translation.

Actuation is provided by a miniature motor *b7* (see appendix 14) coupled to the VSM shaft *b5*. The shafts coupler *b6* join the motor shaft with the VSM shaft and is made of a 1 mm steel rod glued perpendicularly inside the VSM shaft.

The spring was selected based on multiple design constraints. The minimum usable diameter was limited by the motor shaft diameter and the smallest feasible slider size achievable through 3D printing. The spring pitch was chosen to ensure sufficient helix thickness of the slider to withstand cyclic loading. Under the assumption that the pump behaves approximately as a single degree-of-freedom (1 DOF) system, the ratio of maximum to minimum stiffness was set to at least 4 to achieve a resonant frequency shift of $\sqrt{4} = 2$. This is further explained in Chapter 5. Finally, the spring is chosen to be conical to ensure a more stable translation than with a cylindrical spring and prevent buckling during compression. The spring is connected to the mover and the VSM main body with epoxy.

The mover is connected to to the actuator via a threaded interface as illustrated in Fig. 4.6b - *b1* and Fig. 4.4a - *a4*. This solution is chosen as it allows precise positioning of the actuator's plunger. Indeed, given the limited stroke of the actuator (6 mm), the plunger has to be positioned accurately to be able to exploit its entire range of motion. This threaded feature allows us to compensate for dimensional variations introduced by manufacturing tolerances. As an example, assuming a symmetrical motion around its equilibrium position, a simple offset of 1 mm would result in a usable stroke of only 4 mm, in other words, two third of the entire stroke. Finally, this assembly technique ensures that the VSM is not permanently connected to the pump facilitating replacements and experimental testing of the VSM on its own as presented later on in Chapter 7.

The rest of the mover is made of four 1 mm steel rod used to transmit the motion to the lever arms and glued in place on both sides. A lid maintained by four screws hold in place the steel shafts, Fig. 4.6b - *b8*, around which the lever arms rotate.

Protective Tube. To minimize the motor's footprint and simplify assembly, the motor cables are desoldered, replaced by longer and stiffer ones and reoriented to align with the pump's central axis. As shown in Fig. 4.4a - *a2*, the cables (represented in orange) are kept away from the plunger's and mover path by a protrusion inside the tube and travel through an opening in the tube to reach the outside of the pump. Additional protrusions in the tube shown in Fig. 4.4d - *d1* are used as guides to ensure that the VSM is always assembled in the same orientation, improving repeatability between assemblies/disassemblies. The screws in Fig. 4.4d - *d2* ensures the VSM is locked in

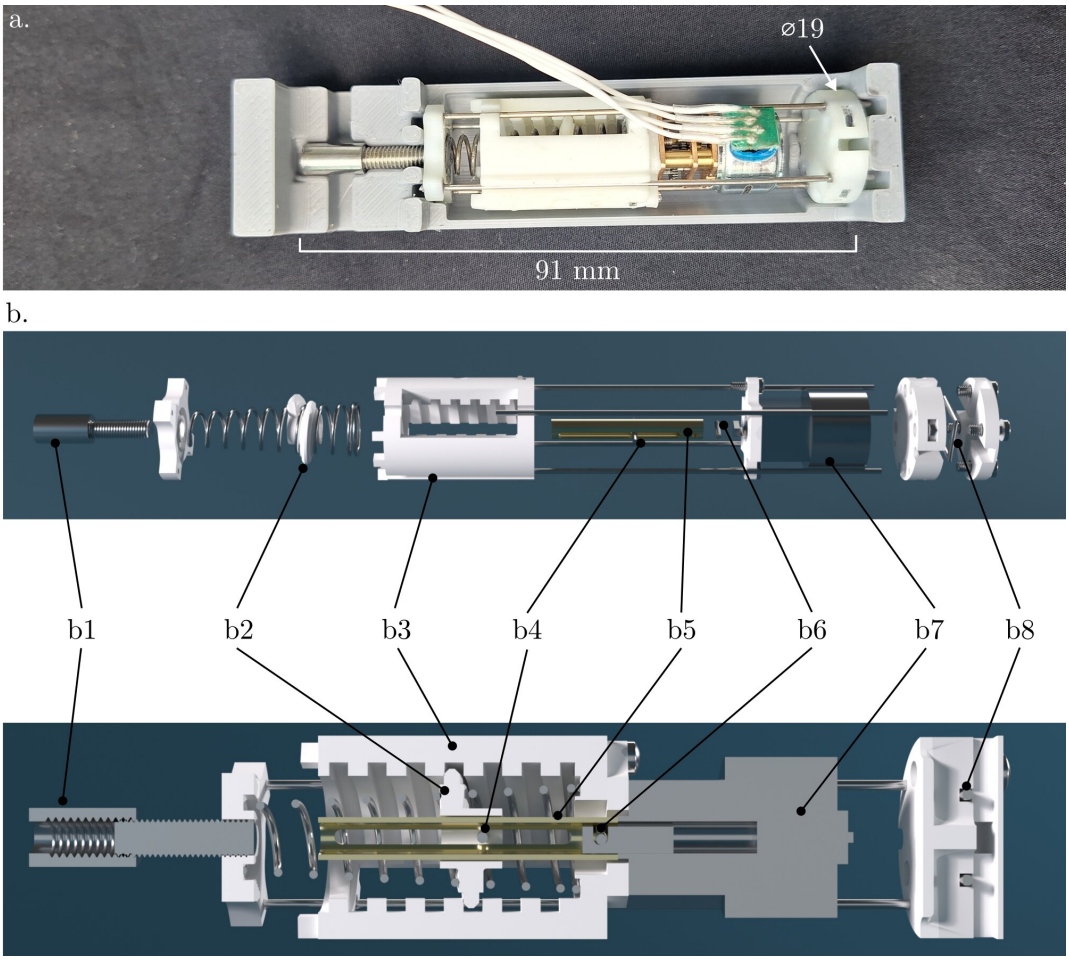

Figure 4.6: a. Prototype of the miniaturized variable stiffness mechanism in its storage case. **b.** Exploded and cut view of the VSM.

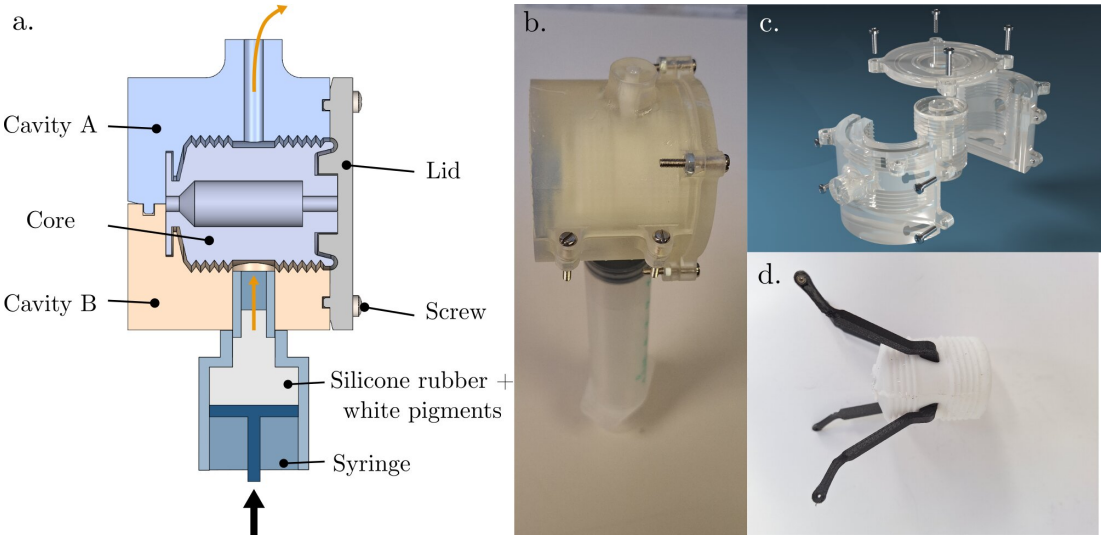

Figure 4.7: a. Cut view of the moulding assembly used to fabricate the protective membrane. **b.** 3D printed moulds connected to the syringe used to inject silicone. **c.** Three dimensional render of the different parts constituting the moulding assembly. **d.** Protective membrane obtained after the moulding process assembled to the lever arms.

place.

On the inlet/outlet side, the tube is held in place with a customized nut and a circlip identified *d4* and *d3* in Fig. 4.4d. The circlip creates a shoulder on which the nut rest against when pulled by the the cone locking mechanism screw. The circlip is removable to allow for the insertion of the VSM. A cut view is provided in Fig. 4.4a *a6*.

The protective membrane is clamped between the tube and the cone locking mechanism and ensures watertightness. On the other side, the protective membrane is secured by glue. The below geometry was chosen to limit radial bulk in order to limit collisions with the lever arms especially during the compression phase. A cut view and an 3D rendered exploded view of the moulds used are presented in Fig. 4.7a and c respectively. Figure 4.7b shows the 3D printed moulds with the silicone curing inside while Figure 4.7c presents the final result with the lever arms assembled to the membrane. White pigments are added to the silicone rubber for aesthetic purposes.

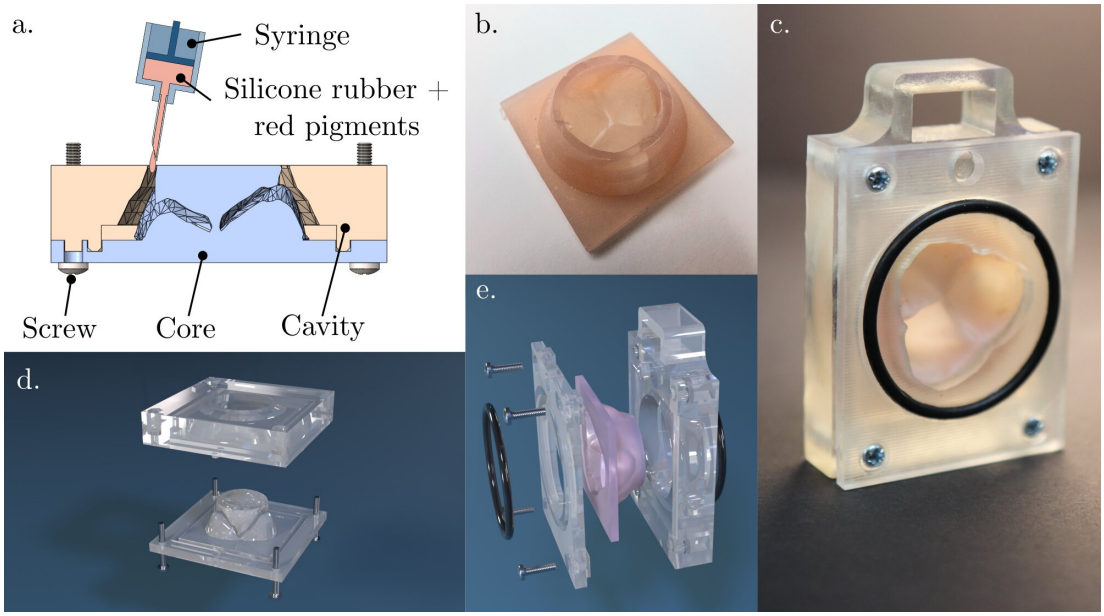

Figure 4.8: a. Cut view of the moulding assembly used to fabricate the one-way valves. **b.** Moulded valve. **c.** Cassette assembly for easy connection to the inlet/outlet manifold. **d.** 3D render of the moulds used for the manufacturing of the pump inlet and outlet valves. **e.** Exploded view of the cassette assembly used to hold the valve.

Inlet/Outlet Manifold. The inlet/outlet manifold ensures the connection between the pump and the valves. The 90 ° angle between inlet and outlet is chosen arbitrarily.

Valves are moulded based on a 3D scan of a semilunar heart valve from the NIH 3D Print Exchange (190). The design was trimmed and scaled to fit our application. While this type of valve is located only on the outlet side on a human heart, the same valve design for both inlet and outlet is used for simplicity. Indeed, the inlet valves of a human heart present much more complex features that could not be embedded in this prototype. A cut view of the moulds assembly is presented in Fig. 4.8a as well as an exploded 3D view in Fig. 4.8d. The resulting valve is shown in Fig. 4.8b to which red pigments were added for aesthetic purposes.

The valve is clamped in a *cassette* assembly as seen in Fig. 4.8c and Fig. 4.8e. This approach is adopted to easily change the valve design without having to reprint the rest of the parts. In addition, the cassette design of the valve assembly enables to connect and disconnect it easily from the overall assembly, simplifying the iteration process.

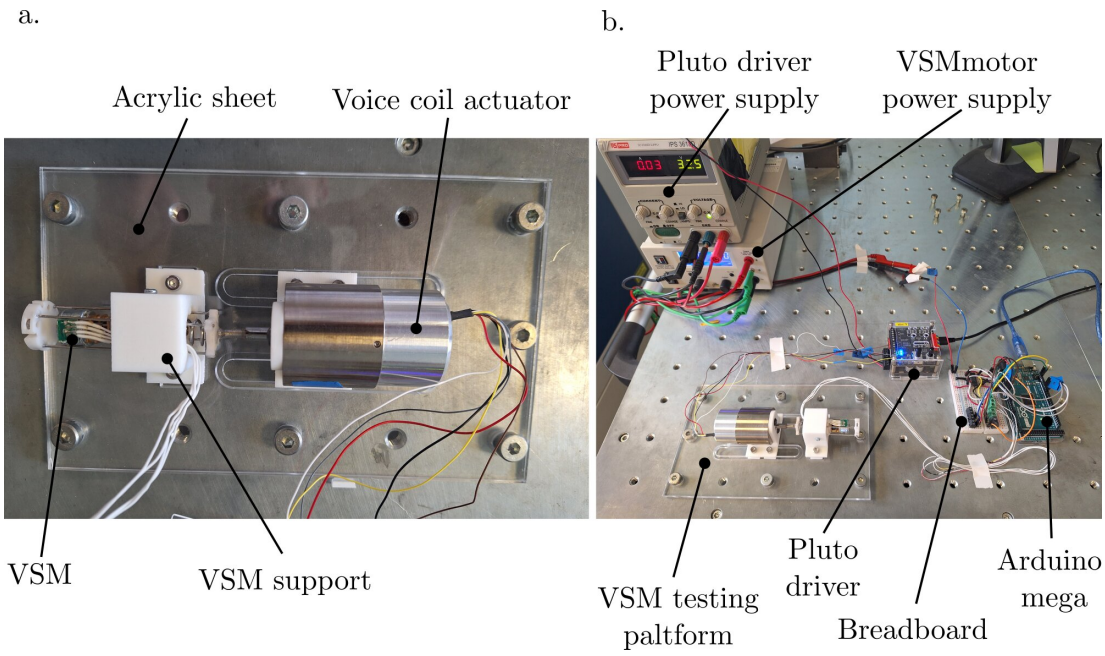

Figure 4.9: Experimental setup used to test the VSM.

4.3 Pump Performances Characterization

This section presents the experimental setups used to evaluate the pump's performances. The different configurations in which the pump is tested as well as the experimental protocol used are presented.

4.3.1 Experimental Setup

Unless otherwise stated, all the supports used to anchor the pump or the VSM are SLA printed with Clear v4 or White v4 resin from Formlabs. The references of the different components used for the experimental setups are all listed in Appendix 10.

Variable Stiffness Setup

The experimental setup for evaluating the stiffness of the VSM is shown in Fig. 4.9. Both the VSM and the voice coil actuator are mounted on rigid supports secured to an acrylic base plate, which is itself bolted to a steel optical table to ensure mechanical stability as seen in Fig. 4.9a. The VSM is fixed to its support using two lateral screws - replicating the mounting configuration used in the actual pump assembly - thereby ensuring that the test conditions closely reflect operational use.

Pump Setup

As shown in Fig. 4.10b, the pump is mounted on supports attached to aluminum extrusions (40x40 mm) and fixed to a ThorLabs anti-vibration platform. A 4 mm acrylic sheet is bolted on the platform to protect it from water. Weights (40 g) are added to the ribs to reduce resonant frequency as seen in Chapter 5. The weights were selected empirically during preliminary tests. Specifically, weights were gradually increased until the natural frequency of the system was reduced as much as possible while still allowing a clear resonant response to be observed within the operating range of the actuator. Once this value was determined, the same set of weights was kept fixed throughout all experiments. Importantly, the weights were not modified when the stiffness was adjusted. Consequently, variations in the resonant frequency across configurations arise solely from changes in the effective stiffness of the system. Both inlet and outlet are connected to a FDM 3D printed water tank (printed with Polyethylene Terephthalate filament for watertightness) (width x length x height = 60 x 140 x 80 mm). Purification tablets and food coloring are used to prevent bacterial proliferation and to easily visualize the water path.

Pump Control

To control the pump and the VSM, the same electronic setup is used for both the VSM setup and the pump setup to ensure consistency in the experimental results. It is shown in Fig. 4.9b.

The electromagnetic force produced by the voice coil actuator is driven by its dedicated control unit, the Pluto Driver. The Pluto Driver is programmed via the MotionLab (v.13.2.691) software. Specifically, the software allows for the tuning of a PID controller to control the amplitude and the frequency of the force produced by the actuator. The PID was tuned empirically until stable behavior was observed. The VSM motor is controlled via an Arduino Mega connected to an H-Bridge on a breadboard. Separate power supplies are used for the motor and the actuator to isolate power requirements and reduce interference.

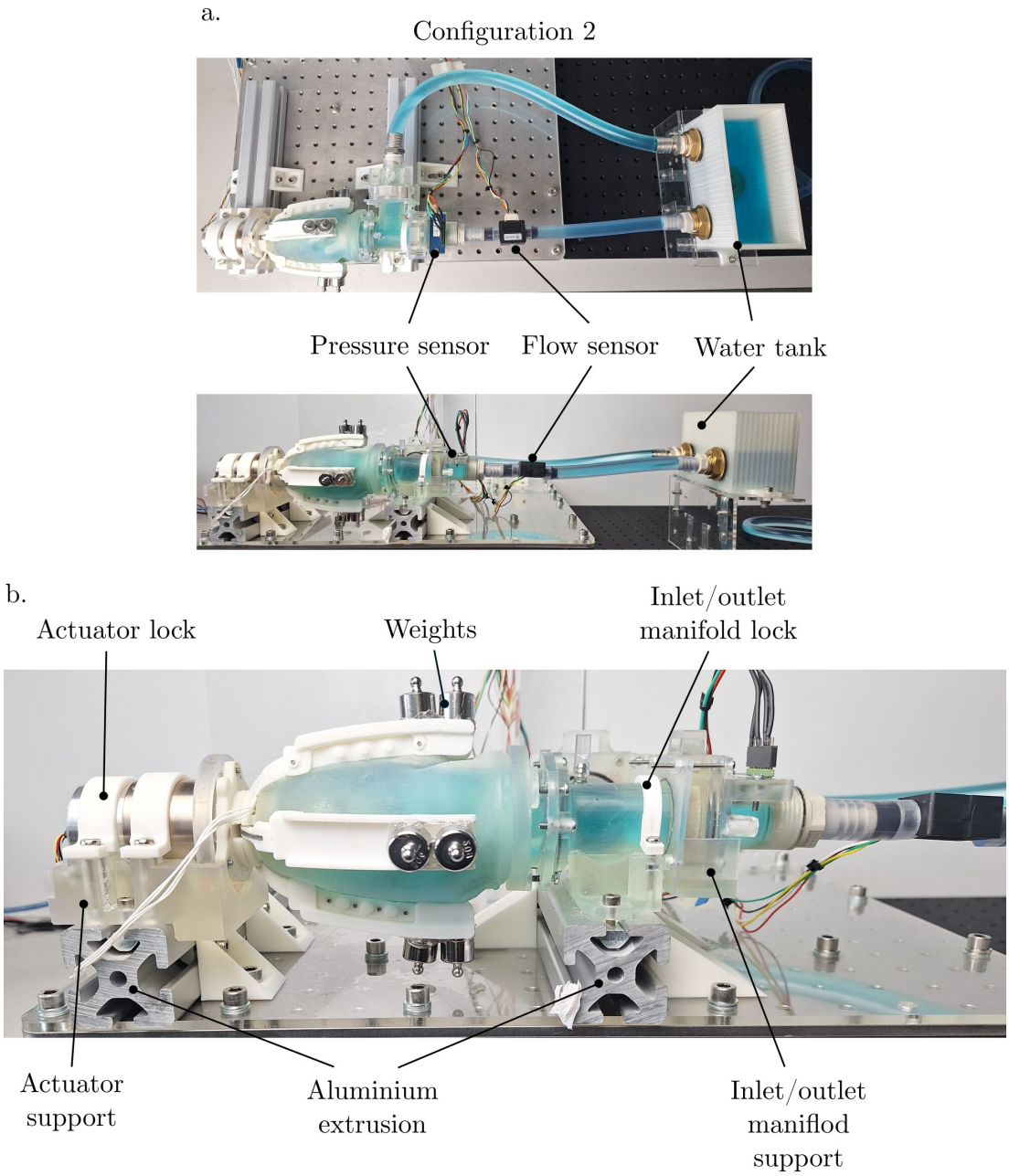

Figure 4.10: a. Top view and side view of the experimental setup used to test the pump. Here the pump is loaded with water as in configuration C. **b.** Zoomed in side view of the pump.

Data Collection

A gauge pressure sensor is installed after the outlet valve as shown in Fig. 4.10at. The outlet tubing also includes a calorimetric flow sensor. Pressure and flow sensor data is collected via Arduino Mega and stored on an SD card. The voice coil actuator includes a built-in position sensor from which the speed is derived automatically by the Pluto Driver. In addition, the Pluto Driver embeds a current sensor used as a control variable for the PID. All the data relative to the actuator is transferred by USB connection from the driver to a computer. The sampling frequencies used during the experiments were determined by the capabilities of the acquisition hardware. On the actuator side, the Pluto Driver allows a maximum sampling rate of 300 Hz. This value was therefore selected to maximize temporal resolution of the actuation signals. For the pressure and flow rate measurements, the sampling frequency was determined by the communication and processing limits of the sensors and the acquisition code. Under these conditions, the effective sampling rate was approximately 125 Hz. These sampling frequencies are well above the characteristic frequencies investigated in this work, where actuation frequencies remained below 19 Hz (see Section 4.3.2). In particular, even when considering the third harmonic of the actuation signal ($\approx 3 \times 19 = 57$ Hz), the 125 Hz sampling rate satisfies the Nyquist criterion, which requires the sampling frequency to be at least twice the highest frequency component present in the signal. Consequently, the acquisition rates provide sufficient temporal resolution to capture the dynamics and harmonic content of the measured signals.

4.3.2 Protocols

Two types of protocol are used to evaluate the pump performances.

Protocol 1 - Quasi-static tests. The objective of this protocol is to determine the system stiffness, the plunger's equilibrium position and the energy losses per cycle. For this protocol, only the force provided by the actuator and the plunger's position are measured. From the plunger's equilibrium position, the actuation force is progressively incremented (0.5 Newtons increments) until the plunger reaches 90 % of its stroke. The force is then decremented until it reaches 10% of the available stroke and finally re-incremented until reaching the equilibrium position. For each force the plunger's position is measured. A delay of one second is used in between each force increment to ensure that the force stabilizes. This cycle is performed three times. A final force-position loop is obtained by averaging the results of the three loops. This

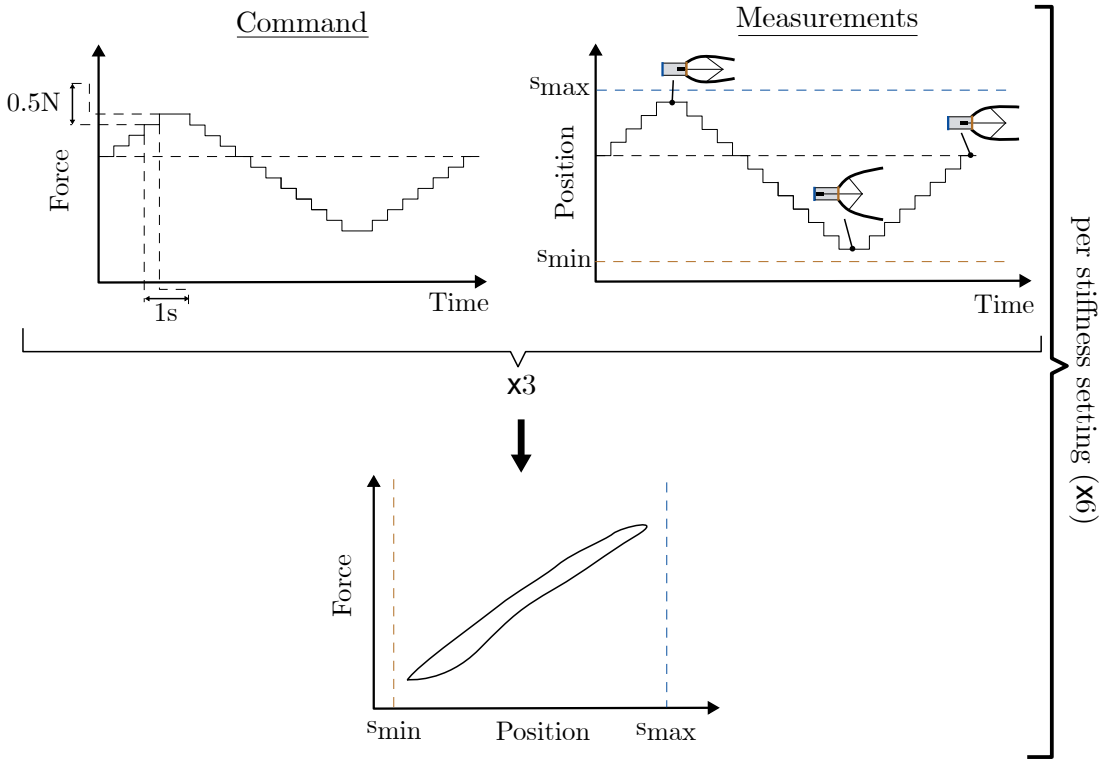

Figure 4.11: Experimental protocol 1: quasi-static tests. For each stiffness, the pump is commanded in force and the position of the plunger is measured. These measurements are repeated three times to obtain an averaged hysteresis loop characterizing the stiffness of the setup.

process is repeated six times for six different stiffness starting from the lowest stiffness provided by the VSM, i.e when the slider is in abutment against the VSM body on the motor's side. Specifically, from the lowest stiffness, the VSM motor is controlled to remove 0.0, 2.0, 3.0, 4.0, 4.5 and 5.0 active coils corresponding to the six stiffness settings. This process is summarized visually in Fig. 4.11.

Protocol 2 - Dynamic tests. The objective of this experimental protocol is to identify the system's resonant frequency and to evaluate the influence of the actuator force amplitude on its dynamic behaviour.

In this protocol, several quantities are recorded simultaneously: the current drawn by the actuator, the outlet flow rate and pressure, as well as the actuator force, and the plunger's position and velocity. Each experimental run lasts six seconds, and the pump is tested under six different stiffness configurations. For each stiffness, five frequency sweeps corresponding to five actuation force amplitudes are performed. The excitation frequency ranges from 1 Hz to 19 Hz in increments of 1 Hz. Thus, in

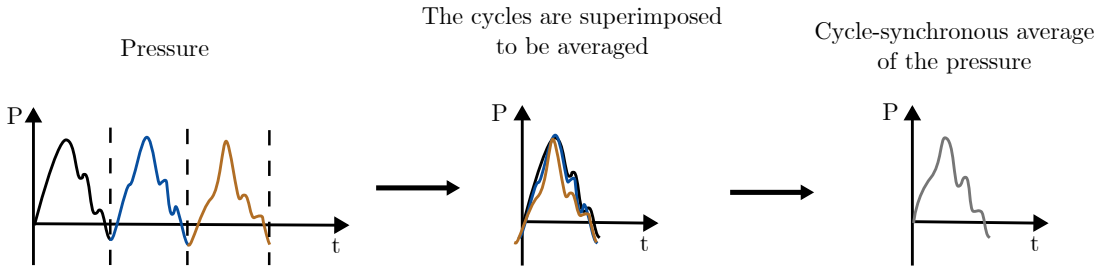

Figure 4.12: Illustration of cycle-synchronous averaging. The measured signal (here pressure) is first segmented into individual cycles based on the actuation period. The cycles are then aligned and superimposed before being averaged, producing a representative waveform that captures the periodic dynamics of the signal while reducing random measurement noise.

total, $5 \times 19 \times 6 = 570$ experimental conditions are investigated. The actuation signal consists of a zero-mean square wave with a 50% duty cycle - the only waveform available with the Pluto driver. A visual summary of this process is provided in Fig. 4.13a.

The five actuation forces used for each stiffness differ, as the force required to open and close the pump increases with stiffness. For each configuration, the maximum usable force before reaching the actuator's mechanical limits is determined empirically. The four remaining force amplitudes are then defined as proportional fractions of this maximum value, as illustrated in Fig. 4.13b.

For clarity, a reference force $F_r = 3100$ mN - corresponding to the lowest actuation force used at the lowest stiffness setting - is defined. All other forces throughout this thesis are expressed as multiples of this reference value.

To reduce measurement noise while preserving the periodic dynamics of the signals, cycle-synchronous averaging was applied to the measured quantities (pressure, flow rate, force, current, position and velocity). The recorded time series were first segmented into individual cycles using the actuation period, after which the cycles were aligned and averaged to obtain a representative waveform of the system's periodic response. The principle of this procedure is illustrated in Fig. 4.12. As an example, for a 12 Hz signal recorded on a duration of six seconds, approximately $12 \times 6 = 72$ cycles are averaged into one. Subsequently, a Fast Fourier Transform (FFT) is performed to decompose each averaged signal into a sum of sinusoidal components to study the impact of the different frequency components. This further describes in Chapter 5.

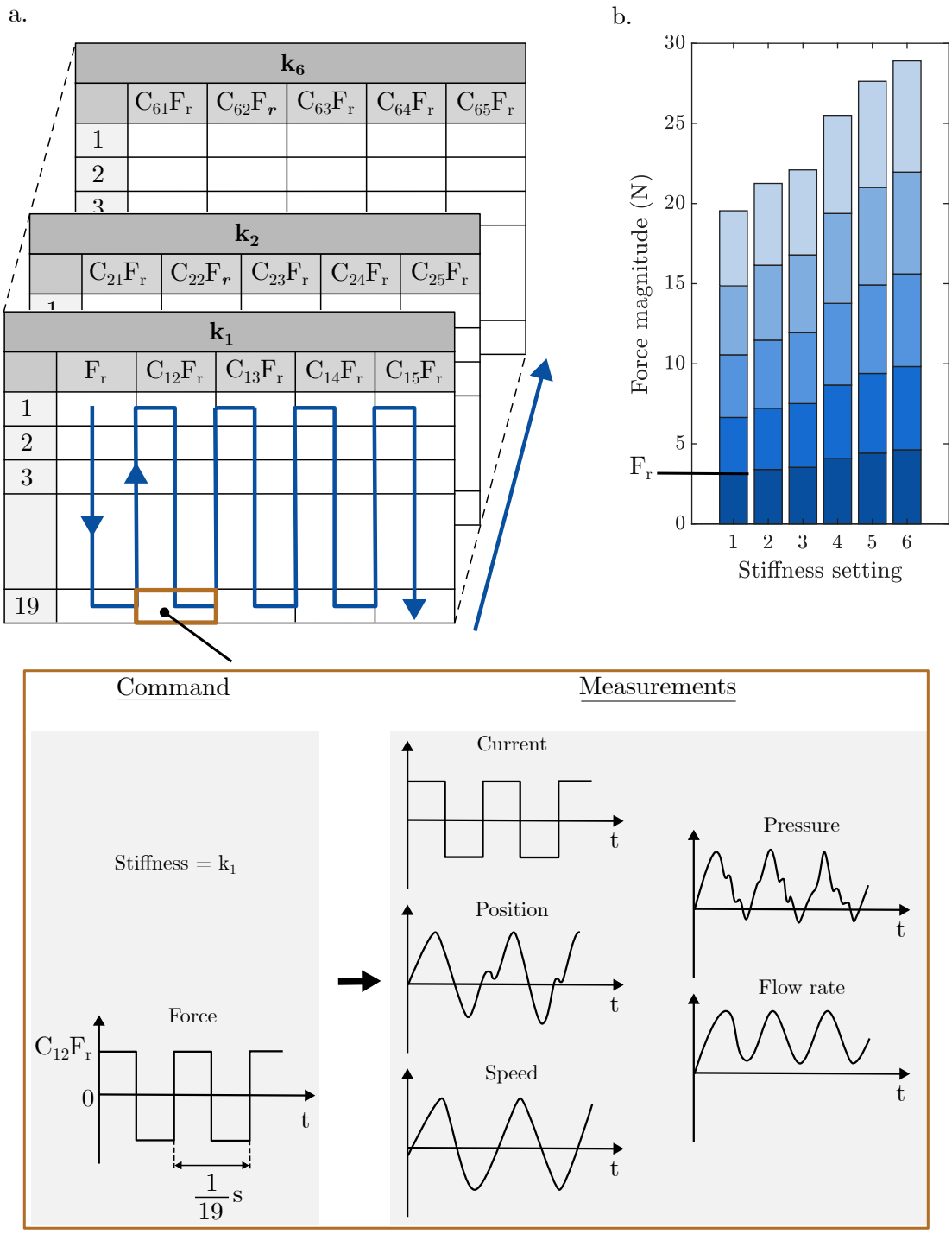

Figure 4.13: Experimental protocol 2: dynamic tests. **a.** Six stiffness, k_1, k_2, k_3, k_4, k_5, k_6 are tested. For each stiffness, the pump is controlled in force with a square wave with five different amplitudes and with nineteen different frequencies of oscillation. The current, the position and speed of the plunger as well as the flow rate and pressure are measured. **b.** Amplitude of the forces used for each stiffness setting. The reference force F_r is used in the rest of this thesis to simplify notations.

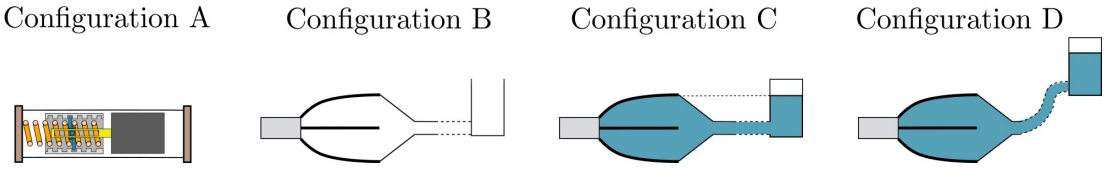

Figure 4.14: The four configurations tested. Configuration A: VSM on its own. Configuration B: pump with VSM with no fluid loading. Configuration C: pump with VSM with fluid loading. Configuration D: pump with VSM with fluid loading and tank elevated to increase hydrostatic pressure.

4.3.3 Configurations

The two protocols are used in different configurations as shown in Figure 4.14. Configuration A corresponds to the spring tested on its own, outside of the pump. Protocol 1 is used for this configuration, the goal being to determine the VSM stiffness. Configurations B to D correspond to different pump configurations embedding the VSM and aiming at evaluating the impact the hydrostatic pressure on the system's stiffness. For these configurations, protocol 1 and 2 are used. In configuration B, the pump and the tank are completely empty. In configuration C, both the tank and the pump are filled with water. The water level is adjusted to be aligned with the top of the pump. In configuration D, the tank is elevated (70 mm, chosen arbitrarily) in order to increase the hydrostatic pressure. In Configuration C and D, the water level in the tank is kept identical.

4.4 Conclusion

The pump development phase resulted in a fully functional prototype that successfully integrates the variable stiffness mechanism with the actuation and hydraulic systems. The use of high-precision 3D printing enabled rapid fabrication and iterative refinement, while the modular architecture ensured compatibility between the mechanical, electrical, and fluidic subsystems. The resulting design replicates the expected compression–expansion behaviour of a biological pumping chamber in a form factor simialr to the human heart and provides a controllable platform for dynamic testing.

The various configurations and test protocols introduced here form the basis for subsequent experimental analyses. Chapter 5 introduces the mathematical framework used to model the pump as a mass-spring-damper (MSD) system, while Chapter 6 and Chapter 7 apply this framework to characterize resonance and quantify its influence on power transfer and efficiency.

Chapter 5

Analytical Modeling of Resonant Dynamics

5.1 Introduction

The purpose of this chapter is to provide a theoretical framework to interpret the experimental behaviour of the developed resonant pump. The model introduced here builds on the mechanical architecture described in Chapter 4, where the pumping chamber, membrane, and actuation system together form a coupled mechanical–hydraulic structure. Although the complete system involves fluid–structure interactions, it can first be approximated by a classical mass–spring–damper (MSD) model, which captures the essential dynamic features required to understand resonance.

The analysis begins with the simplest case: a single-degree-of-freedom mass subjected to a sinusoidal external force. This configuration allows us to describe, in a transparent manner, how displacement, velocity, and phase evolve with frequency and how the mechanical and electrical power scale, particularly around the resonant frequency where these quantities reach their peak. The discussion is then extended to the case of a square-wave actuation. Because the square wave can be decomposed into a series of sinusoidal components through Fourier analysis, this extension reveals how the resonance principles apply to more realistic driving signals such as those used in the experiments of Chapter 6.

Finally, the chapter outlines the limitations of a purely mechanical model when applied to a fluidic system and highlights the key physical quantities - pressure, flow rate, and damping - that will later be investigated experimentally. Together, these analyses establish the analytical foundation for understanding the performance and efficiency of the resonant pump.

5.2 Dynamic Response of a Mass–Spring–Damper System Under Sinusoidal Excitation

To establish a clear theoretical understanding of resonance in the developed pump, this section analyses the canonical case of a mass-spring-damper system subjected to a sinusoidal force input. This simplified model captures the essential dynamics governing the pump's oscillatory behaviour, allowing the relationships between actuation frequency, amplitude, damping, and phase to be derived analytically. By determining the conditions under which displacement and power reach their maxima, the section identifies the characteristic signatures of resonance - amplitude magnification and phase shift - that will later serve as key indicators in the experimental analysis.

5.2.1 Steady-State Solution and Resonance Condition

A degree of freedom is defined as the number of independent generalized coordinates required to describe the configuration of a mechanical system. Although the pump mechanism consists of multiple moving components, including the plunger and the ribs, their motions are kinematically constrained as presented in Chapter 3, Fig .3.1 and Chapter 4, Fig .4.1 . In particular, the rotation of the ribs is directly imposed by the translation of the plunger through the mechanism geometry, such that all motions can be expressed as a function of a single independent variable. As a result, the system can be reduced to an equivalent single degree of freedom representation for the purpose of dynamic modeling. This assumption is analogous to classical mechanisms such as crank–slider systems, where multiple moving parts are present but only one independent coordinate is required to describe the system configuration (20). It should be noted, however, that higher-order effects such as structural flexibility or local deformations could introduce additional degrees of freedom, which are neglected in the present lumped modeling approach.

In addition, in the present modeling framework, it is assumed that the presence of fluid does not introduce additional degrees of freedom. The fluid dynamics are considered to be fully driven by the structural motion and therefore do not constitute an independent generalized coordinate. Under this assumption, fluid–structure interactions are incorporated into the model through equivalent contributions to the effective mass, damping, and stiffness. The system can thus be described as a single degree-of-freedom mass–spring–damper (MSD) oscillator. It should be noted that this assumption neglects distributed effects such as wave propagation, which may require

a higher-order or distributed modeling approach as discussed in Chapter 8.

Figure 5.1 illustrates the model used. The brown components identified in Fig. 4.1, and schematically represented in Fig. 5.1, constitute the effective mass of the system. The equivalent stiffness originates from the spring of the VSM and any additional component acting as a restoring force, while damping arises primarily from mechanical friction within the moving components and from the cyclic compression and expansion of the membranes. The overall dynamics of this simplified system are governed by Newton's second law as shown in Eq. 5.1, where x denotes the plunger position, m the equivalent mass, c is the damping coefficient and k is the system's equivalent stiffness.

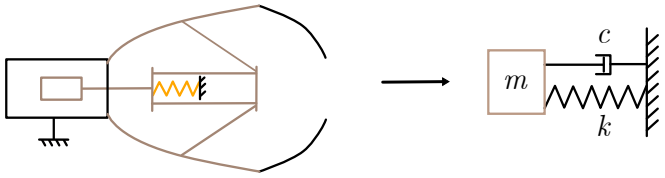

Figure 5.1: The pump is considered to behave as a mass-spring-damper system with an equivalent stiffness k, an equivalent mass m and a damping c.

$$m\ddot{x} + c\dot{x} + kx = F_a \tag{5.1}$$

Under a sinusoidal actuation force F_a, Eq. 5.2, the steady-state response of this differential equation is expressed as shown in Eq. 5.3. The variable ω represents the angular frequency of actuation, F the force amplitude, X the plunger's displacement magnitude, ϕ the phase and t the time. The time derivative of x, i.e the mass speed, is presented in Eq. 5.4 and is equal to the steady-state response shifted by 90° and scaled by ω.

$$F_a = F \sin \omega t \tag{5.2}$$

$$x = X \sin(\omega t - \phi) \tag{5.3}$$

$$\dot{x} = \omega X \cos(\omega t - \phi) = \omega X \sin(\frac{\pi}{2} - (\omega t - \phi)) \tag{5.4}$$

The expression of X is presented in Eq. 5.5 where M is called the amplitude ratio or the magnification factor and is defined in Eq. 5.6. The magnification factor is strongly dependent on the damping ratio ζ and on r, the ratio of the excitation

frequency to the natural frequency ω^* defined in Eq. 5.8. Both are presented in Eq. 5.9 and Eq. 5.7. As seen in Fig. 5.2a. which represents the amplitude ratio versus the frequency ratio for different damping ratio, ζ determines the apparition of a peak around resonance. It both determines the amplitude of the peak and the peaking frequency ratio. Particularly, M peaks exactly at $r^{**} = \sqrt{1-2\zeta^2}$, i.e for an angular frequency $\omega^{**} = \omega^* \sqrt{1-2\zeta^2}$. In other words, as ζ tends towards zero, the peak gets closer to the system's natural frequency and its amplitude increases. It should be noted that this peak only exists for damping ratios satisfying $\zeta < 1/\sqrt{2}$. For larger damping ratios, no resonance peak occurs.

In addition to be dependent on X, the steady response varies with the phase ϕ. As seen in Fig. 5.2b, for a frequency ratio of 1, i.e at resonance, the phase equals 90°.

In summary, this analysis highlights two key aspects of the pump's expected behaviour. First, the plunger motion is predicted to reach its maximum amplitude near resonance, at ω^{**}. Second, at resonance, the phase difference between the applied force and the displacement is expected to be 90°. Since displacement and the speed are inherently 90° out of phase (Eq. 5.3 and 5.4), the force and velocity signals are anticipated to be perfectly in phase.

$$X = \frac{F}{k} M \tag{5.5}$$

$$M = \frac{1}{\sqrt{(1-r^2)^2 + (2\zeta r)^2}} \tag{5.6}$$

$$r = \frac{\omega}{\omega^*} \tag{5.7}$$

$$\omega^* = \sqrt{\frac{k}{m}} \tag{5.8}$$

$$\zeta = \frac{c}{2\sqrt{km}} \tag{5.9}$$

5.2.2 Mechanical and Electrical Power Scaling

General form of the mechanical and electric power

In this section, the mechanical and electric power are derived based on the MSD equations defined above. The mechanical power of the actuator is presented in Eq. 5.10 and is expressed as the averaged product of the actuation force by the plunger' speed over a duration $T = n\frac{2\pi}{\omega}$ expressing an integer number n of periods.

$$P_m = \frac{1}{T} \int_0^T F_a \dot{x} dt \tag{5.10}$$

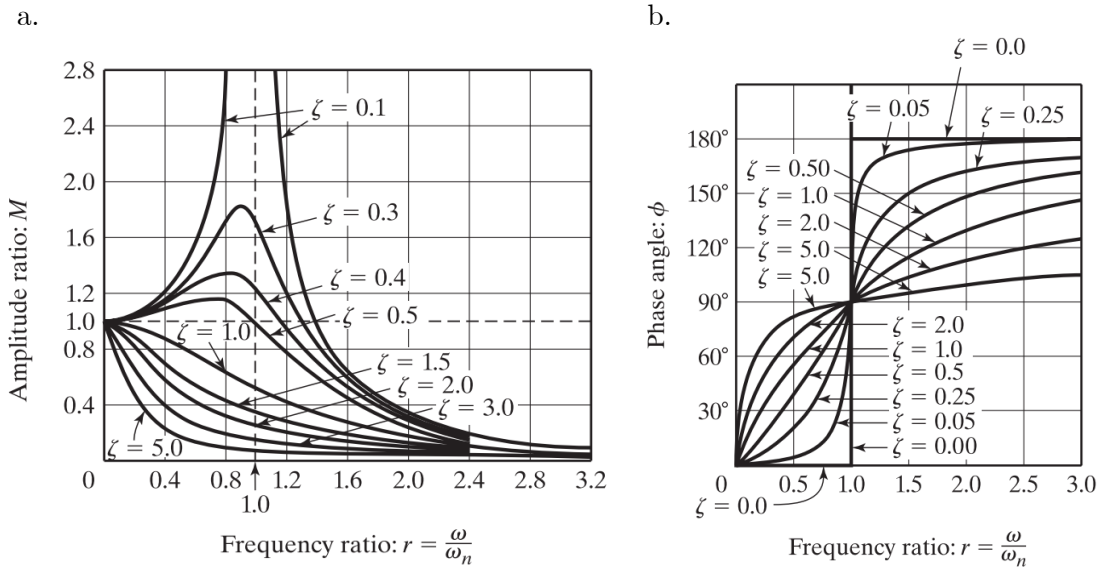

Figure 5.2: Amplitude ratio M (**a.**) and phase angle (**b.**) between force and position versus the frequency ratio r for a mass-spring-damper system (20).

For a MSD system, Eq. 5.10 can be rewritten using Eq. 5.1 resulting in Eq.5.11.

$$P_m = \frac{1}{T}\int_0^T m\ddot{x}\dot{x} + c\dot{x}^2 + kx\dot{x}dt \tag{5.11}$$

Eq. 5.11 is simplified by noting that $\int_0^T \ddot{x}\dot{x}dt = 0$ and $\int_0^T x\dot{x}dt = 0$ giving Eq. 5.12 which highlights that the mechanical power is simply the power needed to overcome the losses induced by the damping c. Once expanded and combined with Eq.5.5, Eq. 5.12 gives the analytic expression of the mechanical power presented in Eq. 5.13.

$$\begin{aligned} P_m &= \frac{1}{T}\int_0^T c\dot{x}^2 dt \\ &= \frac{1}{T}c\omega^2 X^2 \int_0^T \cos^2(\omega t - \phi)dt \\ &= \frac{1}{T}c\omega^2 X^2 \left[\frac{t}{2} + \frac{\sin(2\omega t - 2\phi)}{4\omega}\right]_0^T \end{aligned} \tag{5.12}$$

$$\boxed{P_m = \frac{1}{2}c(\omega\frac{M}{k})^2 F^2} \tag{5.13}$$

Similarly to the mechanical power, the electric power is expressed as the product of the current $i(t)$ by the voltage $u(t)$, Eq. 5.14.

$$P_e = \frac{1}{T}\int_0^T u(t)i(t)dt \tag{5.14}$$

Specifically, for voice coil actuators, the voltage can be modeled as presented in Eq. 5.15 where R is the coils resistance, K_B is the back electromotive constant, K_F is the force constant and L is the coils inductance (191)(192). In addition, the current is proportional to F_a (189), Eq. 5.16. Consequently, combining Eq. 5.14, Eq. 5.15 and Eq. 5.16, Eq. 5.17 is obtained by noting that $\int_0^T F_a \frac{di}{dt}dt = 0$. Noting that K_B and K_F are equal as shown in the actuator datasheet in Appendix 13 (a classical property of voice coil actuators), the resolution of Eq. 5.17 leads to the analytic expression of the electric power shown in Eq. 5.18. The electric power is equal to the sum of the mechanical power plus a term dependent on F, R and K_F. Specifically, both powers scale with F^2. Thus the electromechanical efficiency η_{EM} defined in Eq. 5.19 as the ratio of mechanical to electric efficiency, is independent of the actuation force.

$$u = Ri + K_B\dot{x} + L\frac{di}{dt} \tag{5.15}$$

$$i = F_a K_F \tag{5.16}$$

$$P_e = \frac{1}{T}\left(\frac{R}{K_F^2}\int_0^T F_a^2 dt + \frac{K_B}{K_F}\int_0^T F_a\dot{x}dt\right) \tag{5.17}$$

$$\boxed{P_e = \frac{1}{2}F^2\frac{R}{K_F^2} + P_m} \tag{5.18}$$

$$\boxed{\eta_{EM} = \frac{P_m}{P_e}} \tag{5.19}$$

Mechanical and Electric Power at Resonance

The general equations of the mechanical and electric power as well as the electromechanical efficiency have now been established. The following analysis focuses on determining the analytical values of these quantities at their respective peak conditions. While the displacement response X of a mass-spring-damper reaches its maximum at ω^{**} due to its dependence on the amplitude ratio M, both the mechanical and electrical powers peak at the natural frequency ω^*, as they depend on the product ωM. For brevity, the proof that ωM attains its maximum at ω^* is presented in appendix 16. This directly implies that, when the electric and mechanical powers

peak, the phase between force and speed is equal to $0\ ^\circ$ or equivalently, the phase between force and position is equal to 90°.

Using $\omega = \omega^*$ in Eq. 5.13 and Eq. 5.18, the expression of the mechanical and electric power at resonance, P_m^* and P_e^*, are obtained and presented in Eq. 5.20 and Eq. 5.21 respectively.

$$\boxed{P_m^* = \frac{1}{2}\frac{F^2}{c}} \tag{5.20}$$

$$\boxed{P_e^* = \frac{1}{2}F^2\frac{R}{K_F^2} + P_m^*} \tag{5.21}$$

Remarkably, both the electric and mechanical power at resonance are independent of the system's stiffness and scale with F^2. In addition, the mechanical power scales inversely with the damping coefficient c.

5.3 Extension to Non-Sinusoidal Actuation

This section extends the analytical framework developed for sinusoidal excitation to the case of non-sinusoidal actuation, specifically the 50% duty-cycle, zero-mean square force used in the experiments. Section 5.3.1 introduces the harmonic decomposition of this signal through Fourier series, demonstrating that the scaling laws established for sinusoidal forcing remain valid when the excitation contains multiple harmonics. Section 5.3.2 then applies this formulation to the pump, showing how the periodic nature of the actuation and the fluid–structure coupling allow pressure, flow rate, and power quantities to be expressed as Fourier series.

5.3.1 Square-Wave Excitation and Harmonic Decomposition

The Fourier series is a mathematical tool that allows any periodic function to be represented as a sum of sinusoidal components (193)(194). Consider a periodic signal $g(t)$, as expressed in Eq. 5.22, where t denotes time. The term G_0 is called the zero-frequency or DC component. Each term in the summation corresponds to a harmonic, with the first harmonic, also referred to as the fundamental, having an angular frequency ω_1.

For each harmonic, the amplitude G_j and phase χ_j together with the DC component, determine the overall shape of $g(t)$ and the extent to which it deviates from a

pure sinusoidal signal at the fundamental frequency. The indices j belong to the set of natural numbers, i.e $j \in \mathbb{N}$.

$$g(t) = G_0 + \sum_j G_j \sin(j\omega_1 t - \chi_j) \tag{5.22}$$

In particular, a zero-mean, 50% duty-cycle square wave such as the actuation force $F_a(t)$ used in this study, can be represented as a sum of sine functions containing only odd harmonics as shown in Eq. 5.23, where F denotes the amplitude of the square wave.

$$F_a(t) = \frac{4F}{\pi}(\sin(\omega_1 t) + \frac{1}{3}\sin(3\omega_1 t) + \frac{1}{5}\sin(5\omega_1 t) + ...)$$

$$\boxed{F_a(t) = \frac{4F}{\pi} \sum_{j=1,3,5...} \frac{1}{j} \sin j\omega_1 t} \tag{5.23}$$

In Eq. 5.23, the zero-frequency component is equal to zero because the function has a zero mean. The harmonic magnitudes are given by $\frac{4F}{j\pi}$ and all phase angles are zero. For a mass-spring-damper system subjected to such an excitation, the resulting displacement $x(t)$ is also periodic and can be expressed as shown in Eq. 5.24. The response takes the form of a Fourier series with phase shifts ϕ_j and where the magnitude of each harmonic scales with $\frac{4}{\pi j}X$. Here, X represents the system's response to a sinusoidal force of amplitude F, as defined previously in Eq. 5.5. Equation 5.24 therefore demonstrates that the MSD response continues to scale with the forcing amplitude F, similarly to the sinusoidal excitation case.

$$x(t) = \frac{4}{\pi}X \sum_{j=1,3,5...} \frac{1}{j} \sin(j\omega_1 t + \phi_j) \qquad \text{with} \qquad X = \frac{F}{k} \tag{5.24}$$

In general, for linear-time invariant (LTI) systems under a forcing F_a, the principle of superposition applies (193)(194). A more general formulation of Eq. 5.24 is shown in Eq. 5.25 confirming that the system response scales with F and that only odd harmonics appear, consistent with the square-wave input. The coefficient Y_j depends solely on the specific characteristics of the system, namely its transfer function, and not on the excitation conditions. The explicit expression of Y_j is not provided here, as it is not required for the analyses presented in the following chapters.

$$y(t) = \frac{4F}{\pi} \sum_{j=1,3,5...} \frac{Y_j}{j} \sin(j\omega_1 t + \phi_j) \tag{5.25}$$

5.3.2 Relevance to Pump Operation and Fluid-Structure Coupling

While it is possible to derive an analytical model describing the motion of the plunger, developing equivalent expressions for the pressure and flow rate is considerably more complex. Even establishing the degree of linearity in the system's behaviour presents a significant challenge limiting the possibilities to establish scaling laws to be compared with experimental data. Nevertheless, due to the inherently pulsatile nature of the pump, all output variables, including pressure and flow rate, are expected to exhibit periodic behaviour. Consequently, these quantities can be represented using Fourier series, as introduced in Eq. 5.22. Since all output variables of the pump can be described by Fourier series and the actuation force itself can be expressed in the same form, the general structure of the corresponding power quantities - electrical, mechanical, or hydraulic - can also be predicted. Specifically, the powers always take the form of the average of a product of two Fourier series: velocity times force for the mechanical power, current times voltage for the electric power and pressure p times flow rate Q for the hydraulic power as defined in Eq. 5.26.

$$P_h = \frac{1}{T}\int_0^T pQdt \tag{5.26}$$

For generalization, let us consider the signal g defined in Eq. 5.22 and a second periodic signal h defined in Eq. 5.27 where H_0 is the DC component, H_i is the magnitude and ψ_i is the phase of each harmonic. The functions $h(t)$ and $g(t)$ are depicted schematically in Fig. 5.3.

$$h = H_0 + \sum_i H_i \sin\left(j\omega_1 t - \psi_i\right) \tag{5.27}$$

The averaged product of $g(t)$ by $h(t)$ is defined in Eq. 5.28. Specifically, the product gh can be defined as a sum of four terms A, B, C, D as shown in Eq. 5.29. Each of these terms is detailed in Eq. 5.30, Eq. 5.31, Eq. 5.32 and Eq. 5.33 respectively, where the indices i belong to the set of natural numbers, i.e $i \in \mathbb{N}$.

$$\overline{gh} = \frac{1}{T}\int_0^T gh\,dt \tag{5.28}$$

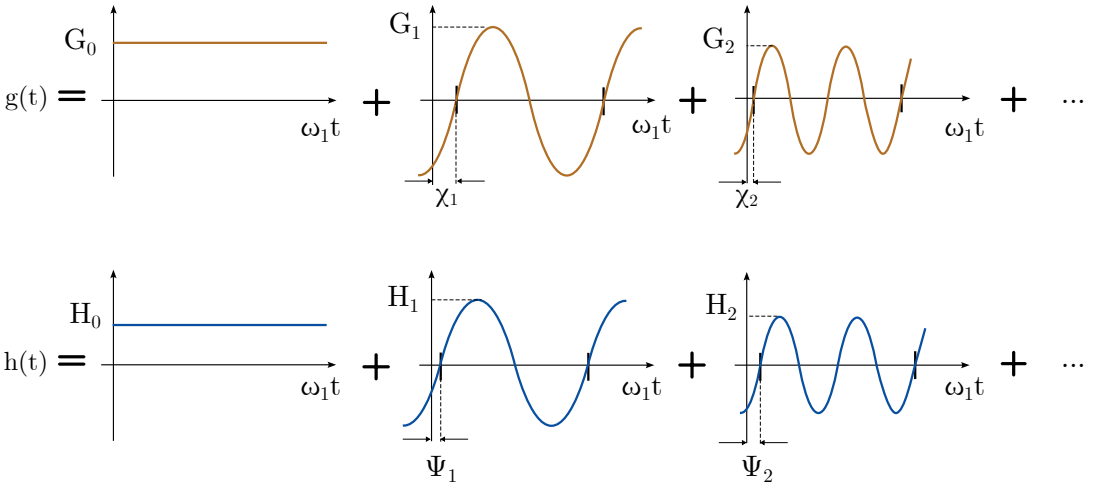

Figure 5.3: Fourier series representation of the functions g and h representing the periodic behavior of the inputs and outputs of the pump.

$$gh = A + B + C + D \tag{5.29}$$

$$A = G_0 H_0 \tag{5.30}$$

$$B = G_0 \sum_i H_i \sin(i\omega_1 t - \psi_i) \tag{5.31}$$

$$C = H_0 \sum_j G_j \sin(j\omega_1 t - \chi_j) \tag{5.32}$$

$$D = \sum_i \sum_j H_i G_j \sin(i\omega_1 t - \psi_i) \sin(j\omega_1 t - \chi_j) \tag{5.33}$$

The average of A remains equal to $G_0 H_0$ as A is a constant. The integrals of the terms B and C equal zero as they represent zero-mean periodic functions. To average the term D, the trigonometric product-to-sum identity is used to write it in an alternative form presented in Eq. 5.34.

$$D = \frac{1}{2} \sum_i \sum_j H_i G_j [\cos((i-j)\omega_1 t - \psi_i + \chi_j) - \cos((i+j)\omega_1 t - \psi_i - \chi_j)] \tag{5.34}$$

The term D can be further decomposed into a sum of two terms D_M and D_C. The former corresponds to the matched-frequency terms, i.e when $i = j$, while the later corresponds to the cross-frequency terms, i.e when $i \neq j$. To be concise, here only the derivation of D_M is shown in Eq. 5.35. However, for the reader's convenience, D_C

and it's step by step averaging is shown in Appendix 15 where it is demonstrated that D_C averages zero and has no effect on $\overline{gh}$.

$$D_M = \frac{1}{2}\sum_i H_i G_i[\cos(\chi_i - \psi_i) - \cos(2i\omega_1 t - \psi_i - \chi_i)] \tag{5.35}$$

The average of D_M is presented in Eq.5.36, resulting in the general expression of $\overline{gh}$ shown in Eq.5.37.

$$\frac{1}{T}\int_0^T D_M \, dt = \frac{1}{2}\sum_i H_i G_i \cos(\chi_i - \psi_i) \tag{5.36}$$

$$\boxed{\overline{gh} = G_0 H_0 + \frac{1}{2}\sum_i H_i G_i \cos(\chi_i - \psi_i)} \tag{5.37}$$

Eq. 5.37 demonstrates that $\overline{gh}$, i.e the powers, are only dependent on the sum of the matched-frequency harmonics. In other words, the powers can be decomposed in the sum of $G_0 H_0$ which will be referred as the *power DC component or the power zero-frequency component* and a sum of terms that will be referred to as the *power harmonics*. Each power harmonic is simply the product of the magnitudes of g and h at that harmonic times the cosine of their phase difference and divided by two. Specifically, the phase difference plays a central role in power generation. Indeed, for a given harmonic, when the equals $0°$, the power harmonic is maximized as $\cos(0) = 1$. On the contrary, when it equals $\pm 180°$, the power harmonic reaches its minimum. More specifically, when the absolute value of the phase difference is higher than $90°$, it creates a negative contribution to the hydraulic power.

This demonstration further confirms the result presented in Section 5.2.2 saying that mechanical and electric power are maximized when the phase between the plunger' speed and the actuation force is null. Here, this conclusion is extended to the hydraulic power.

5.4 Conclusion

This chapter provided the analytical foundation for understanding and interpreting the pump's behaviour under resonant operation. By modeling the system as a mass-spring-damper, the governing equations that relate actuation frequency, stiffness, damping, and displacement were derived. The analysis predicts that the plunger displacement amplitude scales linearly with the actuation force, as shown in Eq. 5.38,and

that both mechanical and electrical powers scale quadratically with the actuation force, as indicated in Eq. 5.39. Furthermore, at resonance, the mechanical power is inversely proportional to the damping coefficient c and independent of the stiffness k, as expressed in Eq. 5.40.

$$X \propto F \qquad (5.38) \qquad P_m.P_e \propto F^2 \qquad (5.39) \qquad P_m^* \propto \frac{F^2}{c} \qquad (5.40)$$

In addition, the chapter demonstrated that since the quantities used to compute power are periodic, the total power can be expressed as the sum of a zero-frequency (DC) component and its harmonics. Each harmonic contribution depends strongly on the phase difference between the corresponding components of the two signals considered. Consequently, maximum power transfer occurs when all relevant harmonics of these signals are perfectly in phase.

The theoretical framework developed here forms the basis for the experimental investigation presented in Chapters 6 and 7, where measured data are compared against these analytical predictions to identify the conditions under which resonance yields optimal energy transfer.

Chapter 6

Experimental Characterization of Resonant Behaviour

6.1 Introduction

This chapter experimentally investigates the dynamic behaviour of the developed pump when operated near its resonant frequency. The objective is to validate the theoretical predictions established in Chapter 5 and to quantify the performance gains achievable through resonance.

In this chapter, only the lowest stiffness setting of the pump is examined in order to isolate and analyse the resonant behaviour and its implications, without yet accounting for stiffness modulation. The influence of varying stiffness is addressed later in Chapter 7.

The mechanism's characterization is structured in a way to systematically investigate the influence of pump configurations on the system's response by distinguishing between quasi-static and dynamic effects. First, the quasi-static tests presented in Chapter 4 are analysed to determine how hydrostatic pressure affects the pump's stiffness. The dynamic analysis that follows examine the system's behavior under periodic excitation to identify the conditions under which the system approaches resonance. The resulting pressure, flow, and displacement signals are decomposed into their harmonic components to assess non-linear effects and to identify the scaling of power and efficiency with actuation amplitude and frequency.

Through this analysis, the chapter aims to identify how resonance enhances the conversion of electrical input power into hydraulic output by exploiting the energy exchange between elastic and kinetic components within the coupled electro-hydro-mechanical system. The overarching objective is to demonstrate that resonance can serve as an effective mechanism for generating pulsatile flow with improved energy efficiency.

6.2 Hydrostatic Pressure Affects Effective Stiffness and Natural Frequency

This section presents a preliminary analysis aiming at identifying key elements affecting the pump resting conditions and dynamic behaviour.

Figures 6.1a and b present the results from Protocol 1 (in quasi-static conditions) across all four experimental configurations. Figure 6.1a represents the actuation force versus the plunger's displacement. By fitting a linear model using least-squares regression to each loop, the stiffness of each configuration is determined and plotted in Fig. 6.1b. Additionally, the plunger's equilibrium position defined by the intersection of the model with the x-axis and the energy lost during a single compression-expansion cycle defined by the area enclosed by each loop, are plotted in Fig. 6.1b. As a reminder, the term expansion refers to the phase during which the pump chamber volume increases as a result of the outward rotation of the ribs, leading to fluid intake into the cavity. Conversely, compression refers to the phase during which the ribs rotate inward, reducing the chamber volume and expelling fluid as introduced in Section 3.2.2.

As shown by the blue dots in Fig. 6.1b, the plunger's equilibrium position changes with configuration, decreasing from configuration B to D. This indicates a progressive increase in the pump expansion caused by the increased hydrostatic pressure. Specifically, the higher water level in configuration D relative to configuration C accounts for the pressure increase. This result highlights how the pump equilibrium position needs to be carefully tuned during the design phase to maximize the range of motion available when loaded with fluid. Indeed, during the expansion phase, the outward rotation of the ribs induces a rearward shift of the plunger's equilibrium position, as the ribs and the plunger are rigidly connected (Fig. 3.1). Here the pump was carefully tuned so that, in configuration C, the plunger can translate on a symmetrical range of distances before hitting the mechanical limits at $0\,mm$ and $+6\,mm$. Configuration A is not shown on the graph since its experimental setup differed from the others, which biased the estimation of the equilibrium position.

Secondly, the energy losses (yellow dots in Fig. 6.1b) increase for each configuration. This is explained by the visco-elastic losses in the two membranes, friction losses at the pivot points, and viscous drag in the fluidics circuit. Specifically, we posit that the increase in water loading from configuration B to D results in higher friction in the different mechanical components of the pump.

Finally, the results reveal a progressive increase in stiffness (black dots in Fig. 6.1b) from configuration A to D. The rise from configuration A (spring alone) to configuration B (empty pump) originates from the additional stiffness contributed by the main membrane. From configurations B to D, the further increase is attributed to hydrostatic pressure effects. The compression and expansion of the pump modify the water level in the tank, producing pressure oscillations within the fluidic circuit that manifest as an added effective stiffness acting on the pump.

This spring-like behaviour becomes more pronounced because the amount of displaced fluid increases for a given plunger displacement Δx. Because the pump is more expanded in configuration D than in configuration C - due to the preload induced by the higher hydrostatic pressure - the volume expelled V_e in configuration D for a given Δx is greater than in configuration C. This occurs because the pump volume scales superlinearly with plunger motion. Here, the term superlinear denotes a relationship in which the volume expelled increases more rapidly than proportionally with the plunger motion, corresponding to a scaling stronger than linear (e.g. $V_e \propto \Delta x^n$ with $n > 1$). As the hydrostatic pressure P_h is proportional to the volume expelled, i.e $P_h \propto V_e$, the relationship between hydrostatic pressure and plunger displacement, is nonlinear (of the type $P_h \propto \Delta x^n$ with $n > 1$), and any preload that shifts the equilibrium position inherently alters the stiffness induced by the hydrostatic pressure and consequently the effective stiffness (as discussed in Chapter 2, Section 2.6.1). This mechanism is illustrated in Fig. 6.2, and accounts for the stiffness increase observed from configuration B to D.

It is noteworthy that, if a cylindrical piston were used instead of the pump, the displaced volume for a given Δx would remain independent of the equilibrium position, as volume would scale linearly with piston displacement, i.e $V_e \propto \Delta x$. In such a case, the stiffness induced by the hydrostatic pressure would be linear, i.e $P_h \propto \Delta x$, and the fluid stiffness would remain constant no matter the plunger's equilibrium position.

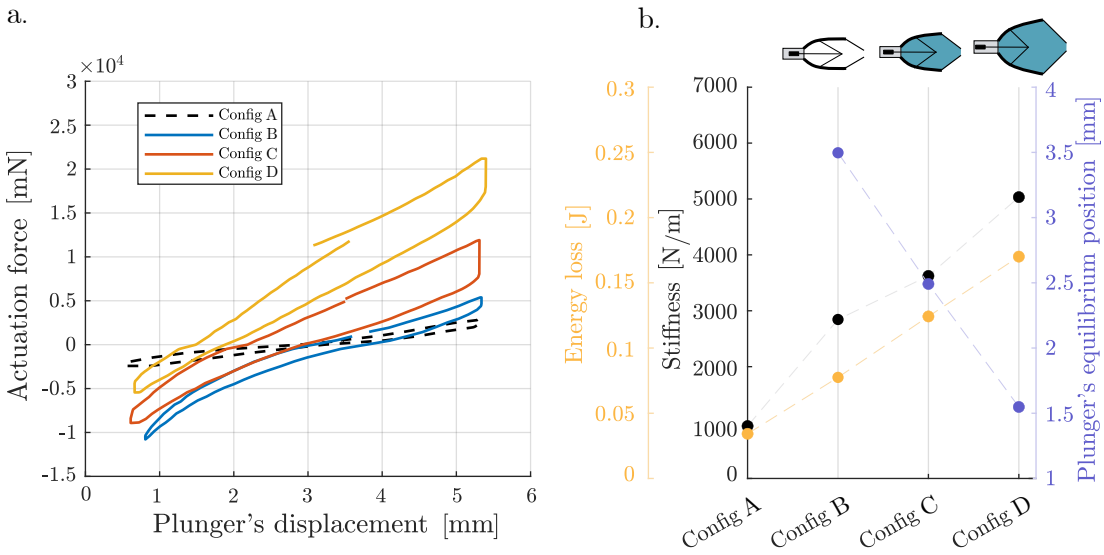

Figure 6.1: a. Impact of the actuation force on the plunger's displacement in static conditions and for the four different configurations. **b.** Evolution of the stiffness (black), the energy losses (yellow) and the plunger's equilibrium point (blue) for the four different configurations tested.

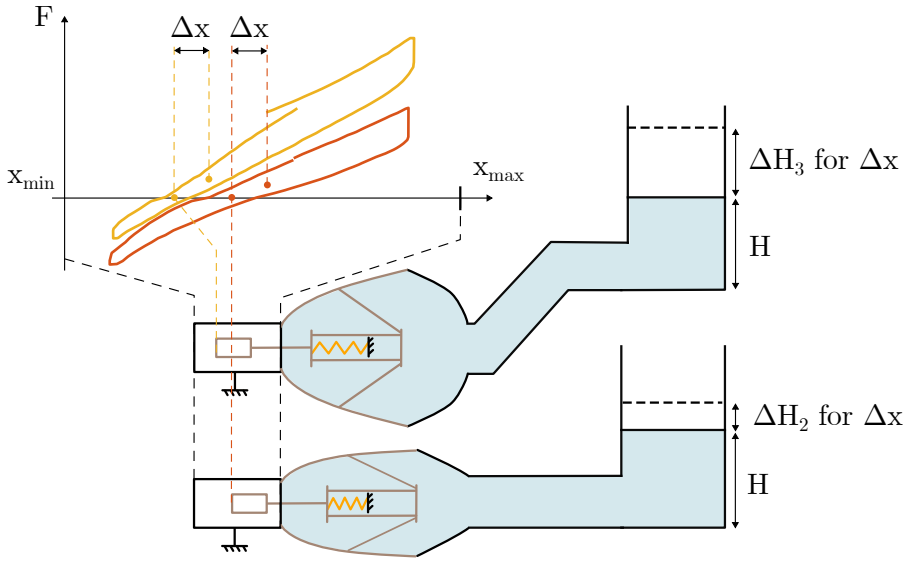

Figure 6.2: The amount of fluid displaced for a given plunger translation Δx is higher in configuration D (ΔH_3) than in configuration C (ΔH_2) because of the difference in expansion at equilibrium. Consequently, the force that the actuator needs to provide to translate the plunger on a distance Δx is higher in configuration D than configuration C resulting in a higher equivalent stiffness.

Figure 6.3a shows results obtained with Protocol 2 (dynamic conditions). Specifically, it presents the peak-to-peak plunger displacement amplitude across a range of actuation frequencies for configurations B through D, using a constant force amplitude

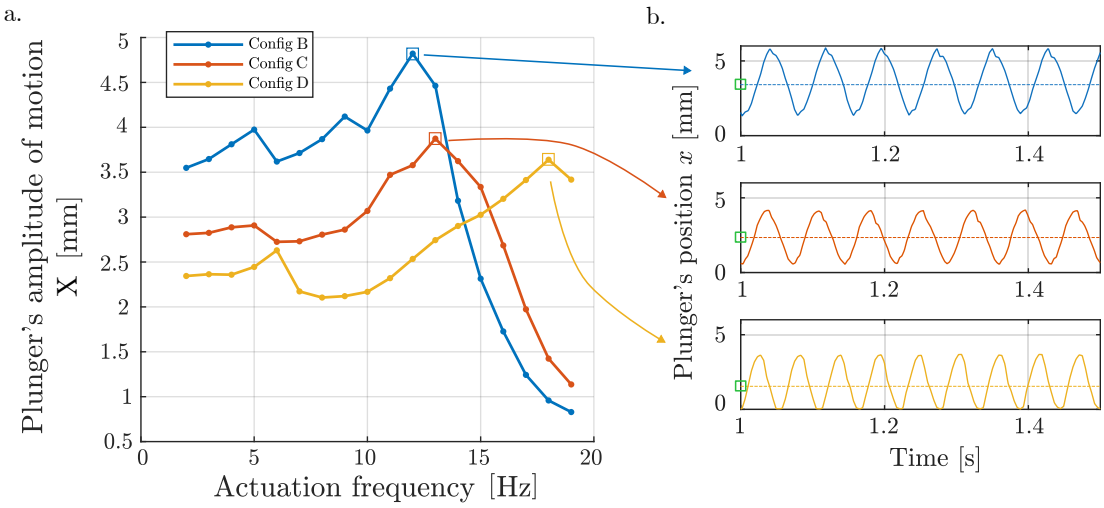

Figure 6.3: a. Impact of the different configurations on the plunger's amplitude of motion for a force amplitude of $1.5F_r$. We observe resonant peaks shifting from 12 Hz to 13 Hz and finally 18 Hz highlighting the significance of the configurations on the pump's dynamic. **b.** Plunger's position at 13 Hz, 14 HZ and 18 Hz, on a 0.5 seconds time window for configuration B, C and D (blue, orange, yellow curves respectively). The mean value of the oscillations reduce with the configuration due to the preload induced by the hydrostatic pressure.

of F_r. Each curve exhibits a clear resonance peak at 12 Hz, 13 Hz and 18 Hz respectively. Furthermore, Fig. 6.3b, shows the plunger's oscillations through time at these frequencies for the three configurations. As expected from the equilibrium position results obtained from the quasi-static tests, the mean value of the oscillations reduces with the configuration (as highlighted by the green squares).

In summary, the quasi-static and dynamic tests highlight that the water acts as a spring whose characteristics will change depending on the initial hydrostatic pressure. Additionally, they confirm the occurrence of resonance in the system and emphasize the influence of asymmetric loading on the resonant frequency. Specifically, each configuration alters the effective stiffness (via hydrostatic pressure), leading to a shift in the natural frequency. The characterization of the fluid's influence on the system stiffness provides the necessary foundation to analyze the pump's dynamic response as it approaches resonance.

For the remainder of this thesis, we focus on configuration B and C, as their resonant frequency lie near the center of the tested frequency range, providing a representative basis for analyzing pump performance around resonance. In addition, the reference frequency $f_r = 12Hz$ corresponding to the peaking frequency in configuration B is defined. This reference will be used to normalize actuation frequencies

and facilitate the comparison of resonant peak shifts across configurations.

6.3 Harmonic Analysis

To evaluate the pump's dynamic performance, its linearity is first examined. Figure 6.4 presents the frequency response map of the plunger displacement magnitude X for configuration B (empty pump) and for the lowest stiffness setting, obtained from the FFT analysis (as explained in Section 4.3.2 and Section 5.3.1). Figures 6.4a, b, and c correspond to actuation force amplitudes of $1F_r$, $1.25F_r$, and $1.5F_r$, respectively. The x-axis represents the actuation frequency, while the y-axis indicates the frequency spectrum of the response f_s. Thus, each vertical line on the map shows the relative magnitudes of the response's frequency components at a given actuation frequency. Blue regions correspond to low magnitudes, whereas yellow regions indicate high magnitudes.

As expected from the input waveform described in Section 5.3.1 and Eq. 5.23, the fundamental frequency, third harmonic, and fifth harmonic are clearly visible at $f_s = f_0$, $f_s = 3f_0$, and $f_s = 5f_0$. In addition, a second harmonic component emerges at $f_s = 2f_0$, revealing a nonlinear behaviour of the pump. Indeed, even harmonics cannot arise in a purely linear system driven by an input containing only odd harmonics.

Figures 6.4d, e, and f show, for the three force amplitudes, the magnitudes of the fundamental, second, and third harmonics normalized by the maximum magnitude of the fundamental as a function of actuation frequency. Overall, the second harmonic amplitude does not exceed 8% of the fundamental's maximum value and falls below 4% around resonance, indicating that its contribution to the overall response is negligible. The third harmonic magnitude is also negligible.

Similarly, Figures 6.5a, b, and c display the plunger displacement magnitude X for configuration C (pump filled with water). Analogous conclusions to the unloaded configuration are drawn with the appearance of odd harmonics as well as a faint second harmonic. This observation is confirmed by Figs. 6.6a, b and c, showing the normalized magnitudes of the first three harmonics of X and where the second and third harmonics appear negligible.

Figures 6.5d, e, f and 6.5g, h, i, illustrate, respectively, the frequency response of flow rate Q and pressure p. While the first and third harmonics appear as expected, the second harmonic exhibits a non-negligible amplitude. In particular, Figs. 6.6d, e, f and 6.6g, h, i show that the second harmonic reaches up to 60% of the fundamental amplitude for the pressure and approximately 40% for the flow rate. This finding is

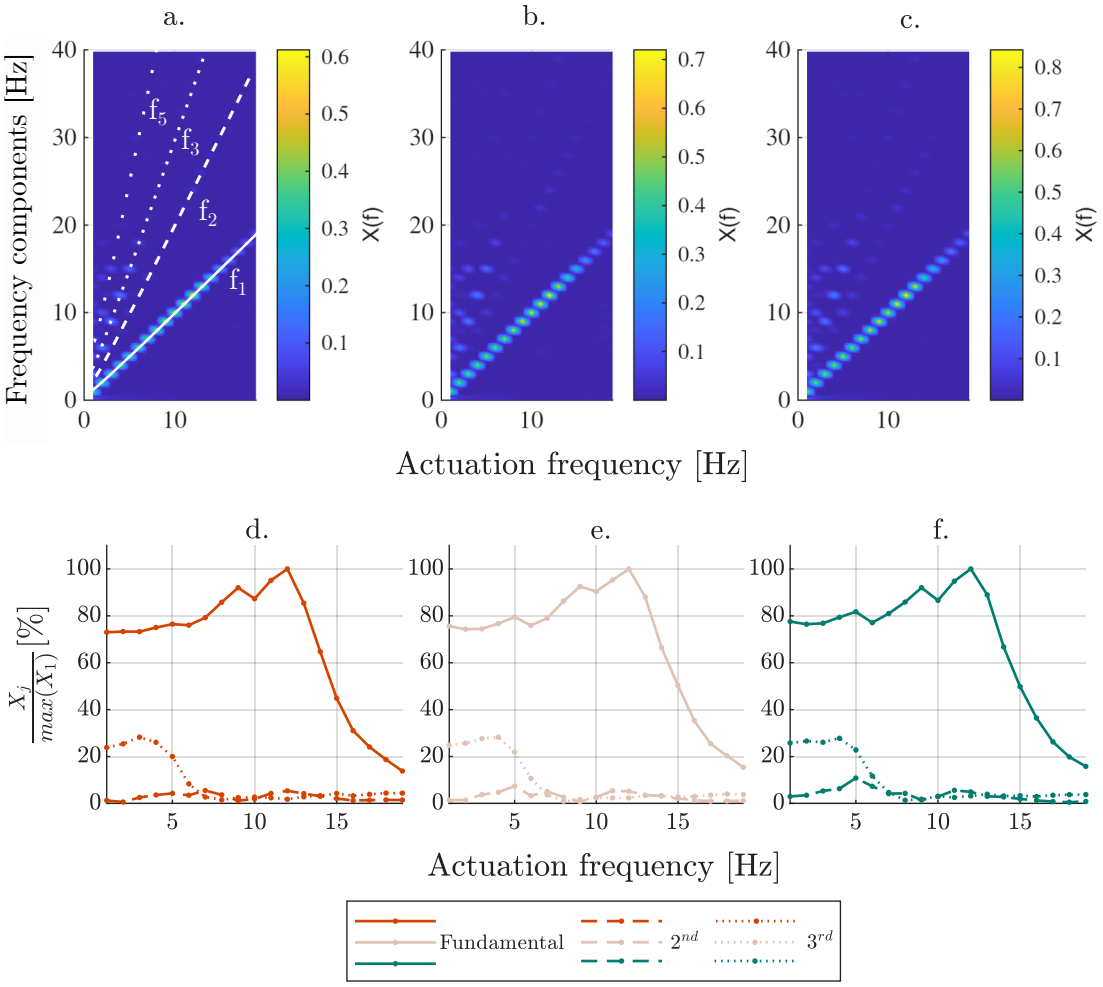

Figure 6.4: FFT analysis for configuration B. **a.b.c.** Fast Fourier Transform of the plunger's displacement for three force amplitudes, $1F_r$, $1.25F_r$, and $1.5F_r$. The odd harmonics present in the input signal appear (f_1, f_3, f_5) as well as the second harmonic (f_2) underlying the system's non-linearity. **d.e.f.** Magnitudes of the fundamental, second and third harmonics normalized by the maximum of the fundamental for the three force amplitudes. The second and third harmonics are negligible compared to the fundamental.

further supported by Fig. 6.7, which shows the time-domain evolution of pressure and flow rate for an actuation force of $1.5F_r$ at frequencies of 7 Hz and 12 Hz. The green rectangles highlight the emergence of the second harmonic.

The near absence of a second harmonic in the plunger's spectral response, contrasted with its clear presence in the flow rate and pressure spectra, strongly suggests that the nonlinearities arise downstream of the outlet one-way valve. Two potential mechanisms may explain this phenomenon. First, wave reflections in the tank may interfere with forward-propagating waves, generating constructive or destructive in-

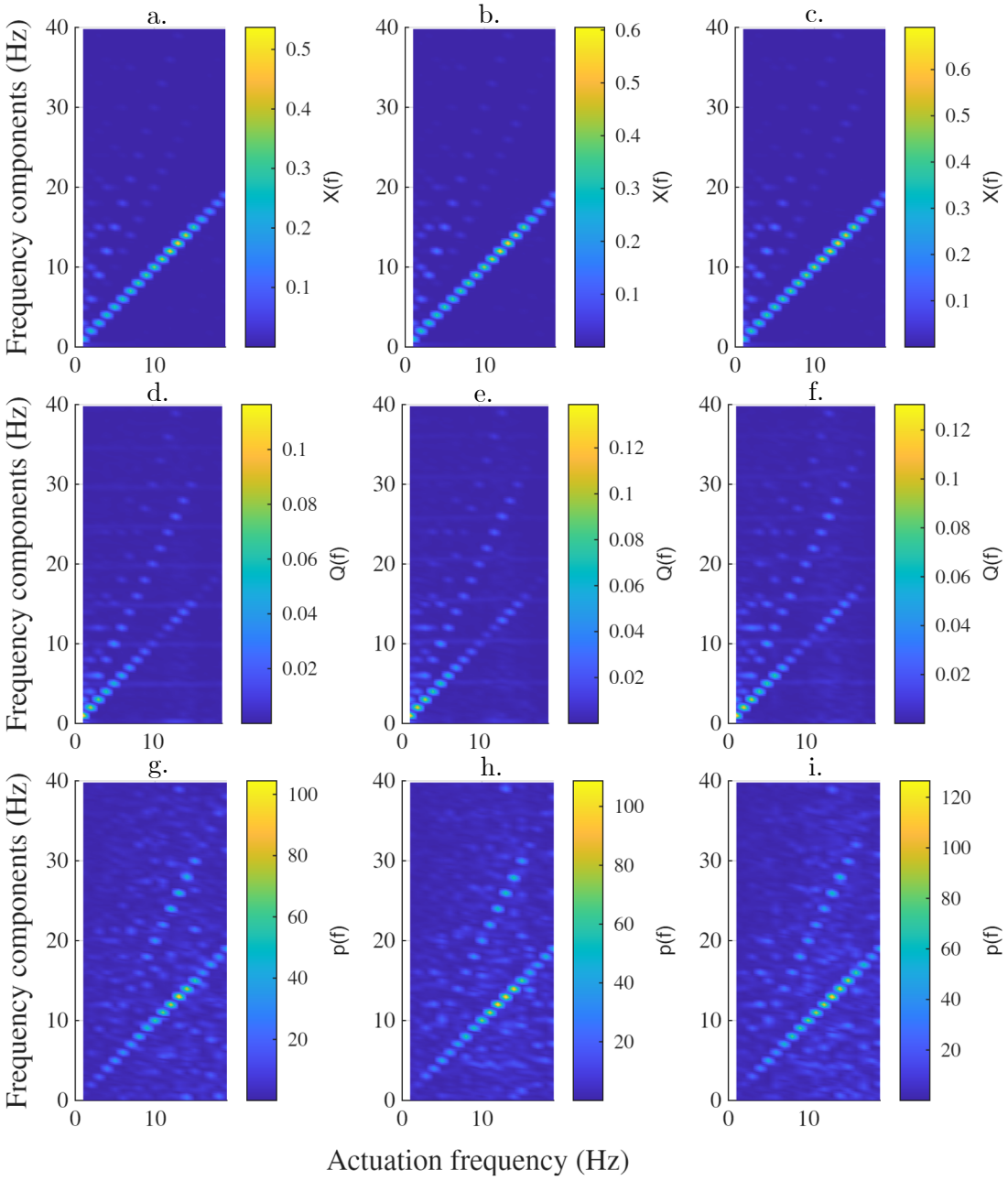

Figure 6.5: Fast Fourier Transform for configuration C and for the three force amplitudes $1F_r$, $1.25F_r$, and $1.5F_r$. 1st row: plunger's position magnitude. 2nd row: flow rate magnitude. 3rd row: pressure magnitude. Similarly to configuration B, second harmonics appear.

terferences that give rise to a second harmonic. The one-way valve likely prevents most of these reflected waves from propagating back into the pump, explaining their minimal impact on the plunger dynamics. Second, the dynamics of the one-way valve itself may alter the flow and pressure waveforms, producing harmonic distortion.

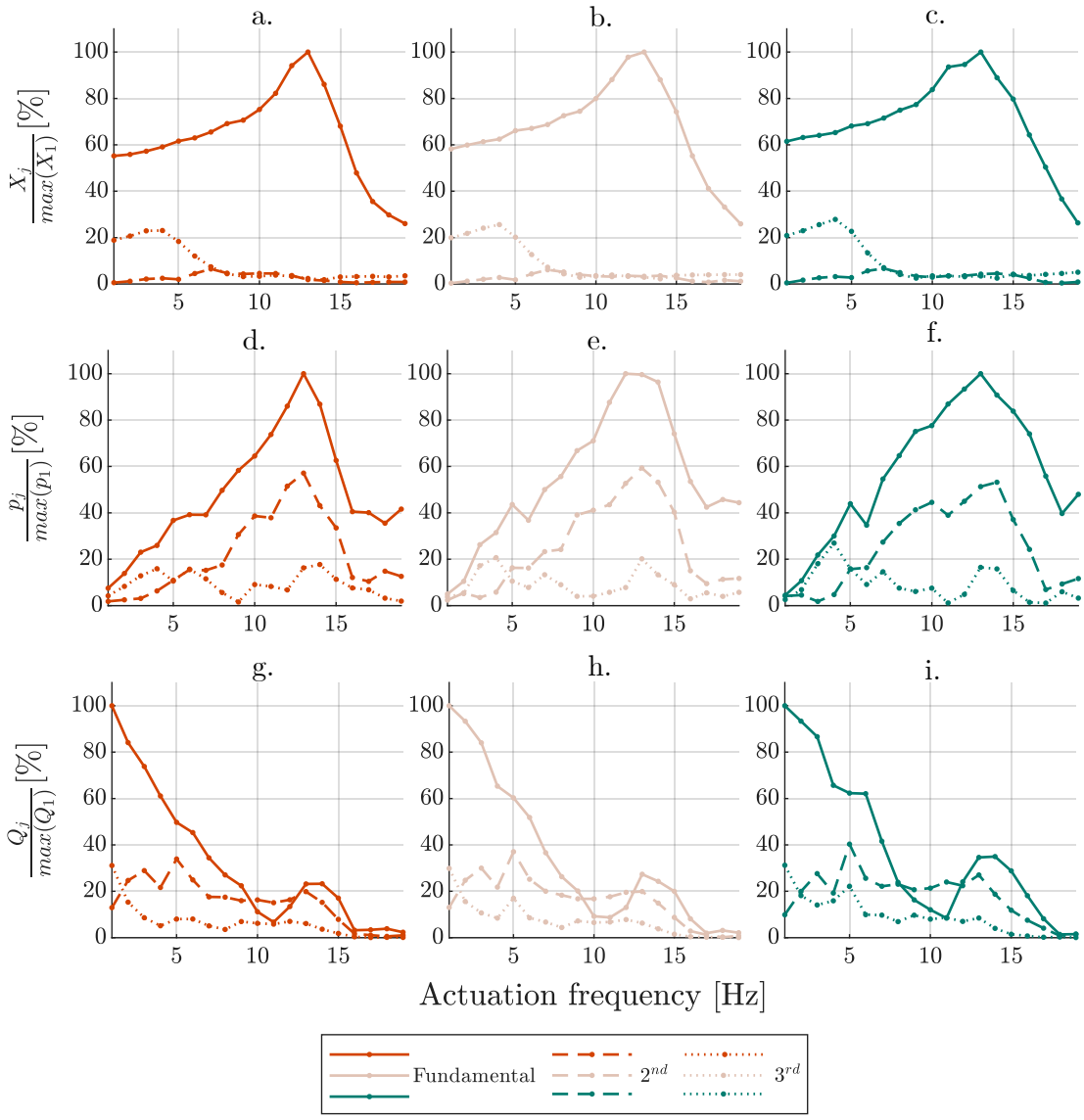

Figure 6.6: Magnitudes of the fundamental, 2nd, 3rd and 5th harmonics normalized by the maximum of the fundamental. First, second and third column correspond respectively to an amplitude of actuation force of $1F_r$, $1.25F_r$, and $1.5F_r$. First row (**a. b. c.**): plunger's position magnitude. Second row (**d. e. f.**): flow rate magnitude. Third row (**g. h. i.**): pressure magnitude.

Based on these observations, only the dominant harmonics will be considered in subsequent analyses. Specifically, the fundamental harmonic will be used to describe variables associated with the actuator plunger, while both the first and second harmonics will be analysed for variables related to the fluid motion.

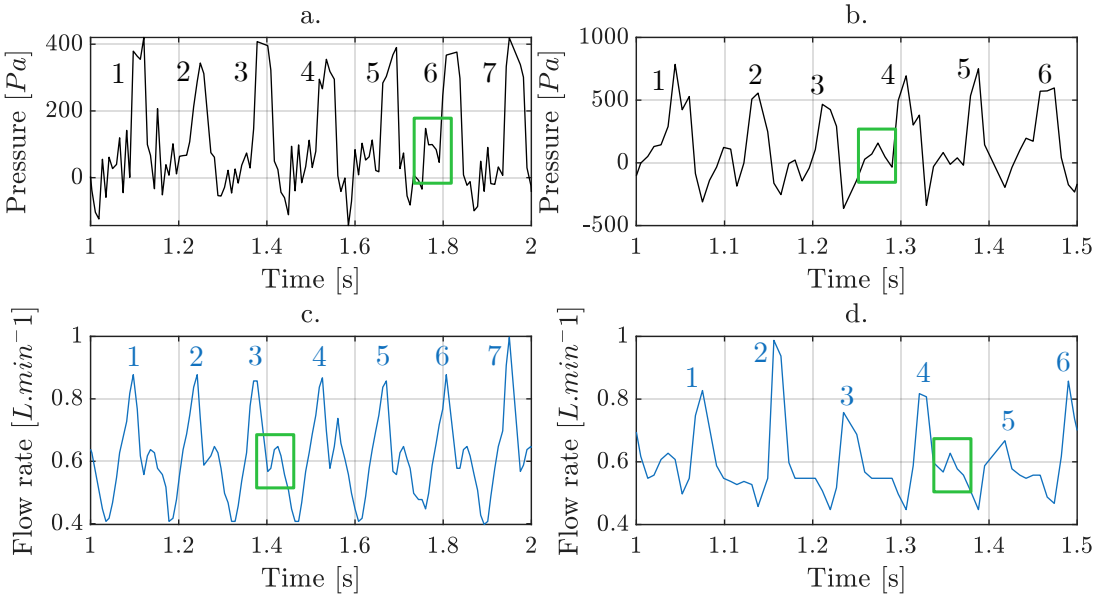

Figure 6.7: Pressure and flow rate for an actuation force of 1.5 F_r and two different actuation frequencies. The green rectangles highlight the apparition of the second harmonic. **a.** Pressure at 7 Hz on a one second interval. **b.** Pressure at 12 Hz on a 0.5 seconds interval. **c.** Flow rate at 7 Hz on a one second interval. **d.** Flow rate at 12 Hz on a 0.5 seconds interval.

6.4 Experimental Mass-Spring-Damper Behaviour Validation

This section analyses the plunger dynamics through its predominant harmonic, the fundamental component, and compares the experimental results with the theoretical scaling laws established in Chapter 5.

Figures 6.8a and b respectively show the amplitude of the plunger's fundamental displacement X_1, scaled by the actuation force amplitude F, and the phase ϕ_{Fx} between the time-varying actuation force F_a and the position fundamental. The x-axis represents the frequency ratio r_r, defined as the actuation frequency normalized by the reference frequency $f_r = 12$Hz.

In both plots, all curves collapse onto a single line, indicating that X_1 scales linearly with F and that ϕ_{Fx} is independent of F. This behaviour is consistent with Eqs. 5.3 and 5.5 in Chapter 5, confirming that the pump in configuration B behaves as a mass–spring–damper (MSD) system. Furthermore, the frequency at which the phase between F_a and x equals -90° coincides with the displacement peak, reinforcing the MSD interpretation and providing information on system damping.

As shown in Chapter 5, the frequency at which the phase equals $-90°$[1] corresponds to the natural frequency ω^*, while the peak displacement occurs at the frequency of maximum response $\omega^{**} = \omega^*\sqrt{1-2\zeta^2}$. Here, both frequencies are approximately 12 Hz ($r_r = 1$), implying a low damping ratio such that $\omega^{**} \approx \omega^*$. Using Fig. 5.2a and b, which depict the magnification factor M and phase versus normalized actuation frequency for a general MSD, the damping ratio ζ can be estimated to lie between 0.1 and 0.3.

Similarly, Figs. 6.8c and d show that, for configuration C, X_1 scales linearly with F and that ϕ_{Fx} remains independent of F. However, the frequency of maximum displacement increases to approximately $1.08 f_r$ (13 Hz) due to the additional stiffness introduced by the fluid, as previously discussed in Section 6.2. Although the individual contributions of fluid inertia and fluid-induced stiffness cannot be quantified directly from the present experimental data, the observed increase in resonant frequency allows their relative influence to be inferred. Since the natural frequency scales as $\omega_n = \sqrt{k_{eff}/m_{eff}}$, an increase in effective mass m_{eff} would result in a reduction of the resonant frequency. The experimentally observed shift toward higher frequencies therefore demonstrates that the increase in effective stiffness k_{eff} induced by the fluid dominates over the added fluid inertia. This highlights the significant role of fluid compliance and fluid–structure interaction in governing the system dynamics. Finally, unlike configuration B, the $-90°$ phase shift now occurs at a higher frequency, indicating that $\omega^{**} \neq \omega^*$ and that the presence of fluid introduces additional damping and energy losses.

The analysis now turns to the electrical and mechanical powers and the corresponding electromechanical efficiency. Figures 6.9a and b show the electrical and mechanical powers, respectively, normalized by F^2 for configuration B. As observed previously in Fig. 6.8a, all curves overlap, confirming the scaling law given by Eq. 5.13 and further validating the MSD model. Both power curves exhibit a resonant peak at $r_r = 1$. The electromechanical efficiency, plotted in Fig. 6.9c, is independent of F, as predicted by Eq. 5.19. At resonance, the efficiency reaches a maximum value of approximately 46%, indicating that, in the absence of fluid loading, the pump converts nearly half of the input electrical power into mechanical work. The remaining losses are attributed to mechanical friction, heat generation in the voice-coil actuator, and viscoelastic deformations of the spring and membranes.

[1] The difference in phase sign between the experiments and the phase plotted in Chapter 5, Fig. 5.2, arises because the minus sign is already included in Eq. 5.5.

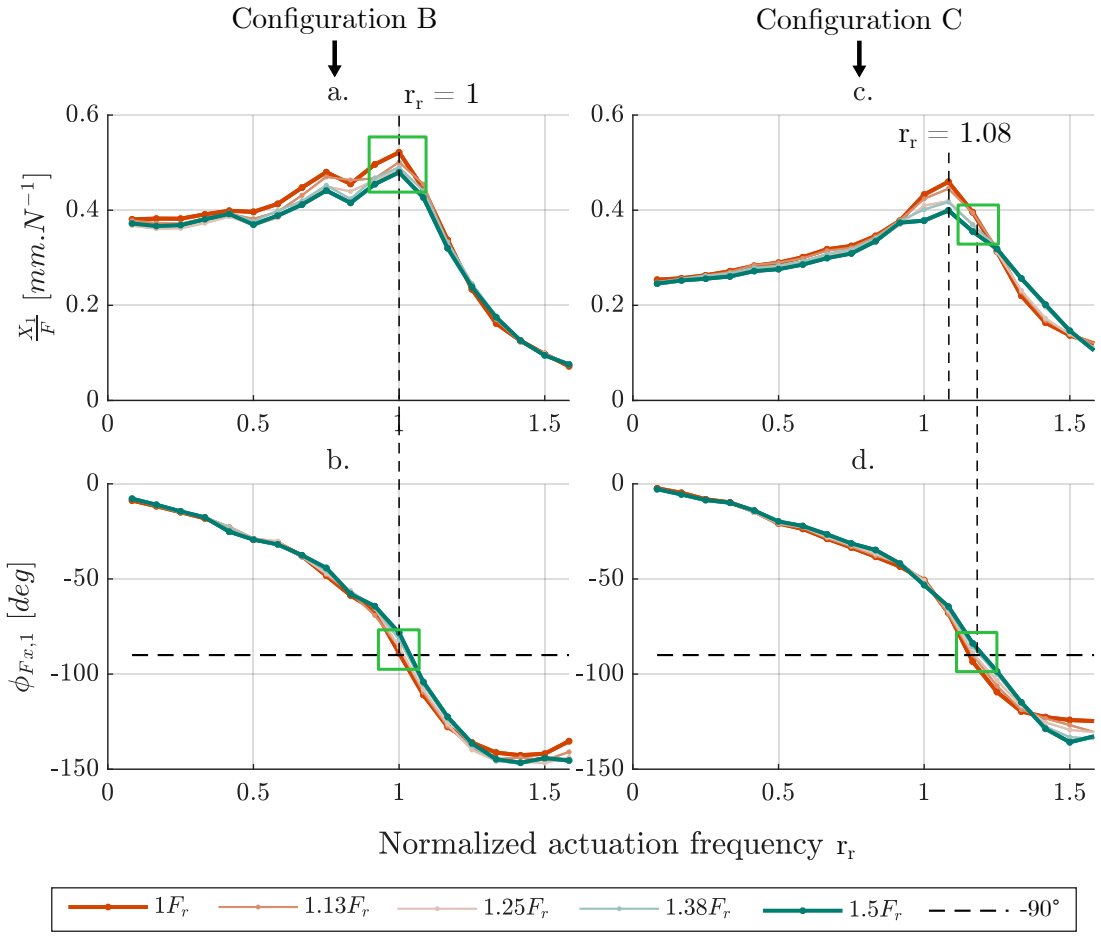

Figure 6.8: The damping in configuration C is higher than in configuration B inducing a misalignment of the $-90°$ point with the resonant peak. In addition, the water loading in configuration C induces a shift in natural frequency from $r_r = 1$ to $r_r = 1.08$. **a. b.** Plunger's amplitude of motion at the fundamental scaled by the actuation force amplitude for configuration B and C. **c. d .**Phase between the actuation force and the plunger's position at the fundamental for configuration B and C.

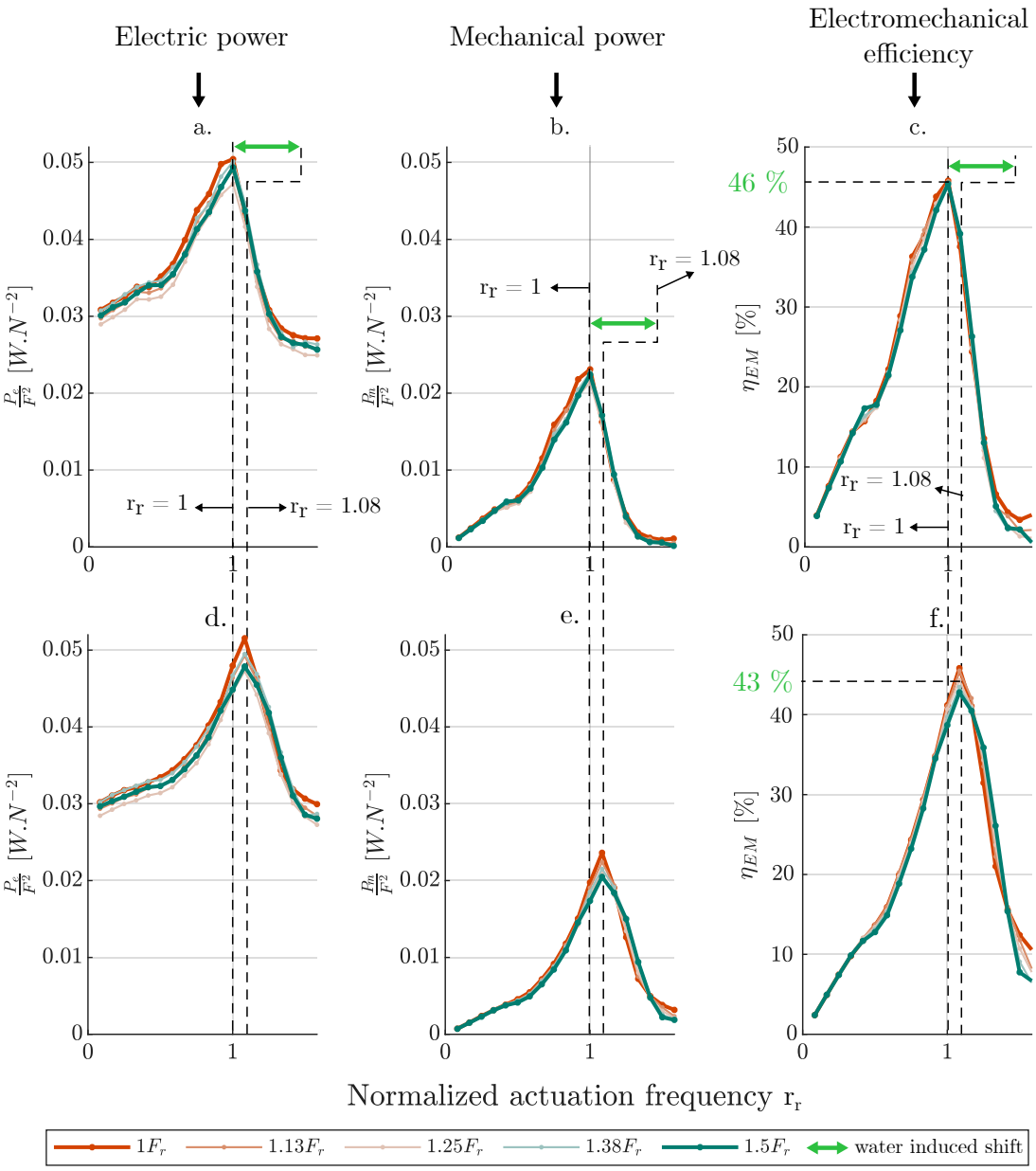

Figure 6.9: The water induced shift is also observed in the electric and mechanical power as well as the electromechanical efficiency. The increases in losses in Configuration C leads to a 3% drop in efficiency. **a. b. c.** Mechanical and electric power normalized by F^2 as well as electromechanical efficiency for configuration B (pump empty). **d. e. f.** Mechanical and electric power normalized by F^2 as well as electromechanical efficiency for configuration C (pump with fluid).

For configuration C, the corresponding results are shown in Figs. 6.9d, e and f. The resonant peaks remain clearly visible despite the additional fluid-induced damping, and the frequency shift due to increased stiffness persists. The added fluid losses lead to a reduction in maximum efficiency of approximately 3%.

These findings confirm that the plunger driven by the voice-coil actuator behaves as a mass–spring–damper system, both in air and when coupled with fluid. This result is critical, as it demonstrates that resonance can be exploited to enhance electromechanical energy conversion efficiency in the pump. Specifically, the plunger displacement at the fundamental scales linearly with the actuation force amplitude ($X_1 \propto F$), while both electrical and mechanical powers scale quadratically with F ($P_e, P_m \propto F^2$). Although damping increases under fluid loading, it remains sufficiently low for the pump to operate in an underdamped regime, maintaining distinct resonant peaks in both power and efficiency.

6.5 Hydraulic Power Dependencies

The experimental analysis of the plunger dynamics confirmed the theoretical predictions established in Chapter 5. The following section extends this investigation to the pressure and flow rate signals in order to identify their respective dynamic behaviours.

6.5.1 Resonance of the pressure and flow rate harmonics

Figure 6.10 presents the magnitudes of the frequency components of pressure and flow rate as functions of the normalized actuation frequency r_r, each scaled by the actuation force amplitude F. In each plot, the five curves correspond to the different actuation force magnitudes tested. Specifically, Figs. 6.10a and d show the zero-frequency components p_0 and Q_0, Figs. 6.10b and e display the fundamental components p_1 and Q_1, and Figs. 6.10c and f show the second harmonics p_2 and Q_2.

The curves corresponding to Q_0, Q_1, Q_2, p_1, and p_2 nearly overlap, suggesting a common scaling with the actuation force amplitude F. Since the same linear relationship was established for X_1 in Section 6.4, this implies that the pressure and flow rate harmonics likely scale proportionally with X_1.

In contrast, the zero-frequency component of the pressure, p_0, follows a distinct scaling law. A clear pattern emerges in which the lowest (dark orange) and highest (dark green) actuation force magnitudes yield the highest and lowest normalized values of p_0/F, respectively. This behaviour is attributed to the contribution of the

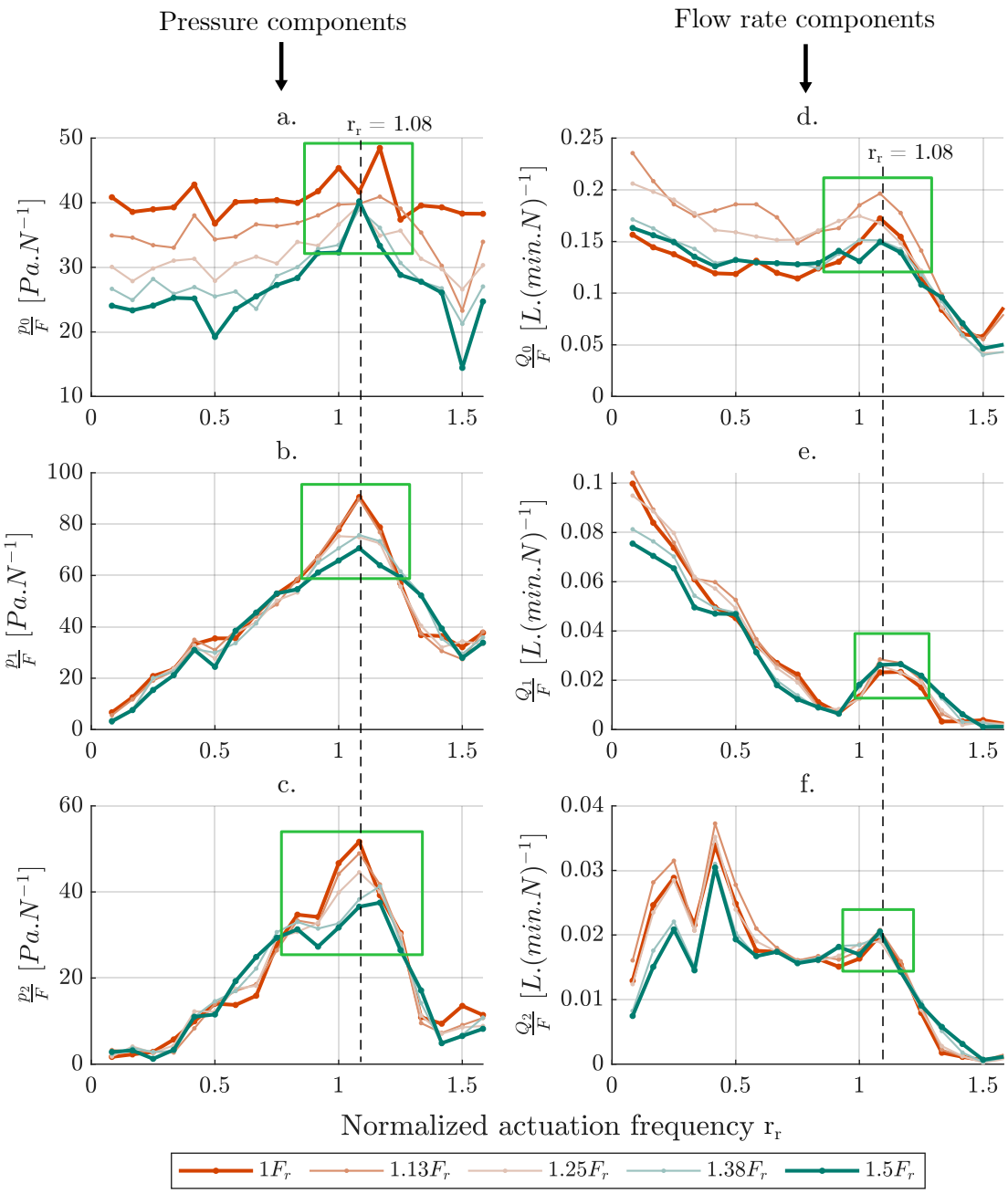

Figure 6.10: Frequency components magnitude of the pressure and flow rate scaled by F versus the normalized actuation r_r for configuration C. **a.** Pressure zero-frequency component. **b.** Pressure fundamental.**c.** Pressure second harmonic.**d.** Flow rate zero-frequency component. **e.** Flow rate fundamental. **f.** Flow rate second harmonic.

static hydrostatic pressure p_s. Indeed, p_0 can be expressed as the sum of a constant hydrostatic term p_s and a dynamic component p_v that depends on the actuation force and frequency, as shown in Eq. 6.1. Because p_s is constant, the curves do not overlap: as F increases, the ratio p_s/F decreases, explaining the observed pattern in p_0/F.

$$p_0 = p_s + p_v(F) \tag{6.1}$$

Across all six subplots, a clear resonant peak appears near the natural frequency at $r_r = 1.08$ (green rectangles), consistent with the behaviour observed previously in Fig. 6.8b. This confirms that the resonance observed on the actuator side is successfully transmitted to the fluidic domain, producing a corresponding resonant response in pressure and flow rate. This result is significant, as it experimentally demonstrates, for the first time to the author's knowledge, the feasibility of resonant pulsatile pumping at the macroscale.

6.5.2 Phase Lag Between Pressure and Flow Rate Dictates Power Benefits

The resonant behaviour of the pressure and flow rate being established, this section now examines how the phase lag between pressure and flow rate influences the hydraulic power.

Figure 6.11 presents for two frequencies - 5 Hz ($r_r = 0.42$) and 13 Hz ($r_r = 1.08$) - the time variations of the pressure and flow rate at an actuation force of $1.5F_r$. Specifically, it illustrates the time delay between the flow rate and pressure signals. Indeed, as shown in Figs. 6.11a and b, at 5 Hz the pressure and flow rate peaks are nearly in phase, whereas at 13 Hz they are almost completely out of phase. This is the experimental evidence of how the actuation frequency alters the pump dynamics and introduces a time offset between these two quantities.

This observation is further confirmed by Figs. 6.12a and b which present the phase between pressure and flow rate at the fundamental (ϕ_{pQ1}) and at the second harmonic (ϕ_{pQ2}) across all frequencies tested. In both cases, the curves coincide for frequencies below $r_r = 1$ but begin to diverge at higher frequencies. These apparent phase jumps are not physical but arise from the Fast Fourier Transform (FFT) process. Indeed, an FFT outputs complex coefficients of the form $a + ib$, where a small uncertainty in the imaginary component b can produce abrupt transitions in phase between $+180^\circ$ and -180°, as illustrated in Fig. 6.13. Hence, the variations observed near

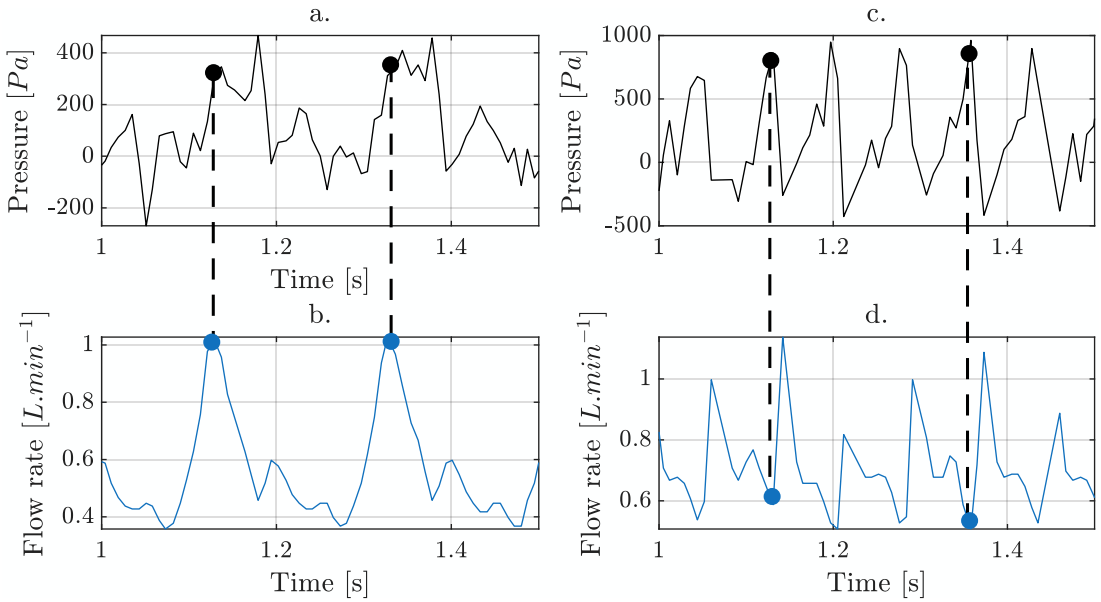

Figure 6.11: Pressure and flow rate at different actuation frequencies illustrating its impact of the phase lag between the two quantities. The force amplitude used is 1.5 F_r. **a.** Pressure at 5 Hz. **b.** Flow rate at 5 Hz.**c.** Pressure at 13 Hz.**d.** Flow rate at 13 Hz.

$\pm 180^\circ$ are numerical artefacts, and the phase is expected to be independent of the actuation force magnitude F.

As described in Chapter 5, phases with absolute values greater than 90° (red regions in Fig. 6.12) correspond to negative power transfer, whereas phases with absolute values below 90° (green regions) correspond to positive power transfer. This interpretation is supported by Figs. 6.14b, c, which display the fundamental, and the second harmonic of the hydraulic power, respectively. As expected, for frequency ratios where the phase exceeds $\pm 90^\circ$, the cosine of the phase becomes negative, leading the fundamental and second harmonic to contribute negatively to the total hydraulic power (red regions). Conversely, when $|\phi| < 90^\circ$, both harmonics contribute positively (green regions). More specifically, although resonance amplifies the magnitudes of the pressure and flow rate harmonics, the phase offset between these quantities around $r_r = 1.08$ causes the power to change sign, effectively reducing the net energy transfer.

Figs. 6.14a show the DC component of the hydraulic power which is independent of phase. Consequently, it systematically contributes positively to the total power across frequencies and reaches its maximum near the natural frequency. It also exhibits nonlinear characteristics inherited from the behaviour of the pressure's DC component p_0.

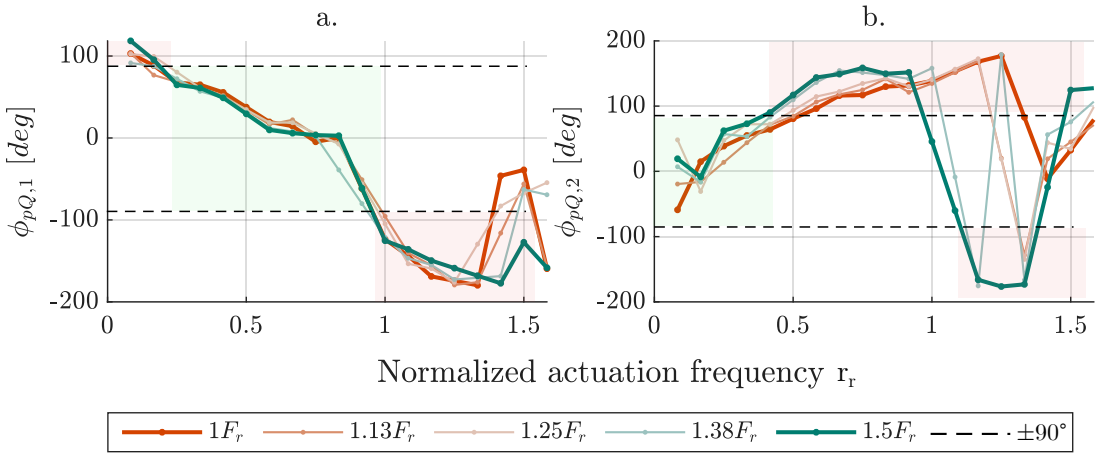

Figure 6.12: Phase between pressure and flow rate at the fundamental and second harmonic for configuration C. **a.** Fundamental. **b.** Second harmonic.

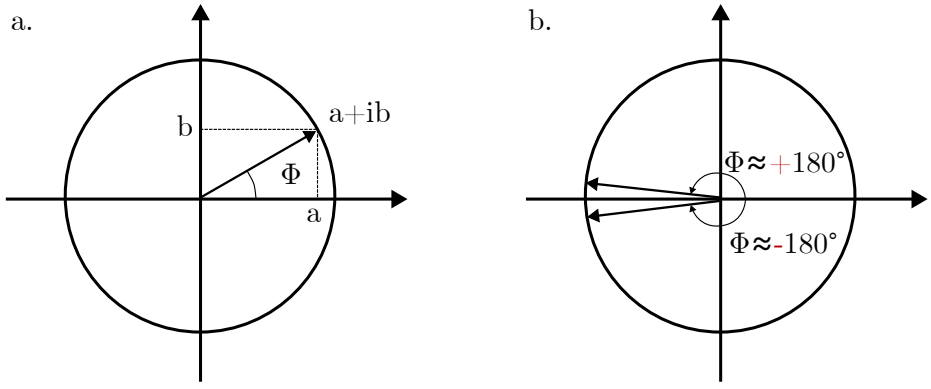

Figure 6.13: a. Complex number representation in the complex plane. **b.** A small uncertainty in the imaginary part b can cause a phase jump from $-180°$ to $+180°$.

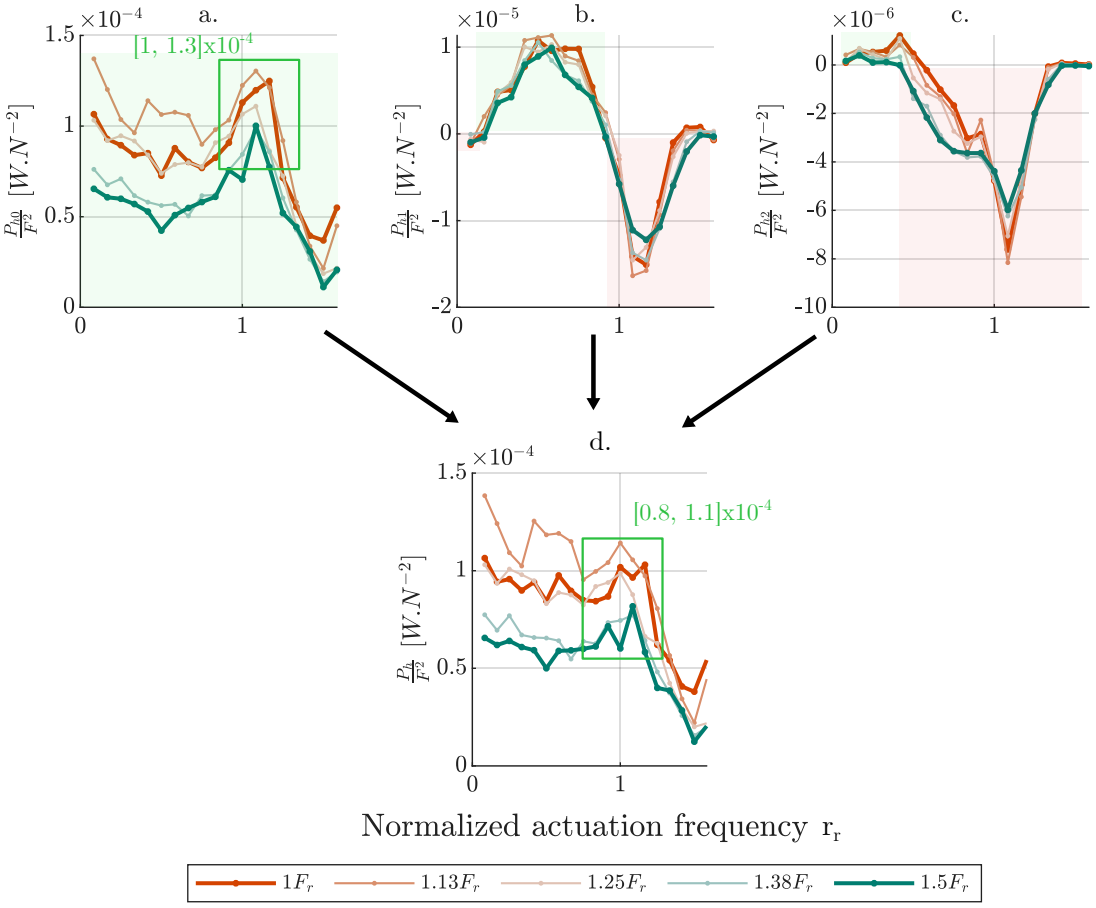

Figure 6.14: Hydraulic power zero-frequency components, fundamental and second harmonic scaled by F^2. **a.** Zero-frequency component. **b.** Fundamental. **c.** Second harmonic.

The total hydraulic power, approximated by the sum of its three main frequency components, is shown in Fig. 6.14d. The negative contributions from the fundamental and second harmonics reduce the overall power near resonance. In particular, comparison between the DC component and the total power at resonance reveals a decrease of approximately 20 (as shown by the green annotations in Fig 6.14a and d). As a result, the resonant peak appears flattened and considerably less pronounced than in the electrical and mechanical power responses.

This result highlights the critical influence of phase lags exceeding $\pm 90^\circ$ on resonant energy transfer, particularly in systems coupled with fluid dynamics. This issue is often overlooked, as analyses typically assume phase variations limited to the $[-90^\circ, +90^\circ]$ interval. Indeed, Womersley (195) demonstrated that, for pulsatile flows in rigid tubes, the phase lag between pressure and flow rate lies within this range, originating from inertial effects due to unsteady motion.

The Womersley number, defined in Eq. 6.2, quantifies the phase lag arising from viscous–inertial interactions and depends on the tube radius R_t, oscillation angular frequency ω, fluid density ρ, and dynamic viscosity μ.

$$\alpha = R_t \sqrt{\frac{\omega \rho}{\mu}} \tag{6.2}$$

For the experimental setup used in this study, where $R_t = 0.01$ m, $\rho = 1000$ kg·m^{-3}, and $\mu = 0.001$ Pa·s (at 20°C), the corresponding Womersley number ranges from approximately 25 to 109. According to Womersley, when $\alpha > 10$, the phase lag approaches -90° and stabilizes. Thus, under the present conditions, a phase lag of approximately -90° would be expected. The larger phase variations observed experimentally therefore suggest the presence of additional dynamic effects, such as restoring, damping, or inertial forces.

The nonlinearities identified earlier in this chapter likely contribute to these increased phase deviations. In particular, reflections of flow waves in the outlet tube may interfere with forward-propagating waves, producing phase shifts similar to those that generate nonlinearities in the flow measurements. Furthermore, the dynamic response of the one-way valve may distort the flow and pressure waveforms, introducing additional harmonic content. Finally, a constant time delay τ between the acquisition of pressure and flow signals can produce an artificial phase lag that increases linearly with frequency, since $\phi = \omega\tau$. Even small sensor or microcontroller latencies can have a significant effect: for instance, a delay of only 20 ms at 12 Hz introduces an apparent phase lag of 86.4°. This example illustrates the extreme sensitivity of phase-

dependent quantities - such as hydraulic power and efficiency - to even minimal timing offsets.

6.5.3 Efficiencies

Figure 6.15 summarizes the various power and efficiency metrics obtained for configuration C. Specifically, Figs. 6.15a, b, c show the electric, mechanical, and hydraulic powers (each normalized by F^2), while Figs. 6.15d, e, f present the corresponding efficiencies: electromechanical, mechanical-to-hydraulic, and electric-to-hydraulic, respectively.

The mechanical-to-hydraulic efficiency η_{MH} is defined as the ratio of hydraulic power to mechanical power, as expressed in Eq. 6.3. Similarly, the electric-to-hydraulic efficiency η_{EH} corresponds to the ratio of hydraulic to electrical power, as given in Eq. 6.4.

$$\eta_{MH} = \frac{P_h}{P_m} \tag{6.3}$$

$$\eta_{EH} = \frac{P_{hy}}{P_e} \tag{6.4}$$

As shown in Fig. 6.15e, the mechanical-to-hydraulic efficiency decreases markedly with increasing frequency, reflecting the reduced hydraulic power observed near resonance. This decline is the result of the $\sim 180^\circ$ phase lag between pressure and flow rate at resonance, which significantly limits effective energy transfer.

These losses are also reflected in the electric-to-hydraulic efficiency η_{EH} (Fig. 6.15f), defined as the product of the electromechanical and mechanical-to-hydraulic efficiencies ($\eta_{EH} = \eta_{EM} \cdot \eta_{MH}$). Consequently, despite the pronounced resonance peak in electromechanical efficiency, no clear resonant enhancement appears in the total electric-to-hydraulic efficiency. Nevertheless, the electromechanical resonance contributes to maintaining the overall efficiency within a narrow range between 0.08% and 0.48%. This behaviour arises because the maxima of η_{EM} and η_{MH} compensate for each other's minima, resulting in a relatively stable global efficiency.

These results highlight that the resonant behaviour of the pump improves energy conversion performance at operating points where efficiency would otherwise drop sharply due to the strong phase offset between pressure and flow rate.

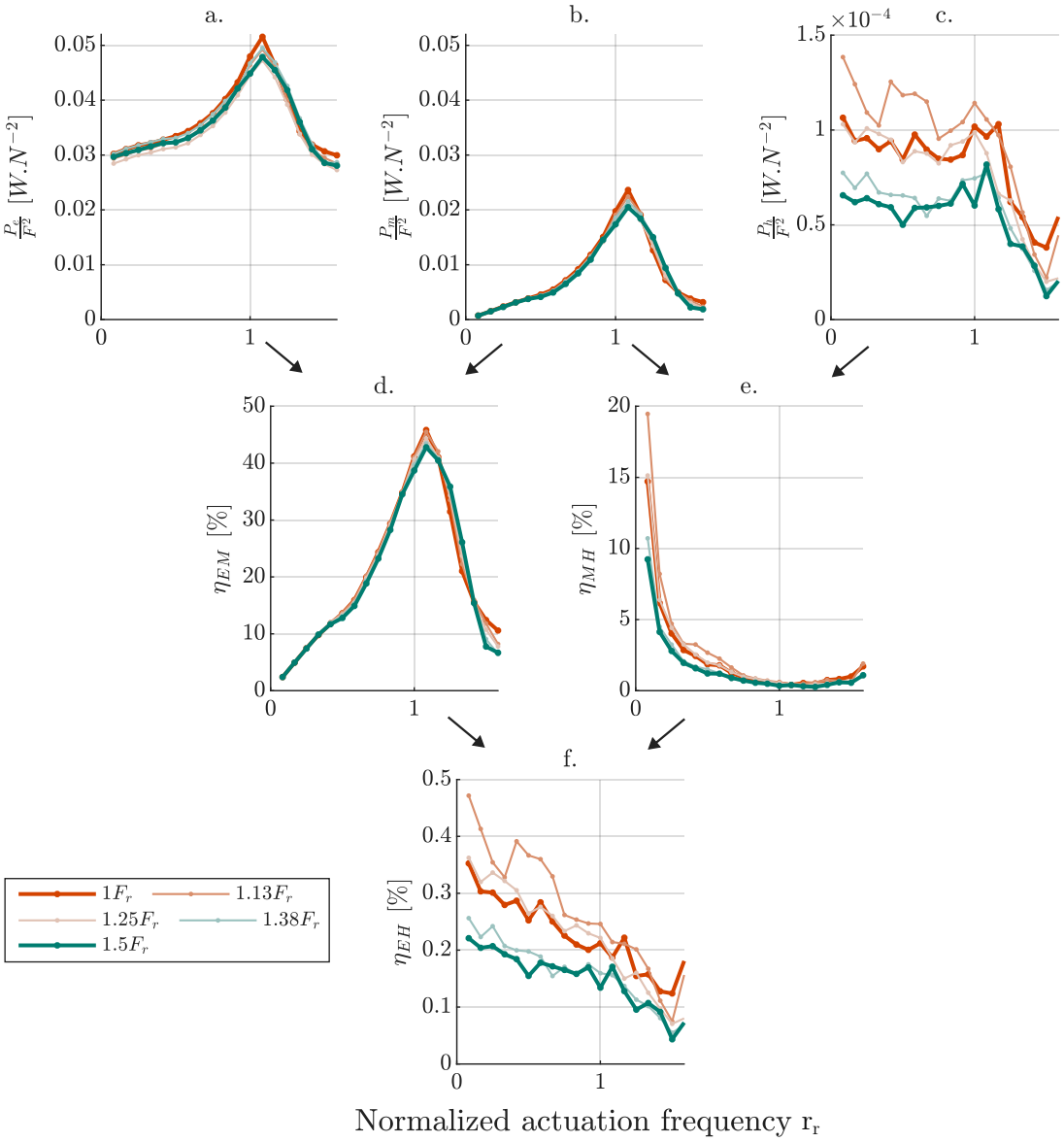

Figure 6.15: Powers scaled by F^2 and efficiencies for configuration C. **a.** Electric power. **b.** Mechanical power. **c.** Hydraulic power. **d.** Electromechanical efficiency. **e.** Mechanical-to-hydraulic efficiency. **f.** Electric-to-hydraulic efficiency.

6.6 Conclusion

In this chapter, the resonant behaviour of the pump has been experimentally validated with a resonant frequency of 13 Hz. The resonance frequency and response amplitude were found to be strongly dependent on hydrostatic pressure which modify the system's equivalent stiffness, shifting the resonance frequency. This highlights the strong dependency of the dynamic properties of the pump on the fluidic circuit it

connects to, similar to what is observed with the human cardiovascular network.

The harmonic analysis revealed that the actuator plunger presents dynamic properties consistent with that of a weakly non-linear mass-spring-damper system while stronger non-linearity appears on the fluid side, likely arising from fluid–structure interactions and valve dynamics. Importantly, these effects do not compromise the overall resonant behaviour. Mechanical and electric powers are found to scale with the actuation force squared confirming the mass-spring-damper hypothesis.

Furthermore, except for the pressure fundamental which is highly dependent on the constant hydrostatic pressure, the pressure and flow rate components scale with the actuation force amplitude analogous to the scaling laws of a MSD. A distinct phase lag between pressure and flow rate was observed, increasing with frequency and reaching values close to -180° near resonance. This lag results in negating the hydraulic power fundamental and second harmonic, partially reducing the amplitude peak of the total hydraulic power.

Nevertheless, the combination of these results demonstrates that operating the pump at or near resonance significantly improves performance. Particularly, the electromechanical efficiency peaks at 43% and contributes to maintain overall efficiency where it would typically decline due to phase misalignment.

Overall, this chapter establishes experimentally, for the first time, that resonance can be effectively leveraged to enhance power generation and the energy efficiency of pulsatile pumps at a macro-scale. It also highlights the sensitivity of the system to the fluidics circuit connected to the pump, specifically hydrostatic pressure and fluid-solid interactions after the valves, pointing to the need for precise control of these parameters in future implementations of resonant pulsatile systems.

Chapter 7

Influence of Stiffness Modulation on Resonant Response

7.1 Introduction

Having established in Chapter 6 that the developed pump exhibits clear resonant behaviour, the present chapter investigates how variations in stiffness modify this dynamic response. The purpose is to determine whether resonance can be predictably tuned through stiffness modulation and to evaluate the resulting effects on amplitude, frequency, and energy transfer.

The chapter begins with the quasi-static characterisation introduced in Chapter 4, used here to quantify how changes in stiffness affect the equilibrium position, effective stiffness, and energy losses as the number of active coils is varied. It then proceeds to the dynamic experiments, which assess how stiffness influences the resonance frequency and amplitude of the electric and mechanical power, testing the theoretical relationships derived from the mass-spring-damper model. Finally, it analyses how the dynamic changes introduced on the actuator side are transmitted to the hydraulic domain, focusing on the evolution of the harmonic content of pressure and flow rate signals, as well as the associated phase variations, which play a central role in determining the timing and efficiency of energy exchange.

Overall, this chapter offers a comprehensive view of how stiffness modulation shapes the resonant behaviour of the pump which represents an important step toward the design of tunable and adaptive pumping systems capable of maintaining optimal performance under variable operating conditions.

7.2 Stiffness Tuning in Quasi-Static Conditions

This section is dedicated to the study of the changes induced by the VSM in the quasi-static experiments for configurations A, B and C. Specifically, similarly to the analysis done in chapter 6, section 6.2, three quantities are evaluated: the equilibrium position, the stiffness and the energy losses.

7.2.1 Number of Active Coils Estimation

To characterise the equilibrium position, damping, and stiffness of the Variable Stiffness Mechanism (VSM) as a function of the number of active coils, it is first necessary to estimate the actual number of coils engaged in the spring.

The estimation follows Eq.7.1 where N denotes the number of active coils, $max(N)$ the maximum possible number of active coils, and n the number of inactive coils, as illustrated in Fig. 7.1.

$$N = max(N) - n \tag{7.1}$$

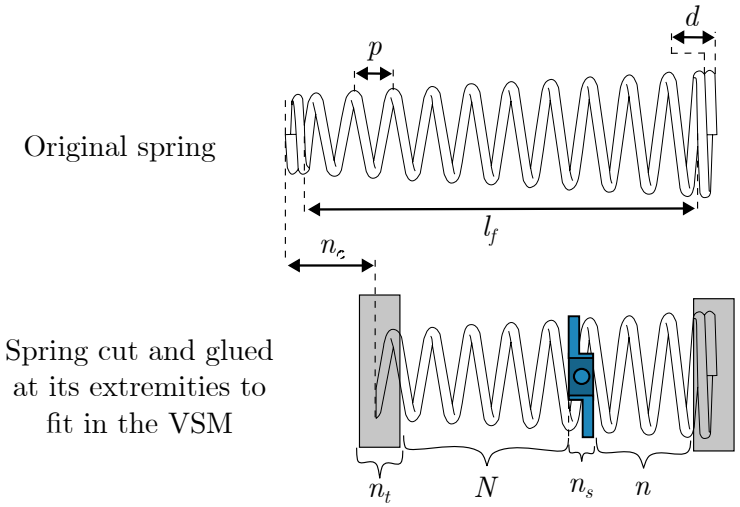

Figure 7.1: Definition of variables used to estimate the effective number of active coils in the VSM.

Because the spring was shortened to fit within the pump assembly, the maximum number of active coils $max(N)$ differs from the original specification $max(N_i)$ provided by the manufacturer (appendix 12). The number of coils removed during cutting is denoted n_c. In addition, some coils at the top, n_t, are bonded to the VSM structure and therefore cannot contribute to deformation. The presence of the slider also

$max(N_i)$	n_s	n_t	d	l_c	l_f
11	1	1	0.787	3.6	35.052

Table 7.1: Numerical values used to calculate the number of active coils. The diameter d, the length cut l_c and the free length l_f are expressed in millimeters.

deactivates one additional coil, n_s. These considerations lead to Eq.7.2.

$$max(N) = max(N_i) - (n_c + n_t + n_s) \tag{7.2}$$

The number of coils removed during cutting, n_c, can be determined from Eq.7.3, given the cut length l_c, wire diameter d and coil pitch p. Since the spring has closed and ground ends, the cut length includes two inactive end coils, each estimated to correspond to one wire diameter.

$$n_c = \frac{l_c - 2d}{p} \tag{7.3}$$

The coil pitch is obtained by dividing the active length of the spring by the initial maximum number of active coils, as shown in Eq.7.4. The active length is approximated as the free length l_f minus four times the wire diameter d to account for the two closed and ground ends

Specifically, the active length is estimated to be equal to the free length minus four times the wire diameter to take into account both closed and grounded ends of the spring.

$$p = \frac{l_f - 4d}{max(N_i)} \tag{7.4}$$

Using the numerical parameters listed in 7.1, the maximum number of active coils of the VSM is found to be 8.3. The rest of the stiffness settings tested in the rest of this thesis are $N = 6.3$, $N = 5.3$, $N = 4.3$, $N = 3.8$, $N = 3.3$.

7.2.2 Stiffness Scales According to Theory

With the number of active coils defined, the relationship between stiffness and coil activation can now be examined.

Figures 7.2a, b, and c present the quasi-static test results for the different numbers of active coils tested, in configurations A, B, and C, respectively. The dark red curves correspond to the lowest stiffness setting, $N = 8.3$, previously analyzed in Section 6.2, while the dark blue curves represent the highest stiffness setting, corresponding to the

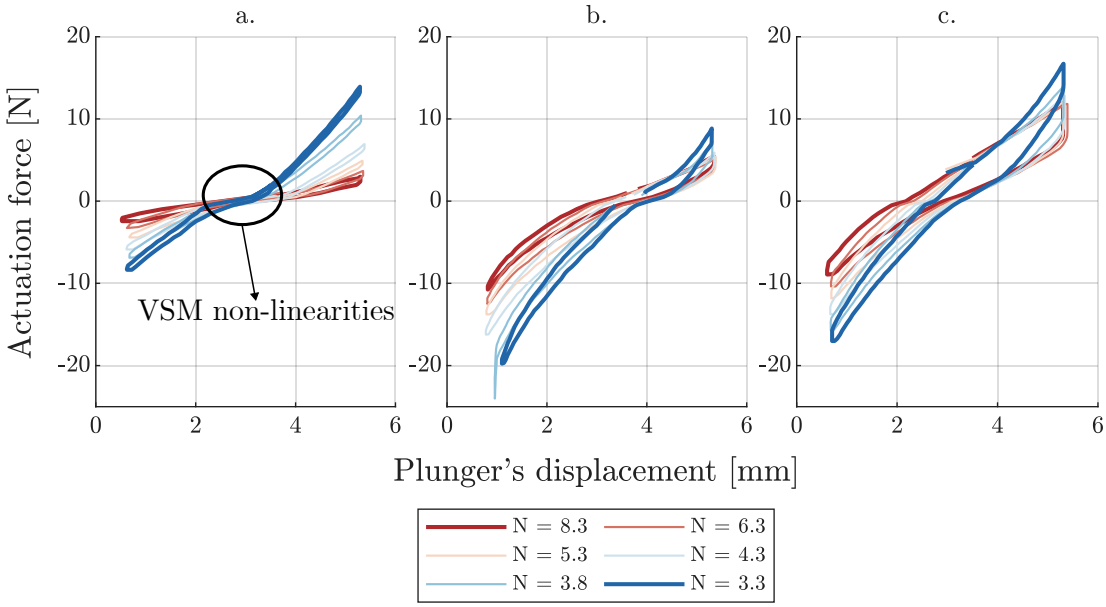

Figure 7.2: Quasi-static tests results for six different stiffness. **a.** Configuration A. **a.** Configuration B. **a.** Configuration C.

smallest number of active coils, $N = 3.3$.

First, as previously observed for the 3D-printed VSMs presented in Chapter 3, Section 3.3.2, the force-displacement curves in Fig. 7.2a exhibit local nonlinearities near the equilibrium position, likely arising from manufacturing tolerances. This feature appears to be an intrinsic characteristic of the VSM concept, consistently observed across different scales. Despite these nonlinearities, the slope of the hysteresis loops, corresponding to stiffness, increases as the number of active coils decreases, as theoretically expected. Moreover, the VSM demonstrates a nearly symmetrical stiffness response, exhibiting comparable stiffness in compression (positive force) and extension (negative force) over the tested displacement range. Figure 7.2b further reveals the additional stiffness contribution from the main membrane. Compared to Fig. 7.2a, the force required to retract the plunger (toward 0 mm) approximately doubles, confirming the trend previously observed for $N = 8.3$ in Chapter 6.

Second, to verify that the mechanism's stiffness scales as predicted by theory, a piecewise linear function with three segments was fitted to the hysteresis loops of configuration A. The stiffness corresponding to each number of active coils was obtained by averaging the slopes of the two outer segments of the fitted function, as illustrated in Fig. 7.3. The slope of the central segment was excluded to prevent bias in the stiffness estimation. Figure 7.4a compares the experimentally estimated stiffness with the theoretical stiffness of a conical spring, calculated from Eq. 7.5 (196), where

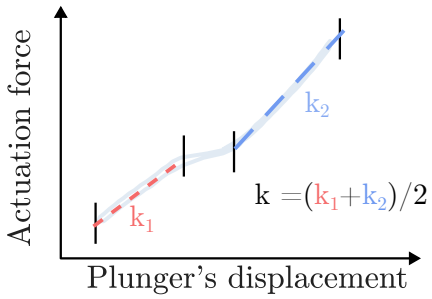

Figure 7.3: To determine the stiffness, a piecewise function is fitted to the loading curves. The non-linearity introduced by the VSM is ignored in the stiffness estimation.

G is the shear modulus, d the wire diameter, N the number of active coils, and D_1 and D_2 the small and large mean diameters, respectively.

$$k_c = \frac{G * d^4}{(2 * N * (D_1 + D_2) * (D_1^2 + D_2^2))} \tag{7.5}$$

The experimental stiffness (blue curve) closely follows the theoretical prediction (black dotted curve), validating the correct operation of the VSM and confirming the feasibility of the C-MAC architecture at a significantly smaller scale than the prototype presented in Chapter 3.

For configurations B and C, the consistent upward shift of the orange and yellow curves along the stiffness axis indicates an additional stiffness contribution from the membrane and the internal fluid. This observation further supports the findings of Chapter 6, demonstrating that the presence of fluid and structural components increases the overall stiffness of the pump system.

7.2.3 Equilibrium Position and Damping Increase With Stiffness

The impact of the VSM on the energy losses and equilibrium position is studied in this section.

Figure 7.4c presents the plunger's equilibrium position, corresponding to the x-intercept of the piecewise functions defined in the previous section, across the six stiffness tested and for configuration A, B and C. Across all stiffness settings, the pump remains more expanded in configuration C than in configuration B, as indicated by the consistently higher displacement values of the orange curve compared to the yellow one. This observation confirms the earlier finding (Chapter 6, Section 6.2) that fluid loading causes an expansion of the pump at rest.

While the equilibrium position in configuration A remains largely unaffected by

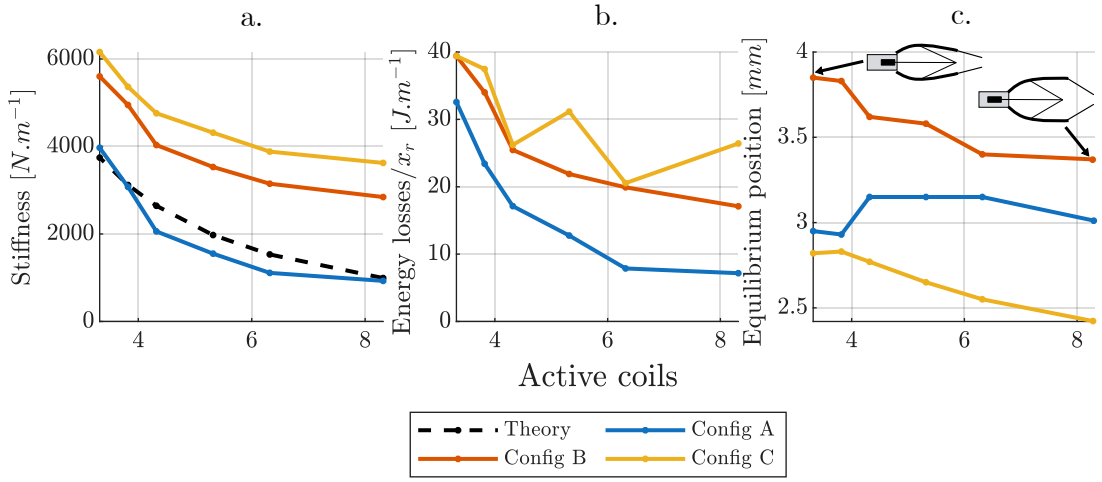

Figure 7.4: Stiffness (**a.**), energy losses scaled by the plunger displacement x_d (**b.**) and plungers' equilibrium position **c.** for configuration A, B and C as a function of the number of active coils

changes in the number of active coils, configurations B and C exhibit an increase in equilibrium position with increasing stiffness. In other words, as the number of active coils decreases, the VSM appears to introduce a progressive preload, pulling the plunger forward and thereby compressing the pump. In both configurations, the measured increase in equilibrium position is approximately 0.5 mm between the lowest and highest stiffness settings, corresponding to about 8 % of the total 6 mm stroke. These variations are primarily attributed to the mechanical constraints introduced by integrating the VSM within the pump, as well as to the influence of the water's weight, which modifies the VSM's operation. This finding highlights that the VSM's behavior is not independent of the configuration: the mass distribution of the fluid and the surrounding structure alter the VSM response, resulting in a progressive preload as stiffness increases. Although, in this study, the resulting shift in equilibrium position remains modest relative to the available stroke, it underscores the importance of carefully selecting the stiffness tuning method to avoid reducing the effective range of motion. It should be noted that these variations in equilibrium position do not change the mass–spring–damper representation. Therefore, the scaling laws derived in this work are therefore not affected, only the initial conditions are modified. However, such effects would need to be explicitly accounted for in a fully derived model to ensure accurate quantitative predictions.

It should be noted that these variations in equilibrium position do not alter its dynamic behaviour. As a result, the mass–spring–damper representation remains valid, and the scaling laws derived in this work are not affected. However, such effects

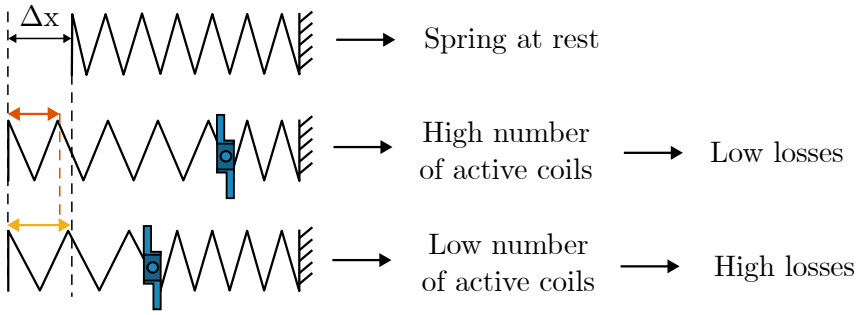

Figure 7.5: The lower the number of active coils, the larger the spring deformation for a given displacement Δ_x. This leads to increasing losses as the number of active coils diminishes.

would need to be explicitly accounted for in a fully derived model to ensure accurate quantitative predictions.

The second quantity investigated is the energy loss associated with the VSM. The areas enclosed within the hysteresis loops in Fig. 7.2, normalized by the plunger displacement x_r, are plotted against the number of active coils for each configuration in Fig. 7.4b. The trend identified in Section 6.2 is confirmed: energy losses are consistently higher in configuration C than in configurations B and A. As the only change between configurations A and B lies in the integration of the variable stiffness mechanism within the pump structure, the increase in losses observed in this transition can therefore be attributed to the mechanical behaviour of the pump itself, in particular the deformation of the structure during operation, including the stretching of the membrane, which can be observed visually during the experiments. Between configurations B and C, the sole modification is the introduction of fluid within the system. The additional losses are therefore attributed to fluid–structure interactions, in particular the asymmetric loading induced by the fluid during the expansion and compression phases.

A key result, however, is the sharp rise in damping as the number of active coils decreases. This increase in energy dissipation with stiffness is explained by the effective shortening of the spring. Fewer active coils correspond to a shorter active length, meaning that, for a given plunger displacement, the relative strain in the spring becomes larger, thereby increasing the energy lost per cycle, as illustrated in Fig. 7.5. This result is central as it highlights that while the VSM does tune stiffness as expected, it also introduces increasing losses as the stiffness augments. The impact of this result on the pump performance is analysed in the next sections.

7.3 Resonant Shift and Amplitude Drop

In this section, the influence of the VSM on the trends of the power peaks is examined. Specifically, two quantities are tracked as a function of the number of active coils: the resonant frequency and the peak amplitude.

As shown in Chapter 6, Section 6.4, the magnitudes of the measured quantities scale linearly with the amplitude of the actuation force F, except for the zero-frequency pressure component p_0. These observations indicate that, for a given stiffness, the curves of the scaled quantities collapse onto one another. This property is exploited in the following analyses: for each stiffness level, the five curves corresponding to the five actuation force amplitudes are averaged to produce a single representative curve. In other words, instead of displaying five nearly overlapping curves per stiffness, only their mean curve is presented. This approach, combined with the cycle-synchronous average technique introduced in Chapter 4, further reinforces any trends and patterns in the experimental results. Finally, for clarity, red and blue are used to compare stiffness levels, whereas orange and green are used to compare actuation forces, consistent with the color scheme applied throughout this thesis.

7.3.1 Expected Resonant Shifts from Quasi-Static Tests

The expected shifts in natural frequency resulting from the stiffness variations observed in the quasi-static tests are analyzed. Table 7.2 summarizes the ratio of the maximum to minimum equivalent stiffness extracted from Fig. 7.4a, denoted r_k, along with the corresponding ratio of natural frequencies $r^* = \sqrt{r_k}$ expected from a MSD system. Interestingly, the natural frequency ratio decreases across the configurations. This reduction arises from the additional stiffness contributed by the pump and the water, which diminishes the relative influence of the VSM-induced stiffness variations.

	$max(k_{eq})$ [N.m]	$min(k_{eq})$ [N.m]	r_k	Expected r^*
Config A	3970	928	4.0	2.1
Config B	5601	2844	2.0	1.4
Config C	6158	3624	1.7	1.3

Table 7.2: Numerical equivalent stiffness values obtained from Fig. 7.4, ratio of the highest to lowest stiffness r_k and expected ratio r^* of the highest to lowest natural frequency.

This result highlights a key consideration in the design of tunable-stiffness pumps: the stiffness range provided by the VSM must be maximized to offset the reduction in r^* caused by additional restoring elements. In practice, the extra stiffness introduced by external components can nearly suppress any resulting shift in resonance frequency.

7.3.2 Electric and Mechanical Power

The expected shifts in natural frequency in quasi-static conditions are compared with the frequency shifts observed in the electric and mechanical power estimations obtained under dynamic conditions. Figures 7.6a, b, and c respectively present the electrical power, mechanical power, and electromechanical efficiency for configuration B. The frequency ratio observed for these three quantities is $1.17/1 = 1.17$, which is close to the expected value of 1.4. The discrepancy between the predicted and experimental ratios can be attributed to uncertainties in the stiffness estimation and to the fact that the pump might not exactly follow the resonant frequency scaling with stiffens of the simple MSD model. A similar trend is observed for configuration C shown in Fig. 7.6c, d and e, where the frequency ratio $1.25/1.08 = 1.16$ remains comparable. Although the presence of water introduces additional stiffness and thus shifts the resonance frequencies (as explained in Section 6.4), its effect is insufficient to significantly alter the frequency ratio. This result is consistent with the natural frequency ratios in quasi-static conditions where from configuration B to C, the ratios only change from 1.4 to 1.3.

Figure 7.6 also show that, for both configurations, an increase in stiffness results in a decrease in power and efficiency. As recalled in Eqs. 5.20 and 5.21, the electrical and mechanical powers scale inversely with the damping coefficient c and are independent of the stiffness. Therefore, if damping remained constant across stiffness levels, the amplitudes of the power peaks would be expected to remain unchanged. The observed reduction in these peaks thus confirms that damping increases as the number of active coils decreases, as previously shown in Fig. 7.4b. However, although configurations B and C exhibit similar power and efficiency at $N = 8.3$, the decrease in electrical power and mechanical power is significantly greater in configuration C. This indicates that, under dynamic conditions, energy losses related to stiffness variations increase more rapidly in the presence of fluid loading. Specifically, from the lowest to the highest stiffness, the efficiency drops by 8 % in configuration B and by 17 %

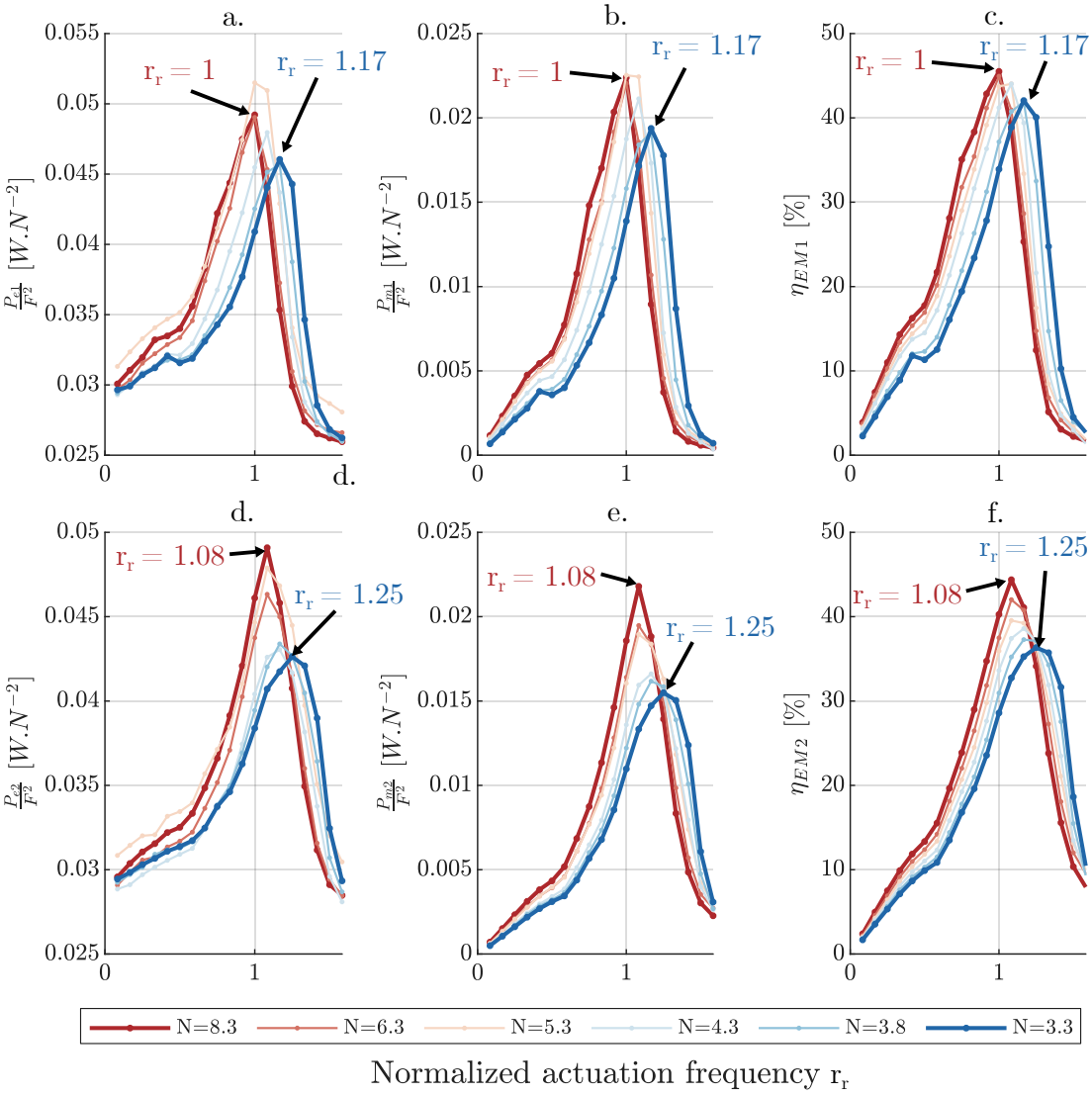

Figure 7.6: Averaged powers normalized by F^2 and efficiencies for configuration B and configuration C. **a.** Config. B: Electrical power . **b.** Config. B: Mechanical power. **c.** Config. B: Electromechanical efficiency. **d.** Config. C: Electrical power . **e.** Config. C: Mechanical power. **f.** Config. C: Electromechanical efficiency.

in configuration C. It is hypothesized that fluid loading alters the alignment of the pump's mechanical components, inducing changes in the scaling of damping with the number of active coils. Additionally, the higher oscillation frequencies at resonance in configuration C may contribute to increased damping within both the voice coil actuator and the fluidic circuit. Both of these results are summarized visually in Fig. 7.7.

$$P_m^* = \frac{1}{2}\frac{F^2}{c} \qquad \text{(5.20 revisited)}$$

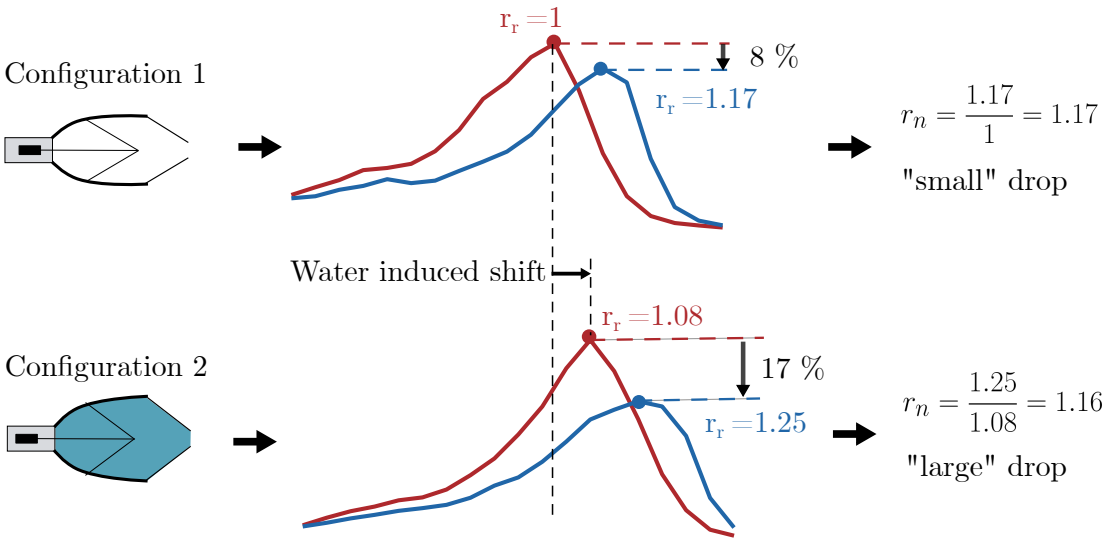

Figure 7.7: The water added stiffness induces a shift in natural frequency. However, it is not strong enough to generate significant variation in the natural frequency ratio r^* which remains approximately the same in both configurations. Finally, the VSM induces higher losses for higher stiffness resulting in the power and efficiency amplitudes to drop. The larger drops observed in configuration C is mostly associated to fluid loading, which alters the VSM functioning, thereby modifying its damping characteristics.

$$P_e^* = \frac{1}{2}F^2\frac{R}{K_F^2} + \frac{K_B}{K_F}P_{mech}^* \qquad \text{(5.21 revisited)}$$

7.3.3 Hydraulic Power Harmonic Content

This section analyzes the frequency components of the pressure, flow rate, and hydraulic power, with the objective of identifying any notable differences from the observations previously made for the electrical and mechanical powers in configuration C.

The first part of the analysis focuses on the fundamental and second harmonics. Figure 7.8 summarizes the contributions of the first two harmonics of pressure and flow rate to the hydraulic power. The first (Figs. 7.8a, e), second (Figs. 7.8b, f), and fourth rows (Figs. 7.8d, h) correspond respectively to the scaled magnitudes of the pressure, flow rate, and power harmonics.

For the second harmonic (right column), no shift of the resonant peak is observed: the natural frequency remains constant at $r_r = 1.08$ between $N = 8.3$ (thick red curve) and $N = 3.3$ (thick blue curve) as shown by the dotted line. In contrast, for the fundamental (left column), the resonant peak clearly shifts from $r_r = 1.08$ to

$r_r = 1.33$, as indicated by the red and blue dotted lines and the green arrow denoted "Shift". This shift is slightly larger than that observed for the electrical and mechanical powers (1.08 to 1.25). The difference is likely attributable to measurement uncertainty rather than a distinct dynamic phenomenon. This result demonstrates that the shift in resonance observed on the actuator's side is effectively transmitted to the fluid domain. Specifically, it highlights the fact that stiffness tuning can displace the peak in the amplitude of the flow rate and pressure oscillations, resulting in a shift of the hydraulic power fundamental. In other words, the extent to which the pressure and flow rate change throughout a pulsation cycle can be consistently maximized throughout different pulsation frequencies.

This behaviour is further illustrated in Fig. 7.9. Fig. 7.9a, b, c, displays the time variations of the flow rate for $N = 8.3$ and $1.5F_r$ at excitation frequencies of 9, 13, and 17 Hz, respectively and for which the DC component has been removed to isolate amplitude variations. As indicated by the green arrows, the flow rate oscillations reach their highest amplitude at 13 Hz - the resonant frequency (Fig. 7.9b). The same trend is observed when the number of active coils is reduced to $N = 3.3$. Figures 7.9d, e, f, corresponding to $N = 3.3$ and $2.22F_r$ at 9, 16, and 19 Hz, show that the largest flow variations occur at the new resonant frequency of 16 Hz (Fig. 7.9e). It is noteworthy that, although the second harmonic does not shift with stiffness, the shift in the fundamental alone is sufficient to cause a corresponding displacement of the overall flow rate amplitude.

To the author's knowledge, this represents the first experimental demonstration of effective variable stiffness tuning in a macro-scale pulsatile pump, enabling the maintenance of maximal pressure and flow rate oscillations across different resonant conditions.

These results demonstrate that the resonance shift observed on the actuator side is effectively transmitted to the fluid domain. In particular, they confirm that stiffness tuning can alter the frequency at which the amplitudes of pressure and flow rate oscillations reach their maxima, thereby shifting the fundamental peak of the hydraulic power. In other words, by adjusting stiffness, the pump can sustain maximal oscillatory amplitudes of pressure and flow rate across different pulsation frequencies.

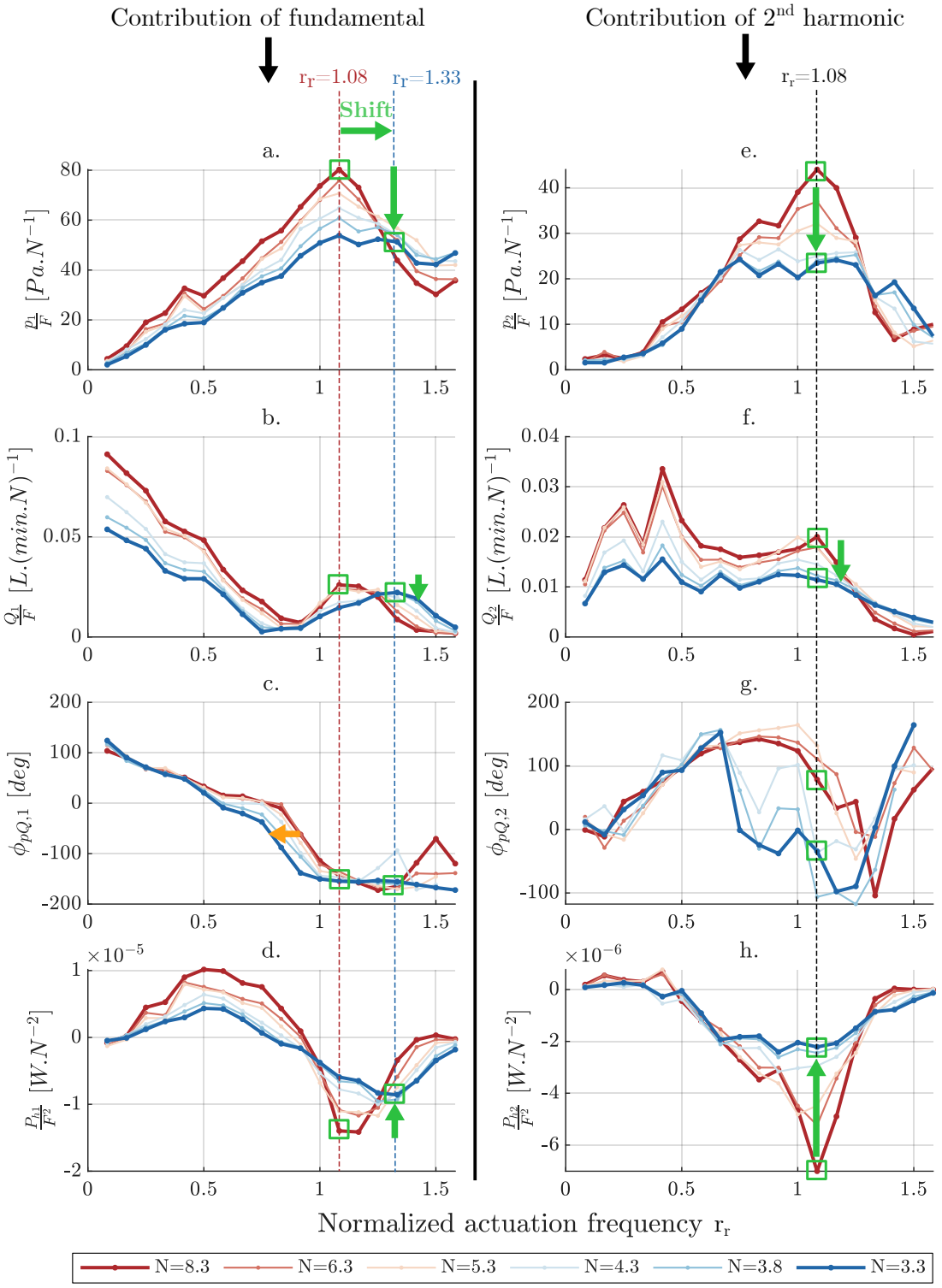

Figure 7.8: Contribution of the fundamental (left column) and second harmonic (right colume) to the hydraulic power. Each row corresponds to a different variable. **a. e.** Scaled amplitude of the pressure. **b. f.** Scaled amplitude of the flow rate. **c. g.** Phase between flow rate and pressure. **d. h.** Scaled hydraulic power.

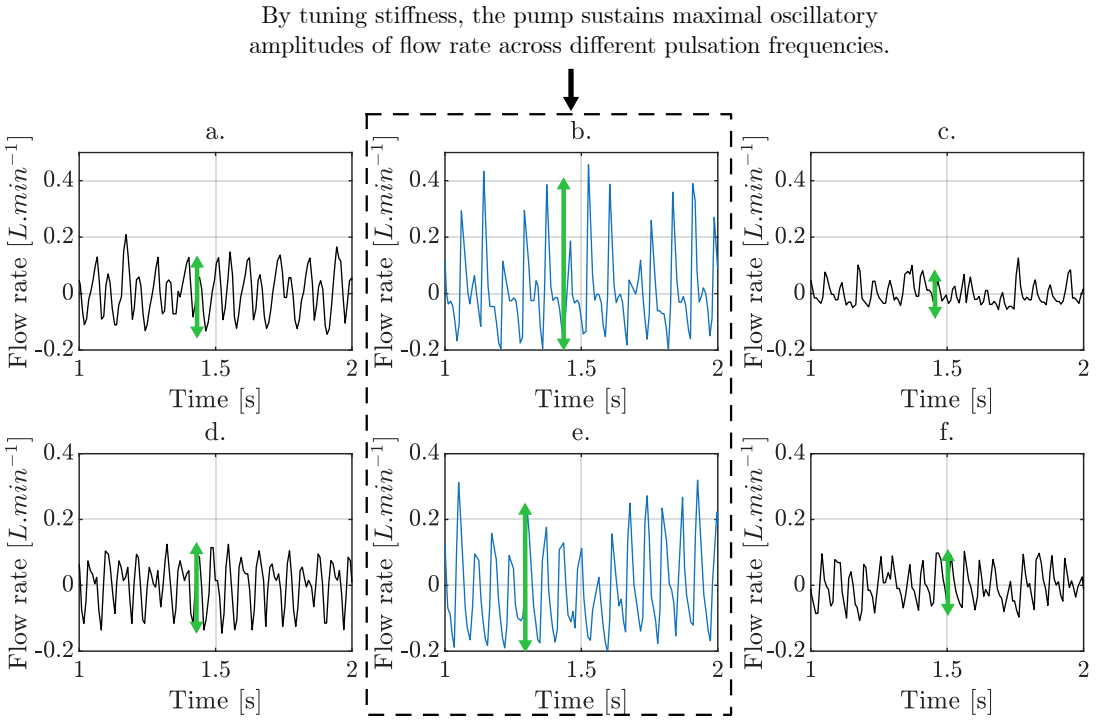

Figure 7.9: Flow rate variations through time to which the DC components has been removed to visualize amplitude variations. First row: $N = 8.3$ and $1.5F_r$. Second row: $N = 3.3$ and $2.22F_r$. **a.** Excitation frequency 9 Hz. **b.** Excitation frequency 13 Hz (resonance). **c.** Excitation frequency 17 Hz. **d.** Excitation frequency 9 Hz. **e.** Excitation frequency 16 Hz (resonance). **f.** Excitation frequency 19 Hz.

In Fig. 7.8, for both harmonics and across all three quantities, a decrease in the amplitude magnitude is observed, as highlighted by the vertical green arrows. This indicates a scaling behavior consistent with that previously identified for the electrical and mechanical powers where damping induced by the VSM results in a drop in power.

The third row (Figs. 7.8c, g) presents the phase difference between the pressure and flow rate for different stiffness values. Interestingly, for the fundamental, as the number of active coils increases, the phase shifts toward lower frequencies (shown by the orange arrow) which is opposite to the trend observed for the magnitude of the pressure, flow rate, and hydraulic power. The cause of this behaviour remains unclear but likely arises from the non-linear behaviour of the fluid. For completeness, the phase difference of the second harmonic is also shown. However, as previously noted in Chapter 6, accurately estimating the phase near 180° is challenging; thus, no meaningful conclusions can be drawn from the averaged curves in Fig. 7.8g.

The second part of this analysis examines the DC (zero-frequency) components of the pressure, flow rate, and hydraulic power, as shown in Fig. 7.10. Because the zero-frequency pressure component does not scale with the actuation force F, averaging the curves, as done in Fig. 7.8, would not be meaningful. Instead, each quantity is presented separately for three selected stiffness settings - $N = 8.3$, $N = 4.3$, and $N = 3.3$ - and for the five corresponding actuation forces.

The first row (Figs. 7.8a, d, g) corresponds to $N = 8.3$, while the second (Figs. 7.8b, e, h) and third (Figs. 7.8c, f, i) correspond to $N = 4.3$ and $N = 3.3$, respectively. Columns one, two, and three represent the scaled DC components of the pressure, flow rate, and hydraulic power.

Across all three quantities, no clear resonant frequency shift is observed between stiffness levels, the resonant peak remaining at $r_r = 1.08$. Although the widening of the peaks in Figs. 7.8e and f could suggest a slight change in natural frequency, the trend remains too weak to confirm. As stiffness increases, the amplitude decreases (indicated by the green intervals on each graph), reinforcing the downward trend observed for the fundamental and second harmonics as well as for the electrical and mechanical powers.

Finally, the magnitude of the DC component of the power is considerably larger than that of the harmonics. At resonance, the DC component is approximately 5–10 times larger than the fundamental, which itself is 2–5 times larger than the second harmonic. Thus, the overall hydraulic power tends to follow the trend imposed by the zero-frequency component. Specifically, Fig. 7.11, which presents the hydraulic power for the same three stiffness levels used in the DC analysis, confirms that no frequency shift occurs ($r_r = 1.08$ for all three stiffness). This shows that the frequency shift of the fundamental is not sufficient to induce a shift in the overall hydarulic power.

7.3.4 Efficiency Under Stiffness Tuning

The relationships between the mechanical-to-hydraulic, electrical-to-hydraulic, and electromechanical efficiencies are now examined.

Figure 7.12 presents the three efficiencies (columns) for $N = 8.3$, $N = 4.3$, and $N = 3.3$ (rows). The electromechanical efficiency presents clear peaks with decreasing amplitude due to the losses induced by the reduction of number of active coils (from 43% to 36%). Although distinct resonant shifts are visible in the electromechanical efficiency, no corresponding shift appears in the mechanical-to-hydraulic efficiency. This is explained by the combined effect of two factors: the

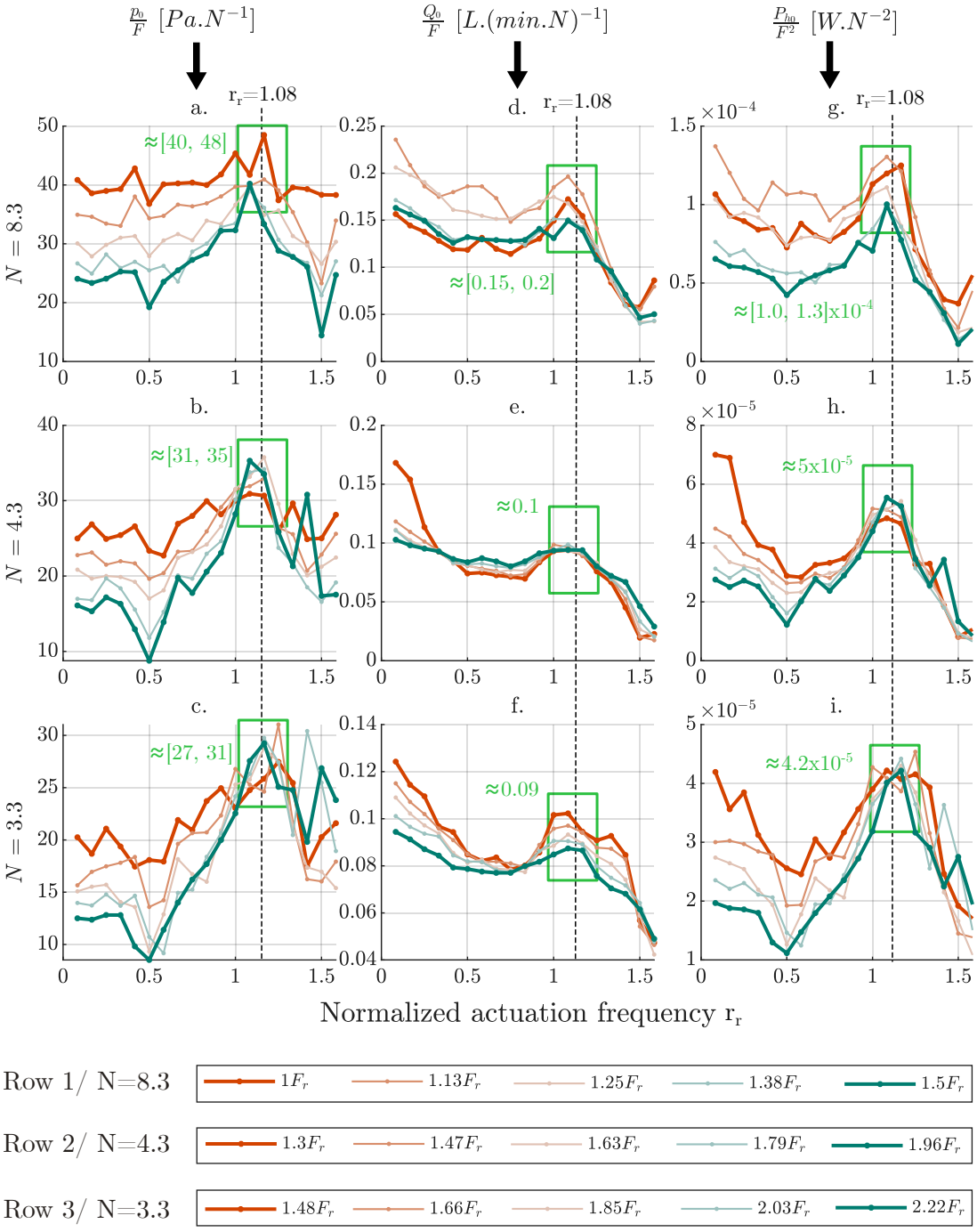

Figure 7.10: Contribution of the zero-frequency components to the hydraulic power. Each column of plots represent a different number of active coils. **a.d.g.** $N = 8.3$. **b.e.h.** $N = 4.3$ **c.f.i.** $N = 3.3$. Each row represent a different variable.**a.b.c.** Scaled pressure. **d.e.f.** Scaled flow rate. **g.h.i.** Scaled hydraulic power.

absence of a clear influence of the VSM on the resonant frequency of the hydraulic power, and the negative contribution of the power harmonics, which together suppress

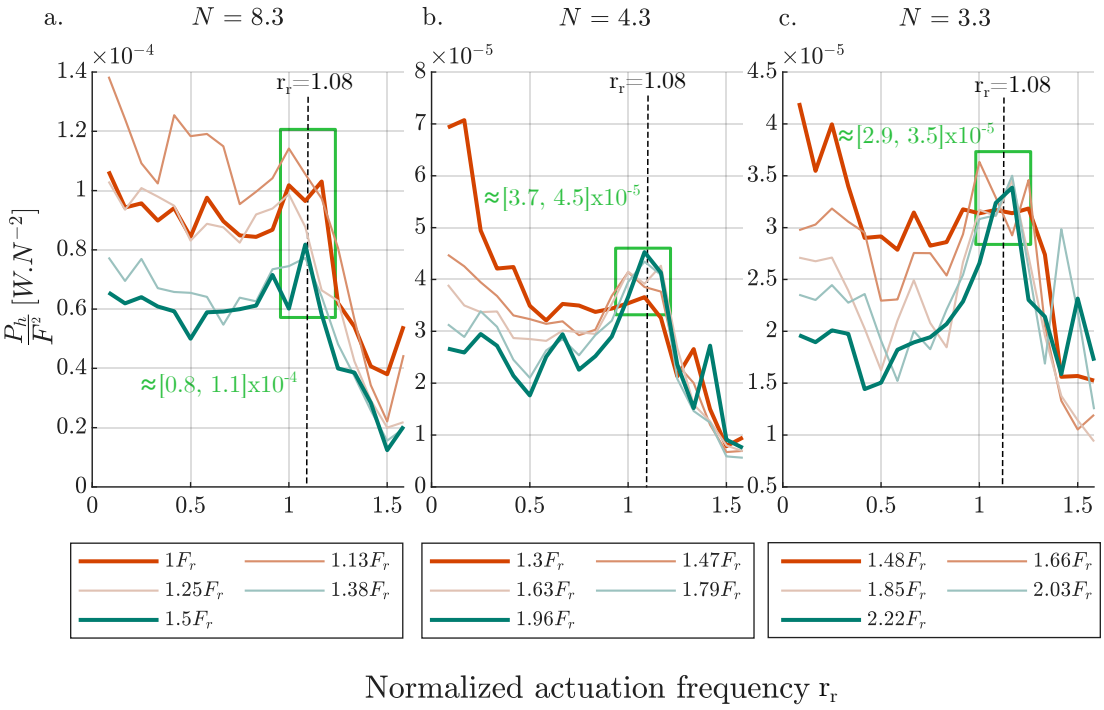

Figure 7.11: Scaled hydraulic power for three different stiffness and their five associated forces. **a.** $N = 8.3$. **b.** $N = 4.3$. **c.** $N = 3.3$.

the manifestation of a resonance shift.

As a result, the electric-to-hydraulic efficiency (Figs. 7.12g, h and i) is similarly unaffected, showing no distinct evidence of resonance displacement. While faint remnants of the electromechanical resonance peaks can be discerned (highlighted by the green squares), no unambiguous resonance behavior is observed in the electric-to-hydraulic efficiency.

Furthermore, as consistently observed throughout this chapter, increasing stiffness leads to greater energy losses, which manifest as a reduction in overall efficiency as the number of active coils decreases. In particular, the efficiency decreases by roughly a factor of two between the lowest stiffness (Fig. 7.12g) and the highest stiffness (Fig. 7.12i) across the entire frequency range tested.

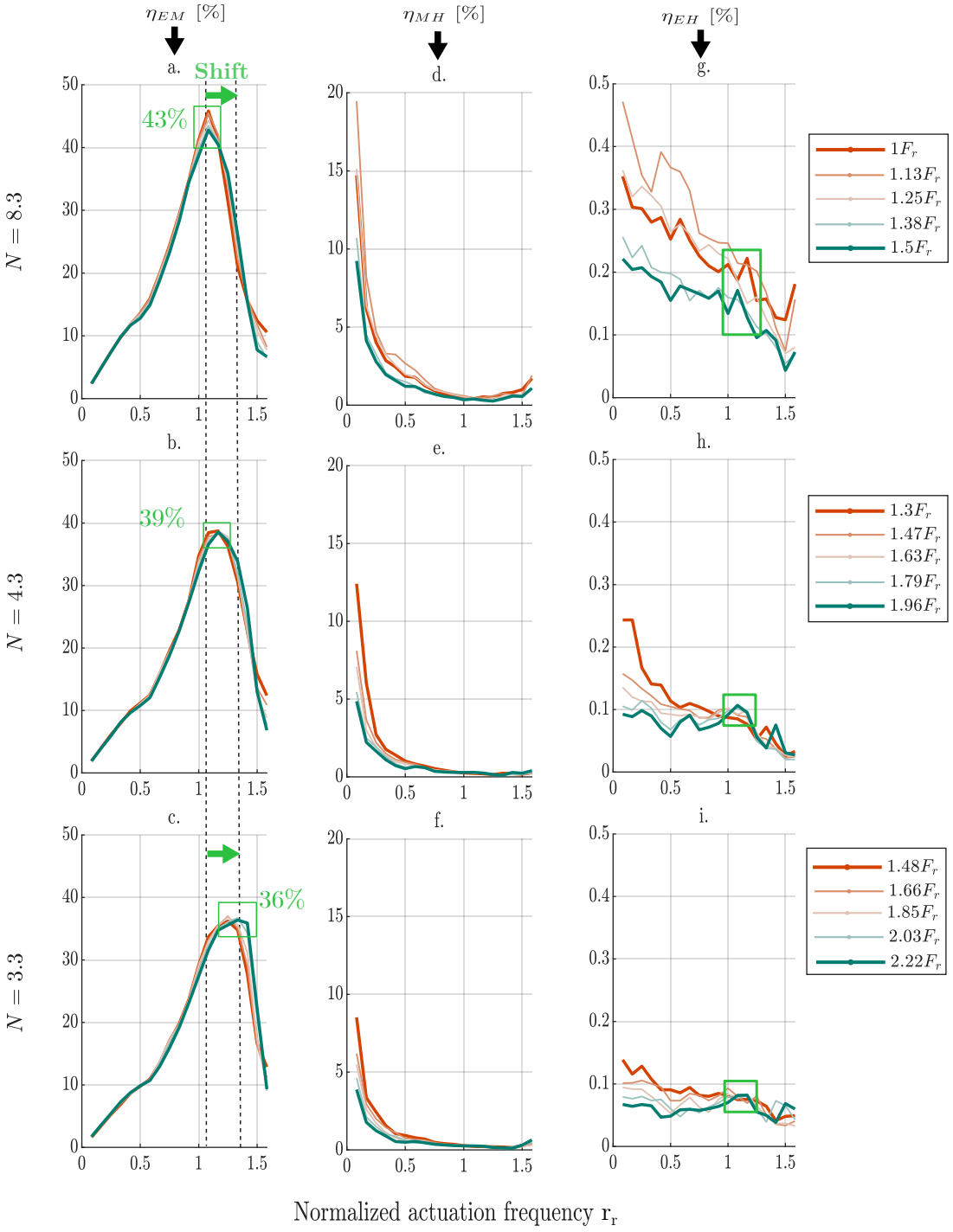

Figure 7.12: Efficiencies for $N = 8.3$, $N = 4.3$ and $N = 3.3$ and their associated forces.**a.b.c.** Electromechanical efficiency. **d.e.f.** Mechanical-to-hydraulic efficiency efficiency.**g.h.i.** Electric-to-hydraulic efficiency.

7.4 Conclusion

This chapter examined how stiffness modulation affects the resonant dynamics and energetic performance of the developed pump. The results demonstrated two major findings that together mark an important step forward in the understanding and control of resonance-based pumping.

First, the variation of stiffness through the variable stiffness mechanism introduced additional losses as the number of active coils decreased. The reduction in active coils shortens the effective elastic length of the spring, so that for a given global extension of the mechanism, the active portion of the spring experiences higher local strain and frictional effects. These factors increase internal energy dissipation, leading to a moderate decline in mechanical and hydraulic power and a corresponding reduction in efficiency. Nonetheless, the dynamic response of the system remained fully consistent with the expected behaviour of a resonant oscillator, confirming that stiffness remains a key parameter governing the distribution of stored and dissipated energy.

Second, and most significantly, the experiments revealed a clear and reproducible shift in the fundamental component of the hydraulic power as stiffness increased. The frequency associated with the power and efficiency maxima moved upward in accordance with the theoretical predictions of the mass-spring-damper model. This observation constitutes, to the author's knowledge, the first experimental demonstration of resonance tuning via stiffness modulation in a macro-scaled pump, highlighting the potential of this approach for achieving adaptive, energy-efficient operation in future devices.

Despite these promising findings, no significant shift was observed in the overall (total) hydraulic power because the DC component remains dominant over the oscillatory terms. This behaviour underscores the importance of separating steady and dynamic contributions when analysing resonance phenomena. Overall, the results presented in this chapter validate the concept of stiffness tuning as a powerful and experimentally achievable method for controlling resonance in pulsatile pumping systems, providing a strong foundation for the development of tunable, bio-inspired assist devices.

The next chapter discusses the broader implications of these findings, the limitations of the current system, and the future directions for optimizing resonance-based cardiac assist technologies.

Chapter 8

Discussion and Conclusion

8.1 Key Findings and their Implications

This thesis introduced, for the first time, the concept of a resonant heart-scaled pump integrating a novel variable-stiffness mechanism, the Compact Mechanically Adjustable Compliance (C-MAC). The results obtained throughout this work demonstrate the feasibility and potential of resonance-based pumping at a realistic physiological scale and open new perspectives for the development of adaptive pulsatile devices for both biomedical and robotic applications.

A first major contribution is the design and experimental validation of the C-MAC, a compact variable-stiffness mechanism derived from the earlier Jack Spring concept. The C-MAC significantly reduces the overall footprint of the system while maintaining a predictable and easily controllable stiffness-displacement relationship, which scales inversely with the number of active coils. Unlike most existing variable-stiffness actuators that are mechanically complex or commercially unavailable (17) (180) (164) (165), the C-MAC can be entirely 3D-printed as a single monolithic component. This feature not only facilitates rapid prototyping but also provides researchers and roboticists with an accessible means of integrating stiffness modulation into compact systems. The simplicity, manufacturability, and scalability of the design position the C-MAC as a valuable technological contribution to the broader field of soft and compliant actuation.

The potential of the C-MAC was then exemplified through its integration into a heart-inspired resonant pump by miniaturizing it to only 9 cm in length and 1.9 cm in diameter. The pump operates through the expansion and compression of an elastic cavity actuated by four ribs, mimicking the cyclic volume change of the cardiac ventricles. It includes inlet and outlet valves inspired by the human heart and achieves an overall scale comparable to that of the human heart, whose characteristic diameter and length are approximately 8 cm and 12 cm respectively (85). By developing the

pump directly at a physiologically relevant scale, this work validates the feasibility of producing resonant pulsatile flow within the geometric and energetic constraints required for potential cardiac-assist applications.

Experimental characterisation confirmed the resonant nature of the system. The membrane and the fluidic circuit were shown to introduce additional effective stiffnesses, leading to a coupled dynamic behaviour reminiscent of the interaction between the myocardium and the arterial network (39). Importantly, oscillations in the fluidic domain contribute to the total system stiffness, which increases non-linearly with actuator displacement owing to the super-linear relationship between plunger motion and displaced fluid volume. The experiments demonstrated that resonance enhances both pressure and flow amplitude, with distinct resonant peaks observed in the harmonic content of these squantities. This finding provides the first direct experimental validation that mechanical resonance can be transmitted from the actuator to the hydraulic domain in a macro-scaled pump.

The harmonic analysis further revealed that while the phase lag between pressure and flow rate deviates from the ideal 90° predicted by theory(195), this deviation, while not explicitly demonstrated in this thesis, can be attributed to fluid–structure interactions and wave reflections in the circuit. In pulsatile flow systems, pressure and flow are influenced not only by local dynamics but also by wave transmission and reflection phenomena. In particular, elements such as valves, geometric discontinuities, and compliance variations lead to partial reflection of pressure and flow waves, which alters their relative phase. As a result, pressure and flow waveforms are no longer in phase and may exhibit distortion and phase dispersion. Such behaviour is very well documented in cardiovascular systems, where wave reflections and distributed compliance contribute to complex pressure–flow relationships (82)(197)(198)(199)(200)(201)(3). These effects underline the realistic complexity of pulsatile fluid systems and are further discussed in Section 8.2.3.

Finally, varying the number of active coils in the C-MAC confirmed that stiffness modulation enables controlled tuning of resonance. Increasing stiffness produced a systematic upward shift in the resonant peaks of mechanical, and electrical power, in line with theoretical predictions derived from a mass-spring-damper model. This shift is also seen in the fundamental of the hydraulic power underscoring for the first time in a man-made pumping device how the amplitude of the pressure and flow rate oscillations can be maximized at different beating frequencies. This observation constitutes the first demonstration of resonance tuning through stiffness modulation in a macro-scale pump, establishing stiffness as an effective design variable for optimizing

dynamic performance. While energy losses increase with stiffness - due to the shorter active spring length and associated local strain - the capacity to modulate resonance frequency represents a powerful mechanism for maintaining efficient operation across variable conditions. This principle echoes biological strategies where adaptive compliance plays a key role in maintaining efficiency across changing workloads (155)(157)(159).

A visual summary of the key findings of the thesis is provided in Fig. 8.1.

In summary, the findings of this thesis collectively demonstrate that (i) resonance can substantially enhance energy transfer in compact pulsatile systems, (ii) stiffness modulation provides a viable means of tuning this resonance adaptively, and (iii) the integration of these principles at a heart-relevant scale is both experimentally and practically achievable. These results lay the foundation for the future development of resonance-based cardiac assist devices and adaptive pumping technologies capable of replicating, and potentially improving upon, the natural efficiency of the human heart.

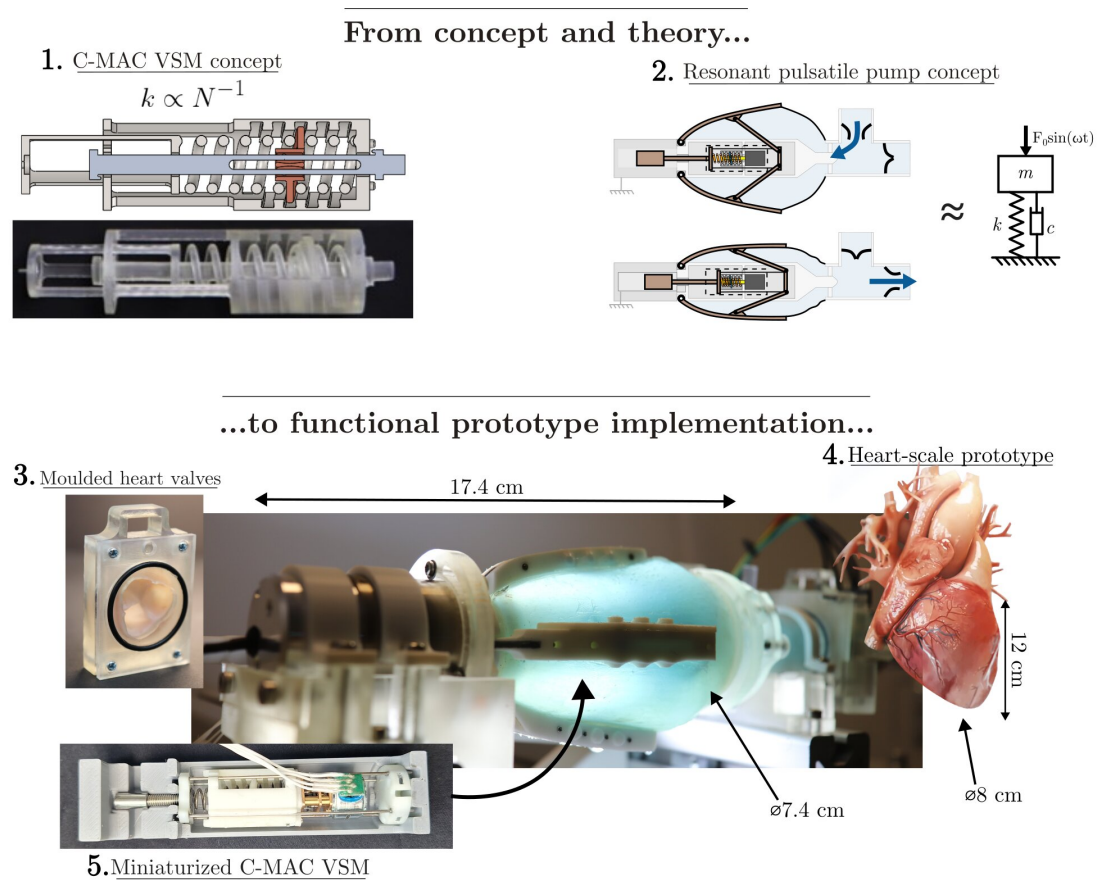

Figure 8.1: Visual summary of some of the key results of the thesis.

8.2 Limitations and Recommendations

The work presented in this thesis pursued two main objectives: first, to demonstrate the potential of resonance to enhance power and efficiency, and second, to show that this behaviour could be achieved within a device whose size is comparable to that required for implantation in humans. Both objectives were successfully accomplished. The results confirmed that resonance can be harnessed to improve energetic performance, and that a compact, heart-scale prototype can be realized without compromising functionality. Nevertheless, several aspects warrant further investigation before this concept can transition from laboratory prototype to a fully functional biomedical system. The following sections outline the current limitations and propose future directions from three complementary perspectives: (i) the practical challenges and design opportunities related to potential biomedical and robotic applications, (ii) the constraints and improvements associated with the experimental setup, and (iii) the open questions concerning the fundamental physics underlying the coupled electro-hydro-mechanical dynamics of the system.

8.2.1 Application

From an application standpoint, several limitations remain before the concept demonstrated in this thesis can evolve into a clinically viable cardiac assist device.

Prototype performances While the pump successfully demonstrated the exploitation of resonance, the absolute values of pressure, flow rate, and efficiency differ substantially from those observed in the human heart. At resonance, the pump produced flow rate oscillations with an amplitude of approximately 0.6 L·min^{-1} around a mean value of 0.8 L·min^{-1}, and pressure oscillations of about 10 mmHg around a mean pressure of 3 mmHg. By comparison, the human heart generates an average cardiac output of approximately 5 L·min^{-1} with pulsations ranging from 0 to 10 L·min^{-1}, and aortic pressures varying between 80 and 110 mmHg (83)(84).

Moreover, the heart operates with an estimated efficiency of about 20% (202), whereas the pump developed in this work achieved an electric-to-hydraulic conversion efficiency between 0.1% and 0.4%. The pump also exhibited resonant behaviour in the frequency range of 12–16 Hz. Although these values are comparable to the resonant frequencies reported for myocardial tissue in the literature (140) (141), they remain well above the physiological beating frequency of the heart, typically between

1 and 3Hz (2).

These performance discrepancies underline the need for further optimisation of the pump design, a topic addressed in the following section.

Technological choices The actuation and variable stiffness mechanisms were primarily selected to facilitate prototyping and to demonstrate the feasibility of resonance-based pumping. However, the design choices made to simplify manufacturing and control inevitably limit performances and biocompatibility.

Future developments should explore alternative actuation strategies more suited to implantable applications. Among these, artificial muscles - such as dielectric elastomer actuators (203), shape-memory alloys (204), or pneumatic artificial muscles (205)(116) - offer promising routes to miniaturization and compliance. Artificial muscles wrapped around an elastic cavity could mimic the contraction of the myocardium while providing distributed actuation and smoother force transmission. Nonetheless, the main current limitations lie in the bulkiness of pressure-driven devices and the high voltages required to operate them (206). Further research in these areas is necessary to improve their long-term reliability and scalability for implantable applications.

Regarding variable stiffness, the current mechanism introduces a coupling between stiffness tuning and equilibrium position, as adjustments in stiffness also induce a shift in the operating point of the system. This behaviour, arising from geometric constraints and fluid loading, could be reduced through improved mechanical design. Future iterations of the mechanism could therefore aim to decouple stiffness variation from equilibrium displacement in order to achieve more controlled and independent tuning of system parameters. Similarly, the damping introduced by the VSM was observed to scale with stiffness. This behaviour is inherent to the current design and, while it could be mitigated through further optimisation, alternative design approaches may be required to maintain a more constant damping across stiffness configurations and thereby improve energy efficiency across actuation frequencies. In addition, integrating stiffness modulation directly into the external membrane could enable operation closer to the natural adaptability of the human heart. Approaches using magnetorheological fluids (207), electroactive polymers (208), or variable pre-strain mechanisms (209) could be investigated. The challenge lies in achieving a broad frequency tuning range while maintaining low energy consumption of the stiffness-control mechanism. A careful trade-off must be found between the achievable stiffness variation, the speed of adjustment, and the thermal or electromagnetic losses introduced by such systems.

From a biocompatibility perspective, the current prototype contains moving mechanical parts in the flow path, which are undesirable in long-term implantable devices due to the risk of thrombosis and hemolysis (183). In future designs, all moving components in contact with the fluid should be removed or encapsulated within compliant membranes. Although valves cannot be eliminated, they must be fabricated from biocompatible and hemocompatible materials (184), ideally reproducing the behaviour of human cardiac valves. Promising examples include polyurethane-based trileaflet valves, silicone heart valve prostheses (210), and polymer scaffolds produced via 3D bioprinting or soft lithography (211). Such designs, already investigated in the field of total artificial hearts, could be adapted to maintain physiological flow patterns and minimize shear stress on blood cells.

8.2.2 Experimental Setup

Improving the experimental setup is essential to validate the pump's performance more accurately and to emulate physiological conditions more closely.

First, the use of water as a working fluid simplifies testing but does not fully reproduce the rheological properties of blood. Replacing it with a water–glycerin mixture would allow the viscosity to match that of human blood (3–4 mPa·s at 37 °C) (212) (213). Blood also exhibits non-Newtonian behaviour, where viscosity decreases with shear rate (214). This characteristic could influence the system's dynamic response, particularly during rapid compression and expansion phases. Incorporating this effect would therefore yield more realistic measurements of hydraulic impedance and flow transitions.

Next, the current sensing setup provides useful trends but limits quantitative precision. Higher-grade pressure and flow sensors - especially those capable of measuring both before and after the valves - would enable more accurate efficiency assessments and detection of backflows. In particular, ultrasonic clamp-on flow sensors (215), widely used in cardiac assist research, offer non-invasive, high-frequency measurements. Embedding a pressure sensor inside the pumping chamber would further improve understanding of internal dynamics and allow comparison with physiological pressure ranges, as well as the timing of valve opening and closure.

Increasing the sampling frequency of all sensors to at least 1 kHz would improve the resolution of oscillatory signals at excitation frequencies up to 20 Hz, enhancing the accuracy of phase-lag estimation between pressure and flow rate. Phase lag proved to be a critical determinant of hydraulic power and efficiency, and insufficient

sampling may explain some of the unexpected phase shifts observed.

Additionally, sensor placement must be optimized to minimize measurement delays. Even small constant time offsets between pressure and flow signals can introduce artificial phase differences, linearly increasing with frequency and leading to misinterpretation of resonant peaks or efficiency values.

While the sensors currently used were adequate for identifying general trends, upgrading to laboratory-grade transducers would reduce uncertainty in absolute power and efficiency estimates. Furthermore, the dynamic behaviour of the valves deserves a dedicated experimental investigation. Valve inertia, hysteresis, and pressure-dependent opening thresholds could explain some of the non-linear effects and higher harmonics detected in the frequency spectra (216) (217).

The choice of actuation signal represents an additional area for improvement. In this study were limited to square wave inputs due to the constraints of the Pluto servo controller. While suitable for demonstrating the system's resonant behaviour, such signals inherently contain multiple harmonic components, which increases the complexity of the analysis and the interpretation of the system response. In contrast, sinusoidal excitation would provide a more direct assessment of the system dynamics by isolating a single frequency component. Furthermore, the use of different actuation waveforms is expected to influence the system's response, particularly in terms of harmonic content, energy transfer, and efficiency. Exploring alternative input signals therefore represents a relevant direction for future work.

Finally, connecting the pump to a mock circulatory loop capable of reproducing physiological compliance and resistance would be a decisive step toward application (218) (219). Such a setup would allow studying the influence of hydrostatic pressure and fluidic loading - shown in this thesis to affect the equivalent stiffness - under realistic operating conditions. It would also help validate the control strategies required for safe and efficient integration into the human cardiovascular system.

8.2.3 Fundamental Physics

Beyond technological and experimental aspects, further progress requires a deeper understanding of the fundamental physics governing the coupled electro-hydro-mechanical dynamics of the pump.

Analytical modeling remains a cornerstone for future optimization. The approach developed in this thesis can be extended to derive a complete equivalent-mass formulation, as presented conceptually in Appendix J. This equivalent mass depends

strongly on the geometry of the transmission mechanism - specifically the lever arm lengths and their angular configuration relative to the pump's axis. Additionally, the shape of pump plays a key role in efficient pumping and requires dedicated studies. Such modeling would facilitate scaling analyses and guide design modifications without extensive experimental trials.

In parallel, damping models should be defined. While experimental results allowed to highlight an increase in damping with fluidic loading, clear scaling could not be established. The overall damping combines viscous, frictional, and hysteretic components, each with distinct frequency dependencies (220). The Bouc–Wen model, widely used to capture non-linear and hysteretic damping in structural systems (221), could provide an analytical framework to describe these effects and to predict how damping influences resonance sharpness and efficiency.

Moreover, extending the model to include fluid compliance and wave propagation effects could bridge the gap between the simplified mass–spring–damper model and the actual cardiovascular environment. The Windkessel model (39), commonly used in haemodynamics, represents the compliance and resistance of blood vessels and could be integrated into the system's equations of motion. Such coupling would improve the accuracy of predicted pressure-flow relationships and assist in designing feedback control laws for physiological load adaptation. In particular, the phase relationship between pressure and flow rate, remains only partially understood in the present work. The experimental results indicate the presence of phase dispersion and harmonic distortion, suggesting that the fluidic circuit behaves as a distributed system in which wave propagation and reflections play a significant role. In haemodynamics and pulsatile flow analysis, such effects are commonly investigated using frequency-domain approaches, where transfer functions and hydraulic impedance are used to characterise both amplitude and phase relationships between pressure and flow (82) (222). In addition, wave separation techniques, such as wave intensity analysis (199), allow signals to be decomposed into forward and backward travelling components, enabling the identification and quantification of wave reflections. These reflections typically arise from impedance mismatches introduced by valves, geometric discontinuities, and compliance variations, and are known to modify pressure and flow differently, leading to phase shifts between the two signals (200)(197). A more comprehensive modeling framework accounting for these effects would therefore be required to accurately capture the observed dynamics.

Achieving resonance at lower frequencies - closer to the 1–3 Hz range of the human heartbeat - remains a major theoretical challenge. Two approaches can be

pursued: reducing equivalent stiffness or increasing equivalent mass (20). Lowering stiffness alone requires a proportional decrease in damping to avoid overdamping, which would suppress resonance. Conversely, increasing equivalent mass lowers both the natural frequency and damping ratio but introduces mechanical constraints and potential increases in system size and weight. Realistically, a combination of these strategies is necessary. Adjusting the transmission geometry to maximize the mechanical advantage or designing configurations that exploit fluid added mass (223) (224) could increase the effective inertia without physically adding mass to the implant. This challenge of achieving low-frequency resonance underscores the importance of developing research prototypes at the application scale, enabling potential design limitations and trade-offs to be identified early in the development process.

In summary, further analytical and experimental investigations into damping mechanisms, equivalent mass, and compliant boundary effects will be key to advancing the fundamental understanding of resonance in pulsatile pumping systems and to guiding the development of miniaturized, efficient cardiac assist devices.

8.3 Final thoughts

For more than half a century, engineers and clinicians have pursued the vision of an artificial heart that can seamlessly replicate the function of the native organ - compact, pulsatile, adaptive, biocompatible and efficient (98). Despite extraordinary advances in materials science, electronics, and control systems, no single design has yet achieved the combination of efficiency, durability, and physiological integration required for a truly optimal cardiac assist device. The repeated efforts of major industrial and academic programs illustrate both the technical complexity and the economic challenges of this pursuit. A striking example is Carmat, whose fully implantable artificial heart represents over three decades of research and development, yet whose recent financial difficulties highlight the fragile boundary between technological innovation and market viability (111).

This persistent gap between scientific progress and clinical or commercial adoption reflects the inherent difficulty of reproducing the heart's multi-physics behaviour - its structural compliance, adaptive control, and energy efficiency - within an engineered system. Achieving pulsatile flow alone is not sufficient: the device must also adapt dynamically to patient-specific physiological variations while remaining safe, reliable, and affordable. The work presented in this thesis contributes to addressing one aspect of this problem by demonstrating how resonance and adaptive stiffness can

be leveraged to improve efficiency, but broader solutions will require a convergence of multiple fields.

Among emerging technologies, biofabrication and bioprinting hold particular promise (225)(226)(227). The ability to print soft, vascularised, and contractile tissues could one day bridge the gap between mechanical design and biological function, enabling hybrid or fully biological assist devices that integrate naturally with the patient's cardiovascular system. While such prospects remain long-term, they signal a paradigm shift—from imitating the heart mechanically to reconstructing it biologically. The continued collaboration between engineers, material scientists, and biologists will therefore be crucial to transform decades of incremental progress into clinically viable, energy-efficient, and truly physiological cardiac assist solutions.

Chapter 9

Publications, Awards, Grants

9.1 Publications

- **Baisamy, P.**, Stokes, A.A., & Serchi, F.G. (2024). "A scalable monolithic 3D printable variable stiffness mechanism". *2024 IEEE International Conference on Robotics and Automation (ICRA)*, 169-175.
- **Baisamy, P.**, Stokes, A.A., & Serchi, F.G. (2025), "Harnessing resonance in pulsatile flow for the design of efficient heart-inspired pumps", *Transaction on Mechatronics*, Under review.

9.2 Awards

- **1st prize**: Baisamy, P. (2024, February 28). "Potential and applications of a new variable stiffness mechanism: the C-MAC" [Poster presentation]. CDT RAS Conference 2024, Edinburgh, UK.
- **1st prize**: Baisamy, P. (2022, November 23). "Large-bandwidth peak efficiency of bioinspired variable stiffness hydraulic actuators" [Quickfire talk]. CDT RAS Conference 2022, Edinburgh, UK.
- **1st prize**: Baisamy, P. (2021, October 01). "Variable stiffness actuator (VSA) for efficient bio-inspired pulsed-jet propulsion" [Poster presentation]. CDT RAS Conference 2021, Edinburgh, UK.

9.3 Grants

- Recipient of the **Innovation Fund of the Centre for Doctoral Training in Robotics and Autonomous Systems**. Awarded **13000£** for the development of a disruptive low energy consumption and pulsatile cardiac assist device.

Awarded on a competitive basis with shortlisted applicants invited to present their idea to a panel of researchers and business advisers (2022, May 12).

Chapter 10

Experimental setup: details

Components	Reference	Supplier
Calorimetric flow sensor	FS1025-DL	RS components
Gauge pressure sensor	MPRLS0300YG00001BB	DigiKey
Actuator controller	Pluto Servo Drive	BEI Kimco
Fluid data collection	Arduino Mega 2560.0	Arduino
SD card	SanDisk Extreme 64GB A2	SanDisk
SD card reader	HW-125	Amazon
H-Bridge	SN754410NE	DigiKey

Table 10.1: List of the key electronic components.

Components	Reference	Supplier
Anti-vibration platform	B4545A	Thorlabs
Tubing	RS 797 366 118913	RS components

Table 10.2: List of the key components used for the experimental setup.

Software	Version	Supplier
Arduino IDE	2.3.2	Arduino
Processing	/	Processing
Motion Lab	2.13.2.691	BEI Kimco

Table 10.3: List of the softwares used to collect data.

Chapter 11

Prototype: technical details

Parts and products	Reference	Supplier
VSM motor	GM15BY-VSM1527-100-10D	Amazon
Voice coil actuator	LAS16-23-000A-P01-4E	BEI Kimco
Ball bearings	DDL-310HA1P25LO1	NMB
Spring	PCC031-250-406-13000-MW-1380-CG-N-IN	The Spring Store
Silicone rubber	DragonSkin 10	Smooth-on Inc
Mold release	Universal Mold Release	Smooth On
Glue	Super Glue Precision	Loctite
3D printer	Bambu Lab P1S	Bambu Lab
Filament	PET-CF	Bambu Lab
3D printer	Formlabs 3+	Formlabs
Resin	Clear V4	Formlabs
Resin	White V4	Formlabs

Table 11.1: List of parts and products used for the fabrication of the resonant pulsatile pump prototype.

Chapter 12

Spring specifications

Chapter 13

Voice coil actuator specifications

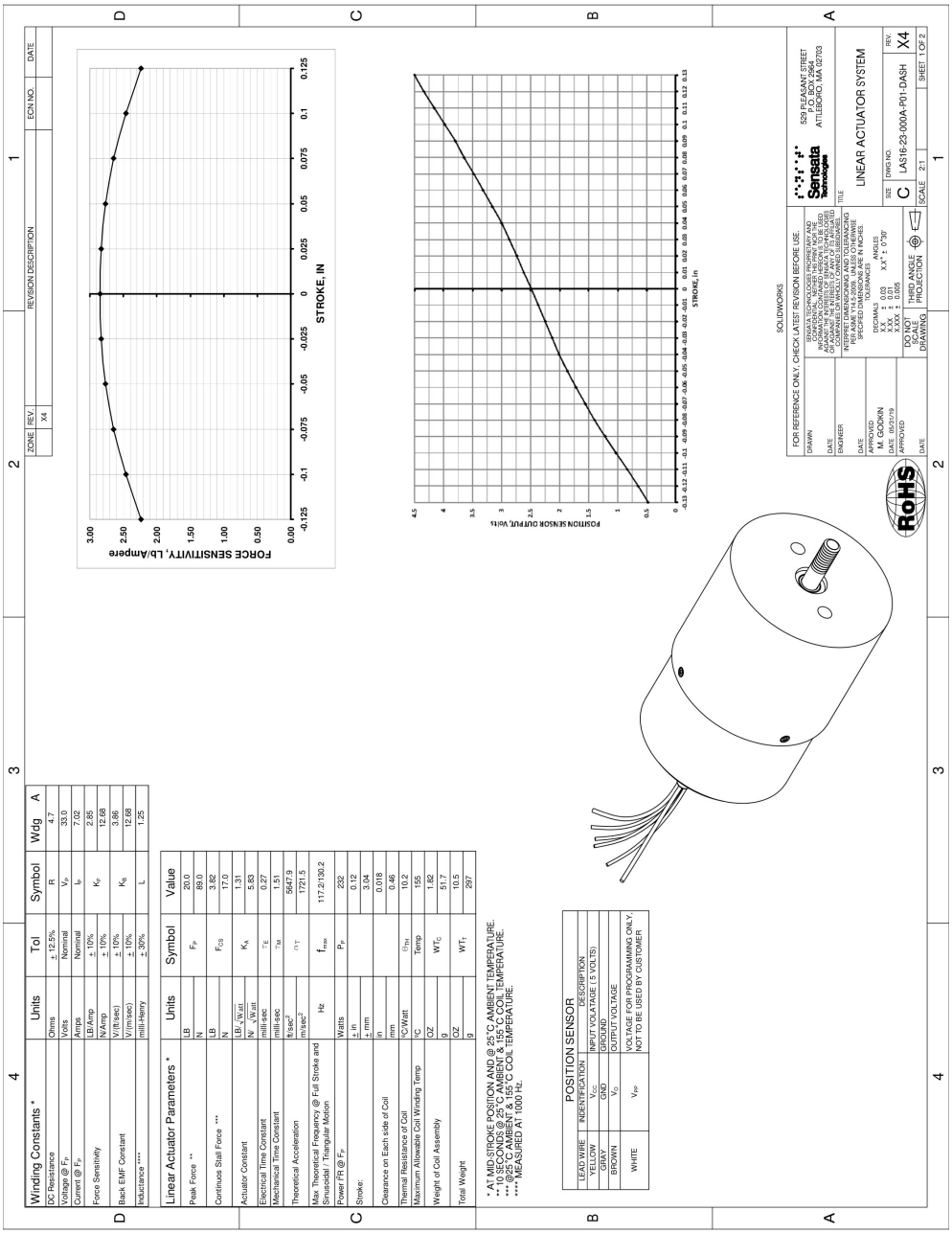

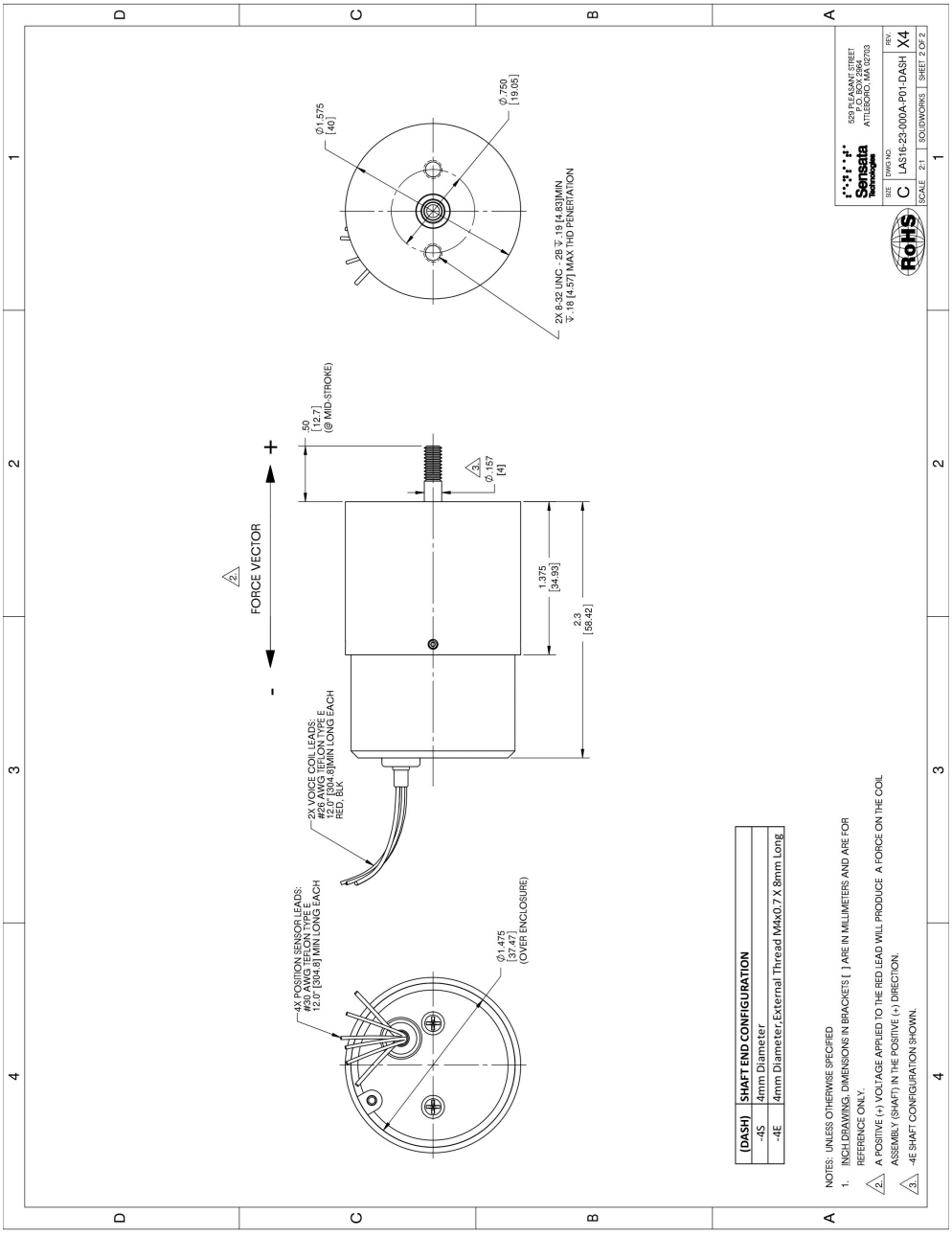
Ø1.575
[40]
Ø.750
[19.05]
2X 8-32 UNC - 2B ↧ .19 [4.83] MIN.
↧ .18 [4.57] MAX THD PENERTATION
50
[12.7]
(@ MID-STROKE)
3
Ø.157
[4]
2
FORCE VECTOR
+
-
1.375
[34.93]
2.3
[58.42]
2X VOICE COIL LEADS:
#26 AWG TEFLON TYPE E
12" [304.8] MIN LONG EACH
RED, BLK
4X POSITION SENSOR LEADS:
#28 AWG TEFLON TYPE E
12.0" [304.8] MIN LONG EACH
Ø1.475
[37.47]
(OVER ENCLOSURE)
(DASH) SHAFT END CONFIGURATION
-4S 4mm Diameter
-4E 4mm Diameter;External Thread M4x0.7 X 8mm Long
NOTES: UNLESS OTHERWISE SPECIFIED
1. INCH DRAWING. DIMENSIONS IN BRACKETS [ ] ARE IN MILLIMETERS AND ARE FOR REFERENCE ONLY.
2. A POSITIVE (+) VOLTAGE APPLIED TO THE RED LEAD WILL PRODUCE A FORCE ON THE COIL ASSEMBLY (SHAFT) IN THE POSITIVE (+) DIRECTION.
3. -4E SHAFT CONFIGURATION SHOWN.
RoHS
Sensata Technologies
529 PLEASANT STREET
P.O. BOX 2964
ATTLEBORO, MA 02703
SIZE C
DWG NO. LAS16-23-000A-P01-DASH
REV. X4
SCALE 2:1
SOLIDWORKS
SHEET 2 OF 2

Chapter 14

Variable stiffness unit motor

5. 产品照片 (The product photos)

6. 产品外形图 (Product drawings)

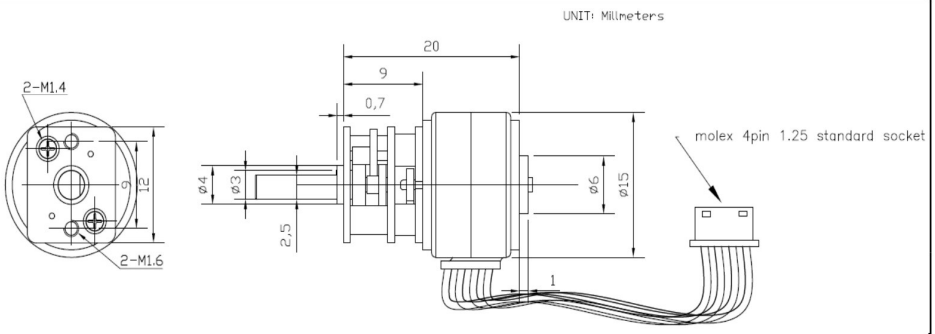

7. 接线图 (Wiring diagram)

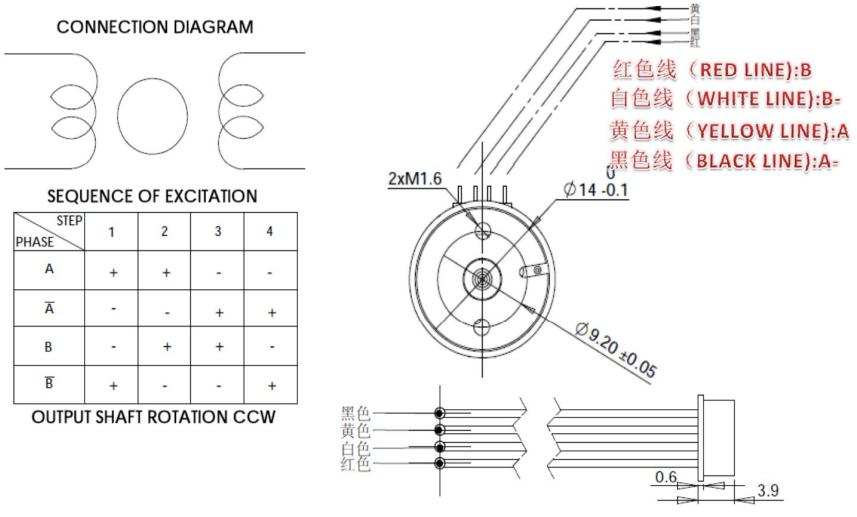

微型直流电机仕样规格书

产品型号：GM15BY-VSM1527-100-10D			
1. 标准使用条件 (Standard Operating Conditions)			
NO.	項 目(Item)	規 格(Specification)	检验方法 (Test Method)
1.1	額定电压 (Rated Voltage)	DC 12.0V	电压表 (Multimeter)
1.2	速比 (Gear Ratio)	1/100	
1.3	马达转向 (Rotation)	CW&CCW	手感 (Handle)
1.4	姿 势(Motor Position)	检查时水平 (All position in horizontal)	手感 (Handle)
1.5	检测时时温度范围 Temperature	0 Degree - 30 Degree Celsius	温度计 (Thermometer)
1.6	检测时时湿度范围 Humidity	30% ~ 95%	湿度计 (Hygroscope)
2. 电机性能 (Performance Of Motors)			
NO.	项 目(Item)	规 格(Specification)	检验方法 (Test Method)
2.1	线圈电阻 (Coil resistance)	30Ω±10%	电阻测试表 (Resistance testing instrument)
2.2	相数 (NO. Of Phases)	2 PHASES	
2.3	步进角 (Step Angle)	18° / Step	角度仪 (Angle gauge)
2.4	最大起动响应频率 (MAX.Starting Frequency)	900PPS min	步进测试仪 (Step motor test instrument)
2.5	最大连续响应频率 (MAX.Slewing Frequency)	1200 PPS min	步进测试仪 (Step motor test instrument)
2.6	引入力矩 (Pull IN Torque)	6gf-cm min	步进测试仪 (Step motor test instrument)
2.7	脱出力矩 (Lead Out torque)	10gf-cm min	步进测试仪 (Step motor test instrument)
2.8	绝缘阻抗耐压 (Insulation impedance voltage)	50MΩ DC100V/300VAC	绝缘耐压测试仪 Dielectric withstanding voltage tester
3. 整机性能 (Performance of Gear motors)			
NO.	项 目(Item)	规 格(Specification)	检验方法 (Test Method)
3.1	步进角 (Step Angle)	18/100° / Step	角度仪 (Angle gauge)
3.2	最大起动响应频率 (MAX.Starting Frequency)	900PPS min	步进测试仪 (Step motor test instrument)
3.3	最大连续响应频率 (MAX.Slewing Frequency)	1200 PPS min	步进测试仪 (Step motor test instrument)
3.4	引入力矩 (Pull IN Torque)	0.5 Kgf-cm min	步进测试仪 (Step motor test instrument)
3.5	脱出力矩 (Lead Out torque)	0.8 kgf-cm Max	步进测试仪 (Step motor test instrument)
4. 基本尺寸 (The Dimension)			
NO.	项 目(Item)	规 格 (Specification)	检验方法 (Test Method)
4.1	轴伸尺寸 (The Outside Shaft Length)	10mm	卡尺 (Vernier Calipers)
4.2	轴向间隙 (Shaft End Play)	0.05-0.30mm	治具 (Frock)
4.3	螺孔 (Screw Size)	M1.6*0.35	治具 (Frock)
4.4	出轴直径 (Dia.of shaft)	Φ3*D2.5mm	卡尺 (Vernier Calipers)
4.5	外形安装尺寸 (Outline Mounting Dimension)	Refer to the Outline Drawing	治具和卡尺 Calipe

Chapter 15

Average of the cross frequencies product D_C

This appendix demonstrates how the cross frequency terms of a product of two Fourier series cancel out (see Chapter 5, Section 5.3.2). The cross frequency terms D_C are defined in Eq. 15.1 where $i \neq j$.

$$D_C = \sum_i \sum_j H_i G_j \sin(i\omega_1 t - \psi_i) \sin(j\omega_1 t - \chi_j) \tag{15.1}$$

Using the trigonometric product-to-sum identity, Eq. 15.1 is written in an alternative form presented in Eq. 15.2, with the terms A and B expressed in Eq. 15.3 and Eq. 15.4.

$$D_C = \frac{1}{2} \sum_i \sum_j H_i G_j (A - B) \tag{15.2}$$

$$A = \cos((i-j)\omega_1 t - \psi_i + \chi_j) \tag{15.3}$$

$$B = \cos((i+j)\omega_1 t - \psi_i - \chi_j) \tag{15.4}$$

Since $i \neq j$, $(i-j)$ is never equal to zero. Consequently, the term A, never reduces to a constant and always expresses a zero-mean periodic function. Similarly, the term B is a zero-mean periodic function for any values of i and j. By definition, the time integral, i.e the average, of such a function is zero which proves that when integrated, the cross frequency terms D_C cancel out.

Chapter 16

Mechanical power peaks at resonance

This appendix aims at finding the frequency at which the mechanical and, hence the electric power peaks. The mechanical power is dependent on ωM with ω the excitation frequency and M the amplitude ratio. The excitation frequency can be expressed as $\omega = \omega^* r$ with ω^* the natural frequency and r the ratio of the excitation frequency to the natural frequency. As a consequence, ωM can be expressed as shown in Eq. 16.1.

$$\omega M = \frac{\omega^* r}{\sqrt{(1-r^2)^2 + (2\zeta r)^2}}, \qquad r > 0,\ \zeta \geq 0,\ \omega_n > 0. \tag{16.1}$$

Since $\omega^* > 0$ is a constant, maximizing ωM is equivalent to maximizing Eq. 16.2.

$$G(r) = \frac{r^2}{(1-r^2)^2 + 4\zeta^2 r^2} = \frac{r^2}{H(r)}, \quad H(r) = (1-r^2)^2 + 4\zeta^2 r^2. \tag{16.2}$$

For $r > 0$, the derivative of $G(r)$ with respect to r is shown in Eq. 16.3.

$$\frac{dG(r)}{dr} = \frac{2rH(r) - r^2 \frac{dH(r)}{dr}}{H(r)^2}, \tag{16.3}$$

Consequently, the critical points of $G(r)$ satisfy Eq. 16.4.

$$2H(r) = r\frac{dH(r)}{dr} \tag{16.4}$$

Equation 16.5 presents the derivative of $H(r)$ with respect to r.

$$\frac{dH(r)}{dr} = 2(1-r^2)(-2r) + 8\zeta^2 r = 4r(r^2 + 2\zeta^2 - 1) \tag{16.5}$$

Combining Eq. 16.4 with Eq. 16.5 results in Eq. 16.6 which once solved leads to

Eq. 16.7.

$$2((1-r^2)^2+4\zeta^2r^2) = r4r(r^2+2\zeta^2-1). \tag{16.6}$$

$$\boxed{r=1} \Longrightarrow \boxed{\omega=\omega^*} \tag{16.7}$$

The study of the limits show that for $r=1$, $G(r)$ reaches a global maximum as shown in Eq. 16.8.

$$\lim_{r\to 0^+} G(r) = 0, \qquad \lim_{r\to\infty} G(r) = 0, \tag{16.8}$$

This proves that $G(r)$ and consequently ωM, the electric and mechanical power peak at resonance.

Chapter 17

Cycle synchronous average

17.1 Principle

Cycle Synchronous Averaging (CSA) is a signal processing technique used to extract the repeatable, cycle-locked component of a signal from noisy measurements. It is well suited to systems that operate periodically (e.g., rotating machinery, reciprocating pumps, or oscillatory actuators), where each cycle is expected to follow a similar waveform. The central assumption is that the signal of interest is phase-locked to a known periodic event (a trigger), whereas additive noise and non-synchronous disturbances vary randomly from cycle to cycle. By aligning and averaging successive cycles, the random components are attenuated and the synchronous component is enhanced.

Let $s_i(t)$ denote the i-th recorded cycle of a periodic signal with period T, after segmentation and time normalization (see below). The cycle-synchronous average $\bar{s}(t)$ is

$$\bar{s}(t) \;=\; \frac{1}{N}\sum_{i=1}^{N} s_i(t), \tag{17.1}$$

where N is the number of cycles averaged.

17.2 Implementation

1. **Cycle identification.** Use a reference signal (e.g., actuation command, encoder index, or external trigger) to detect the start of each cycle.

2. **Segmentation.** Partition the time series into individual cycles of duration T based on the detected trigger indices.

3. **Time normalization.** Resample (interpolate) each cycle to the same number of samples so that all cycles share a common phase axis, even if small period

variations occur. This produces segments $s_i(t)$ on a normalized domain $t \in [0, T]$ or on a dimensionless phase axis $\theta \in [0, 100]\%$.

4. **Averaging.** Compute the pointwise mean across cycles as in Eq. (17.1).

Chapter 18

Equivalent mass model

To determine the equivalent mass of the pump, an analytic model can be derived. To do so, the sum of the kinetic energy of the actuator's plunger,T_p, with the kinetic energy of the weights placed on the ribs, T_r, is assumed to be equal to the kinetic energy of the equivalent mass, T_{eq} (Eq 18.1).

$$T_{eq} = T_p + 4T_r \tag{18.1}$$

The kinetic energies T_p, T_r and T_{eq} are respectively calculated with Eq.18.2, Eq.18.3, Eq.18.4 where m_P is the mass of the plunger, x_A is the position of point A and $\dot{x}_A$ its speed, J_o is the moment of inertia of the weights on one rib around point O, γ is the angle between the horizontal and the segment OB and m_{eq} is the equivalent mass.

$$T_p = \frac{1}{2} m_P \dot{x}_A^2 \tag{18.2}$$

$$T_r = \frac{1}{2} J_o \dot{\gamma}^2 \tag{18.3}$$

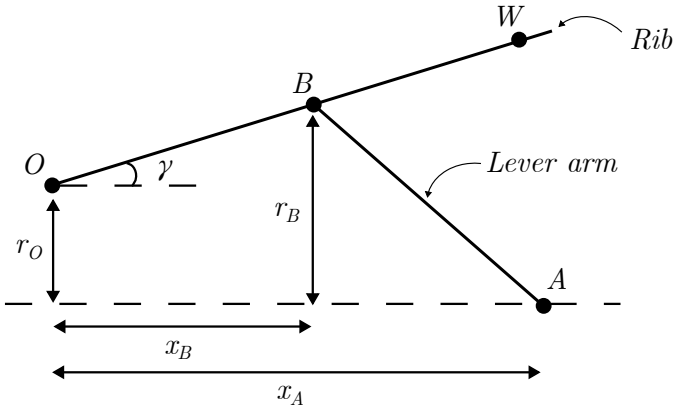

Figure 18.1: Lengths and variables used for the equivalent mass model.

$$T_{eq} = \frac{1}{2} m_{eq} \dot{x}_A^2 \tag{18.4}$$

The moment of inertia J_O is defined as $m|OW|^2$, with m the weight placed on each rib and and $|OW|$ the distance between the points O and A. The angular speed $\dot{\gamma}$ is expressed as the product of the derivative of γ with respect to x_A with the linear speed $\dot{x}_A$, Eq.18.5.

$$\frac{d\gamma}{dt} = \frac{d\gamma}{dx_A}\frac{dx_A}{dt} \quad \Leftrightarrow \quad \dot{\gamma} = \frac{d\gamma}{dx_A}\dot{x}_A \tag{18.5}$$

Combining Eq.18.1, 18.2,18.3, 18.4 and Eq.18.5, we obtain Eq. 18.6.

$$m_{eq}\dot{x}_A^2 = m_P \dot{x}_A^2 + 4m|OW|^2 (\frac{d\gamma}{dx_A}\dot{x}_A)^2 \tag{18.6}$$

The derivative $\frac{d\gamma}{dx_A}$ is obtained by looking at the pump's kinematics which allows to write the system of equations 18.7.

$$\begin{cases} x_A - x_B = \sqrt{|AB|^2 - r_B^2} \\ x_B = |OB|\cos\gamma \\ r_B = |OB|\sin\gamma + r_O \end{cases} \tag{18.7}$$

We also define the following quantities for clarity purposes:

$$e = \frac{r_O}{|OB|} \tag{18.8}$$

$$\lambda = \frac{|AB|}{|OB|} \tag{18.9}$$

Combining the equations of system 18.7 with Eq.18.8 and Eq.18.9, we obtain Eq.18.10.

$$x_A = |OB|(\sqrt{\lambda^2 - (\sin\gamma - e)^2} + \cos\gamma) \tag{18.10}$$

Eq.18.10 allows us to express $\frac{dx_A}{d\gamma}$ with Eq.18.11.

$$\frac{dx_A}{d\gamma} = |OB|(-\sin\gamma - \frac{\cos\gamma(\sin\gamma + e)}{\sqrt{\lambda^2 - (\sin\gamma + e)^2}} \tag{18.11}$$

Finally, Eq.18.6 with Eq.18.11 gives Eq.18.12, the final expression of the pump's equivalent mass m_{eq}.

$$\boxed{m_{eq} = m_P + 4m\left(\frac{|OW|}{|OB|}\frac{1}{\sin\gamma + \frac{\cos\gamma(\sin\gamma+e)}{\sqrt{\lambda^2-(\sin\gamma+e)^2}}}\right)^2} \tag{18.12}$$

Bibliography

[1] R. L. Drake, W. Vogl, and A. W. M. Mitchell, *Gray's anatomy for students*. Anatomy for students, Philadelphia, PA: Elsevier, fifth edition. ed., 2024. Includes bibliographical references and index.

[2] J. E. Hall and M. E. Hall, *Guyton and Hall textbook of medical physiology*. Textbook of medical physiology, Philadelphia, PA: Elsevier, fourteenth edition. ed., 2021. Includes bibliographical references.

[3] J. E. Hall and M. E. Hall, *Guyton and Hall textbook of medical physiology*. Textbook of medical physiology, Philadelphia, PA: Elsevier, fourteenth edition. ed., 2021. Includes bibliographical references. (John Edward) (Michael E.).

[4] Abbott, "Heartmat 3 lvad."

[5] Corwave, "Corwave lvas," 2025.

[6] Carmat, "Carmat heart," 2025.

[7] V. Gaillard, *NBIC Convergence in the Healthcare Market: How NBIC technologies are expected to be welcomed and spread across the healthcare industry?* Thesis, 2021.

[8] M. Arfaee, L. C. van Laake, S. Zou, C. Bording, J. Kluin, and J. T. B. Overvelde, "Toward developing a compact total artificial heart using a soft robotic fluidic transmission system," *Science advances*, vol. 11, no. 27, p. eadv4854, 2025.

[9] M. Arfaee, A. Vis, P. A. A. Bartels, L. C. van Laake, L. Lorenzon, D. M. Ibrahim, D. Zrinscak, A. I. P. M. Smits, A. Henseler, M. Cianchetti, P. Y. W. Dankers, C. V. C. Bouten, J. T. B. Overvelde, and J. Kluin, "A soft robotic total artificial hybrid heart," *Nature communications*, vol. 16, no. 1, pp. 5146–14, 2025.

[10] C. J. Payne, I. Wamala, C. Abah, T. Thalhofer, M. Saeed, D. Bautista-Salinas, M. A. Horvath, N. V. Vasilyev, E. T. Roche, F. A. Pigula, and C. J. Walsh, "An implantable extracardiac soft robotic device for the failing heart: Mechanical coupling and synchronization," *Soft robotics*, vol. 4, no. 3, pp. 241–250, 2017.

[11] M. Y. Saeed, D. Van Story, C. J. Payne, I. Wamala, B. Shin, D. Bautista-Salinas, D. Zurakowski, P. J. del Nido, C. J. Walsh, and N. V. Vasilyev, "Dynamic

augmentation of left ventricle and mitral valve function with an implantable soft robotic device," *JACC: Basic to Translational Science*, vol. 5, no. 3, pp. 229–242, 2020.

[12] E. T. Roche, M. A. Horvath, I. Wamala, A. Alazmani, S.-E. Song, W. Whyte, Z. Machaidze, C. J. Payne, J. C. Weaver, G. Fishbein, J. Kuebler, N. V. Vasilyev, D. J. Mooney, F. A. Pigula, and C. J. Walsh, "Soft robotic sleeve supports heart function," *Science translational medicine*, vol. 9, no. 373, 2017.

[13] D. Zrinscak, C. M. De Chirico, L. Lorenzon, F. Coluccia, M. De Luca, M. Maselli, J. Kluin, J. T. B. Overvelde, and M. Cianchetti, "Design of a soft robotic artificial cardiac wall," *Artificial Organs*, vol. 49, no. 8, pp. 1265–1276, 2025.

[14] A. Jafari, N. G. Tsagarakis, and D. G. Caldwell, "Exploiting natural dynamics for energy minimization using an actuator with adjustable stiffness (awas)," in *2011 IEEE International Conference on Robotics and Automation*, pp. 4632–4637.

[15] S. B. Behbahani and X. Tan, "Design and dynamic modeling of electrorheological fluid-based variable-stiffness fin for robotic fish," *Smart materials and structures*, vol. 26, no. 8, pp. 85014–, 2017.

[16] K. W. Hollander, T. G. Sugar, and D. E. Herring, "Adjustable robotic tendon using a 'jack spring'," 2005.

[17] B. Vanderborght, A. Albu-Schaeffer, A. Bicchi, E. Burdet, D. G. Caldwell, R. Carloni, M. Catalano, O. Eiberger, W. Friedl, G. Ganesh, M. Garabini, M. Grebenstein, G. Grioli, S. Haddadin, H. Hoppner, A. Jafari, M. Laffranchi, D. Lefeber, F. Petit, S. Stramigioli, N. Tsagarakis, M. Van Damme, R. Van Ham, L. C. Visser, and S. Wolf, "Variable impedance actuators: A review," *Robotics and Autonomous Systems*, vol. 61, no. 12, pp. 1601–1614, 2013.

[18] K. C. Galloway, J. E. Clark, M. Yim, and D. E. Koditschek, "Experimental investigations into the role of passive variable compliant legs for dynamic robotic locomotion," pp. 1243–1249, IEEE.

[19] Q. Zhong, J. Zhu, F. E. Fish, S. J. Kerr, A. M. Downs, H. Bart-Smith, and D. B. Quinn, "Tunable stiffness enables fast and efficient swimming in fish-like robots," *Science robotics*, vol. 6, no. 57, 2021.

[20] S. S. Rao, *Mechanical vibrations*. Pearson Education, 2017.

[21] J. Lu, X. Yao, H. Zheng, X. Yan, H. Liu, and T. Wu, "Analysis of unsteady internal flow and its induced structural response in a circulating water pump," *Water*, vol. 16, p. 1294, 2024.

[22] C. Wang, T. Zhao, W. Cheng, Z. Ni, and N. Xiang, "Microfluidic strategies in soft robotics: Actuators, control systems, and pumps," *Device*, vol. 2, no. 9, p. 100551, 2024.

[23] B. Gamus, L. Salem, E. Ben-Haim, A. Gat, and Y. Or, "Interaction between inertia, viscosity, and elasticity in soft robotic actuator with fluidic network," *IEEE Transactions on Robotics*, vol. PP, pp. 1–10, 2017.

[24] J. E. Richter and D. O. Castell, *The esophagus*. Hoboken, NJ: Wiley-Blackwell, sixth edition. ed., 2020.

[25] H.-m. Cheng, K. K. Mah, and K. Seluakumaran, *Defining physiology. Volume 2, Neurophysiology and gastrointestinal systems : principles, themes, concepts*. Cham, Switzerland: Springer, 1st 2020. ed., 2020.

[26] M. G. Levitzky, *Pulmonary Physiology*. McGraw-Hill's AccessMedicine, New York, N.Y: McGraw-Hill Education LLC., tenth edition ed., 2022. Includes bibliographical references and indexes.

[27] C. R. Chapple, W. D. Steers, and C. P. Evans, *Urologic Principles and Practice*. Springer Specialist Surgery Series, Cham: Springer International Publishing, 2nd 2020. ed., 2020.

[28] G. Lippi and F. Sanchis-Gomar, "Global epidemiology and future trends of heart failure," *AME Medical Journal*, vol. 5, 2020.

[29] M. Urbich, G. Globe, K. Pantiri, M. Heisen, C. Bennison, H. S. Wirtz, and G. L. Di Tanna, "A systematic review of medical costs associated with heart failure in the usa (2014–2020)," *PharmacoEconomics*, vol. 38, no. 11, pp. 1219–1236, 2020.

[30] T. H. F. P. Network, "The handbook of multidisciplinary and integrated heart failure care," 2018.

[31] M. R. Cowie, S. D. Anker, J. G. F. Cleland, G. M. Felker, G. Filippatos, T. Jaarsma, P. Jourdain, E. Knight, B. Massie, P. Ponikowski, and J. López-Sendón, "Improving care for patients with acute heart failure: before, during and after hospitalization," *ESC Heart Failure*, vol. 1, no. 2, pp. 110–145, 2014.

[32] R. Magari and W. Hijikata, "Development of a novel axial blood pump with a thrust force levitation technology-device design and levitation experiments," *IEEE/ASME transactions on mechatronics*, vol. 29, no. 1, pp. 499–509, 2024.

[33] Y. Okada, N. Yamashiro, K. Ohmori, T. Masuzawa, T. Yamane, Y. Konishi, and S. Ueno, "Mixed flow artificial heart pump with axial self-bearing motor," *IEEE/ASME transactions on mechatronics*, vol. 10, no. 6, pp. 658–665, 2005.

[34] R. C. Starling, N. Moazami, S. C. Silvestry, G. Ewald, J. G. Rogers, C. A. Milano, J. E. Rame, M. A. Acker, E. H. Blackstone, J. Ehrlinger, L. Thuita, M. M. Mountis, E. G. Soltesz, B. W. Lytle, and N. G. Smedira, "Unexpected abrupt increase in left ventricular assist device thrombosis," *New England Journal of Medicine*, vol. 370, no. 1, pp. 33–40, 2013.

[35] V. Gambillara, T. Thacher, P. Silacci, and N. Stergiopulos, "Effects of reduced cyclic stretch on vascular smooth muscle cell function of pig carotids perfused ex vivo," *American Journal of Hypertension*, vol. 21, no. 4, pp. 425–431, 2008.

[36] T. Thacher, V. Gambillara, R. F. da Silva, P. Silacci, and N. Stergiopulos, "Reduced cyclic stretch, endothelial dysfunction, and oxidative stress: an ex vivo model," *Cardiovascular Pathology*, vol. 19, no. 4, pp. e91–e98, 2010.

[37] Z. T. M. D. Demirozu, R. M. D. Radovancevic, L. F. M. D. Hochman, I. D. M. D. Gregoric, G. V. M. D. Letsou, B. M. D. Kar, R. C. M. D. Bogaev, and O. H. M. Frazier, "Arteriovenous malformation and gastrointestinal bleeding in patients with the heartmate ii left ventricular assist device," *The Journal of heart and lung transplantation*, vol. 30, no. 8, pp. 849–853, 2011.

[38] A. C. Patel, R. B. Dodson, W. K. Cornwell, K. S. Hunter, J. C. Cleveland, A. Brieke, J. Lindenfeld, and A. V. Ambardekar, "Dynamic changes in aortic vascular stiffness in patients bridged to transplant with continuous-flow left ventricular assist devices," *JACC: Heart Failure*, vol. 5, no. 6, pp. 449–459, 2017.

[39] N. Westerhof, J.-W. Lankhaar, and B. E. Westerhof, "The arterial windkessel," *Medical and Biological Engineering and Computing*, vol. 47, no. 2, pp. 131–141, 2009.

[40] B. J. Gemmell, J. H. Costello, S. P. Colin, C. J. Stewart, J. O. Dabiri, D. Tafti, and S. Priya, "Passive energy recapture in jellyfish contributes to propulsive

advantage over other metazoans," *Proceedings of the National Academy of Sciences*, vol. 110, no. 44, p. 17904, 2013.

[41] B. K. Ahlborn, R. W. Blake, and W. M. Megill, "Frequency tuning in animal locomotion," *Zoology*, vol. 109, no. 1, pp. 43–53, 2006.

[42] E. A. O. P. Manufacturers, "Guide to the selection of rotodynamic pumps," report, European Association Of Pump Manufacturers, 2016.

[43] I. A. Sultan and T. H. Phung, *Positive displacement machines : modern design innovations and tools*. London: Academic Press, first edition. ed., 2019. Includes bibliographical references and index.

[44] K. M. Srinivasan and ProQuest, *Rotodynamic pumps : centrifugal and axial*. London, UK: New Academic Science, second edition. ed., 2017. Includes bibliographical references and index. (Firm).

[45] R. K. Turton, *Principles of axial and mixed flow pumps*. United Kingdom: Cambridge University Press, 2009.

[46] C. American Institute of Chemical Engineers. Equipment Testing Procedures, *Positive displacement pumps : a guide to performance evaluation*. AIChE equipment testing procedure, Hoboken, NJ: John Wiley and Sons, 1st edition ed., 2007. Includes bibliographical references (page 73) and index.

[47] X. Li, Z. Zhu, Y. Li, and X. Chen, "Experimental and numerical investigations of head-flow curve instability of a single-stage centrifugal pump with volute casing," *Proceedings of the Institution of Mechanical Engineers, Part A: Journal of Power and Energy*, vol. 230, no. 7, pp. 633–647, 2016. doi: 10.1177/0957650916663326.

[48] J. Langewis, C. and C. W. Gleeson, "Practical hydraulics of positive displacement pumps for high-pressure waterflood installations," *Journal of Petroleum Technology*, vol. 23, no. 02, pp. 173–179, 1971.

[49] J. F. Gülich, *Centrifugal Pumps*. Cham: Springer International Publishing, 4th 2020. ed., 2020.

[50] A. R. Al-Obaidi, "Investigation of effect of pump rotational speed on performance and detection of cavitation within a centrifugal pump using vibration analysis," *Heliyon*, vol. 5, no. 6, p. e01910, 2019.

[51] Y. M. Fouda, "A selection method of variable speed centrifugal pumps for maximum hydraulic efficiency," *Journal of the Brazilian Society of Mechanical Sciences and Engineering*, vol. 45, no. 11, p. 560, 2023.

[52] D. Popescu, "The control of variable speed pumps in series operation,"

[53] P. Casoli, C. M. Vescovini, F. Scolari, and M. Rundo, "Theoretical analysis of active flow ripple control in positive displacement pumps," *Energies*, vol. 15, no. 13, p. 4703, 2022.

[54] D. Bordeasu, O. Prostean, I. Filip, and C. Vasar, "Adaptive control strategy for a pumping system using a variable frequency drive," 2023.

[55] M. D. Biviano, M. V. Paludan, A. H. Christensen, E. V. Østergaard, and K. H. Jensen, "Smoothing oscillatory peristaltic pump flow with bioinspired passive components," *Physical Review Applied*, vol. 18, no. 6, p. 064013, 2022. PRAPPLIED.

[56] D. Bach, F. Schmich, T. Masselter, and T. Speck, "A review of selected pumping systems in nature and engineering—potential biomimetic concepts for improving displacement pumps and pulsation damping," *Bioinspiration and Biomimetics*, vol. 10, p. 051001, 2015.

[57] E. J. Challita, P. Rohilla, and M. S. Bhamla, "Fluid ejections in nature," *Annual review of chemical and biomolecular engineering*, vol. 15, no. 1, pp. 187–217, 2024.

[58] M. Salathe, "Regulation of mammalian ciliary beating," *Annual review of physiology*, vol. 69, no. 1, pp. 401–422, 2007.

[59] V. Kumar, Z. Umair, S. Kumar, R. S. Goutam, S. Park, and J. Kim, "The regulatory roles of motile cilia in csf circulation and hydrocephalus," *Fluids and barriers of the CNS*, vol. 18, no. 1, pp. 31–11, 2021.

[60] W. Ji, Z. Tang, Y. Chen, C. Wang, C. Tan, J. Liao, L. Tong, and G. Xiao, "Ependymal cilia: Physiology and role in hydrocephalus," *Frontiers in molecular neuroscience*, vol. 15, p. 927479, 2022.

[61] H. Ashraf, A. M. Siddiqui, and M. A. Rana, "Fallopian tube analysis of the peristaltic-ciliary flow of third grade fluid in a finite narrow tube," *Chinese Journal of Physics*, vol. 56, no. 2, pp. 605–621, 2018.

[62] B. J. Gemmell, J. O. Dabiri, S. P. Colin, J. H. Costello, J. P. Townsend, and K. R. Sutherland, "Cool your jets: biological jet propulsion in marine invertebrates," *Journal of experimental biology*, vol. 224, no. 12, 2021.

[63] M. J. McHenry and J. Jed, "The ontogenetic scaling of hydrodynamics and swimming performance in jellyfish (aurelia aurita)," *Journal of experimental biology*, vol. 206, no. 22, pp. 4125–4137, 2003.

[64] J. H. Costello, S. P. Colin, J. O. Dabiri, B. J. Gemmell, K. N. Lucas, and K. R. Sutherland, "The hydrodynamics of jellyfish swimming," *Annual review of marine science*, vol. 13, no. 1, pp. 375–396, 2021.

[65] J. M. Gosline and M. E. DeMont, "Jet-propelled swimming in squids," *Scientific American*, vol. 252, no. 1, pp. 96–103, 1985.

[66] I. K. Bartol, P. S. Krueger, W. J. Stewart, and J. T. Thompson, "Hydrodynamics of pulsed jetting in juvenile and adult brief squid lolliguncula brevis: evidence of multiple jet 'modes' and their implications for propulsive efficiency," *Journal of Experimental Biology*, vol. 212, no. 12, p. 1889, 2009.

[67] C. Roh, *Hydrodynamics of Insects. Part 1. Jetting of the Dragonfly Larvae. Part 2. Honeybee at the Air-water Interface: Surfing with the Capillary Wave*. Thesis.

[68] D. J. Coughlin, J. D. Chrostek, and D. J. Ellerby, "Intermittent propulsion in largemouth bass, micropterus salmoides, increases power production at low swimming speeds," *Biology Letters*, vol. 18, no. 5, p. 20210658, 2022. doi: 10.1098/rsbl.2021.0658.

[69] K. Liu, H. Huang, and X.-Y. Lu, "Hydrodynamic benefits of intermittent locomotion of a self-propelled flapping plate," *Physical Review E*, vol. 102, no. 5, p. 053106, 2020. PRE.

[70] L.-l. Kang, S.-x. Gong, X.-Y. Lu, W.-c. Cui, and D.-x. Fan, "Scaling laws for the intermittent swimming performance of a flexible plate at low reynolds number," *Journal of Hydrodynamics*, vol. 35, no. 4, pp. 803–810, 2023.

[71] A. Bejan, U. Gunes, and H. Almahmoud, "Locomotion rhythm makes power and speed," *Scientific Reports*, vol. 13, no. 1, p. 14018, 2023.

[72] D. L. Kramer and R. L. McLaughlin, "The behavioral ecology of intermittent locomotion1," *American Zoologist*, vol. 41, no. 2, pp. 137–153, 2015.

[73] M. O'Neil, J. Urquhart, A. Badhwar, and L. Guo, "Pulsatile versus nonpulsatile flow during cardiopulmonary bypass: Microcirculatory and systemic effects," *The Annals of thoracic surgery*, vol. 94, 2012.

[74] B. Ji and A. Undar, "An evaluation of the benefits of pulsatile versus nonpulsatile perfusion during cardiopulmonary bypass procedures in pediatric and adult cardiac patients," *Asaio j*, vol. 52, no. 4, pp. 357–61, 2006. Ji, Bingyang Undar, Akif Comparative Study Editorial Review United States 2006/08/03 ASAIO J. 2006 Jul-Aug;52(4):357-61. doi: 10.1097/01.mat.0000225266.80021.9b.

[75] D. Lu and G. S. Kassab, "Role of shear stress and stretch in vascular mechanobiology," *J R Soc Interface*, vol. 8, no. 63, pp. 1379–85, 2011. 1742-5662 Lu, Deshun Kassab, Ghassan S HL-055 554-12/HL/NHLBI NIH HHS/United States HL-084 529/HL/NHLBI NIH HHS/United States HL055 554-11/HL/NHLBI NIH HHS/United States HL084 529/HL/NHLBI NIH HHS/United States Journal Article Research Support, N.I.H., Extramural Review England 2011/07/08 J R Soc Interface. 2011 Oct 7;8(63):1379-85. doi: 10.1098/rsif.2011.0177. Epub 2011 Jul 6.

[76] J. Niebauer and J. P. Cooke, "Cardiovascular effects of exercise: role of endothelial shear stress," *J Am Coll Cardiol*, vol. 28, no. 7, pp. 1652–60, 1996. Niebauer, J Cooke, J P HL48638/HL/NHLBI NIH HHS/United States K07HC02660/HC/NHLBI NIH HHS/United States Journal Article Research Support, Non-U.S. Gov't Research Support, U.S. Gov't, P.H.S. United States 1996/12/01 J Am Coll Cardiol. 1996 Dec;28(7):1652-60. doi: 10.1016/S0735-1097(96)00393-2.

[77] M. C. Gash, P. F. Kandle, I. V. Murray, and M. A. Varacallo, *Physiology, Muscle Contraction*. Treasure Island (FL): StatPearls Publishing Copyright © 2025, StatPearls Publishing LLC., 2025. Gash, Matthew C Kandle, Patricia F Murray, Ian V Varacallo, Matthew A Study Guide Book Chapter Disclosure: Matthew Gash declares no relevant financial relationships with ineligible companies. Disclosure: Patricia Kandle declares no relevant financial relationships with ineligible companies. Disclosure: Ian Murray declares no relevant financial relationships with ineligible companies. Disclosure: Matthew Varacallo declares no relevant financial relationships with ineligible companies. NBK537140 [bookaccession].

[78] H. L. Sweeney and D. W. Hammers, "Muscle contraction," *Cold Spring Harb Perspect Biol*, vol. 10, no. 2, 2018. 1943-0264 Sweeney, H Lee Hammers, David W Journal Article Review United States 2018/02/09 Cold Spring Harb Perspect Biol. 2018 Feb 1;10(2):a023200. doi: 10.1101/cshperspect.a023200.

[79] A. V. Hill, "The heat of shortening and the dynamic constants of muscle," *Proceedings of the Royal Society of London. Series B, Biological sciences*, vol. 126, no. 843, pp. 136–195, 1938.

[80] C. Y. Seow, "Hill's equation of muscle performance and its hidden insight on molecular mechanisms," *J Gen Physiol*, vol. 142, no. 6, pp. 561–73, 2013. 1540-7748 Seow, Chun Y MOP-13271/Canadian Institutes of Health Research/Canada MOP-37924/Canadian Institutes of Health Research/Canada Journal Article Research Support, Non-U.S. Gov't Review United States 2013/11/28 J Gen Physiol. 2013 Dec;142(6):561-73. doi: 10.1085/jgp.201311107.

[81] K. Sagawa, *Cardiac contraction and the pressure-volume relationship*. New York ;: Oxford University Press, 1988.

[82] D. A. McDonald, W. W. Nichols, M. F. O'Rourke, E. R. Edelman, and C. Vlachopoulos, *McDonald's Blood flow in arteries : theoretical, experimental and clinical principles*. Florida, United States: Boca Raton, FL : CRC Press, 2024.

[83] R. Chaudry, J. Miao, and A. Rehman, "Physiology, cardiovascular," 2025.

[84] J. Pollock and A. Makaryus, "Physiology, cardiac cycle," 2025.

[85] OpenStax, *Anatomy and physiology, 2e*. Houston, Texas: OpenStax, 2e. ed., 2022. Includes bibliographical references and index. (Nonprofit organization).

[86] J. P. Mynard, A. Kondiboyina, R. Kowalski, M. M. H. Cheung, and J. J. Smolich, "Measurement, analysis and interpretation of pressure/flow waves in blood vessels," *Frontiers in physiology*, vol. 11, p. 1085, 2020.

[87] W. W. Chen, H. Gao, X. Y. Luo, and N. A. Hill, "Study of cardiovascular function using a coupled left ventricle and systemic circulation model," *Journal of biomechanics*, vol. 49, no. 12, pp. 2445–2454, 2016.

[88] A. P. Voorhees and H. C. Han, "Biomechanics of cardiac function," *Compr Physiol*, vol. 5, no. 4, pp. 1623–44, 2015. 2040-4603 Voorhees, Andrew P Han, Hai-Chao N01-HV-00244/HV/NHLBI NIH HHS/United States HL095852/HL/NHLBI NIH HHS/United States R01 HL075360/HL/NHLBI NIH HHS/United States R01 HL095852/HL/NHLBI NIH HHS/United States HHSN268201000036C/HL/NHLBI NIH HHS/United States Journal Article Research Support, N.I.H., Extramural Review United States 2015/10/02 Compr Physiol. 2015 Sep 20;5(4):1623-44. doi: 10.1002/cphy.c140070.

[89] K. D. Dwyer and K. L. K. Coulombe, "Cardiac mechanostructure: Using mechanics and anisotropy as inspiration for developing epicardial therapies in treating myocardial infarction," *Bioact Mater*, vol. 6, no. 7, pp. 2198–2220, 2021. 2452-199x Dwyer, Kiera D Coulombe, Kareen L K R01 HL135091/HL/NHLBI NIH HHS/United States Journal Article Review China 2021/02/09 Bioact Mater. 2021 Jan 20;6(7):2198-2220. doi: 10.1016/j.bioactmat.2020.12.015. eCollection 2021 Jul.

[90] W. Liu and Z. Wang, "Current understanding of the biomechanics of ventricular tissues in heart failure," 2020.

[91] R. E. Klabunde, W. Lippincott, and Wilkins, *Cardiovascular physiology concepts*. Philadelphia: Wolters Kluwer, 3rd edition ed., 2022.

[92] Y. Chen-Izu, T. Banyasz, J. A. Shaw, and L. T. Izu, "The heart is a smart pump: Mechanotransduction mechanisms of the frank-starling law and the anrep effect," *Annual Review of Physiology*, vol. 87, no. 1, pp. 53–77, 2025.

[93] S. Kosta and P. C. Dauby, "Frank-starling mechanism, fluid responsiveness, and length-dependent activation: Unravelling the multiscale behaviors with an in silico analysis," *PLoS Comput Biol*, vol. 17, no. 10, p. e1009469, 2021. 1553-7358 Kosta, Sarah Orcid: 0000-0001-8995-7391 Dauby, Pierre C Orcid: 0000-0002-7003-0059 Journal Article United States 2021/10/12 PLoS Comput Biol. 2021 Oct 11;17(10):e1009469. doi: 10.1371/journal.pcbi.1009469. eCollection 2021 Oct.

[94] W. W. Nichols, M. F. O'Rourke, and D. A. McDonald, *McDonald's blood flow in arteries : theoretical, experimental and clinical principles*. Blood flow in arteries, London: Hodder Arnold, sixth edition / wilmer w. nichols and michael f. o'rourke. ed., 2011. Includes bibliographical references and index.

[95] A. Noordergraaf, *Circulatory system dynamics*. Biophysics and bioengineering series ; v. 1, New York: Academic Press, 1978. Includes bibliographical references and index.

[96] V. Atti, M. A. Narayanan, B. Patel, S. Balla, A. Siddique, S. Lundgren, and P. Velagapudi, "A comprehensive review of mechanical circulatory support devices," *Heart international*, vol. 16, no. 1, p. 37, 2022.

[97] A. Vis, M. Arfaee, H. Khambati, M. S. Slaughter, J. F. Gummert, J. T. B. Overvelde, and J. Kluin, "The ongoing quest for the first total artificial heart as destination therapy," *Nature Reviews Cardiology*, vol. 19, no. 12, pp. 813–828, 2022.

[98] D. Masarone, R. Gravino, L. Falco, D. Catapano, F. Valente, C. Amarelli, C. Marra, M. Kittleson, P. D. Silverio, and E. d. Lorenzo, "The total artificial heart: A historical perspective," *Journal of clinical medicine*, vol. 14, no. 17, p. 6290, 2025.

[99] M. Shin, N. Ganjoo, O. Toubat, R. Shad, and P. Atluri, "Durable left ventricular assist devices: a contemporary review of their benefits and drawbacks," *Expert Review of Medical Devices*, vol. 21, no. 12, pp. 1111–1120, 2024. doi: 10.1080/17434440.2024.2433716.

[100] M. R. Mehra, J. C. Cleveland, N. Uriel, J. A. Cowger, S. Hall, D. Horstmanshof, Y. Naka, C. T. Salerno, J. Chuang, C. Williams, and D. J. Goldstein, "Primary results of long-term outcomes in the momentum 3 pivotal trial and continued access protocol study phase: a study of 2200 heartmate 3 left ventricular assist device implants," *European journal of heart failure*, vol. 23, no. 8, pp. 1392–1400, 2021.

[101] S. Zhao, C. Liu, J. Wang, H. Wang, T. Luo, X. Hao, X. Yang, M. Wen, J. Han, H. Zhang, and M. Gong, "Ch-vad left ventricular assist implantation combined with the bentall procedure and coronary artery bypass grafting," *ESC Heart Failure*, vol. 11, no. 4, pp. 2405–2409, 2024.

[102] P. Wu, K.-J. Zhang, W.-J. Xiang, and G.-T. Du, "Turbulent flow field in maglev centrifugal blood pumps of ch-vad and heartmate iii: secondary flow and its effects on pump performance," *Biomechanics and modeling in mechanobiology*, vol. 23, no. 5, pp. 1571–1589, 2024.

[103] J. H. Karimov, R. C. Starling, and K. Fukamachi, *Mechanical support for heart failure : current solutions and new technologies*. Cham, Switzerland: Springer, 1st ed., 2020. Includes bibliographical references and index.

[104] T. Snyder, A. Bourquin, F. Cornat, J. Biasetti, and C. Botterbusch, "Corwave lvad development update," *The Journal of heart and lung transplantation*, vol. 38, no. 4, pp. S341–S342, 2019.

[105] Corwave, "Corwave announces presentation of late breaking results from its first-in-human implant at hfsa annual scientific meeting," 2025.

[106] A. Razumov, M. Burri, A. Zittermann, D. Radakovic, V. Lauenroth, S. V. Rojas, H. Fox, R. Schramm, J. Gummert, M. Deutsch, and M. Morshuis, "Outcomes after syncardia® temporary total artificial heart implantation: A 20-year single-center experience in 196 patients," *Artificial organs*, vol. 49, no. 2, pp. 266–275, 2025.

[107] F. A. Arabía and C. F. Murray, "The total artificial heart: where have we been, where are we now, where are we going?," *Indian journal of thoracic and cardiovascular surgery*, vol. 39, no. Suppl 1, pp. 198–205, 2023.

[108] J. Malas, Q. Chen, A. Akhmerov, L. P. Tremblay, N. Egorova, A. Krishnan, J. Moriguchi, J. Kobashigawa, L. Czer, R. Cole, D. Emerson, J. Chikwe, F. Arabia, and F. Esmailian, "Experience with syncardia total artificial heart as a bridge to transplantation in 100 patients," *The Annals of thoracic surgery*, vol. 115, no. 3, pp. 725–732, 2023.

[109] A. Carpentier, C. Latrémouille, B. Cholley, D. M. Smadja, J.-C. Roussel, E. Boissier, J.-N. Trochu, J.-P. Gueffet, M. Treillot, P. Bizouarn, D. Méléard, M.-F. Boughenou, O. Ponzio, M. Grimmé, A. Capel, P. Jansen, A. Hagège, M. Desnos, J.-N. Fabiani, and D. Duveau, "First clinical use of a bioprosthetic total artificial heart: report of two cases," *The Lancet*, vol. 386, no. 10003, pp. 1556–1563, 2015.

[110] P. Mohacsi and P. Leprince, "The carmat total artificial heart," *European journal of cardio-thoracic surgery*, vol. 46, no. 6, pp. 933–934, 2014.

[111] Carmat, "Carmat announces filing today for insolvency and requesting being placed in receivership," 2025.

[112] A. M. Shah, “First successful implant of bivacor ’s total artificial heart,” *Artificial organs*, vol. 48, no. 10, pp. 1075–1076, 2024.

[113] A. E. Shafii, C. A. Milano, F. A. Arabia, R. D. Dowling, J. N. Schroder, O. L. Amabile, A. B. Civitello, A. D. Devore, R. S. Gopalan, M. Freundt, G. F. Egnaczyk, T. R. Powell, O. R. Suero, S. L. McCartney, A. B. Dahl, T. M. Gluck, N. A. Greatrex, M. Kleinheyer, W. Cohn, D. Timms, J. G. Rogers, and O. Frazier, “(148) - initial clinical experience with the bivacor total artificial heart,” *The Journal of heart and lung transplantation*, vol. 44, no. 4, pp. S73–S73, 2025.

[114] M. Zhu, T. N. Do, E. Hawkes, and Y. Visell, “Fluidic fabric muscle sheets for wearable and soft robotics,” *arXiv [cs.RO]*, 2019.

[115] J. Rogatinsky, D. Recco, J. Feichtmeier, Y. Kang, N. Kneier, P. Hammer, E. O’Leary, D. Mah, D. Hoganson, N. V. Vasilyev, and T. Ranzani, “A multifunctional soft robot for cardiac interventions,” *Science Advances*, vol. 9, no. 43, p. eadi5559. doi: 10.1126/sciadv.adi5559.

[116] M. Arfaee, A. Vis, P. A. A. Bartels, L. C. van Laake, L. Lorenzon, D. M. Ibrahim, D. Zrinscak, A. I. P. M. Smits, A. Henseler, M. Cianchetti, P. Y. W. Dankers, C. V. C. Bouten, J. T. B. Overvelde, and J. Kluin, “A soft robotic total artificial hybrid heart,” *Nature communications*, vol. 16, no. 1, pp. 5146–14, 2025.

[117] A. Weymann, J. Foroughi, R. Vardanyan, P. P. Punjabi, B. Schmack, S. Aloko, G. M. Spinks, C. H. Wang, A. Arjomandi Rad, and A. Ruhparwar, “Artificial muscles and soft robotic devices for treatment of end-stage heart failure,” *Advanced Materials*, vol. 35, no. 19, p. 2207390, 2023.

[118] D. Bluestein, K. B. Chandran, and K. B. Manning, “Towards non-thrombogenic performance of blood recirculating devices,” *Annals of biomedical engineering*, vol. 38, no. 3, pp. 1236–1256, 2010.

[119] M. R. Mehra, Y. Naka, N. Uriel, D. J. Goldstein, J. C. Cleveland, P. C. Colombo, M. N. Walsh, C. A. Milano, C. B. Patel, U. P. Jorde, F. D. Pagani, K. D. Aaronson, D. A. Dean, K. McCants, A. Itoh, G. A. Ewald, D. Horstmanshof, J. W. Long, and C. Salerno, “A fully magnetically levitated circulatory pump for advanced heart failure,” *The New England journal of medicine*, vol. 376, no. 5, pp. 440–450, 2017.

[120] S. Jana, “Endothelialization of cardiovascular devices,” *Acta biomaterialia*, vol. 99, pp. 53–71, 2019.

[121] K. H. Fraser, M. E. Taskin, B. P. Griffith, and Z. J. Wu, "The use of computational fluid dynamics in the development of ventricular assist devices," *Medical engineering and physics*, vol. 33, no. 3, pp. 263–280, 2011.

[122] W.-T. Wu, F. Yang, J. Wu, N. Aubry, M. Massoudi, and J. F. Antaki, "High fidelity computational simulation of thrombus formation in thoratec heartmate ii continuous flow ventricular assist device," *Scientific Reports*, vol. 6, no. 1, p. 38025, 2016.

[123] Y. Qu, Z. Guo, J. Zhang, G. Li, S. Zhang, and D. Li, "Hemodynamic investigation and in vitro evaluation of a novel mixed-flow blood pump," *Artificial organs*, vol. 46, no. 8, pp. 1533–1543, 2022.

[124] R. B. Shepard, D. C. Simpson, and J. F. Sharp, "Energy equivalent pressure," *Archives of Surgery*, vol. 93, no. 5, pp. 730–740, 1966.

[125] A. Undar, "Energy equivalent pressure formula is for precise quantification of different perfusion modes," *The Annals of thoracic surgery*, vol. 76, no. 5, pp. 1777–1778, 2003.

[126] A. Shiose, K. Nowak, D. J. Horvath, A. L. Massiello, L. A. R. Golding, and K. Fukamachi, "Speed modulation of the continuous-flow total artificial heart to simulate a physiologic arterial pressure waveform," *ASAIO journal (1992)*, vol. 56, no. 5, pp. 403–409, 2010.

[127] K. G. Soucy, G. A. Giridharan, Y. Choi, M. A. Sobieski, G. Monreal, A. Cheng, E. Schumer, M. S. Slaughter, and S. C. Koenig, "Rotary pump speed modulation for generating pulsatile flow and phasic left ventricular volume unloading in a bovine model of chronic ischemic heart failure," *The Journal of heart and lung transplantation*, vol. 34, no. 1, pp. 122–131, 2015.

[128] T. Pirbodaghi, C. Cotter, and K. Bourque, "Power consumption of rotary blood pumps: Pulsatile versus constant-speed mode: Power consumption of rotary blood pumps," *Artificial organs*, vol. 38, no. 12, pp. 1024–1028, 2014.

[129] K. H. Fraser, M. E. Taskin, B. P. Griffith, and Z. J. Wu, "The use of computational fluid dynamics in the development of ventricular assist devices," *Medical engineering and physics*, vol. 33, no. 3, pp. 263–280, 2011.

[130] R. Wolfe, A. Strother, S. Wang, A. Kunselman, and A. Undar, "Impact of pulsatility and flow rates on hemodynamic energy transmission in an adult extracorporeal life support system," *Artificial organs*, vol. 39, 2015.

[131] M. D. Jeronimo and D. E. Rival, “On the lifespan of recirculating suspensions with pulsatile flow,” *Journal of fluid mechanics*, vol. 928, 2021.

[132] J. Martin, *CFD Analysis Comparing Steady Flow and Pulsatile Flow Through the Aorta and its Main Branches*. 2016.

[133] Y. S. Morsi, “In vitro comparison of steady and pulsatile flow characteristics of jellyfish heart valve,” *Journal of artificial organs*, vol. 3, no. 2, pp. 143–148, 2000.

[134] S. Chun, I. C. Christov, and J. Feng, “Experimental investigation of the flow rate–pressure drop relation of a viscoelastic boger fluid in a deformable channel,” *Physical Review Applied*, vol. 24, no. 3, p. 034001, 2025. PRAPPLIED.

[135] Y. Kassif, M. Zilbershlag, M. Levi, A. Plotkin, and S. Schueler, “A new universal wireless transcutaneous energy transfer (tet) system for implantable lvads – preliminary in vitro and in vivo results,” *The Journal of heart and lung transplantation*, vol. 32, no. 4, pp. S140–S141, 2013.

[136] Y. Pya and A. Abdiorazova, “Elimination of drive exit line: transcutaneous energy transmission,” *Annals of cardiothoracic surgery*, vol. 10, no. 3, pp. 393–395, 2021.

[137] S. S. Nair, D. S. Nagesh, S. J. Shenoy, and S. Harikrishnan, “Performance evaluation of an automatically controlled transcutaneous energy transfer system powering left ventricular assist device,” *Artificial organs*, vol. 49, no. 3, pp. 390–400, 2025.

[138] R. K. Odor and D. M. Webber, “Invertebrate athletes - trade-offs between transport efficiency and power-density in cephalopod evolution,” *Journal of experimental biology*, vol. 160, no. 1, pp. 93–112, 1991.

[139] G. Schumacher, J. J. Kaden, and F. Trinkmann, “Multiple coupled resonances in the human vascular tree: refining the westerhof model of the arterial system,” *Journal of applied physiology (1985)*, vol. 124, no. 1, pp. 131–139, 2018.

[140] F. Clara, J. Alfie, G. Blanco, and A. Casarini, “Spectral analysis of arterial system resonance,” *Journal of Clinical Cardiology and Cardiology Research*, 2025.

[141] H. Bahramali, D. Melkonian, and O. O'Connell, "Self regulation of the heart: Natural frequency and damping of the heart contractions," *The open cybernetics and systemics journal*, vol. 2, no. 1, pp. 1–10, 2008.

[142] C. Papadacci, V. Finel, O. Villemain, M. Tanter, and M. Pernot, "4d ultrafast ultrasound imaging of naturally occurring shear waves in the human heart," *IEEE transactions on medical imaging*, vol. 39, no. 12, pp. 4436–4444, 2020.

[143] S. Collins, A. Ruina, R. Tedrake, and M. Wisse, "Efficient bipedal robots based on passive-dynamic walkers," *Science (American Association for the Advancement of Science)*, vol. 307, no. 5712, pp. 1082–1085, 2005.

[144] McGeer, "Passive dynamic walking," *The International Journal of Robotics Research*, vol. 9, no. 2, pp. 62–82, 1990. doi: 10.1177/027836499000900206.

[145] D. W. Haldane, M. M. Plecnik, J. K. Yim, and R. S. Fearing, "Robotic vertical jumping agility via series-elastic power modulation," *Science robotics*, vol. 1, no. 1, 2016.

[146] C. Zhang, W. Zou, L. Ma, and Z. Wang, "Biologically inspired jumping robots: A comprehensive review," *Robotics and Autonomous Systems*, vol. 124, p. 103362, 2020.

[147] M. Raibert, M. Chepponis, and H. Brown, "Running on four legs as though they were one," *IEEE journal of robotics and automation*, vol. 2, no. 2, pp. 70–82, 1986.

[148] S. Sangok, A. Wang, M. Y. Chuah, H. Dong Jin, L. Jongwoo, D. M. Otten, J. H. Lang, and K. Sangbae, "Design principles for energy-efficient legged locomotion and implementation on the mit cheetah robot," *IEEE/ASME transactions on mechatronics*, vol. 20, no. 3, pp. 1117–1129, 2015.

[149] M. Stosiak, P. Bury, and M. Karpenko, "The influence of hydraulic hose length on dynamic pressure waveforms including wave phenomena," *Scientific Reports*, vol. 15, no. 1, p. 31548, 2025.

[150] S. Kottapalli, R. van de Meerendonk, N. Waterson, G. Nakiboglu, A. Hirschberg, and D. M. J. Smeulders, "Analytical modelling and experimental validation of compliance-based low-frequency resonators for water circuits," *Acta acustica*, vol. 6, no. 7, pp. 56–1673, 2022.

[151] J. Ni, W. Xuan, Y. Li, J. Chen, W. Li, Z. Cao, S. Dong, H. Jin, L. Sun, and J. Luo, "Analytical and experimental study of a valveless piezoelectric micropump with high flowrate and pressure load," *Microsystems and nanoengineering*, vol. 9, no. 1, pp. 72–72, 2023.

[152] J. Wang, X. Zhao, X. Chen, and H. Yang, "A piezoelectric resonance pump based on a flexible support," *Micromachines (Basel)*, vol. 10, no. 3, p. 169, 2019.

[153] Y. Zhang, Z. Wang, Y. Zhao, Q. Wei, H. Zheng, D. Zhang, and X. Guo, "An integratible acoustic micropump based on the resonance of on-substrate sharp-edge micropillar arrays," *Lab on a chip*, vol. 25, no. 1, pp. 2338–2348, 2025.

[154] T. Bujard, F. Giorgio-Serchi, and G. D. Weymouth, "A resonant squid-inspired robot unlocks biological propulsive efficiency," *Science Robotics*, vol. 6, no. 50, p. eabd2971, 2021.

[155] R. M. Alexander, *Elastic mechanisms in animal movement*. Cambridge: Cambridge University Press, 1988.

[156] R. Blickhan, "The spring-mass model for running and hopping," *Journal of biomechanics*, vol. 22, no. 11, pp. 1217–1227, 1989.

[157] D. P. Ferris, M. Louie, and C. T. Farley, "Running in the real world: adjusting leg stiffness for different surfaces," *Proceedings of the Royal Society B : Biological Sciences*, vol. 265, no. 1400, pp. 989–994, 1998.

[158] C. T. Farley, R. Blickhan, J. Saito, and C. R. Taylor, "Hopping frequency in humans: a test of how springs set stride frequency in bouncing gaits," *Journal of applied physiology (1985)*, vol. 71, no. 6, pp. 2127–2132, 1991.

[159] C. T. Farley and O. González, "Leg stiffness and stride frequency in human running," *Journal of biomechanics*, vol. 29, no. 2, pp. 181–186, 1996.

[160] R. Kram and C. R. Taylor, "Energetics of running: a new perspective," *Nature (London)*, vol. 346, no. 6281, pp. 265–267, 1990.

[161] R. J. Pewowaruk and A. D. Gepner, "Smooth muscle tone alters arterial stiffness: the importance of the extracellular matrix to vascular smooth muscle stiffness ratio," *J Hypertens*, vol. 40, no. 3, pp. 512–519, 2022. 1473-5598 Pewowaruk, Ryan J Gepner, Adam D T32 HL007936/HL/NHLBI

NIH HHS/United States Journal Article Research Support, N.I.H., Extramural Netherlands 2021/11/10 J Hypertens. 2022 Mar 1;40(3):512-519. doi: 10.1097/HJH.0000000000003039.

[162] P. Lacolley, V. Regnault, P. Segers, and S. Laurent, "Vascular smooth muscle cells and arterial stiffening: Relevance in development, aging, and disease," *Physiological Reviews*, vol. 97, no. 4, pp. 1555–1617, 2017. doi: 10.1152/physrev.00003.2017.

[163] M. J. Herzog, P. Müller, K. Lechner, M. Stiebler, P. Arndt, M. Kunz, D. Ahrens, A. Schmeißer, S. Schreiber, and R. C. Braun-Dullaeus, "Arterial stiffness and vascular aging: mechanisms, prevention, and therapy," *Signal Transduction and Targeted Therapy*, vol. 10, no. 1, p. 282, 2025.

[164] V. R. Ham, T. G. Sugar, B. Vanderborght, K. W. Hollander, and D. Lefeber, "Compliant actuator designs: Review of actuators with passive adjustable compliance/controllable stiffness for robotic applications," *IEEE robotics and automation magazine*, vol. 16, no. 3, pp. 81–94, 2009.

[165] G. Grioli, S. Wolf, M. Garabini, M. Catalano, E. Burdet, D. Caldwell, R. Carloni, W. Friedl, M. Grebenstein, M. Laffranchi, D. Lefeber, S. Stramigioli, N. Tsagarakis, M. van Damme, B. Vanderborght, A. Albu-Shaeffer, and A. Bicchi, "Variable stiffness actuators: the user's point of view," *The International journal of robotics research*, vol. 34, no. 6, pp. 727–743, 2015.

[166] L. C. Visser, R. Carloni, and S. Stramigioli, "Energy-efficient variable stiffness actuators," *IEEE transactions on robotics*, vol. 27, no. 5, pp. 865–875, 2011.

[167] E. Mobedi and M. Can Dede, "A continuously variable transmission-based variable stiffness actuator for phri: Design optimization and performance verification," *Journal of mechanisms and robotics*, vol. 16, no. 8, 2024.

[168] J. Hur, H. Song, and S. Jeong, "Continuously variable transmission and stiffness actuator based on actively variable four-bar linkage for highly dynamic robot systems," *IEEE robotics and automation letters*, vol. 9, no. 8, pp. 7118–7125, 2024.

[169] J. E. Shigley, *Shigley's mechanical engineering design*. Tata McGraw-Hill Education, 2011.

[170] A. Mekaouche, F. Chapelle, and X. Balandraud, "A compliant mechanism with variable stiffness achieved by rotary actuators and shape-memory alloy," *Meccanica (Milan)*, vol. 53, no. 10, pp. 2555–2571, 2018.

[171] D. Nalini, D. Josephine Selvarani Ruth, and K. Dhanalakshmi, "Investigation of functional characteristics of a synergistically configured parallel-type shape memory alloy variable stiffness actuator," *Journal of intelligent material systems and structures*, vol. 30, no. 12, pp. 1772–1788, 2019.

[172] F. Jin, C. Zang, G. Xing, Y. Ma, S. Yuan, and Z. Jia, "Resonant peak reduction of a rotor system based on gradually variable stiffness of supports with shape memory alloy springs," *Journal of sound and vibration*, vol. 591, pp. 118626–, 2024.

[173] E. I. Rivin, *Nonlinear and Variable Stiffness Systems; Preloading*, p. 0. ASME Press, 2010.

[174] C. English and D. Russell, "Implementation of variable joint stiffness through antagonistic actuation using rolamite springs," *Mechanism and machine theory*, vol. 34, no. 1, pp. 27–40, 1999.

[175] G. Tonietti, R. Schiavi, and A. Bicchi, "Design and control of a variable stiffness actuator for safe and fast physical human/robot interaction," in *Proceedings of the 2005 IEEE International Conference on Robotics and Automation*, pp. 526–531, IEEE, 2005.

[176] J. W. Hurst, J. E. Chestnutt, and A. A. Rizzi, "An actuator with physically variable stiffness for highly dynamic legged locomotion," vol. 5, pp. 4662–4667 Vol.5, IEEE.

[177] M. H. Raibert, *Legged robots that balance*. MIT Press series in artificial intelligence, Cambridge, Mass. ;: MIT, 1986.

[178] K. C. Galloway, J. E. Clark, and D. E. Koditschek, "Variable stiffness legs for robust, efficient, and stable dynamic running," *Journal of mechanisms and robotics*, vol. 5, no. 1, pp. 1–11, 2013.

[179] T. W. Secord, H. H. Asada, J. Trinkle, J. A. Castellanos, and Y. Matsuoka, *Cellular Muscle Actuators with Variable Resonant Frequencies*, vol. 5, pp. 249–256. United States: The MIT Press, 2010.

[180] S. Wolf, G. Grioli, O. Eiberger, W. Friedl, M. Grebenstein, H. Höppner, E. Burdet, D. G. Caldwell, R. Carloni, M. G. Catalano, D. Lefeber, S. Stramigioli, N. Tsagarakis, M. V. Damme, R. V. Ham, B. Vanderborght, L. C. Visser, A. Bicchi, and A. Albu-Schäffer, "Variable stiffness actuators: Review on design and components," *IEEE/ASME Transactions on Mechatronics*, vol. 21, no. 5, pp. 2418–2430, 2016.

[181] L. Kangkang, H. Jiang, S. Wang, and J. Yu, "A soft robotic fish with variable-stiffness decoupled mechanisms," *Journal of Bionic Engineering*, vol. 15, pp. 599–609, 2018.

[182] P. Lu, B. Dong, X. Gao, F. Zhang, Y. Song, Z. Liu, and Z. Zhang, "Variable-stiffness underwater robotic systems: A review," 2025.

[183] A. Nascimbene, D. Bark, and D. M. Smadja, "Hemocompatibility and biophysical interface of left ventricular assist devices and total artificial hearts," *Blood*, vol. 143, no. 8, pp. 661–672, 2024. 1528-0020 Nascimbene, Angelo Bark, David Orcid: 0000-0002-9865-6176 Smadja, David M Orcid: 0000-0001-7731-9202 R01 HL163549/HL/NHLBI NIH HHS/United States R01 HL164424/HL/NHLBI NIH HHS/United States R21 EB034579/EB/NIBIB NIH HHS/United States Journal Article Research Support, N.I.H., Extramural Research Support, Non-U.S. Gov't Review United States 2023/10/27 Blood. 2024 Feb 22;143(8):661-672. doi: 10.1182/blood.2022018096.

[184] A. Ahmed, *Biocompatible materials of pulsatile and blood rotary pumps*. 2020.

[185] P. Baisamy, "A scalable monolithic 3d printable variable stiffness mechanism." Available at: https://github.com/pbaisamy/A-scalable-monolithic-3D-printable-variable-stiffness-mechanism, 2023. GitHub.

[186] F. Cosmi and A. Dal Maso, "A mechanical characterization of sla 3d-printed specimens for low-budget applications," *MATERIALS TODAY-PROCEEDINGS*, vol. 32, pp. 194–201, 2020.

[187] W. D. Callister, *Fundamentals of materials science and engineering : an interactive e-text / William D. Callister, Jr.* New York ;: Wiley, 2001. Includes bibliographical references and index.

[188] Formlabs, "Materials library," 2019.

[189] L. M. Tips, "Voice coil actuator basics," 2025.

[190] BioVisUser123, “Human heart model. version 2.1.,” 2024.

[191] M. F. Khandaker, H. Hong, and L. Rodrigues, “Modeling and controller design for a voice coil actuated engine valve,” pp. 1234–1239, IEEE.

[192] R. Oboe, F. Marcassa, and G. Maiocchi, “Hard disk drive with voltage-driven voice coil motor and model-based control,” *IEEE transactions on magnetics*, vol. 41, no. 2, pp. 784–790, 2005.

[193] R. Bhatia, *Fourier series*. Classroom resource materials, Washington: Mathematical Association of America, 1st ed., 2005. Includes bibliographical references (p. 113-115) and indexes.

[194] W. Bolton, *Fourier series*. Mathematics for engineers ; 4, Harlow: Longman Scientific and Technical, 1995.

[195] J. R. Womersley, “Method for the calculation of velocity, rate of flow and viscous drag in arteries when the pressure gradient is known,” *The Journal of physiology*, vol. 127, no. 3, pp. 553–563, 1955.

[196] E. Rodriguez, M. Paredes, and M. Sartor, “Analytical behavior law for a constant pitch conical compression spring,” *Journal of mechanical design (1990)*, vol. 128, no. 6, pp. 1352–1356, 2006.

[197] N. Westerhof and B. E. Westerhof, “Waves and windkessels reviewed,” *Artery research*, vol. 18, no. 1, pp. 102–111, 2017.

[198] B. E. Westerhof and N. Westerhof, “Magnitude and return time of the reflected wave: the effects of large artery stiffness and aortic geometry,” *Journal of hypertension*, vol. 30, no. 5, pp. 932–939, 2012.

[199] K. H. Parker, “introduction to wave intensity analysis,” *Medical biological engineering computing*, vol. 47, no. 2, pp. 175–188, 2009.

[200] J. P. Mynard, A. Kondiboyina, R. Kowalski, M. M. H. Cheung, and J. J. Smolich, “Measurement, analysis and interpretation of pressure/flow waves in blood vessels,” *Frontiers in physiology*, vol. 11, pp. 1085–, 2020.

[201] H. Fok, A. Guilcher, Y. Li, S. Brett, A. Shah, B. Clapp, and P. Chowienczyk, “Augmentation pressure is influenced by ventricular contractility/relaxation dynamics,” *Hypertension*, vol. 63, no. 5, pp. 1050–1055, 2014.

[202] N. Westerhof, "Cardiac work and efficiency," *Cardiovascular Research*, vol. 48, no. 1, pp. 4–7, 2000.

[203] E. Hajiesmaili and D. R. Clarke, "Dielectric elastomer actuators," *Journal of Applied Physics*, vol. 129, no. 15, p. 151102, 2021.

[204] M. H. Elahinia, *Shape memory alloy actuators : design, fabrication, and experimental evaluation*. Chichester, West Sussex: John Wiley and Sons, Ltd., 2015. Includes bibliographical references and index.

[205] B. Kalita, A. Leonessa, and S. K. Dwivedy, "A review on the development of pneumatic artificial muscle actuators: Force model and application," 2022.

[206] J. Zhang, J. Sheng, C. T. Oneill, C. J. Walsh, R. J. Wood, J. H. Ryu, J. P. Desai, and M. C. Yip, "Robotic artificial muscles: Current progress and future perspectives," *IEEE transactions on robotics*, vol. 35, no. 3, pp. 1–21, 2019.

[207] H. Deng, X. Lian, and X. Gong, "A brief review of variable stiffness and damping magnetorheological fluid dampers," *Frontiers in materials*, vol. 9, 2022.

[208] D. Narvaez and B. Newell, "A review of electroactive polymers in sensing and actuator applications," 2025.

[209] T. Atakuru, G. Züngör, and E. Samur, "Layer jamming of magnetorheological elastomers for variable stiffness in soft robots," *Experimental Mechanics*, vol. 64, no. 3, pp. 393–404, 2024.

[210] S. K. Singh, M. Kachel, E. Castillero, Y. Xue, D. Kalfa, G. Ferrari, and I. George, "Polymeric prosthetic heart valves: A review of current technologies and future directions," *Front Cardiovasc Med*, vol. 10, p. 1137827, 2023. 2297-055x Singh, Sameer K Kachel, Mateusz Castillero, Estibaliz Xue, Yingfei Kalfa, David Ferrari, Giovanni George, Isaac Journal Article Review Switzerland 2023/03/28 Front Cardiovasc Med. 2023 Mar 9;10:1137827. doi: 10.3389/fcvm.2023.1137827. eCollection 2023.

[211] A. Ertas, E. Farley-Talamantes, O. Cuvalci, and O. Gecgel, "3d-printing of artificial aortic heart valve using uv-cured silicone: Design and performance analysis," 2025.

[212] K. A. Brookshier and J. M. Tarbell, "Evaluation of a transparent blood analog fluid: aqueous xanthan gum/glycerin," *Biorheology*, vol. 30, no. 2, pp. 107–16,

1993. Brookshier, K A Tarbell, J M HL35549/HL/NHLBI NIH HHS/United States Journal Article Research Support, U.S. Gov't, P.H.S. United States 1993/03/01 Biorheology. 1993 Mar-Apr;30(2):107-16. doi: 10.3233/bir-1993-30202.

[213] S. H. Sadek, M. Rubio, R. Lima, and E. J. Vega, "Blood particulate analogue fluids: A review," *Materials (Basel)*, vol. 14, no. 9, 2021. 1996-1944 Sadek, Samir Hassan Orcid: 0000-0001-6129-4231 Rubio, Manuel Orcid: 0000-0002-2380-9545 Lima, Rui Orcid: 0000-0003-3428-637x Vega, Emilio José Orcid: 0000-0003-1891-0531 PID2019-108278RB/Spanish Ministry of Science and Education/ GR18175 and IB18005/Junta de Extremadura (Spain)/ UIDB/04077/2020, UIDB/00532/2020/Fundação para a Ciência e a Tecnologia (FCT)/ project NORTE-01-0145-FEDER-030171 (PTDC/EME-SIS/30171/2017)/COMPETE2020, NORTE 2020, PORTUGAL 2020, Lisb@2020 and FEDER/ Journal Article Review Switzerland 2021/06/03 Materials (Basel). 2021 May 9;14(9):2451. doi: 10.3390/ma14092451.

[214] Y. Cho and K. Kensey, "Effects of the non-newtonian viscosity of blood on flows in a diseased arterial vessel. part 1: Steady flows," *Biorheology*, vol. 28, pp. 241–62, 1991.

[215] M. Wu, D. Zheng, Y. Xu, Z. Zheng, C. Yv, X. Chen, and H. Fan, "Development and performance testing of an ecmo ultrasonic blood flow sensor," *Flow measurement and instrumentation*, vol. 106, p. 103040, 2025.

[216] D. Padovani, M. Rundo, and G. Altare, "The working hydraulics of valve-controlled mobile machines: Classification and review," *Journal of Dynamic Systems, Measurement, and Control*, vol. 142, 2020.

[217] R. Li, W. Wei, Y. Lai, H. Lu, T. Cao, J. Ye, and H. Liu, "Experimental and numerical study on valve dynamic impact contact characteristics and fault diagnosis of a reciprocating piston pump," *Sci Prog*, vol. 108, no. 1, p. 368504251325327, 2025. 2047-7163 Li, Ran Orcid: 0000-0002-1359-7024 Wei, WenShu Lai, YueHua Orcid: 0000-0002-8071-3507 Lu, HaiCheng Cao, TianZe Ye, Jian Liu, Hao Journal Article England 2025/03/17 Sci Prog. 2025 Jan-Mar;108(1):368504251325327. doi: 10.1177/00368504251325327. Epub 2025 Mar 17.

[218] K.-W. Xu, Q. Gao, M. Wan, and K. Zhang, "Mock circulatory loop applications for testing cardiovascular assist devices and in vitro studies," *Frontiers in physiology*, vol. 14, p. 1175919, 2023.

[219] W. Hong, V. Tewari, J. Chen, A. P. Sawchuk, and H. Yu, "A comprehensive review of mock circulation loop systems for experimental hemodynamics of cardiovascular diseases," 2025.

[220] T. Al-Hababi, M. Cao, B. Saleh, N. F. Alkayem, and H. Xu, "A critical review of nonlinear damping identification in structural dynamics: Methods, applications, and challenges," *Sensors (Basel)*, vol. 20, no. 24, 2020. 1424-8220 Al-Hababi, Tareq Orcid: 0000-0001-5992-8055 Cao, Maosen Saleh, Bassiouny Orcid: 0000-0001-5239-2673 Alkayem, Nizar Faisal Orcid: 0000-0002-6598-8713 Xu, Hao No. MS22019016/Nantong Science and Technology Plan Project/ No. 2019Z02/Transportation Science Research Project of Jiangsu Province/ Journal Article Review Switzerland 2020/12/24 Sensors (Basel). 2020 Dec 19;20(24):7303. doi: 10.3390/s20247303.

[221] M. Heredia-Pérez, D. A. Alvarez, and D. Bedoya-Ruiz, "A state-of-the-art review of the bouc-wen class model of hysteresis: Origin, evolution and current state," *Archives of Computational Methods in Engineering*, 2025.

[222] A. D. Hughes and K. H. Parker, "Forward and backward waves in the arterial system: impedance or wave intensity analysis?," *Medical biological engineering computing*, vol. 47, no. 2, pp. 207–210, 2009.

[223] F. Giorgio-Serchi and G. D. Weymouth, "Drag cancellation by added-mass pumping," *Journal of Fluid Mechanics*, vol. 798, p. R3, 2016.

[224] S. C. Steele, G. D. Weymouth, and M. S. Triantafyllou, "Added mass energy recovery of octopus-inspired shape change," *Journal of fluid mechanics*, vol. 810, pp. 155–174, 2017.

[225] J. M. Bliley, M. A. Stang, A. Behre, and A. W. Feinberg, "Advances in 3d bioprinted cardiac tissue using stem cell-derived cardiomyocytes," *Stem Cells Translational Medicine*, vol. 13, no. 5, pp. 425–435, 2024.

[226] D. Kalhori, N. Zakeri, M. Zafar-Jafarzadeh, L. Moroni, and M. Solati-Hashjin, "Cardiovascular 3d bioprinting: A review on cardiac tissue development," *Bioprinting*, vol. 28, p. e00221, 2022.

[227] D. Zhang, R. He, Y. Qu, C. He, and B. Chu, "Application of biomaterials in cardiac tissue engineering: Current status and prospects," *MedComm – Biomaterials and Applications*, vol. 3, no. 4, p. e103, 2024.